UNIVERSITY OF OXFORD

Characterisation and modelling of biodegradable biomedical fibres

Thales (Θαλήζ) ZANETTI FERREIRA

DEPARTMENT OF ENGINEERING SCIENCE
SOLID MECHANICS & MATERIALS ENGINEERING GROUP
EXETER COLLEGE

A thesis submitted for the degree of
DOCTOR OF PHILOSOPHY

Michaelmas 2025

Dedication

This thesis is dedicated to my family: Mauricio, Christiana, Luigi, Pietro, and Chiara; and to my supervisor, *Prof. Laurence Brassart.*

To my family, especially my parents, whose unwavering love and personal sacrifices paved the way for this opportunity and moulded me in more ways than I can count. You opened doors to opportunities, relentlessly encouraged me to pursue a greater purpose, and stood with me through the hardest stretches. Without you, I would not be the person I am today, nor would I have believed in what I could achieve.

A special note to my mother, *Dr. Christiana Zanetti*, father, *Mr. Mauricio Ferreira*, and my younger brother, *Dr. Luigi Zanetti.* In the final months of my undergraduate degree, one of the most demanding periods of my life, you carried me through the storm of deadlines, exams, and interviews. All of you turned our kitchen (a.k.a. Gladstone Street University) into a 24-hour support hub. You supported me with interview preparation, continuous feedback sessions, and being extra brain-power when I could no longer think. The family emotional support and guidance helped me focus on the most important opportunity before me, so that one day I could dream of pursuing a DPhil. Thank you for laying the foundation of this journey; I dedicate this work to my family in the hope it makes you proud.

To my supervisor, *Prof. Laurence Brassart*, whose remarkable dedication, rigour, and achievements continue to inspire. Thank you for believing in me, inviting me to see science through a new lens, and holding me to the highest standards. From our early scholarship searches to the submission of this thesis, your support has been steady and transformative. Most importantly, you changed the trajectory of my life. Studying at Oxford is something I never imagined possible; the door you opened helped me build faith, confidence, and grit to meet the challenges I am bound to face in my lifetime. My time at Oxford has been one of the most magical, formative and joyful periods of my life. For this, I am deeply and enduringly grateful.

Acknowledgements

Professional

First and foremost, I would like to express my deepest gratitude to *Prof. Laurence Brassart* for your unwavering support and guidance throughout this journey. Your work ethic, insistence on excellence, ingenuity, and depth of understanding continually inspired me to raise my standards and push beyond limits I did not know I had. Like any long journey, we encountered difficult moments, both in the research itself and in the natural challenges of collaboration, but your composure, clarity of thought, and steady leadership never faltered. Beyond your technical expertise, I am especially grateful for your ability to challenge my thinking while still providing the support needed to grow in confidence and independence as a researcher. You encouraged me to approach problems with rigour and creativity, and to develop a deeper appreciation for both the theoretical and practical aspects of scientific work. Your mentorship has influenced not only this thesis but also my outlook on life, providing perspectives that continue to shape how I think and grow. You have been an outstanding supervisor, offering invaluable mentorship and clear direction from the very beginning of my DPhil to its completion. I am profoundly grateful for all your support; I would not have made it here without you.

I would also like to extend my heartfelt thanks to *Prof. Pierre-Alexis Mouthuy* for your continued support and guidance throughout my DPhil project. Your insight, encouragement, and generosity with your time and expertise have been greatly appreciated. You provided thoughtful perspectives, particularly at key stages of the project, which helped to refine both the direction and the quality of this work. I am especially grateful for your constructive feedback and for fostering a collaborative and supportive research environment. Your contributions have played an important role in shaping this thesis, and I sincerely appreciate your guidance throughout.

To *Prof. Julie Karel*, who mentored me even before the start of my DPhil, thank you for encouraging me to take this leap and embrace the journey ahead. From the early days of writing my application, through your annual check-ins, guidance, and care, you reminded me that I was never alone in this process. It has truly been 100% worth it, and I am deeply grateful for the way you looked out for me. I hope that one day I can support Axel and Zelda with the same kindness, generosity, and belief that you showed me.

My warmest thanks go to the members of Brassart and Mouthuy labs, who have continually supported me throughout this process. To name only a few: Dr. Lucas Mangas, Prof. Zhouzhou Pan (the most beautiful man), Yifei Bai, Jie Zhu, and Dr. Huanming (Jimmy) Chen from the Brassart Lab; and Nicole, Giulia, Kaili, and Tania from the Mouthuy Lab. I owe a special debt of gratitude to *Dr. Gordon Kumar*. You have been my anchor. Your patience, kindness, and wisdom guided me through some of my darkest and most overwhelming moments. Beyond the science, you gave me friendship, coffee breaks that became therapy sessions, balcony chats that healed the spirit, donut days that reminded me to smile, and conversations about life that left me stronger. I can truly say that this DPhil would not exist without you. Thank you, from the bottom of my heart.

To members of staff of the engineering department, especially Dr. Aaron Graham, Dr. Nick Hawkins and Dr. Igor Dyson, thank you for all the experimental support, invaluable guidance, and your willingness to share knowledge. Thank you for keeping an eye on me, your advice, constant encouragement, and practical help with experiments ensured I stayed on the right track; I am immensely grateful for your watchfulness and generosity.

Personal

Beyond the academic sphere, I would like to express my heartfelt gratitude to the friendships that have shaped and sustained me throughout the past few years. Beginning with the Lunch Boys: Alex Swallow, Miles Judd, Gordon Kumar, Daniel McNamara, and Marcel Seger, who were a constant source of laughter, perspective, and joy during my time at Oxford. Our lunches were often outrageous, always memorable, and provided a much-needed counterbalance to the demands of research. Thank you for having been among my closest friends and offered unwavering emotional support, honest advice, and encouragement when it mattered most.

I am also grateful to my friends in the Engineering Department: Lizzi, Yanis, Tim, Phoebe, Alice, Aaron, Peihao, and many others, who made the department a more welcoming and vibrant place. Each conversation, shared coffee, or chance encounter in the corridors or pub brought lightness to long days, and I am thankful for the sense of community you all helped create.

I would also like to extend my sincere gratitude to the extra-curricular communities that provided not only moments of rest and mental clarity, but also discipline, camaraderie, and joy throughout this

journey. While they occasionally delivered a fair share of physical pain, they consistently lifted my spirits and helped me persevere during demanding periods. In particular, I am grateful to the Exeter College Middle Common Room, Exeter College Football Club, the Oxford University Triathlon Club, and the Oxford University Salsa Society community and Performance Team for fostering a sense of balance, belonging, and well-being during my time at Oxford.

A huge thank you to the Exeter College staff (especially kitchen) for looking after me throughout my degree and ensuring that I was always well fed. Your warmth and generosity made the college feel like a home away from home, and I am sincerely grateful for the care you showed every day. Special thanks to Ramesh, Liby, Jonny, Natasha, Elena, Meba, Sandra, and all the others whose hard work, kindness, and dedication so often went unnoticed but made a genuine difference to my daily life.

A special thank you goes to the many individuals who crossed my path during this journey and helped make it as rich and memorable as it has been: Lilli, Milot, Kin, Lila, Gina (GG Biceps), Yann, Martina, Gianluca, Rachel, Fiona, Mia, Sofia, Jemima, Katie, Angus, Pedro, Howie, Laly, Awa, Alex, Sergio, Duncan, Brianna, Assata, Ellie, Francesca and the countless friends who brought joy, laughter, and lightness into my life along the way. Each of you, in different moments and contexts, contributed to a sense of community and belonging that extended far beyond the academic sphere, making Oxford a place that will remain magical and enduring in my life. Among these connections, a special mention goes to Sofia Medina. Thank you for reminding me of the importance of staying true to oneself and approaching others with kindness and sincerity. Having our paths cross again after so many years was a powerful reminder of how enduring genuine friendships can be, and reconnecting with you has been profoundly special.

I wish to express my heartfelt thanks to Jone de Roode Jauregi for your unwavering support throughout the last stretch of the journey. Your patience, understanding, and emotional generosity were a constant source of strength during moments of uncertainty, grounding me and reminding me of what truly matters beyond deadlines and expectations. I am grateful for the love, reassurance, and stability you provided when everything felt overwhelming.

Finally, to my family, thank you for everything you have done for me. Your unconditional support, encouragement, and belief in me have been the foundation upon which this work, and much more, has been built. You have given me the freedom to pursue my ambitions, the confidence to trust myself, and the reassurance that I was never alone, no matter how challenging the path became. I am profoundly grateful for your sacrifices, patience, and constant presence throughout this journey.

"We didn't realise we were making memories. We just knew we were having fun."

— Winnie the Pooh

Abstract

Biodegradable fibrous scaffolds offer a route for soft tissue repair by providing temporary mechanical support while eliminating the need for retrieval surgery. Among fabrication techniques, electrospinning enables the production of micro- and nanoscale fibrous architectures that resemble the hierarchical structure of native tendons and ligaments. The fabrication of continuous electrospun filaments further allows textile processing, such as braiding, to produce scaffolds with tailored mechanical properties. However, translating these materials into biomedical implants requires an understanding of their microstructure, mechanical behaviour, and stability under physiological and degradative conditions. This thesis addresses these challenges through a systematic experimental investigation of electrospun poly(ε-caprolactone) filaments, combining thermal analysis, mechanical testing, topographical characterisation, and constitutive modelling. Mechanical characterisation using dynamic mechanical analysis and uniaxial tensile testing revealed an initially linear elastic response followed by plastic yielding with two-stage hardening, which was correlated with microstructural evolution observed via SEM, including fibre disentanglement, alignment, and stretching. A large-deformation viscoelastic–viscoplastic constitutive model was developed and shown to capture the filament response under non-monotonic loading. The measured mechanical response was found to depend strongly on the gripping configuration, highlighting implications on strain measurement accuracy and microstructural evolution. The thesis further examined degradation under combined thermal and mechanical loading, showing that pre-stretched filaments undergo molecular degradation over short time scales, with applied tensile loads accelerating the degradation rate. Degradation-induced microstructural changes increased stiffness and strength but reduced ductility with exposure time, demonstrating the coupling between mechanical loading, degradation kinetics, and evolving filament properties. To this end, this work establishes links between processing, structure, thermo-mechanical response, and degradation behaviour, informing the design of electrospun fibrous scaffolds for tendon and ligament repair.

Contents

Chapter 1

Introduction

1.1 General Introduction

The anterior cruciate ligament (ACL) plays an important role in providing mechanical and rotational stability to the knee joint, but can be easily ruptured due to excessive twisting. ACL tears are especially common in young and active individuals performing athletic activities, leading to significant long-term complications, reducing physical activity and quality of life. In the United States alone, approximately 100,000-200,000 acute ACL ruptures have been reported each year and around 15,000-20,000 in the United Kingdom (Gabr and Haddad, 2022; Sanders et al., 2016). Surgical intervention involving the use of an autologous hamstring or patellar tendon autograft is often the outcome considered. Unfortunately, around 15-20% of cases face complications, such as donor site morbidity and often require revision for second surgery (Kartus et al., 2001; Nau and Teuschl, 2015). In the long term, individuals who have undergone ACL reconstruction have demonstrated recurrent knee instability and increased susceptibility to developing knee osteoarthritis (Lohmander et al., 2004; Roos, 2005). The ACL's limited healing capability and consequent need for reconstructive surgery has become an enticing challenge for tissue engineering, whereby substituting autologous tissue with artificial grafts or ligament devices offer a promising future for the decreasing need in ligament grafting procedures and reducing the risks associated with them.

Several artificial scaffolds have been proposed for tendon and ligament reconstruction, but minimal success has been reported. Approaches using of natural biopolymers, such as collagen fibrils (Bellincampi et al., 1998; Dunn et al., 1995) and chitosan (Majima et al., 2005) have reported inadequate mechanical strength relative to a natural ACL. Alternatively, non-degradable synthetic polymers, including nylon (Legnani et al., 2010), poly-(tetrafluoroethylene) (PTFE) (Dahlstedt et al., 1990; Indelicato et al., 1989; Paulos et al., 1992), and polyester (Barrett et al., 1993; Lukianov et al., 1989; Pinar and Gillquist, 1989) have also been proposed. While these materials possess the mechanical strength, are easily accessible, and manufactured, they often suffer from permanent elongation and poor fatigue life leading to device failure. Additionally, long-term problems involving chronic tissue inflammation and device rejection were also reported. As a result, the lack of success in these methods have driven innovative approaches in leveraging the principles of soft tissue augmentation and regenerative repair, focusing on preserving the native ligament while enhancing its healing capabilities. This paradigm shift is driving a new design for biomaterials scaffolds. Ideally, novel devices should be biocompatible and biodegradable to be safely absorbed by the body after fulfilling their intended functions, thereby suppressing the need for a secondary device retrieval surgery and avoiding long-term health risks with permanent devices being in the body (Casalini, 2017; Laycock et al., 2017; Li et al., 2020). Nevertheless, biomaterials should also be carefully designed to maintain mechanical integrity during the implantation to shield nascent tissue from excessive physiological stresses whilst the regenerated tissue remodels itself towards a scaffold-free structure (Engelmayr and Sacks, 2006; Mazza and Ehret, 2015; Zadpoor, 2015). Therefore, it is critical that scaffolds are designed to have the mechanical properties consistent with the anatomical site. Finally, these devices should mimic the complex physiochemical properties of natural tissue to enable to interconnectivity between biological organisms, nutrients, and fluids to encourage rapid and quality regeneration.

Electrospinning (ES) has presented itself as a prominent candidate as a simple yet powerful method of producing these scaffolds, by generating high strength micro- to nano- sized fibres, which when aggregated are able to closely mimic the topology of the native extracellular matrix (ECM) (Amoroso et al., 2011; Bosworth, 2014; Ratner et al., 2004). This technique utilises electrostatic forces to uniaxially stretch a charged viscoelastic polymer solution under the presence of an electric field to generate fibres which are continuously deposited onto a collecting device leading to an interconnected fibrous non-woven mesh (Fang et al., 2008). The resultant product has the potential to serve a diverse range of biomedical applications (Ibrahim and Klingner, 2020; Khodadadi et al., 2020; Liu et al., 2021; Nangare et al., 2020) due to its unique microstructural characteristics, including high surface-to-volume ratios, variable fibre diameter control, stable physical and chemical properties, and mechanical performance (i.e. high stiffness and tensile strength) (Rashid et al., 2021). The high porosity acts as a channel for medium to transport among fibres, leading to faster and higher quality tissue repair (Liu et al., 2020; Sensini and Cristofolini, 2018). Nowadays, a growing interest is to establish a robust method of reproducing electrospun scaffolds and upscaling production for commercial applications (Mouthuy et al., 2015; Vass et al., 2020).

Prof. P.-A. Mouthuy at Botnar Research Centre (NDORMS) at Oxford University has developed a novel technique which is able to manufacture continuous electrospun filaments that can then be processed into braided structures to generate scaffolds with tailorable mechanical properties, as shown in Figure 1.1 (Lach et al., 2019; Mouthuy et al., 2015; Savić et al., 2021). BioLig is an emerging technology stemming from this novel technique. BioLig is an electrospun cord that comprises of 216 electrospun filaments braided together, as shown in Figure 1.2. The cord will be looped through the knee joint, being held by a screw in one end and a fixation device to maintain tension. The primary function of BioLig is to act as a scaffold empowering the regrowth and regeneration of the ACL. The scaffold's increased load capacity and stability through braiding, alongside the ECM-mimicking structure facilitate the attachment of biological organisms enabling this to become a promising sythetic scaffold for ACL reconstruction. BioLig is produced using poly(ε-caprolactone) (PCL), which was selected for this product due to its slow degrading properties and minimal inflammatory response when present in the body (Bartnikowski et al., 2019; Malikmammadov et al., 2018). Compared to other polyesters, such as, poly(glycolic acid) and poly(lactic acid), PCL deteriorates significantly slower (i.e 2-4 years) due to its stable chemical structure (Manoukian et al., 2019; Sun et al., 2006). PCL degrades via hydrolysis of its ester linkages in the human body and at very low molecular weights, it fragments and is able to be consumed by macrophages and intracellular activity (Lanza et al., 2020; Li et al., 2020), allowing any by-product to be fully excreted from the body (Manoukian et al., 2019; Pitt et al., 1981a). For these reasons, this material presents ideal properties to maintain cohesion during the required implantation period. However, this novel scaffold has not been characterised and a critical concern is understanding if BioLig's mechanical and degradation properties are adequate to support tissue regeneration during the implantation period.

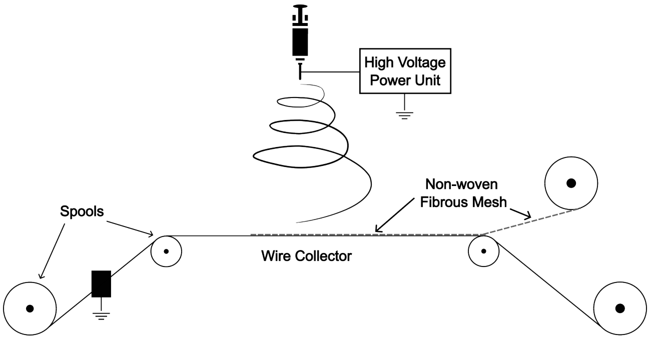

Figure 1.1: Schematic of novel electrospinning collection technique. The method consists of electrospinning PCL fibres onto a stainless steel wire progressing at a speed of 0.4 mm s^{-1}. The electrospun mesh is separated from the wire and collected in the form of a continuous filament.

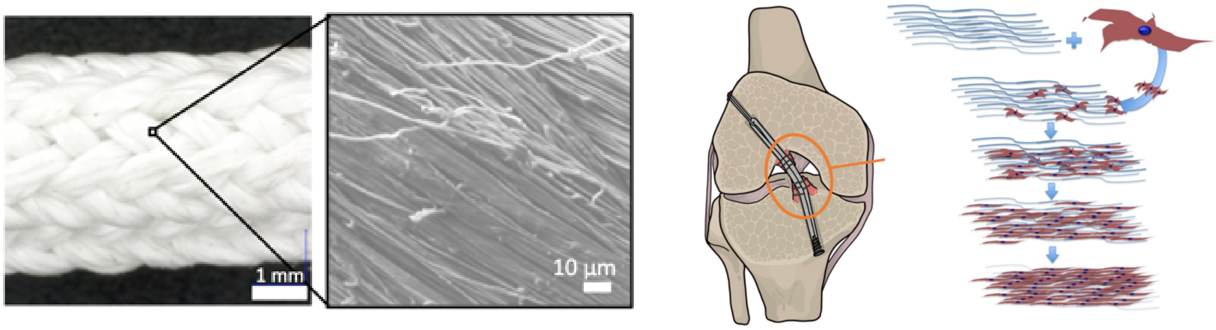

(a)

(b)

Figure 1.2: (a) SEM micrographs of final BioLig product, which consists of 216 braided filaments. Each filament is further composed of fibres. (b) Schematic of BioLig application on the knee joint. Image on the left displays how the BioLig cord is looped through the knee joint, being held by a screw and fixation device. Image on the right displays the process in which biological organisms attach to the synthetic scaffold.

To this end, this thesis aims to experimentally and mathematically characterise the relationship between microstructure, mechanical, and degradation behaviour of electrospun poly(ε-caprolactone) filaments being developed at Botnar Research Centre (NDORMS) at Oxford University for future tendon and ligament reconstruction applications (Mouthuy et al., 2015; Savić et al., 2021).

1.2 Thesis Objectives and Structure

ES filaments are considered promising candidates for tendon and ligament reconstruction. However, before such materials can be considered viable for clinical use, a comprehensive understanding of their fundamental material properties is essential. This includes not only their mechanical performance under physiological conditions but also their degradation behaviour over time, which directly affects the integrity and longevity of the implant.

The overarching aim of this thesis is to evaluate and model the material performance of electrospun PCL filaments under conditions relevant to biomedical use. To this end, the specific objectives are as follows:

- To experimentally characterise the thermo-mechanical and microstructural behaviour of electrospun PCL filaments and fibres.
- To investigate the degradation and corresponding microstructural evolution of electrospun PCL fibres, both under free and mechanically loaded conditions, in order to quantify the effect of stress on degradation kinetics.

- To develop a constitutive model capable of predicting both mechanical and degradation behaviour of ES PCL networks under physiologically relevant loading and environmental conditions.

The subsequent chapters of this thesis are organised systematically to address these objectives. Through this analysis, the potential of this device for ACL reconstruction and broader biomedical applications can be critically assessed and better understood.

1. **Characterisation and modelling of continuous electrospun poly(ε-caprolactone) filaments for biological tissue repair.** This chapter presents a detailed experimental study of the thermo-mechanical and microstructural behaviour of electrospun PCL filaments and fiber assemblies. A viscoelastic–viscoplastic (VE–VP) phenomenological model is proposed and validated, capable of accurately capturing the mechanical response of filaments under non-monotonic loading conditions.

2. **Hydrolytic degradation of electrospun poly(ε-caprolactone) filaments for biological tissue repair.** Building on the mechanical characterization, this chapter focuses on the degradation behaviour of electrospun PCL fibres at an elevated temperature (45°C). The study explores the effects of mechanical loading on degradation kinetics, providing critical insight into the degradation performance of these materials.

3. **Thermo-mechanical characterisation and modelling of hydrolytically degraded electrospun poly(ε-caprolactone) filaments for biological tissue repair.** This chapter extends the degradation study to physiologically relevant temperatures (37°C) and evaluates how degradation influences the thermo-mechanical properties of the material. A viscoelastic framework is proposed, followed by a preliminary analysis between the coupling of degradation effects on microstructural elements evolution.

Chapter 2

Literature Review

In this chapter, we first contextualise the significance of the fibrous networks under investigation. The background begins with an overview of the electrospinning process, followed by a detailed discussion of the mechanics of electrospun networks. This is complemented by a review of models proposed in the literature to describe their behaviour. Finally, the chapter concludes with an examination of the fundamentals of polymer degradation, with particular emphasis on poly(ε-caprolactone) (PCL).

2.1 Fibrous Networks

Fibrous networks are ubiquitous and naturally occurring. For example, the extracellular matrix (ECM) is composed of an interconnected polymer network, primarily made up of collagen, which organizes into fibrillar bundles, such as those found in tendons, to provide essential mechanical support to tissues (Manoukian et al., 2019; Picu, 2011). To replicate the structural and functional characteristics of the ECM, contemporary biomaterials research has focused on developing closely mimicking scaffolds fabricated from soft, flexible polymers. Advances in polymer processing techniques have enabled fine control over fibre diameter, alignment, and porosity, leading to scaffolds with high surface-area-to-volume ratios, favourable stiffness-to-weight characteristics, and the dynamic remodelling capacity necessary for effective cell migration and tissue integration (Nikolova and Chavali, 2019; Roach et al., 2007).

Fibrous scaffolds are broadly classified into two categories: (1) woven and (2) non-woven networks. Woven scaffolds are constructed by interlacing fibres at defined angles, providing directional strength and stability. In contrast, non-woven scaffolds consist of randomly oriented fibres bonded by friction, adhesion, or entanglement, resulting in isotropic mechanical behaviour and structural complexity that more closely resembles the native ECM (Picu, 2011). Owing to this resemblance, non-woven structures have gained prominence in tissue engineering applications. Among the available fabrication techniques, electrospinning has emerged as the most versatile and widely adopted method for producing non-woven nano-fibrous scaffolds, offering reasonable control over fibre morphology and scalability.

Alongside advancements in scaffold fabrication, there has been growing interest in the use of biodegradable polymers, both natural and synthetic, as the base materials for electrospun networks. These materials provide essential features for biomedical applications, including biocompatibility, controlled degradation rates, and adaptable mechanical properties. Among the wide array of polymers used in electrospinning, synthetic biodegradable polymers have attracted particular attention due to their reproducible performance, processability, and tunable degradation kinetics. Polymers such as poly(lactic acid) (PLA), poly(glycolic acid) (PGA), poly(lactic-co-glycolic acid) (PLGA), and poly(ε-caprolactone) (PCL) have proven especially suitable for applications in tissue engineering, wound healing, and drug delivery (Kohane and Langer, 2008; Manoukian et al., 2019; Nikolova and Chavali, 2019).

2.2 Electrospinning

2.2.1 Fundamentals of Electrospinning

Electrospinning, or electrostatic spinning, is a unique manufacturing technique that electrically charges a polymer solution to deposit a continuous fibre, leading to an interconnected non-woven mesh that is highly porous with high surface-to-volume ratio (Amoroso et al., 2011; Greiner and Wendorff, 2007; Liu et al., 2019; Ratner et al., 2004). The formation of these micro-/nano- fibres are based on the uniaxial stretching of a viscoelastic solution through electrostatic forces (Teo and Ramakrishna, 2006). To comprehend the electrospinning process, we first have to understand the set-up. Contemporary electrospinning systems consist of three major components: (1) a high voltage power supply, (2) a spinneret (i.e. a pipette or needle), and (3) a conductive fibre collecting plate (i.e. a static metallic plate, rotating mandrel, or a wire (Mouthuy et al., 2015)) at a defined distance (Bhardwaj and Kundu, 2010; Garg and Bowlin, 2011). In addition, a syringe pump may be used to control the flow rate of the polymer solution (Baji et al., 2010). Electrospinning can be performed both vertically or horizontally. A schematic of a horizontal needle electrospinning set-up is illustrated in Figure 2.1.

Due to the novelty of electrospinning, most research is conducted in laboratories (Vass et al., 2020). The most common set-up consists of a syringe holding a polymer solution with a blunt needle tip as

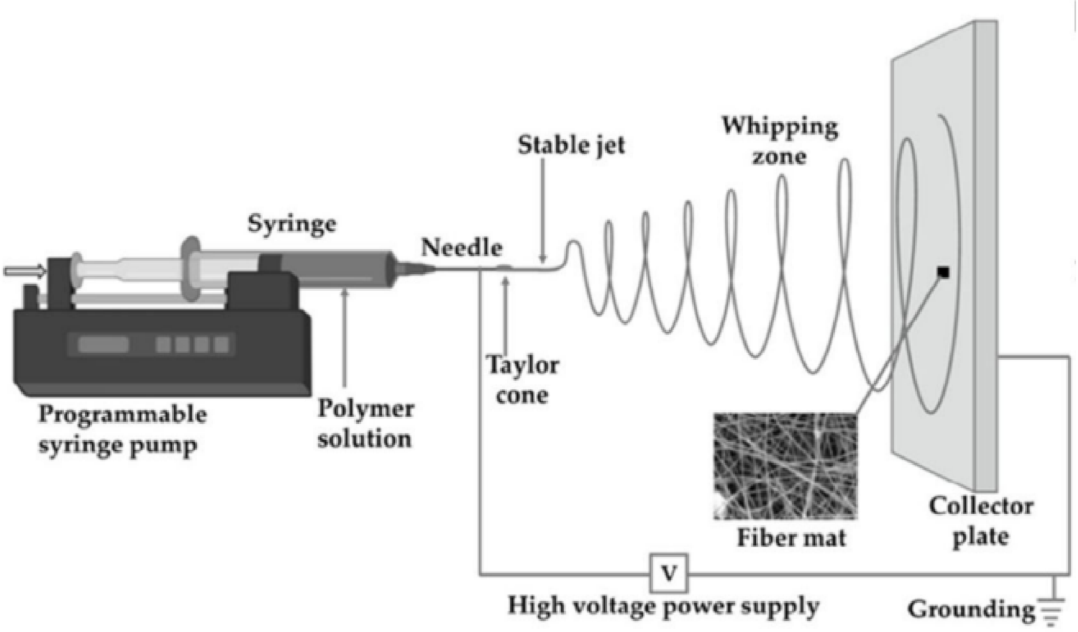

Figure 2.1: Schematic illustration of a traditional needle electrospinning set-up (TNES). The apparatus consists of a programmable syringe pump, conductive needle tip, a DC high-voltage power source, and a collecting mechanism. Reproduced with permission from Rashid et al. (2021). (License Number: 6107680129990)

the spinneret. The syringe pump is utilised for the solution to be fed at a constant and controllable rate to create a pendant droplet (Garg and Bowlin, 2011). An electrode of the power supply is connected to the needle holding the spinning solution to charge the pendant droplet, whilst the other end is attached to the metallic collector, with the intention to create an electric field. A high voltage (typically ranging between 5-20 kV) is applied at the spinneret tip (Garg and Bowlin, 2011). At this stage, the droplet is held by its own surface tension and becomes electrostatically charged at the pendant droplet. As a result, the droplet experiences two forces: (1) mutual electrostatic repulsion between surface charges and (2) Coulombic forces due to the applied external electric field. The increasing Coulomb repulsion between positive and negative ions transforms the initial pendant droplet into a hemispherical shape, which is further elongated with the intensified electrostatic field to form a conical shape called the Taylor cone (Rashid et al., 2021). This is best illustrated in Figure 2.2.

Once the intensity of the electric field is sufficient to overcome surface tension of the polymer solution, a highly charged and unstable jet is ejected from the tip of the Taylor cone towards the metallic collector, due to charges being attracted to the opposite end of the electric field (Rashid et al., 2021). The instability of the straight travelling jet arises from several forces with opposing effects, such as, change in shape, uneven number of charges per unit area of the jet due to its elongation, and evaporation of solvent. These factors alter the balance between the surface tension and electrical field,

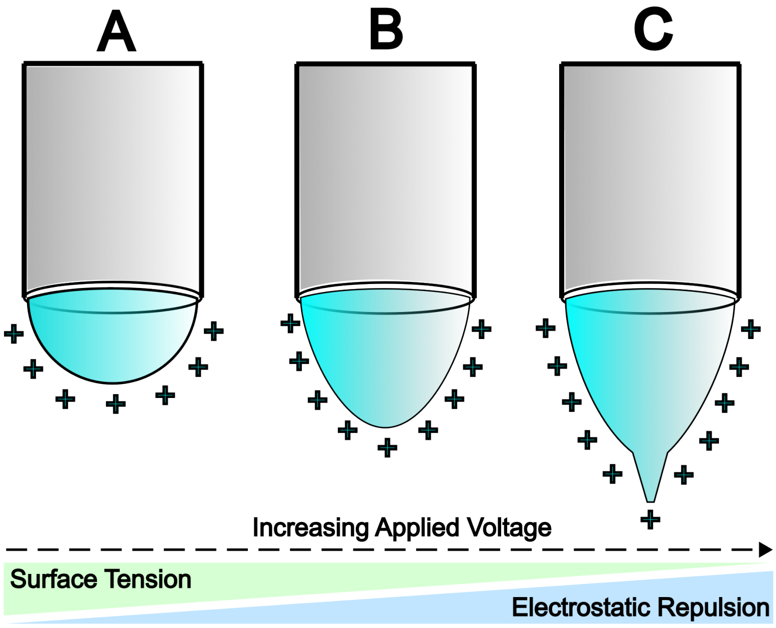

Figure 2.2: Schematic illustration of Taylor cone formation. (A) Pendant droplet is formed and surface charges are accumulating on the surface. (B) Electrostatic repulsion begins to dominate the surface tension and elongation of the pendant droplet takes place. (C) Taylor cone is formed and charge-charge repulsion completely dominates leading to smooth continuous jet. Illustration was inspired from Baji et al. (2010) and Ameer et al. (2019).

causing the jet to become unstable (Garg and Bowlin, 2011).

The jet instability plays a fundamental role in reducing the fibre diameter from micrometre to nanometre. The instability is decomposed into two components: (1) bending (axisymmetric) and (2) whipping instabilities (non-axisymmetric) (Baji et al., 2010; Garg and Bowlin, 2011; Xue et al., 2019). The instabilities commence immediately with jet formation; solvent rapidly evaporates with the fast elongation and charges do not have sufficient time to redistribute along the jet. As a result, an electrostatic gradient is developed along the jet and the uneven charges induce greater electrostatic repulsion, further elongating the jet in the direction of its axis (Rutledge and Fridrikh, 2007). The jet tip velocity is incredibly high, inducing bending and a series of lateral excursions that grow in a spiral loop, producing a wave or dumb-bell shape. This is best illustrated in Figure 2.3. Through each of these loops, the fibre grows longer and thinner (Baji et al., 2010; Garg and Bowlin, 2011). The high speed of elongation leads to continual solvent evaporation and ultra-fine fibres formation, which are deposited onto a conductive ground collector with the resultant product being a non-woven network in the form of a mat or filament.

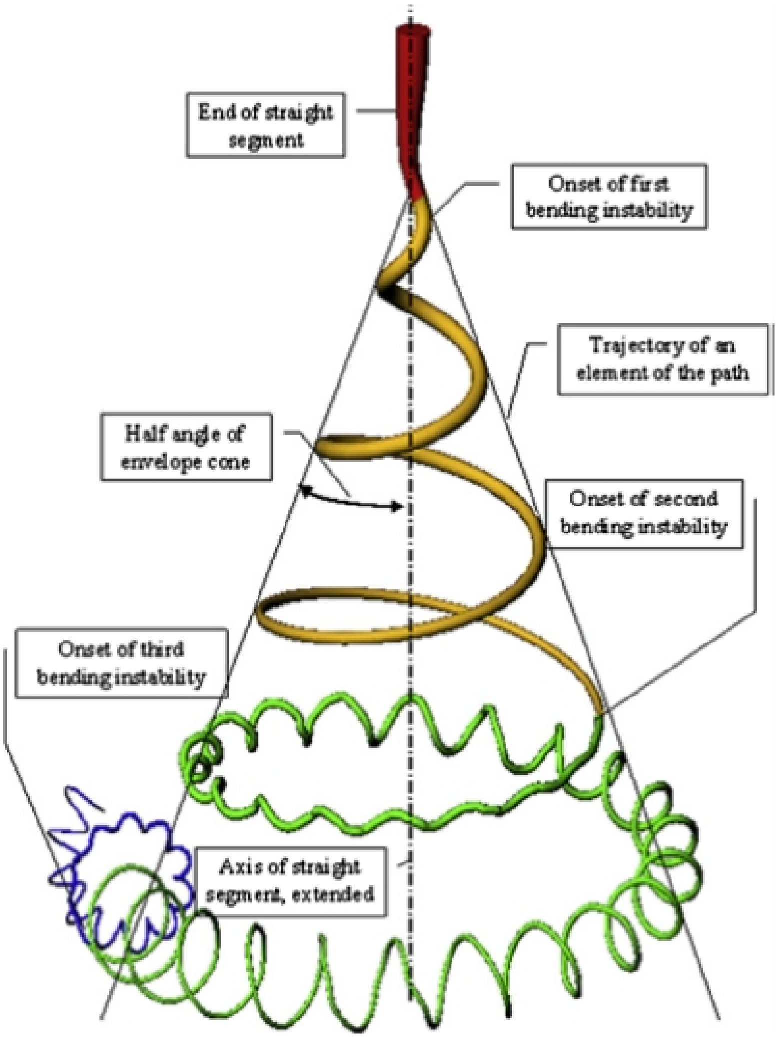

Figure 2.3: Schematic illustration of the onset and development of bending instabilities. Image was sourced from Garg and Bowlin (2011) and Xue et al. (2019), which has re-printing permission from Reneker and Fong (2006).

2.2.2 Key Electrospinning Parameters

One of the challenges or caveats of electrospinning are the number of parameters that affect the morphology of electrospun material being produced (Duling et al., 2008). These variables can be divided into (1) the solution properties which include polymer concentration, viscosity, choice of solvent, conductivity, molecular weight, and surface tension; (2) process governing variables such as electrical potential between capillary tip and collector, working distance, type of collector, and flow rate; and (3) ambient parameters, including ambient temperature, humidity, air velocity in chamber, and solution temperature (Bhardwaj and Kundu, 2010; Duling et al., 2008; Rashid et al., 2021). The effect of these parameters are summarised in Table 2.1.

Table 2.1: Electrospinning parameters (solution, processing and ambient) and their effects on fibre and microstructural morphology (Alfaro De Prá et al., 2017; Bhardwaj and Kundu, 2010; Courtney et al., 2006; Gaumer et al., 2009; Ibrahim and Klingner, 2020; Mondesert, 2020; Rashid et al., 2021; Tao and Shivkumar, 2007; Teo and Ramakrishna, 2006)

Parameters	Effect on Morphology
Solution Parameters	
Polymer Type	Polymer type dictates fundamental molecular properties, such as molecular weight and chain flexibility, which influence solvent–polymer interactions and, consequently, the extent of chain entanglement that governs solution behaviour during electrospinning.
Solvent Type	Solvent type influences the viscosity, surface tension, and charge density of the solution.
Evaporation Rate of Solvent	Solvent evaporation temperature should be carefully chosen as a high evaporation temperature will prevent solvent evaporation leading to thicker fibres and microstructural beads. A low evaporation temperature could lead to dry fibres and prevent fusion between fibres.
Solution Conductivity	Solution conductivity influences the accumulation of charges under the electric field. Increasing solution conductivity results in greater fibre stretching and a reduction in fibre diameter. Excessive conductivity increases instability leading to broad diameter distribution.
Molecular Weight of Polymer	Molecular weight controls the rheology and electrical properties of solution. Increased molecular weight increases the entanglement of polymer chains in solution, leading to greater viscosity, conductivity and surface tension of the solution.
Surface Tension	Surface tension controls the shape and stability of the pendant droplet. Lower surface tension facilitates the electrospinning process by reducing the required voltage to generate the Taylor cone. Surface tension can be controlled by type of solvent.
Polymer Concentration / Viscosity	Polymer concentration strongly influences solution viscosity and the degree of chain entanglement. Solutions with low viscosity lack sufficient chain entanglement to sustain continuous fibre formation, often resulting in bead formation or jet breakup. Conversely, excessively high viscosity can hinder polymer solubility and restrict jet initiation, making it difficult to form a stable Taylor cone.
Processing Parameters	
Applied Voltage	The applied voltage directly affects the shape of the initiating droplet, which influence the shape morphology of fibres. Increasing the voltage, increases electrostatic repulsion between ions, sharpening the Taylor cone and reducing fibre diameter.
Tip-Collector Distance	The deposition distance influences the solvent evaporation and fibre definition. A low working distance does not allow the solvent to fully evaporate often leading to beaded structures and inhomogeneous fibres. Increasing working distance may result in dryer fibres, which cannot fuse together due to the absence of solvent. An excessive working distance reduces the electric potential between tip and collector, reducing the chances of electrospinning from occurring.
Collector Type	Collector type influences alignment of fibres. Static collectors result in an isotropic non-woven network, whilst rotating drums lead to highly anisotropic mats. Wire-collectors are sensitive to perturbations in the electric field due to their small collection surface.

Flow Rate	Flow rate controls the quantity of solution feed through the nozzle, directly influencing the shape of the Taylor cone. Increased flow rate leads to aggregated solution at the needle tip, often leading to greater fibre diameters. An excessively high flow rate prevents the formation of a Taylor cone. A low flow rate may inhibit the ability of a pendant droplet from forming.
Ambient Parameters	
Humidity	Humidity influences solvent evaporation by reducing the vapour pressure gradient between the solvent and the surrounding air. At higher humidity, the air is closer to saturation, which slows solvent evaporation. This can lead to increased surface tension effects and greater difficulty in stable fibre formation during electrospinning.
Temperature	Temperature influences the rate of evaporation of solvent and viscosity of solution. Higher temperatures increase the rate of evaporation of solvent, leading to drier fibres which affects fibre-fibre adhesion within the mesh. Furthermore, higher temperatures can increase the viscosity of the solution.

2.2.3 Electrospun Filaments & Yarns

In most studies, electrospun meshes are produced in the form of planar sheets, which limits their suitability for further processing into structures that meet the functional demands of soft tissue repair (Abhari et al., 2018a,b). For this reason, in developing electrospun scaffolds for the surgical repair of soft tissues such as tendons and ligaments, careful consideration must be given to the method of production (Venugopal and Ramakrishna, 2005). Structurally, soft tissues are characterised by highly aligned collagen fibres; therefore, generating anisotropic architectures is particularly attractive, as it enables closer replication of the natural extracellular matrix (ECM) (Cai et al., 2012; Little et al., 2010; Rothrauff et al., 2017; Zhang et al., 2012).

The collector assembly is the most influential parameter in the electrospinning process to achieve such structure, as it governs fibre deposition and thereby dictates the final textile geometry and fibre orientation (Bhardwaj and Kundu, 2010; Teo and Ramakrishna, 2006). To augment the functionality of soft tissue scaffolds, researchers have developed fibre assemblies in the form of filaments and yarns (Ali et al., 2012; Chainani et al., 2013; Fennessey and Farris, 2004; Hu et al., 2010; Mouthuy et al., 2015; Rothrauff et al., 2017; Zhu et al., 2008). Abhari et al. (2018a) provides a comprehensive review of these methods and classifies collector systems for filaments into two categories: (1) discontinuous and (2) continuous collectors. Discontinuous filaments can be produced using either static or dynamic collection units, such as flat plates, parallel plates, or rotating drums and discs, whereas continuous filament production relies exclusively on dynamic collection systems, including rotating discs, funnels, and wires. The key distinction between these approaches lies in fibre orientation: stationary collectors yield randomly deposited, isotropic fibres that typically require post-processing, while dynamic collectors facilitate alignment, generating anisotropic microstructures (Courtney et al., 2006; Gaumer et al., 2009).

In this thesis, filaments were collected dynamically using a wire-based electrospinning system. Due to the relatively low translational speed of the wire, fibres were deposited in a predominantly random orientation; however, the resulting filaments could subsequently be post-processed to enhance alignment and mechanical performance. Compared with filaments produced using rotating drums or discs, electrospinning onto a thin wire promotes the formation of a highly interconnected mesh that can be directly removed as a continuous filament. This approach yields structures that are denser, stronger, and easier to handle, while the small contact area between the fibrous structure and the wire facilitates simple and consistent detachment. To further refine filament properties, post-processing techniques such as mechanical drawing were employed. In this process, filaments are stretched along their longitudinal axis. This technique serves multiple purposes: it increases fibre strength and stiffness, preconditions the filament to minimise subsequent plastic deformation, reduces fibre diameter, modifies pore size distribution, enhances crystallinity, and promotes molecular alignment in the fibre direction (Abhari et al., 2018a,b; Chandler et al., 2025; Ferreira et al., 2025; Lach et al., 2019; Noh et al., 2023).

Building on this capability, Mouthuy et al. (2015) demonstrated how electrospun filaments can be assembled into complex multi-filament yarns using textile-inspired techniques such as twisting, braiding, and weaving. This advancement has opened new opportunities for the development of biomaterials with enhanced structural and functional performance (Lin et al., 2025; Savić et al., 2021). Such textile-based approaches not only enable tailoring of mechanical properties to meet the functional demands of soft tissue repair but also replicate the hierarchical architecture of collagen fibres. Importantly, these assemblies preserve essential structural features, such as porosity and high surface area, that are critical for cellular infiltration and tissue integration. To aid clarity, the hierarchical organisation of electrospun structures across different length scales is illustrated in Fig. 2.4.

2.3 Network Architecture

The mechanics of non-woven fibrous networks is inherently complex, requiring the response to be considered across multiple scales. At the macroscopic level, the mechanical behaviour is governed primarily by the constitutive response of individual fibres, which is determined by both their microstructural arrangement and intrinsic material properties. The global strain response arises from

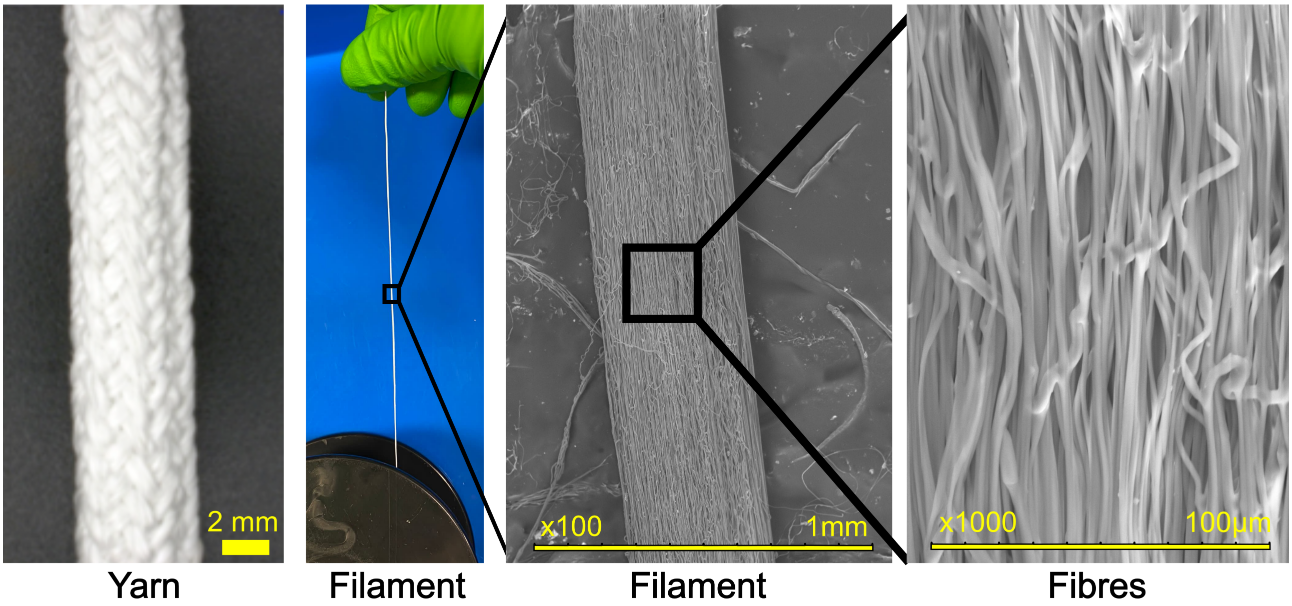

Figure 2.4: Hierarchical structure of electrospun constructs across multiple length scales. From left to right: a braided multifilament yarn composed of electrospun filaments; a single electrospun filament collected using a dynamic wire collector; SEM micrograph of the filament surface at low magnification (x100) showing the morphology of drawn filament consisting of densely packed, aligned fibres; and a high-magnification micrograph (x1000) illustrating the nanoscale arrangement of individual fibres within the filament.

several non-linear deformation mechanisms that depend on fibre orientation and position relative to the applied loading direction. Additionally, the strength and stability of bond points control fibre rotation and reorientation under load, with the extent of this behaviour varying according to fibre location and local stress distribution (Rawal, 2022; Rawal et al., 2019). At the mesoscopic scale, fibre behaviour is also influenced by properties at the polymer chain level, including degree of crystallinity, molecular orientation, and chain entanglements. The fibres themselves may undergo additional straining, further complicating the accurate quantification of total network deformation. These multi-scale dependencies highlight the challenge of linking local fibre mechanics to the overall macroscopic response (Rashid et al., 2021).

Despite the significant research output in non-woven networks, there are still several challenges in characterising the behaviour of these materials under complex loading conditions. Recent studies have mostly focused on investigating the effect of fibre deposition (Courtney et al., 2006) and mechanics of individual fibres (Alexeev et al., 2020; Baker et al., 2012, 2015; Carlisle et al., 2009; Croisier et al., 2012; Delp et al., 2021; Lee et al., 2005; Rashid et al., 2021; Tan et al., 2004). However, there are still several parameters that remain inadequately understood, such as, fibre size distribution, porosity (Bazgir et al., 2021; Rutledge et al., 2009), individual fibre orientation, fibre-fibre slippage (Goutianos et al., 2018), fusion of fibre network, multi-scale deformation, necking (Andersson et al., 2015), multi-scale fracture mechanics, fatigue, and fibre entanglements. These complexities arise because these factors cannot be easily isolated and experimentally tested (Baji et al., 2010; Wei et al., 2009).

2.3.1 Fibre Distribution: Orientation & Tortuosity

Fibre orientation, defined as the angle between the tangent of a fibre curl and the principal loading axis, is a key structural parameter that governs how fibres engage under load (Rawal, 2022). Experimental studies have characterised this property by modifying fibre deposition during electrospinning through the use of different collectors, thereby generating anisotropic structures and comparing them to randomly oriented mats (Alfaro De Prá et al., 2017; Courtney et al., 2006; Gaumer et al., 2009; Kim et al., 2004; Kongkhlang et al., 2008). Randomly oriented mats typically exhibit relatively low stiffness but large deformability, as fibres can readily rotate, reorient, and slide past one another during tensile loading. In contrast, highly aligned networks display increased tensile strength and modulus along the axis of alignment, since load transfer occurs more efficiently along the fibre direction. However, this improvement is often accompanied by a reduction in properties transverse to the alignment, resulting in a strongly anisotropic mechanical response.

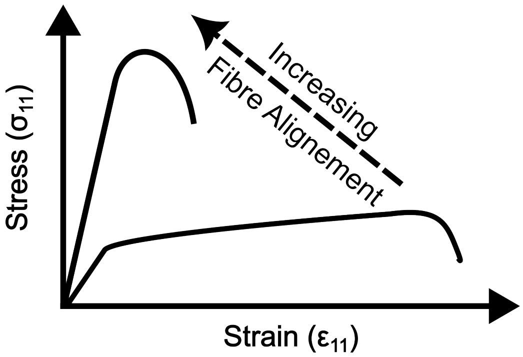

Figure 2.5: Effect of fibre alignment on stress-strain behaviour of a non-woven network.

In addition to fibre orientation, the tortuosity or waviness of fibres plays a decisive role in dictating the initial compliance and energy absorption capacity of non-woven mats. Quantifying tortuosity experimentally remains challenging; as a result, many studies have relied on modelling approaches to capture its effects on network mechanics (Caballero et al., 2022; Domaschke and Ehret, 2020; Kulachenko and Uesaka, 2012; Kumar and Rawal, 2017; Rizvi et al., 2012; Zhang et al., 2021). Tortuous fibres behave as mechanical reservoirs, progressively straightening under load before fully engaging in stress transfer. From a mechanical perspective, high tortuosity imparts flexibility, ductility, and enhanced energy dissipation, making the network more resilient to deformation. Conversely, low tortuosity promotes stiffness and immediate load transfer, characteristics desirable in applications where rigidity and dimensional stability are required (Pai et al., 2011). The degree of tortuosity is not intrinsic to the material but is instead influenced by electrospinning conditions, predominantly by the collector geometry, as well as post-spinning treatments including mechanical drawing.

2.3.2 Inter-Fibre Interactions

The mechanics of non-woven networks are also governed by the nature of fibre–fibre interactions. These interactions occur through physical contacts, entanglements, frictional sliding, or welded junctions formed during deposition (Picu, 2011). The quality and type of fibre–fibre junctions play a decisive role in determining the mechanical integrity of electrospun networks. Direct experimental characterisation of inter-bond strength remains challenging; nevertheless, groups have attempted such measurements (Chen and Silberstein, 2018, 2019; Huang et al., 2009; Schmied et al., 2012; Stachewicz et al., 2014), while others have employed modelling approaches to estimate their contribution to network mechanics (Caballero et al., 2022; Chavoshnejad and Razavi, 2020; Goutianos et al., 2018; Kulachenko and Uesaka, 2012; Negi and Picu, 2019). Broadly, weak physical contacts or point entanglements lead to networks that are compliant and susceptible to fibre slippage under load. By contrast, welded or fused junctions, often formed when residual solvent remains at the fibre–fibre interface during deposition, create strong local bonds that act as efficient load-transfer sites, enhancing stiffness and strength. The density and quality of these connections dictate whether the network behaves as a loosely entangled assembly of filaments or as a coherent, cross-linked load-bearing sheet.

2.3.3 Network Density & Porosity

Network density and porosity are interrelated properties influencing the mechanics of non-woven networks. At a fundamental level, porosity represents the volumetric fraction of voids within a fibrous assembly, while network density corresponds to the complementary solid fraction. Experimental studies, such as that of Bazgir et al. (2021), which characterised the mechanical properties of PCL and PLGA electrospun scaffolds produced with varying spinning times, have shown that increasing deposition time yields denser scaffolds with improved mechanical robustness. Complementary to such experimental work, most studies investigated this relationship through mathematical modelling, typically by examining fibre volume fraction as the proportion of the total volume occupied (Goutianos et al., 2018; Rawal et al., 2019; Zhang et al., 2019; Zündel et al., 2017). Together, these analyses consistently demonstrate that density and porosity exert profound effects on the mechanical integrity of fibrous networks, particularly influencing stiffness and strength.

In denser networks, where inter-fibre spacing is small, the likelihood of fibre–fibre contact and bonding increases, thereby promoting stress transfer, elevating the effective modulus, and reducing overall deformability. By contrast, networks with larger inter-fibre spacing, or equivalently, higher porosity, contain fewer junctions and permit fibres to rotate and reorient more freely before engaging in load transfer (Croisier et al., 2012). While this enhances compliance and deformability, it generally reduces strength and stiffness. Equally important is the spatial distribution of porosity (Chen et al., 2016). Networks with a homogeneous fibre distribution typically promote isotropic behaviour, whereas heterogeneities such as clustering, fibre-free regions, or local density variations result in uneven stress distributions and localised weak points. Such microstructural inhomogeneities can significantly alter both the elastic and failure responses of electrospun mats, underscoring the importance of controlling porosity not only in magnitude but also in spatial uniformity.

2.4 Characteristics of Electrospun Fibres

The electrospun fibre serves as the fundamental building block that dictates both the architecture and mechanical behaviour of fibrous networks. For a highly functional network, fibres should ideally possess a smooth, cylindrical morphology that promotes uniform stress distribution and consistent mechanical response. Achieving such morphology, however, requires precise optimisation of processing parameters, including polymer concentration, solution viscosity, applied voltage, and working distance, which collectively govern jet stability and fibre formation (Baji et al., 2010; Eda and Shivkumar, 2007; Rashid et al., 2021; Zuo et al., 2005). When these parameters are not carefully controlled, fibres may exhibit surface roughness, irregular cross-sections, or develop defects such as beads and bead-on-string morphologies (Greiner and Wendorff, 2007; Gupta and Moghe, 2013; Huang et al., 2016, 2004; Ibrahim and Klingner, 2020; Lasprilla-Botero et al., 2018; Megelski et al., 2002).

2.4.1 Fibre Morphology

Understanding fibre morphology requires careful consideration of how processing history shapes both the molecular alignment and structural organisation of electrospun fibres. During electrospinning, the formation of fibres involves rapid, non-equilibrium chain dynamics. As the electrified polymer jet accelerates towards the collector, the polymer solution is subjected to intense elongational and shear forces that stretch and orient the polymer chains along the fibre axis (Reneker and Yarin, 2008). Simultaneously, solvent evaporation and rapid solidification kinetically trap the chains in this extended conformation, preventing relaxation back toward equilibrium. As a result, electrospun fibres display a higher degree of molecular orientation compared with bulk-processed materials (Fennessey and Farris, 2004). For semi-crystalline polymers, these high strain rates and fast solvent removal strongly limit chain mobility, leaving insufficient time for crystalline nuclei to form and grow. Consequently, the resulting fibres often exhibit incomplete or disordered crystallisation, characterised by small crystalline domains embedded within a largely amorphous matrix. In some cases, metastable crystalline polymorphs can also emerge due to kinetic trapping (Kongkhlang et al., 2008; Yee et al., 2008). These microstructural features give rise to a topological fibrillar arrangement, composed of alternating crystalline lamellae and amorphous tie-chain regions are aligned along the fibre axis at the nanoscale (Tan and Lim, 2006, 2004). Lim et al. (2008) observed that fibre diameter strongly influences this semi-crystalline morphology. Small-diameter fibres exhibited densely packed and highly aligned lamellae with well-organised fibrillar structures. In contrast, larger-diameter fibres showed more disordered and misaligned lamellae with an absence of distinct fibrillar features. The amorphous phase in small-diameter fibres was dominated by stretched and extended tie chains, whereas in large fibres it consisted mainly of relaxed, misoriented lamellae.

Numerous studies have shown that decreasing fibre diameter during processing generally leads to an increase in the elastic modulus of electrospun fibres (Alexeev et al., 2020; Lim et al., 2008; Pai et al., 2011; Wong et al., 2008). Two prevailing models explain this behaviour (Richard-Lacroix and Pellerin, 2013). The first, the surface-oriented layer model, suggests that strong elongational and electrostatic forces during electrospinning produce a thin layer of highly oriented polymer chains at the fibre surface (Ji et al., 2006, 2008). As the diameter decreases, opposing surfaces become mechanically coupled, creating uniform molecular orientation across the fibre cross-section and yielding mechanical properties approaching those of bulk-oriented polymers. The second, the skin–core (or core–shell) morphology model, describes the fibre as a two-phase material with a rigid, oriented outer shell surrounding a solvent-rich, isotropic core (Arinstein et al., 2007; Stachewicz et al., 2012). Rapid solidification of the outer shell limits solvent diffusion from the core, producing a dense, crystalline exterior and a more amorphous interior. As fibre diameter decreases, the volume fraction of the shell increases, and the mechanical response becomes dominated by the stiff, oriented surface layer.

2.4.2 Mechanics of Individual Fibres

This semi-crystalline structure plays a critical role in dictating the mechanical response and deformation mechanisms of electrospun fibres. Unlike fully amorphous polymers, where deformation is dominated by molecular chain mobility, or highly crystalline polymers, which behave in a brittle manner, semi-crystalline polymers exhibit a balance of stiffness, strength, and ductility. This arises from the dual-phase morphology, in which ordered crystalline lamellae are interspersed with disordered amorphous regions (Galeski, 2003; Gleadall, 2015). The spatial arrangement, size, and connectivity of these two phases govern how the fibre stores and dissipates mechanical energy under load. Crystalline domains act as rigid, load-bearing regions that provide dimensional stability and high modulus, while amorphous tie chains act as flexible connectors, accommodating strain through segmental motion and allowing limited plastic deformation (Callister, 2005; Struik, 1987). The degree of crystallinity, lamellar orientation, and the density of tie chains therefore determine the fibre's ability to transfer stress, resist permanent deformation, and recover its original configuration after unloading.

Uniaxial deformation in a semi-crystalline polymer typically proceeds through several sequential stages (Gleadall, 2015; Lin and Argon, 1994; Men, 2020; Mirkhalaf and Vadizadeh, 2024). At small strains, the deformation is predominantly elastic, governed by the stretching of amorphous tie chains and the slight bending or stretching of bonds within the crystalline lamellae. Upon further stretching, deformation mechanisms characteristic of the crystalline phase become activated, primarily crystallographic slip, which involves the shearing or gliding of lamellae relative to one another (Seguela, 2005; van Dommelen et al., 2003). This stage marks the transition from elastic to plastic deformation. At even higher strains, plastic deformation is often accompanied by lamellar fragmentation, inter-lamellar shear, and the rotation or alignment of crystalline blocks along the loading direction. Simultaneously, tie chains in the amorphous regions may disentangle or slip, allowing stress redistribution throughout the microstructure. The overall ductility of a semi-crystalline polymer thus depends strongly on the relative proportions and connectivity of the crystalline and amorphous phases, as well as the ability of the amorphous chains to undergo cooperative motion (Lustiger and Markham, 1983). In addition, the mechanical response is not purely elastic–plastic but also exhibits time-dependence due to the viscoelastic nature of the polymer chains. Studies by Alharbi et al. (2023); Alharbi and Guthold (2024) and Baker et al. (2015) have shown that electrospun fibres display viscoelastic behaviour that intensifies with increasing strain, a phenomenon attributed to molecular chain reorganisation under load. Beyond a critical strain, however, plastic deformation dominates, as stress-induced reorientation and restructuring of chains impair the fibre's ability to recover stored energy during subsequent reloading.

2.5 Mechanical Properties of Non-Woven Networks

The loading behaviour and associated microstructural evolution of electrospun networks has been studied and characterised by several groups (Bazgir et al. (2021); Bolgen et al. (2005); Croisier et al. (2012); Johnson et al. (2009); Jubera et al. (2014); Molnar et al. (2012); Nerurkar et al. (2007); Rizvi et al. (2012); Sethuraman et al. (2013); Sozumert and Silberschmidt (2022)). The typical behaviour is bilinear, as illustrated in Fig. 2.6. Under uniaxial loading, the applied stress is transmitted through both the fibres and their cross-linking points. As loading progresses, fibres rotate around their bonding sites and gradually align with the loading direction (Picu, 2011). With continued deformation, fibres oriented at small angles to the loading direction become increasingly recruited to carry the load. Once these fibres reach their failure threshold, they begin to fracture in randomly distributed regions, prompting load redistribution to neighbouring fibres. Their mechanical behaviour is generally decomposed into three regimes (Molnar et al., 2012; Negi and Picu, 2019; Picu, 2020).

- **Regime 1**: At small strains, the network response is linear elastic with an effective elastic modulus and apparent yield point. The stiffness in this regime is governed by fibre orientation, tortuosity, inter-fibre bonding, and other microstructural factors discussed previously.
- **Regime 2**: With increasing strain, the network undergoes progressive fibre recruitment and rotation, leading to alignment of fibres along the loading direction. This results in a progressive strain-hardening response, as fibre recruitment and alignment increase the number of load-bearing fibres with increasing strain.
- **Regime 3**: At large strains, individual fibres begin to rupture, junctions break, and localised damage accumulates. This ultimately leads to macroscopic network failure.

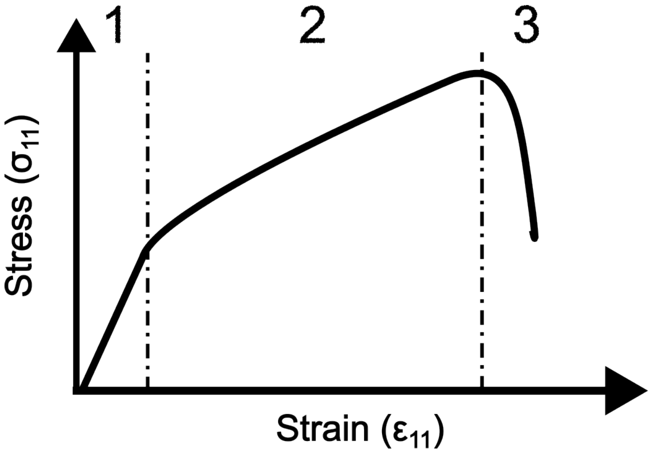

Figure 2.6: Schematic of typical uniaxial stress-strain behaviour of electrospun mats presented in the literature.

2.5.1 Yield and Failure Mechanisms

Apparent Yield Response

The yielding behaviour of electrospun fibrous networks arises from collective deformation mechanisms that reflect their disordered and interconnected architecture rather than the intrinsic strength of individual fibres. At small strains, deformation is accommodated through fibre tortuosity, sliding, and gradual reorientation within the network, allowing load redistribution without significant damage. As strain increases, frictional resistance at fibre junctions is progressively overcome, initiating slippage, plastic flow, and local bond rupture (Negi and Picu, 2019; Picu, 2020). The presence of permanent junctions constrains fibre mobility and modifies load-transfer mechanisms, producing a pronounced knee region in the stress–strain curve that marks apparent yielding. Experimental studies on both thermally bonded non-wovens (Jubera et al., 2014; Ridruejo et al., 2011; Sozumert et al., 2020) and modelling of entangled mats stabilised by adhesion and friction (Molnar et al., 2012; Negi and Picu, 2019) demonstrate that progressive junction failure and fibre rearrangement underpin the marked non-linearity of the stress–strain curve. Yielding, therefore, does occurs as a gradual process marking the onset of sliding and plastic flow once junction forces exceed the frictional threshold.

Damage and Failure of Networks

In fibrous networks, failure typically initiates with the early rupture of inter-fibre bonds during loading, leading to a rapid reduction in stiffness. Each rupture event introduces local micro-damage, and as fibres reorient and align with the loading direction, the progressive accumulation of these micro-failures evolves into localised fracture zones (Jubera et al., 2014; Ridruejo et al., 2011). Damage initiation commonly occurs in regions of lower fibre density or weaker bonding, with locations distributed irregularly throughout the network. As deformation progresses, fibre breakage becomes increasingly prevalent and emerges as the dominant mechanism driving damage localisation. This process often unfolds as a cascade, where local fibre failure triggers stress redistribution to adjacent fibres, which subsequently fail in turn (Sozumert et al., 2020). The overall progression of damage is therefore spatially heterogeneous and governed by collective interactions among fibres, highlighting the diffuse and interdependent nature of fracture in non-woven fibrous networks.

2.5.2 Time-Dependent Behaviour

Non-woven fibre networks display time-dependent mechanical behaviour, arising from the viscoelastic nature of their polymeric constituents and the unique architecture of fibrous assemblies (Waheed et al., 2018). Unlike bulk polymers, where viscoelasticity primarily reflects molecular relaxation processes, fibrous mats exhibit additional structural mechanisms such as dissipative interactions of fibres in contact, arising from the process of crosslink rupture and re-formation in transient contact points. As a result, their time-dependent response must be understood as the outcome of multi-scale interactions between polymer physics and network architecture (Picu, 2022).

Electrospun fibres are composed of viscoelastic polymer chains, meaning that their mechanical response is inherently time- and rate-dependent. The rate sensitivity of the overall fibrous network is therefore governed not only by the intrinsic viscoelastic behaviour of the polymer but also by how the fibres are organised and interconnected within the network. In the idealised case of a highly dense, perfectly cross-linked network, strain energy would be distributed uniformly, and all fibres would deform affinely with the macroscopic strain field. In practice, however, electrospun mats exhibit heterogeneous architectures: fibres are oriented in different directions, subjected to different local strains, and connected through junctions of varying strength. As a result, the viscoelastic response of the network is not uniform but instead spans a spectrum, such that the time-dependent response will vary from fibre to fibre (Picu, 2022). This structural heterogeneity gives rise to varying rate-dependent behaviours such as non-linear creep, stress relaxation, and hysteresis (Amjad and Picu, 2022; Sethuraman et al., 2013; Waheed et al., 2018).

This phenomenon was illustrated by Chen et al. (2016), who investigated the deformation mechanisms of thermally bonded polypropylene nonwovens using in-situ X-ray analysis. Their findings showed that the relaxation response of the material depends strongly on the integrity of inter-fibre bonds. In compact networks with numerous intact junctions, stress relaxation was governed primarily by the intrinsic viscoelasticity of the fibres themselves. By contrast, when inter-fibre bonds ruptured, fibres were able to reorient during relaxation, introducing an additional structural contribution to the time-dependent behaviour.

Such interplay between fibre viscoelasticity and bond integrity is also evident in cyclic loading experiments, which consistently reveal pronounced hysteresis in the stress–strain response of electrospun networks. Ridruejo et al. (2011), for example, investigated the micro-mechanisms of deformation and fracture in thermally bonded polypropylene nonwoven fabrics under varying temperatures and strain rates. Their results showed that hysteresis loops during unloading–reloading cycles widened progressively with increasing deformation. This behaviour was attributed to fibre buckling in compression and frictional sliding between fibres whose bonds had fractured during loading. Both mechanisms strongly influence the unloading response: bond breakage effectively increases the free length of fibres while simultaneously lowering the critical load for buckling. As a result, the network exhibited higher fibre tortuosity or weaker junctions, thus enlarging the hysteresis loops, reflecting greater energy dissipation per cycle.

2.6 Constitutive Models for Non-Woven Networks

Existing models on the mechanics of non-woven networks can be divided into three main categories: (1) phenomenological, (2) micro-mechanical, and (3) discrete. Each of these techniques will be discussed in sub-sections below.

2.6.1 Phenomenological Models

In the context of biomaterials and rubber elasticity, phenomenological modelling has been commonly employed to relate deformation to stress-state of the material (Arruda and Boyce, 1993; Boyce and Arruda, 2000; Holzapfel, 2005; Wex et al., 2015). However, modelling the continuum mechanical response of electrospun networks through phenomenological approaches is uncommon in the literature. Duling et al. (2008) experimentally characterised the mechanical behaviour of electrospun PCL membranes and subsequently utilised both Fung's quasilinear viscoelastic (QLV) model (Fung et al., 1972) and the Arruda and Boyce eight-chain model (Arruda and Boyce, 1993) to fit experimental data. Although, Fung's QLV phenomenological approximation best captured the loading and relaxation phases of the material response, the response was only predicted at small strains and fails to precisely capture the rate-dependent behaviour of electrospun mats. Wong et al. (2019) proposed a simple phenomenological model aiming to capture the individual fibre response and inter-fibre interactions through hyperplastic and large strain elasto-plastic frameworks. Results were compared with experimental data from PVDF electrospun membranes. The model demonstrated good agreement with uniaxial and cyclic loading tests with slight underestimation of stress-stretch response, but was oversimplified such that time-dependency is neglected.

Phenomenological modelling is advantageous in that it provides a direct method of predicting material response in a computationally-efficient way. However, this method lacks the ability to relate physical microstructural parameters to model variables. Therefore, micromechanics-based models are highly desired.

2.6.2 Micro-Mechanical Models

The fundamental goal of a micromechanical model is to predict the macroscopic response of materials on the basis of microstructure geometry and properties of individual phases (Sadd, 2019). Micromechanical approaches rely on the definition of a representative volume element (RVE) to calculate averaged properties. Regarding electrospun networks (ESNs), specific challenges arise from complex geometric arrangement of individual fibres, fibre-fibre interactions, heterogeneous fibre deformation, and microstructural evolution. Depending on the proposed RVE, models have adopted the transition between micro- and macro- through semi-analytical and numerical approaches.

Semi-Analytical Models

Semi-analytical micro-mechanical models have approached multi-scale transition using unit cells with three or four representative fibres (Arslan and Boyce (2006); Caballero et al. (2019); Pai et al. (2011); Silberstein et al. (2012)). This approach was first attempted by Arslan and Boyce (2006) using a triangulated structure RVE to mimic the mechanical behaviour of spectrin, a protein which plays an important role in cytoskeletal structure. Pai et al. (2011) proposed a RVE with four representative fibres in order to investigate the Young's moduli and yield strength of electrospun poly(trimethyl hexamethylene terephthalamide) fibres under uniaxial tension. The study evaluated the influence of fibre curvature by comparing two micro-mechanical models assuming straight and curved fibres. These authors concluded that the governing factors affecting the mechanical properties of non-woven mats are porosity, intrinsic fibre modulus, fibre diameter, curvature and distance betweeen fibre-fibre junctions. Similarly, Silberstein et al. (2012) investigated the elastic-plastic response of electrospun polyamide through a multi-layered idealised triangulated RVE with adaptable fibre properties, network geometry, and density. Individual fibres are modelled as elastic-plastic, and contain an initial curvature to capture effects of bending and stretching. Ultimately, the model was able to capture with good agreement the mechanical response of several uniaxial tests including, elastic-plastic axial stress-strain behaviour, transverse strain, cyclic loading, and elastic stiff evolution with plastic strain. Expanding on Silberstein's model, Caballero et al. (2019) utilised a statistical approach with the idealised triangulated RVE as a base framework to investigate the effect of fibre tortuosity and progressive recruitment to better capture the macroscopic non-linear mechanical behaviour of ESNs.

Statistical averaging has also been considered by Rizvi et al. (2012). The proposed study investigated the influence of fibre assembly on macroscopic mechanical properties of non-woven fibrous materials. The model utilised a theoretical RVE matrix with three different micro-structural fibre categories, (1) curved non-loading bearing fibres, (2) straight-load bearing fibres, and (3) broken non-load bearing fibres. Simulations strictly assumed straight fibres were the only contributors to the overall macroscopic response, and curved fibres were progressively recruited to contribute to the overall response. The theoretical results demonstrated good agreement with experimental data. Although the model was able to predict the mechanical behaviour trend, it ignored important details, such as the friction between fibres. The conclusion made it clear that fibre alignment plays a fundamental role in the mechanical properties of ESNs and scaffold design should focus on optimising structural configuration to achieve desired mechanical properties.

Computational Models

Discrete network models (DNMs) are based on RVEs containing a long number of random oriented fibres. The macroscopic loading is applied at the RVE boundaries and the RVE response is calculated using finite element methods (FEM). Several research groups have adopted DNMs to model non-woven fibre networks (Argento et al., 2012; Caballero et al., 2022; Carleton et al., 2017; Domaschke and Ehret, 2020; Domaschke et al., 2020, 2019; D'Amore et al., 2014; Goutianos et al., 2018; Kulachenko and Uesaka, 2012; Kumar and Rawal, 2017; Stylianopoulos et al., 2008; Wan et al., 2015; Wei et al., 2009; Zhang et al., 2019, 2021; Zündel et al., 2019, 2017). Most of these studies investigated the relation of macroscopic properties with volume fraction and fibre mechanics (i.e. alignment, aspect ratio, stiffness, tortuosity, and orientation) (Argento et al., 2012; Caballero et al., 2022; Carleton et al., 2017; Domaschke et al., 2019; Stylianopoulos et al., 2008; Zhang et al., 2019, 2021). Other studies have focused on analysing the inter-fibre bonding and deformation (Goutianos et al., 2018; Kulachenko and Uesaka, 2012; Wei et al., 2009); or topological evolution through, pore size, pore orientation, fibre diameter, and physical cross-linking between fibres (Zündel et al., 2017); and even the biocompatibility of electrospun substrates by evaluating microscopic stiffness with cellular compatibility (Zündel et al., 2019).

An advantage of DNMs is the geometrical resemblance these models are able to produce, which enables the study of microstructural features, such as, pore size, pore density, fibre shape, tortuosity, orientation, and inter-fibre interactions, to name a few. Additionally, these models are capable of dealing with arbitrary fibre behaviour and contact interactions. On the other hand, this approach is computationally expensive and thus are not situated for concurrent multi-scale simulations. These also require dedicated algorithms to produce random microstructures that are not trivial.

2.7 Biodegradable Polymers

2.7.1 Fundamentals of Polymer Degradation

Biodegradable polymers degrade primarily through a chemical reaction in the polymer matrix resulting in a cleavage of covalent bonds (Göpferich, 1996; Li et al., 2020; Ratner et al., 2004). The primary mode of degradation of biodegradable polyesters (e.g. PCL, PLA, PGA, PHB) is chain scission through hydrolysis by reaction of ester bonds with water, which leads to a reduction in molecular weight, mechanical properties, mass, and volume. The rate of degradation can be influenced by several factors including, temperature (Polak-Kraśna et al., 2021), molecular weight, crystallinity (Zong et al., 1999), pH (Jung et al., 2006; Sailema-Palate et al., 2016), enzymatic reactions (Pena et al., 2006), device geometry (Bosworth and Downes, 2010; Natu et al., 2013), and mechanical loading (Deng et al., 2005; Guo et al., 2016; Li et al., 2010; Samanta et al., 2025). While the mechanisms of degradation are well understood, the core challenge remains in understanding how each factor ultimately controls the degradation time and how polymers maintain their structural integrity and properties when exposed to different environments (Casalini, 2017; Iordanskii et al., 2015; Laycock et al., 2017; Ozdil et al., 2017).

Polyesters such as poly(lactic acid) (PLA), poly(glycolic acid) (PGA), and poly(ε-caprolactone) degrade via random chain scission when water molecules access and cleave backbone ester linkages (Woodard and Grunlan, 2018). Hydrophobic, aromatic polyester backbones exclude water and degrade extremely slowly, whereas aliphatic polyesters with short methylene segments between esters, permit sufficient water penetration for observable hydrolysis kinetics (Edlund and Albertsson, 2003). For example, in the case of PCL, chain scission occurs preferentially in amorphous regions due to the loose structural packing within the microstructure, making ester bonds exposed to attack of water molecules. Ester bonds are subsequently cleaved from the polymer backbone, shortening the chain length resulting in the formation of carboxylic acid (Bosworth and Downes, 2010). This process is illustrated in Figure 2.7.

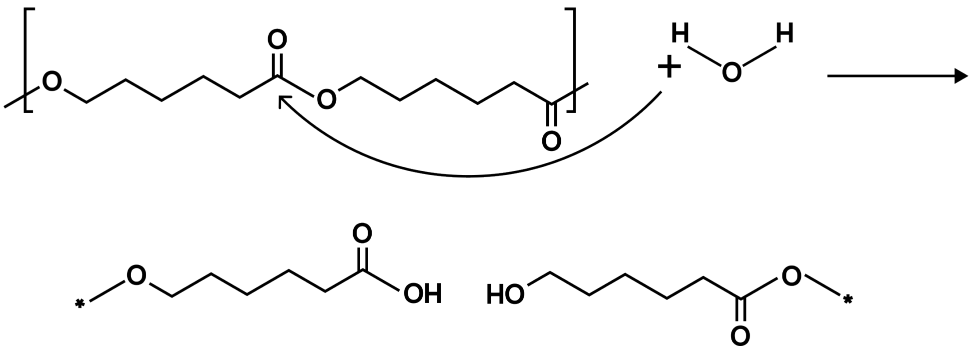

Figure 2.7: Schematic representation of hydrolytic degradation of poly(ε-caprolactone), showing attack of water on the ester linkage, resulting in chain scission and the formation of hydroxyl- and carboxylic acid-terminated fragments.

The interplay between water ingress and oligomer diffusion into the surroundings determines whether degradation proceeds via surface erosion or bulk degradation. Three degradation models are commonly distinguished (Laycock et al., 2017; Lin and Anseth, 2013; Vieira et al., 2011; Woodruff and

Hutmacher, 2010). The first model is surface erosion, which occurs when the hydrolytic chain-scission rate at the polymer–water interface exceeds the rate of water penetration into the bulk, oligomers and monomers are cleaved and diffuse away faster than water can advance. The result is a gradual thinning of the material's surface while the internal molecular weight remains essentially unchanged over time. The advantage of surface degradation is the predictability of the process (Göpferich, 1996). The second model is bulk degradation (homogenous degradation) occurs if water readily permeates the entire polymer matrix, hydrolysis occurs uniformly throughout. Random chain scission reduces molecular weight across the whole sample. Oligomer diffusion keeps pace with water ingress, maintaining a steady-state diffusion–reaction balance until substantial mass loss begins. Lastly, the case for autocatalyic bulk erosion (acid-accelerated interior degradation) occurs when the diffusion-reaction equilibrium is disturbed. In this case, the carboxyl and hydroxyl end groups generated by hydrolysis cannot diffuse out as quickly as they form, leading to an acidic interior gradient. This trapped acidity accelerates interior chain scission, producing a low-molecular-weight core beneath a higher-molecular-weight "skin". Autocatalytic degradation mechanism becomes defined by a bimodal molecular weight distribution. Once the core oligomers become small enough, they rapidly diffuse out, triggering a phase of noticeable weight loss and the formation of a hollowed-out structure (Li, 1999; Therin et al., 1992).

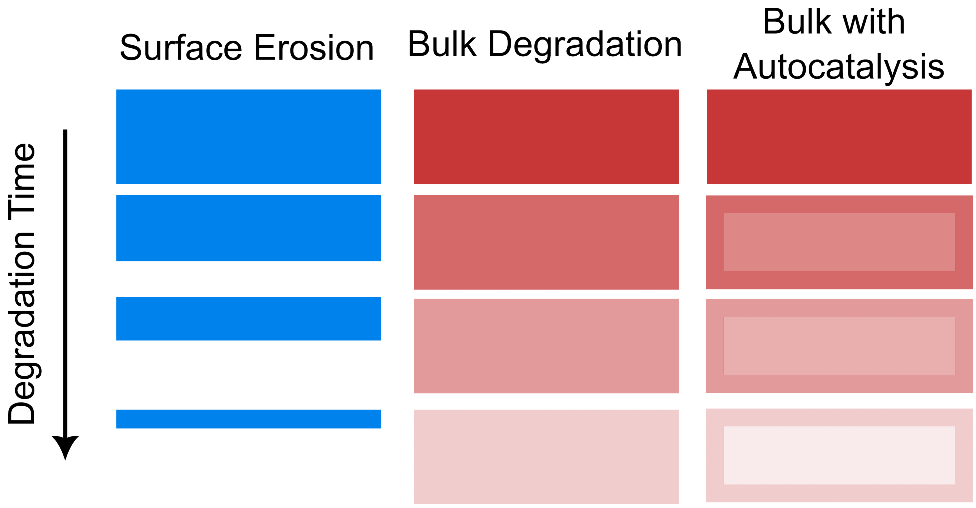

Figure 2.8: Degradation modes for degradable polymer: Surface erosion, bulk degradation, and bulk degradation with autocatalysis.

The kinetics of bond cleavage in the main polymer chain is dependent on many factors including: the polymer chain length, crystallinity, molecular weight distribution, swellability, size, shape and geometry of polymer matrix, surface pretreatment, porosity, pore size and distribution, pore geometry, processing conditions, and water diffusivity in the polymer matrix (Laycock et al., 2017; Lucas et al., 2008). But in general, methods that increase penetration of water, accelerate hydrolysis. Key methods to evaluate the degradation of a polymeric material can include: changes in crystallinity, solution pH, molecular weight distribution, glass transition temperature (T_g), and melting temperature (T_m) (Chandra and Rustgi, 1998; Reddy, 2013).

2.7.2 Poly(ε-caprolactone)

Poly(ε-caprolactone) or PCL, is a hydrophobic, semi-crystalline aliphatic polyester (Dhanasekaran et al., 2022). PCL has high solubility properties, excellent ability to form blends, and a low melting temperature (T_m = 60°C; T_g = -60°C) (Ratner et al., 2004). Reported bulk properties include a Young's modulus in the range of 210 – 440 MPa, a yield stress (σ_y) of 8 – 18 MPa, and a tensile strength (σ_m) between 10.5 and 27 MPa (Bartnikowski et al., 2019; Labet and Thielemans, 2009). These properties are strongly influenced by the degree of crystallinity and molecular weight of the polymer. PCL typically exhibits an initial crystallinity of approximately 45%, which can increase to as high as 80% during degradation due to chain scission and subsequent recrystallisation (Pitt et al., 1981a). Compared to other polyesters, PCL exhibits significantly slower degradation (approximately 2–4 years to full breakdown) due to the presence of five hydrophobic $-CH_2$ moieties in its repeating units, which increase its resistance to hydrolysis (Dwivedi et al., 2020). These properties enhance the material's ability to maintain its intended function throughout its lifespan, making it suitable for long-term biomedical applications. It is produced via ring-opening polymerization of ε-caprolactone and a schematic of the chemical structure is illustrated in Figure 2.9.

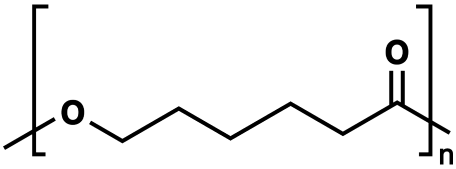

Figure 2.9: Schematic illustration of PCL chemical structure.

Poly(ε-caprolactone) was first synthesized in 1930s and was commercially available soon thereafter (Natta et al., 1934), but widespread interest in biodegradable polymers did not emerge until several decades later. In the 1970s and 1980s, renewed attention to resorbable polymers arose around their use in drug-delivery devices, driven by the need for materials with tailorable degradation kinetics, tunable mechanical properties, and ease of processing. However, PCL's inherently slow hydrolytic rate limited its adoption, by contrast, poly(lactide) (PLA) and poly(glycolide) (PGA) could be fully resorbed within two to four months post-implantation, making them more attractive for early medical applications (Woodruff and Hutmacher, 2010). The modern resurgence of PCL began in the 1990s with the rise of tissue engineering. Researchers recognized PCL's superior rheological and viscoelastic properties, such as low melting temperature and high elongation at break, alongside its amenability to advanced scaffold-fabrication techniques (e.g., electrospinning and 3D printing). Consequently, PCL became a cornerstone material for applications ranging from soft-tissue repair to controlled-release systems (Lee et al., 2003; Luciani et al., 2008).

2.7.3 Degradation of Poly(ε-caprolactone)

Physiological Conditions

The degradation behavior of PCL has been extensively studied across various conditions (Bartnikowski et al., 2019; Woodruff and Hutmacher, 2010). *In vitro* studies have examined its response in different media, including phosphate-buffered saline (PBS) (Fernández et al., 2015, 2012, 2013), simulated body fluid (SBF) (Domingos et al., 2010), and Ringer's solution (Bolgen et al., 2005). Complementary *in vivo* investigations have typically employed subcutaneous (SC) implantation models, commonly in the form of capsules, in animal models such as rabbits (Lam et al., 2009) and rats (Bolgen et al., 2005; Sun et al., 2006). Across these studies, a consistent two-stage degradation mechanism for PCL has been identified. The initial phase involves non-enzymatic hydrolytic cleavage of ester bonds. Once the polymer reaches a critical molecular weight threshold (approximately 5000 Da), the resulting oligomers and fragments undergo cellular uptake and intracellular degradation, primarily mediated by macrophages (Lanza et al., 2020; Pitt et al., 1981a; Woodward et al., 1985), ultimately enabling complete metabolization and excretion of degradation by-products (Li et al., 2020). Bartnikowski et al. (2019) conducted a numerical analysis synthesizing trends in molecular weight, elastic modulus, and mass loss across more than 25 studies performed both *in vivo* and *in vitro*. A key observation was that while molecular weight consistently decreased in all cases, the degradation kinetics differed depending on the environment. *In vitro* data exhibited zero-order behaviour, characterized by linear molecular weight decline, suggesting end-chain scission and constant chain shortening, accompanied by the irreversible loss of soluble oligomers and monomers into the surrounding medium. In contrast, *in vivo* degradation followed apparent first-order kinetics, implying a random chain cleavage mechanism, where longer chains degrade more rapidly, leading to an exponential decline in molecular weight. These differences underscore the significant mechanistic and kinetic distinctions between *in vivo* and *in vitro* degradation conditions.

Autocatalysis of PCL

It is possible for PCL to exhibit autocatalytic degradation behaviour as water penetrates the polymer matrix and hydrolyses ester bonds, generating carboxylic end groups that, in turn, catalyse further chain scission. Pitt et al. (1981a,b) and Woodward et al. (1985), who investigated the *in vivo* degradation of PCL, observed first-order kinetic behaviour, evidenced by a linear relationship between $\ln M_n$ and degradation time, with negligible mass loss. The molecular weight during degradation was reported to evolve toward a bimodal form, consistent with autocatalytic chain cleavage. The underlying mechanism of polyester breakdown, which is self-accelerated by the accumulation of carboxylic acid end groups, can be expressed as:

$$-\frac{d[\text{Ester}]}{dt} = k[COOH][\text{Ester}][H_2O] \tag{2.1}$$

where [Ester] is the concentration of ester bonds in the polymer, $[H_2O]$ is the concentration of water, $[COOH]$ is the concentration of carboxylic end groups, t is the degradation time, and k is the kinetic rate of degradation. Since each polymer chain contains a finite number of end groups, the concentration of carboxylic acid end groups is directly proportional to the number of chains per unit volume. For a linear polymer, the number of chains scales inversely with the number-average molecular weight, such that the molar concentration of chains is given by ρ/M_n, where ρ is the polymer density. As each chain contributes approximately one carboxylic acid end group, it follows that $[COOH] \propto 1/M_n$ (Lyu et al., 2007). Consequently, as hydrolysis proceeds and chains are cleaved, the number of chains increases, leading to a rise in $[COOH]$, which further accelerates ester bond cleavage and gives rise to autocatalytic behaviour. Substituting this relationship into the rate expression yields a degradation rate that is inversely dependent on molecular weight, resulting in first-order kinetics with respect to M_n. This leads to an exponential decay in molecular weight of the form:

$$M_n = M_0 \exp(-kt) \tag{2.2}$$

Extending these findings to controlled *in vitro* conditions, Pitt and Gu (1987) examined the effect of ethoxylation on the hydrolytic degradation of PCL to test the hypothesis of autocatalysis. The modified polymer displayed a slower rate of chain scission, thereby providing evidence that the unmodified PCL degrades through an autocatalytic pathway. Likewise, Pena et al. (2006) identified autocatalytic behaviour through a bimodal molecular weight evolution, where the first regime corresponded to autocatalytic cleavage of ester bonds, while the second reflected the emergence of crystalline domains formed from shorter chains generated during degradation.

While these studies elucidated the molecular-level kinetics of chain scission, subsequent research has shown that the manifestation of autocatalysis is also influenced by scaffold architecture. Zhang et al. (2013) conducted a 72-week *in vitro* study on PCL scaffolds of varying porosities to investigate the effect of structural architecture on degradation kinetics. Their findings showed that highly porous scaffolds degraded substantially faster due to enhanced water ingress and greater surface area, whereas low-porosity scaffolds exhibited minimal evidence of internal acid-catalysed degradation. The authors attributed this to the efficient diffusion of acidic oligomers out of the porous structures, which prevented their accumulation and the self-catalytic acceleration of hydrolysis. In contrast, Larrañaga et al. (2014) reported partially opposing results, observing that non-porous PCL and PLA scaffolds degraded more rapidly than their porous counterparts. This behaviour was attributed to restricted diffusion of acidic degradation products in the dense matrices, leading to internal acidification and enhanced autocatalysis.

Influence of Degradation on Crystallinity and Thermal Properties of PCL

The degradation behaviour of PCL is closely governed by its semi-crystalline morphology, with degradation occurring preferentially in the amorphous regions due to their lower density and greater accessibility to water molecules. This selective hydrolysis results in progressive increases in crystallinity, as the remaining material becomes enriched in crystalline domains. Additionally, hydrolytic chain scission enhances polymer chain mobility, particularly at physiological temperatures where PCL remains well above its low glass transition temperature ($T_g \approx -60°\mathrm{C}$). This facilitates chain rearrangement and recrystallisation, further contributing to crystallinity increases through annealing-like effects.

Across multiple studies, consistent trends have been observed regarding the structural evolution of PCL during degradation: crystallinity tends to increase during the early to mid-stages, often accompanied by rises in melting temperature (T_m) and glass transition temperature (T_g), reflecting the growth and stabilization of crystalline domains (Ali et al., 1993; Bosworth and Downes, 2010; Coombes et al., 2004; Lam et al., 2008; Larrañaga et al., 2014; Little et al., 2009; Natu et al., 2013; Pena et al., 2006). Notably, Little et al. (2009), under accelerated degradation conditions, reported a distinctive bimodal crystallinity pattern over seven months, an initial rapid increase attributed to plasticization and reorganization of amorphous regions, followed by a slower, sustained rise. Similarly, Natu et al. (2013) observed crystallinity enhancement driven by water-induced chain rearrangement, with subsequent crystallisation of entrapped degradation fragments (oligomers) within the bulk. Over extended degradation periods, however, a decline in crystallinity has been documented, corresponding to the onset of hydrolysis within the crystalline regions. This later-stage phenomenon was also marked in the study by Bosworth and Downes (2010), where differential scanning calorimetry (DSC) revealed pre-melting peaks, indicative of structural polymorphism and the thermal transitions of less stable or intermediate crystalline phases.

Influence of Degradation on Mechanical Properties and Mass Loss of PCL

The degradation of PCL has a pronounced impact on its mechanical properties, including elastic modulus, yield strength, flexibility, and elongation at break. In terms of stiffness and elastic modulus, a biphasic trend is commonly observed. In the short term, PCL often exhibits an increase in stiffness and modulus (Lam et al., 2009, 2008; Zhang et al., 2013), primarily attributed to increased crystallinity. This arises from the preferential degradation of amorphous regions, which enriches the crystalline content and enhances structural rigidity (Little et al., 2009). However, over prolonged degradation periods, as hydrolysis begins to affect the crystalline domains, the elastic modulus eventually declines, coinciding with structural deterioration and mass loss (Pitt et al., 1981a). The behavior of yield stress is more variable. Some studies have reported short-term increases (Lam et al., 2009), likely due to crystallinity enhancement, whereas others found negligible changes over comparable periods (Little et al., 2009; Yavuz et al., 2002), suggesting this property is highly sensitive to testing conditions and sample morphology.

In contrast, the elongation at break exhibits a consistent and significant decline with degradation. This reflects a loss in ductility, as the material becomes increasingly brittle over time (Bolgen et al., 2005; Lam et al., 2008). The key mechanisms underlying these mechanical changes include: (1) molecular weight reduction, which compromises chain entanglement and load transfer; (2) crystallinity evolution, which alters phase morphology; and (3) the formation of microcracks and pores, which act as stress concentrators and facilitate failure (Ali et al., 1993; Lam et al., 2008).

2.8 Degradation of Non-Woven Networks

The degradation behaviour of electrospun fibre networks diverges from that of bulk polymers due to differences in morphology, architecture, and surface exposure. While the underlying chemical pathways (e.g., hydrolytic or enzymatic cleavage of ester bonds in biodegradable aliphatic polyesters) are the same, the kinetics, spatial progression, and mechanical consequences of degradation are structure-dependent. Several groups have attempted to capture these distinctions and to identify the mechanisms that control degradation kinetics in electrospun systems (Abdullah and Molnár, 2024; Bazgir et al., 2021; Bolgen et al., 2005; Carniel et al., 2021; Johnson et al., 2009; Khiste et al., 2013; Kim et al., 2003; Limbert et al., 2016; Mouthuy et al., 2015; Natu et al., 2013; Sailema-Palate et al., 2016; Vaid et al., 2021).

One of the primary distinctions is the large surface-area-to-volume ratio of electrospun fibres, which accelerates water uptake and the diffusion of small molecules. This facilitates earlier onset of hydrolytic and enzymatic attack compared with bulk specimens (Bolgen et al., 2005; Cipitria et al., 2011). In particular, smaller fibre diameters shorten the diffusion path length for acidic degradation products, allowing faster clearance into the medium and mitigating autocatalytic effects (Bosworth and Downes, 2010; Kim et al., 2003). However, the porous nature of electrospun scaffolds means that degradation pathways may vary depending on the local environment. For instance, Lam et al. (2008) showed that PCL scaffolds degraded under alkaline conditions via surface erosion, characterised by fibre thinning with little change in molecular weight. By contrast, long-term studies under physiological conditions typically reveal bulk-degradation behaviour, with significant molecular weight reduction but limited mass loss. Furthermore, the rate of molecular weight decrease has been shown to scale with porosity, as greater pore connectivity enhances medium accessibility (Natu et al., 2011; Zhang et al., 2013).

Another critical feature relates to the interplay between amorphous and crystalline domains. Amorphous regions are preferentially attacked due to their higher chain mobility and accessibility, leaving behind an enriched crystalline fraction. However, the situation in electrospun fibres is more nuanced: rapid jet stretching and solidification during processing generate metastable crystalline phases, high internal stresses, and non-equilibrium molecular orientations. These factors render the amorphous–crystalline interface more dynamic, making secondary crystallisation or chain realignment more likely during degradation compared with bulk polymers. Consequently, degradation often begins with scission of amorphous domains, temporarily increasing relative crystallinity, before progressing into crystalline regions. This transition leads to chain shortening, embrittlement, and reduced fibre integrity, ultimately undermining the mechanical robustness of the network (Abdullah and Molnár, 2024; Vaid et al., 2021).

Overall, the degradation of non-woven scaffolds is not merely a function of polymer chemistry but also of fibre morphology and network architecture. These parameters must be carefully controlled during fabrication and characterised during scaffold design, as they influence not only the rate of degradation but also its mechanical and biological consequences.

Chapter 3

Characterisation and modelling of continuous electrospun poly(ε-caprolactone) filaments for biological tissue repair

This chapter presents an investigation into the thermo-mechanical behaviour of electrospun PCL filaments. It also establishes the experimental and theoretical foundation necessary for developing predictive models. The experimental methods and data discussed herein are based in the work published in: Ferreira, T. Z., Pan, Z., Mouthuy, P.-A., & Brassart, L. (2025). Characterisation and modelling of continuous electrospun poly(ε- caprolactone) filaments for biological tissue repair. *Journal of the Mechanical Behavior of Biomedical Materials*, 161, 106810. https://doi.org/10.1016/j.jmbbm.2024.106810.

Each author contributed to the article as follows:

- **Thales Zanetti Ferreira**: Writing - review & editing, Writing - original draft, Software, Methodology, Investigation, Formal analysis, Conceptualization.
- **Zhouzhou Pan**: Writing - review & editing, Software, Formal analysis.
- **Pierre-Alexis Mouthuy**: Writing - review & editing, Supervision, Resources, Methodology, Funding acquisition, Conceptualization.
- **Laurence Brassart**: Writing - review & editing, Writing - original draft, Supervision, Software, Resources, Methodology, Funding acquisition, Formal analysis, Conceptualization.

3.1 Introduction

Electrospinning (ES) is a simple yet powerful method for producing ultra-lightweight non-woven textiles made of micro- to nano-sized fibres (Amoroso et al., 2011; Bosworth, 2014; Ratner et al., 2004). This technique utilises electrostatic forces to draw fibres from a viscoelastic polymer solution. The drawn fibres are continuously deposited onto a collecting device to produce an interconnected non-woven mesh (Fang et al., 2008). Due to their highly porous structure, high surface-to-volume ratio, and tunable architecture, ES materials have been used in a broad range of applications, including biomedical, pharmaceutical, packaging, and textile applications (Fang et al., 2008; Liu et al., 2020, 2021; Nangare et al., 2020; Zhao et al., 2020). ES meshes are particularly attractive for tissue engineering applications, where they can be designed to mimic the extracellular matrix architecture, promoting tissue growth (Liu et al., 2020; Mouthuy et al., 2015; Sensini and Cristofolini, 2018).

In the search for robust and scalable ES methods, a novel automated technique was recently introduced by (Mouthuy et al., 2015) to produce continuous ES filaments by depositing the fibres onto a continuous guiding wire. This technique differs from traditional ES setups, which collect fibres onto the surface of plates, bars, and disks (Teo and Ramakrishna, 2006). Compared to planar constructs, the advantage of continuous ES filaments is that they can be further processed into woven, knitted, or braided structures, which can be used to create a variety of scaffolds. For example, multifilament yarns made of twisted or woven ES filaments have shown great promise for ligament and tendon repair (Mouthuy et al., 2015; Savić et al., 2021). However, the mechanical behaviour of such ES filaments has not been fully characterised and understood.

The objective of this work is to characterise the thermo-mechanical behaviour of poly(ε-caprolactone) (PCL) ES filaments produced following the technique developed by (Mouthuy et al., 2015). Previous studies investigated the mechanical response of polydioxanone ES filaments in the context of suture applications (Abhari et al., 2018a,b, 2017; Lach et al., 2019). Here, PCL was selected due to its wide use in tissue engineering, exhibiting a slow degradation rate and minimal inflammatory response (Bartnikowski et al., 2019; Malikmammadov et al., 2018). Thermo-mechanical characterisation tests considered in this study include Differential Scanning Calorimetry (DSC), Dynamic Mechanical Analysis (DMA), as well as quasi-static uniaxial tension tests. Our results show that the filament response is rate-dependent and involves plastic yielding followed by re-hardening at large deformations. The different stages of the deformation are correlated to the evolution of the microscopic fibrous network, observed using Scanning Electron Microscopy (SEM). The sensitivity of the measured mechanical response to the type of mechanical grips used is highlighted. We further develop a viscoelastic-viscoplastic constitutive model to phenomenologically capture the mechanical response.

3.2 Experimental Methods

3.2.1 Polymer Solution Preparation

Electrospinning solutions were prepared by dissolving PCL with molecular weight $M_w = 167$ kDa (Ashland Specialities, Ireland) into 1,1,1,3,3,3-hexafluoroisopropanol (HFIP) (Apollo Scientific Ltd, UK). The solution was prepared at a concentration of 10% (w/v), corresponding to 10 g of PCL dissolved in 100 mL of HFIP. Solutions were agitated at room temperature at a speed of 21 rpm using a roller mixer (Stuart SRT9D, UK) for at least 24h to ensure complete dissolution of the polymer.

3.2.2 Electrospinning

ES filaments were produced by depositing a continuous fibre on a thin guided wire, creating a dense and narrow mesh that can be detached as a long continuous thread, as shown in Figure 3.1. A detailed description of the production technique can be found in (Mouthuy et al., 2015). Electrospinning was performed with a single nozzle setup, a continuous wire (100 μm diameter) (Goodfellow, UK), an SL30P30/230 high voltage power supply (30 kV)(Spellman, UK) and a syringe pump (World Precision Instruments Limited, US). The metallic wire was cleaned with 70% ethanol prior to setup. The process was conducted inside a glove box under constant airflow to prevent organic vapour from interacting with the process. Environmental factors were controlled with the room temperature set to $22 \pm 3°C$ and humidity to $40 \pm 3\%$. The polymer solution was fed at a rate of 1 ml hr^{-1}. The distance between the nozzle tip and wire was 20 cm and the applied voltage ranged between 7 kV and 10.5 kV. The wire displaced perpendicular to the nozzle tip at a speed of 0.4 mm s^{-1}. The resultant product is a metallic wire coated in a continuous ES mesh. Following the exit of the wire from the glovebox, the ES filament was detached from the wire and automatically collected on a rotating spool. The filament spool was stored in a desiccator until required for characterisation testing.

3.2.3 Thermal Properties

Differential scanning calorimetry (DSC) was used to investigate the thermal properties of ES PCL filaments. Experimental tests were performed with a DSC Q2000 differential scanning calorimeter (TA Instruments, US) in a nitrogen atmosphere with a flow rate of 50 mL min^{-1} and standard aluminium cups with lid. Prior to testing, samples were stretched at an extension rate of 75 mm min^{-1} to different

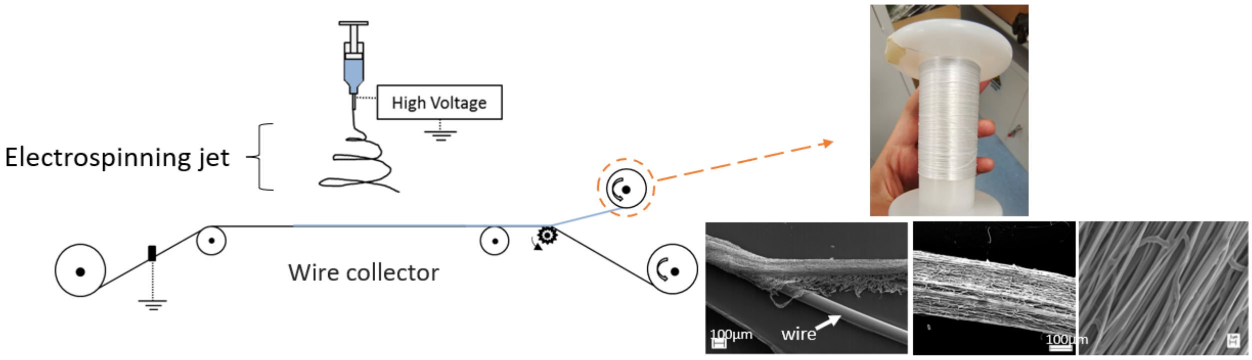

Figure 3.1: Schematic of the novel electrospinning collection technique. The method consists of electrospinning PCL fibres onto a stainless steel wire progressing at a speed of 0.4 mm s^{-1}. The electrospun mesh is separated from the wire and collected in the form of a continuous filament.

nominal strains ($\varepsilon_n = 0, 1, 2, 4, 7$, and 9) using bollard grips, (see Section 3.2.4) to examine whether stretching induced an increase in crystallinity.

Accurate DSC measurements rely on good thermal contact between the sample and the pan. Poor contact introduces additional thermal resistance, leading to a lag between the programmed furnace temperature and the actual sample temperature. This can result in shifts in apparent transition temperatures, peak broadening, and reduced accuracy in the measured enthalpy. These effects are particularly relevant for electrospun fibrous materials, which are low-density and do not naturally conform to the pan surface. To minimise these artefacts, particular care was taken in sample preparation. Three samples were tested for each strain to ensure reproducibility. A minimum sample mass of approximately 5 mg was used to ensure sufficient material to adequately cover the base of the pan. The filaments were gently coiled prior to placement to increase packing density and promote more uniform contact with the pan surface, thereby reducing air gaps and improving heat transfer during the scan. This preparation procedure improved the repeatability and reliability of the measurements.

Each sample was first cooled to -90°C to establish a uniform thermal baseline, followed by heating at 10°C min^{-1} up to 80°C. The samples were then cooled at 10°C min^{-1} down to -30°C. The heat flow per unit mass (W g^{-1}) was recorded to identify thermal transitions, and the resulting thermograms were analysed using TA Universal Analysis software.

3.2.4 Mechanical Testing

The small-strain viscoelastic properties of filaments were characterised via dynamic mechanical analysis (DMA). Uniaxial tension tests were performed using a Q800 dynamic mechanical analyser (TA Instruments, US) using a thin-film clamp at room temperature (27 ± 2°C) and environmental humidity conditions. Samples were prepared by glueing filaments onto a cardboard window frame to increase the clamping surface area, as illustrated in Fig. 3.2. Temperature sweep tests ranging between -92°C and 46°C were conducted with six frequencies ranging between 0.1 Hz and 10 Hz and a 0.1% strain. The storage modulus (E'), loss modulus (E''), and loss tangent ($\tan\delta$) were recorded.

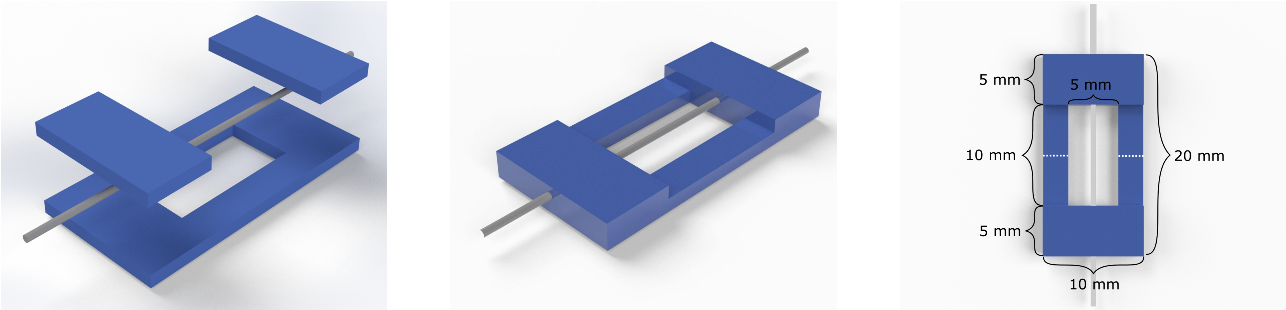

(a) **(b)** **(c)**

Figure 3.2: (a) Electrospun filaments were cut to a standardised size of 25 mm and placed on top of a pre-cut window-style paper cardboard frame. Filaments were glued using superglue (Loctite, US) onto the frame. (b) An additional layer of cardboard paper was glued on top of the filament. (c) The frame was mounted onto testing apparatus with a 10 mm gauge length and the cardboard frame was cut along the white discontinuous lines.

The mechanical response of ES PCL filaments at large strains was characterised using an Instron 5582 electromechanical tensile tester (Instron, UK) with a 100N load cell. Tests were performed with two different grip methods outlined in ISO 2307:2019 (ISO, 2019).

(i) **Bollard grips:** Filaments were cut to a standardised length of 120 mm as this was the minimum length required to wrap the filaments around the grips. Filaments were first wrapped around the top bollard and clamped. Wrapping around the lower component was carefully conducted to ensure vertical alignment and prevent any torsion of the filament. A 45 mm gauge length was defined by the two contact points at which the filament tangentially contact the grips, as illustrated in Fig. 3.3a. Mounting the filaments introduced some pre-load in the range 0.05-0.1 N.

(ii) **Screw-side grips:** Samples tested with screw-driven tensile grips were prepared with the same cardboard methodology as outlined in Fig. 3.2. The gauge length was 10 mm. The cardboard frame was mounted onto the grips and tightened using the screws, as illustrated in Fig. 3.3b.

Uniaxial tensile tests were conducted at room temperature under ambient humidity conditions. Filaments were tested at extension rates of 5, 75, and 150 mm min^{-1} until failure. The nominal strain was defined as $\varepsilon_n = \frac{L-L_0}{L_0} = \lambda - 1$, where L_0 and L are the initial and deformed gauge lengths, respectively, and λ is the stretch ratio. The nominal stress was calculated by dividing the measured force by the initial cross-sectional area, determined from the filament diameter measured using SEM

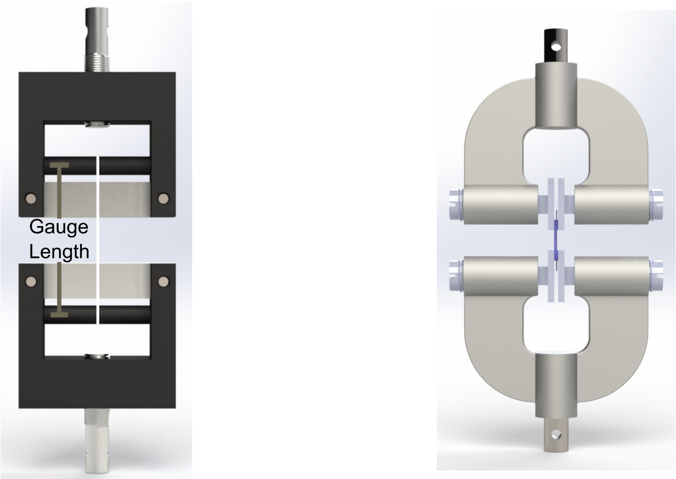

(a) **(b)**

Figure 3.3: Illustration of (a) bollard grips and (b) screw-side tensile grips.

(see Section 3.2.5) and assuming a circular cross-section. In practice, the filament geometry deviates slightly from circularity, exhibiting a shallow U-shaped profile due to detachment from the collection wire. To ensure consistency, diameter measurements were taken from the flatter (deposition) side of the filament. The reference diameter used to convert force–displacement data to stress–strain was 832.2 ± 10.1 μm. Important to note that the filament diameter is influenced by local fibre packing and varies along its length due to the non-uniform nature of the electrospinning process. To account for this variability, multiple measurements were taken within each micrograph and across different samples. The reported value therefore represents an average diameter rather than a specimen-specific measurement. Individual diameter measurements were not performed for every tested filament. Consequently, some uncertainty is introduced in the calculated stress values, as variations in diameter between specimens are not explicitly captured. Nevertheless, as all data were processed using the same approach, the relative differences between conditions remain meaningful.

The apparent elastic modulus was obtained from a linear fit to the initial portion of the stress–strain curve. The yield stress was determined using a 0.2% strain offset. Additional loading–unloading tests at 75 mm min^{-1} were conducted to assess irreversible deformation. Stress relaxation experiments were performed by loading the filament to a prescribed force at 75 mm min^{-1}, followed by a hold at constant displacement. Cyclic loading tests were carried out on filaments pre-stretched to eight times their original length, using 10 cycles at 75 mm min^{-1}.

Statistical analysis was conducted using OriginPro (OriginLab Corp., US). Differences between groups were evaluated using one-way ANOVA with Tukey post hoc comparisons. Statistical significance was defined as $p \leq 0.05$.

3.2.5 Microstructural Characterisation

The microstructure of pre-stretched filaments was characterised using a TM3030Plus tabletop scanning electron microscope (Hitashi, Japan). Independent filaments were first stretched to specific strains using an electromechanical tensile testing with a 75 mm min^{-1} extension rate. Filaments were then unmounted from the machine and given time to fully relax (at least 30 min). The middle portion of each stretched filament was then cut in several shorter sub-filaments using scissors. The sub-filaments were mounted onto an aluminium stub using a carbon adhesive disk. The SEM was operated under variable pressure with a 15 kV acceleration voltage and 4.4-4.8 mm working distance. Micrographs were taken at magnifications between ×100 and ×5000. The filament and fibre apparent diameters were measured using the ImageJ software. All average diameter values reported in the paper were calculated based on micrographs corresponding to three different sub-filaments, and at least 10 diameters were measured in each micrograph. Surface porosity was estimated based on the area fraction of the dark region relative to the white fibrous region in contrasted images in ImageJ. The reported porosity values presented in the paper were obtained based on a single micrograph.

Alternatively, the continuous evolution of the filament microstructure during deformation was characterised through *in-situ* tensile testing. Samples were tested with a Deben Microtest tensile stage (Judges Scientific, UK) with a 20N load cell. The stage was designed to fit into an Evo LS15 Environmental SEM (Carl Zeiss, Germany) for *in-situ* microscopy testing. Specimens were prepared using the cardboard method outlined in Fig. 3.2 and required no metallic coating as the SEM was operated under environmental variable pressure at 15 kV acceleration voltage and 14 mm working distance. Samples were stretched at a deformation rate of 5 mm min^{-1} and held at constant strain while images were taken.

3.3 Experimental Results

3.3.1 Thermal Properties

Fig. 3.4(a) shows DSC thermographs of the average response of ES filaments stretched to six different nominal strains (ε_n = 0, 1, 2, 4, 7, and 9). Each curve corresponds to the average of three filament responses. Thermographs all show the same response overall, although two subtle differences arise from stretching the filaments. Firstly, the heat flow curve in the glass transition region presents an

'S' shape for the un-stretched filaments, whereas it gradually becomes linear as the level of pre-strain increases (Fig. 3.4(b)). Secondly, the endothermic heat flow peak amplitude gradually reduces and its spread increases with increasing strain (Fig. 3.4(c)). However, the exothermic (i.e. recrystallisation) peak appears largely independent of the level of pre-strain (Fig. 3.4(d)).

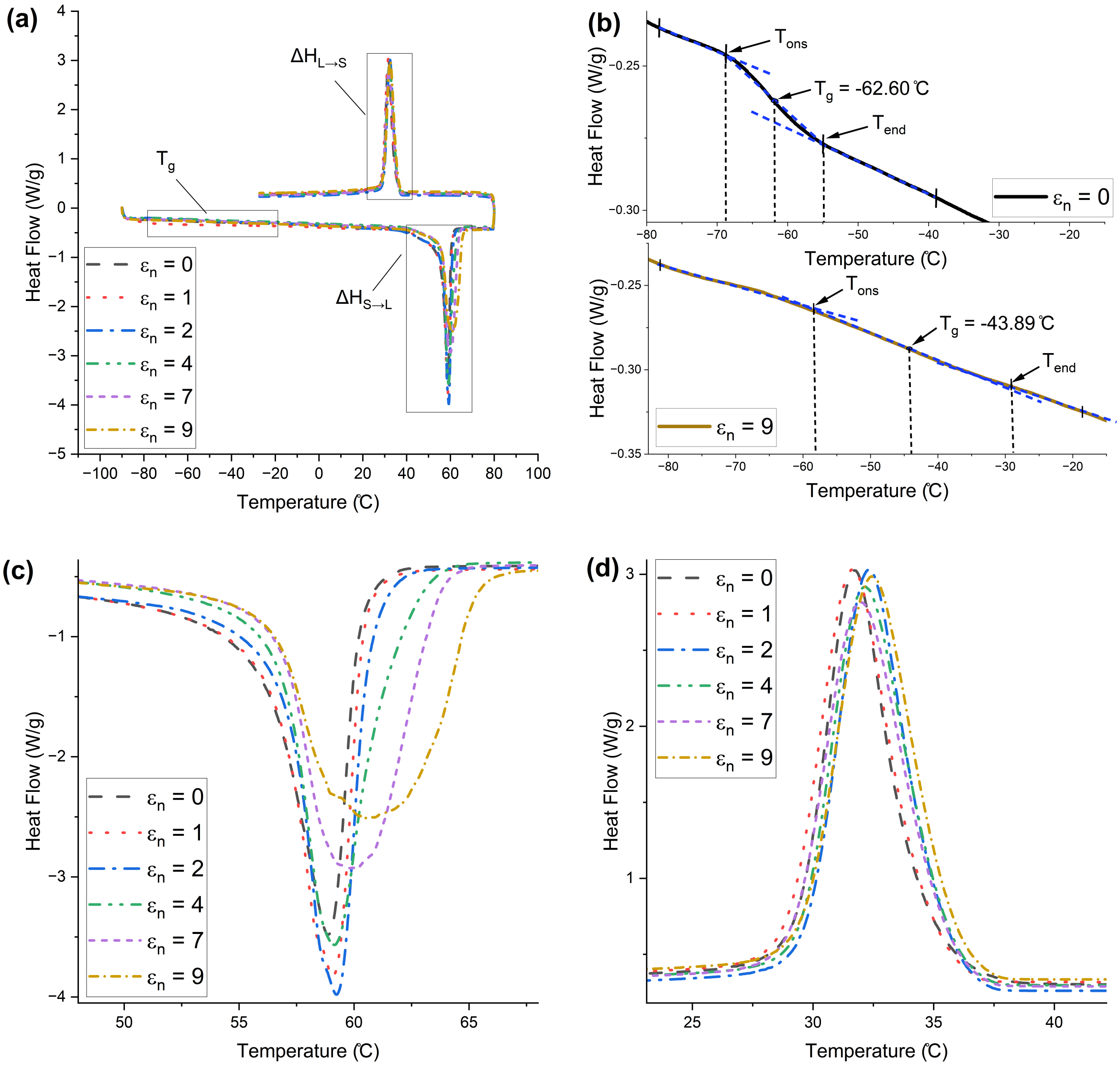

Figure 3.4: (a) DSC thermographs for electrospun PCL filaments at different level of pre-strain (ε_n = 0, 1, 2, 4, 7, and 9). Exothermic reaction upwards. (b) Zoom on the glass transition region for unstrained filaments (top) and filaments with a prestrain of 9 (bottom). (c) Zoom on the endothermic (i.e. melting) peaks during heating. (d) Zoom on the exothermic (i.e. recrystallisation) peaks during cooling.

The glass transition temperature T_g was determined using a conventional tangent construct method (Menczel and Prime, 2009), illustrated in Fig. 3.4(b). First, two tangents to the heat flow curve were drawn, passing through temperature points respectively before and after the glass transition. A third construct was drawn tangent to the heat flow curve in the transition region. Intersection points between the tangents defined the extrapolated onset and endset temperatures, T_{ons} and T_{end}, and the glass transition temperature was obtained as the midpoint between these two temperatures ("half-width" method). The melting temperature T_m was identified as the minimum value of the endothermic peak. The enthalpy of fusion from solid to liquid ($\Delta H_{S\rightarrow L}$) and recrystallisation enthalpy ($\Delta H_{L\rightarrow S}$) were determined by from areas under the respective peaks. The results are summarised in Table 3.1. Un-stretched samples present a glass transition temperature of -62 ± 2°C and a melting temperature of 58 ± 2°C. These results are consistent with bulk material properties for PCL reported in the literature: $T_g \approx -60°C$ and $T_m \approx 60°C$ (Bartnikowski et al., 2019). This indicates that electrospinning process does not significantly influence the intrinsic thermal properties of PCL, with the unstretched fibres retaining bulk-like behaviour. The glass transition and melting temperatures increase with the degree of pre-strain.

The degree of crystallinity $\%K$ of the ES samples was estimated using the following formula:

$$\%K = \frac{\Delta H}{\Delta H_0} \tag{3.1}$$

where ΔH is the experimentally-measured melting enthalpy ($\Delta H_{S\rightarrow L}$ or $\Delta H_{L\rightarrow S}$), and ΔH_0 is the reference value for 100% crystalline material, reported as 139.5 J g^{-1} (Lam et al., 2008; Pitt et al., 1981a). Un-stretched samples showed a 61 ± 1% crystallinity, which progressively increased up to 69% at a strain of 9, indicating some degree of strain-induced crystallisation. This is consistent with the increase in T_g as the pre-strain increases, as increased crystallinity constrains the mobility of the amorphous phase through interphase interactions and reduced free volume. On the other hand, the degree of crystallinity reached upon cooling the material from the melt was about 47 ± 2%, independent of the level of pre-strain. Comparing the degrees of crystallinity in an ES filament and a recrystallised filament at zero strain, the electrospinning process contributes to an approximate 13% increase in crystallinity.

3.3.2 Viscoelastic Properties

The storage modulus, loss modulus, and loss tangent measured by DMA in temperature sweeps at varying frequencies are shown in Fig. 3.5. The glass transition temperature at each loading frequency was estimated in three different ways: (i) from the drop in storage modulus, (ii) from the loss modulus peak, and (iii) from the loss tangent peak, and values are reported in Table 3.2. Regardless of the

Table 3.1: The glass transition temperature (T_g), melting temperature (T_m), enthalpy of fusion from solid to liquid ($\Delta H_{S\to L}$), the recrystallisation enthalpy ($\Delta H_{L\to S}$), and degree of crystallinity calculated from $\Delta H_{S\to L}$ and $\Delta H_{L\to S}$, respectively, for pre-stretched filaments.

ε_n	T_g (°C)	T_m (°C)	$\Delta H_{S\to L}$ ($J\ g^{-1}$)	$\Delta H_{L\to S}$ ($J\ g^{-1}$)	% Crystallinity $\Delta H_{S\to L}$	% Crystallinity $\Delta H_{L\to S}$
0	-62.60	58.88	85.96	67.61	61.62%	48.47%
1	-63.42	59.08	88.24	65.18	63.25%	46.72%
2	-62.58	59.24	90.62	66.14	64.96%	47.41%
4	-58.88	59.14	91.27	65.23	65.43%	46.76%
7	-45.81	60.11	92.11	65.69	66.03%	47.09%
9	-43.89	60.54	97.03	67.67	69.56%	48.51%

method, the glass transition temperature increases with the loading frequency. The frequency dependence of the glass transition temperature results from the kinetic and relaxation character of the glass transition (Perez, 2018). We also find that the glass transition temperature of un-stretched filament measured from DSC is intermediate between the values obtained from the storage and loss moduli curves, whereas the glass transition temperature obtained from the loss tangent peak is systematically larger than the corresponding value measured from DSC. Variations in measured values of T_g using the three techniques have been attributed to the broad temperature range of the transition region and the fact that different definitions reflect different aspects of the transition (Hagen et al., 1994).

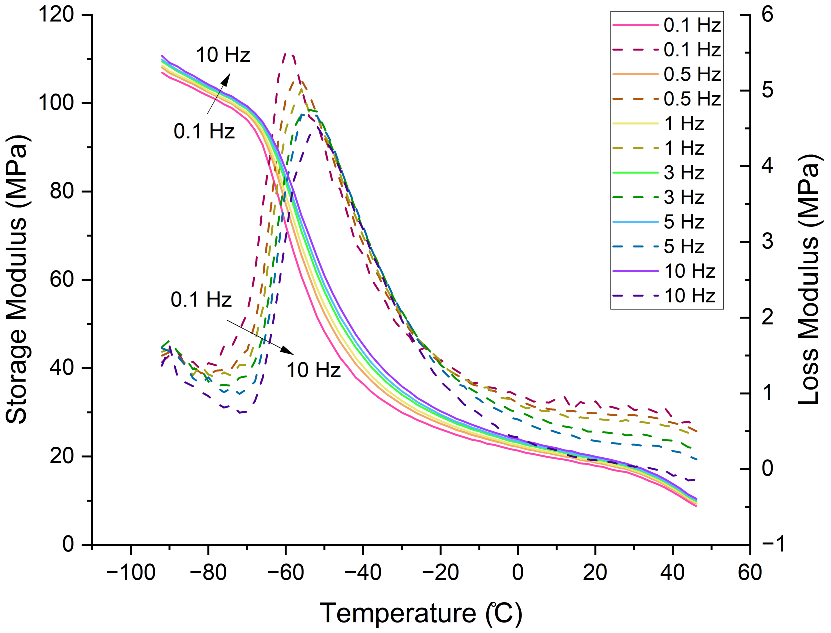

Figure 3.5: Storage modulus (E', solid lines) and loss modulus (E'', dashed lines) of un-stretched electrospun PCL filaments measured by DMA in temperature sweeps at 0.1, 0.5, 1, 3, 5, and 10 Hz.

We used the Time-Temperature Superposition (TTS) principle (Ward and Sweeney, 2012) to

Table 3.2: The glass transition temperature (T_g) values determined from DMA measurements of the storage and loss modulus.

Frequency (Hz)	T_g (°C) determined from $E^{'}$	T_g (°C) determined from $E^{''}$	T_g (°C) determined from $\tan\delta$
0.1	-67.09	-59.93	-51.96
0.5	-66.37	-55.92	-47.94
1	-65.50	-55.93	-47.94
3	-65.08	-53.92	-45.92
5	-64.98	-55.94	-47.94
10	-64.21	-51.93	-45.93

obtain the frequency dependence of E' and E'' from temperature sweeps reported in Fig. 3.5. For each temperature, data for the storage modulus were first plotted as a function of the logarithm of the frequency, and then shifted to produce a smooth master curve at the reference temperature 26.1 °C. The same shift factors were then used to obtain the corresponding master curve for the loss modulus. Experimental master curves are shown in Fig. 3.6. We then fitted the experimental master curves for the storage and loss moduli using the generalised Maxwell model:

$$E' = E_\infty + \sum_{i=1}^{N} E^{(i)} \frac{\omega^2(\tau^{(i)})^2}{1+\omega^2(\tau^{(i)})^2}, \tag{3.2}$$

$$E'' = \sum_{i=1}^{N} E^{(i)} \frac{\omega\tau^{(i)}}{1+\omega^2(\tau^{(i)})^2}, \tag{3.3}$$

where ω is the angular frequency, $E^{(i)}$ and $\tau^{(i)}$ are the elastic constant and relaxation time for each Maxwell element, and E_∞ is the relaxed modulus. We found that $N = 37$ Maxwell elements were needed to correctly fit the master curves with one element per decade, see Fig. 3.6. Fitted parameters are reported in Table 3.6. The large number of relaxation times needed is explained by the very broad range of frequencies resulting from application of the TTS principle, spanning 40 decades. It is important to emphasise that the use of $N = 37$ Maxwell elements should not be interpreted as providing a physically meaningful decomposition of the material behaviour. The number of elements required to fit the master curve is large, and the corresponding values of $E^{(i)}$ and $\tau^{(i)}$ are therefore not unique and do not represent discrete relaxation mechanisms. Instead, the generalised Maxwell model in this context should be regarded purely as a numerical curve-fitting tool, employed to reproduce the smooth variation of the viscoelastic response over the wide frequency range generated by the TTS procedure.

For this reason, the fitted parameters are not interpreted individually; instead, the overall quality of the fit is assessed based on the agreement between the model and experimental curves across the full frequency domain. The high-order representation is therefore used as an intermediate step, from which reduced and more physically interpretable models are developed and employed in the remainder of the thesis.

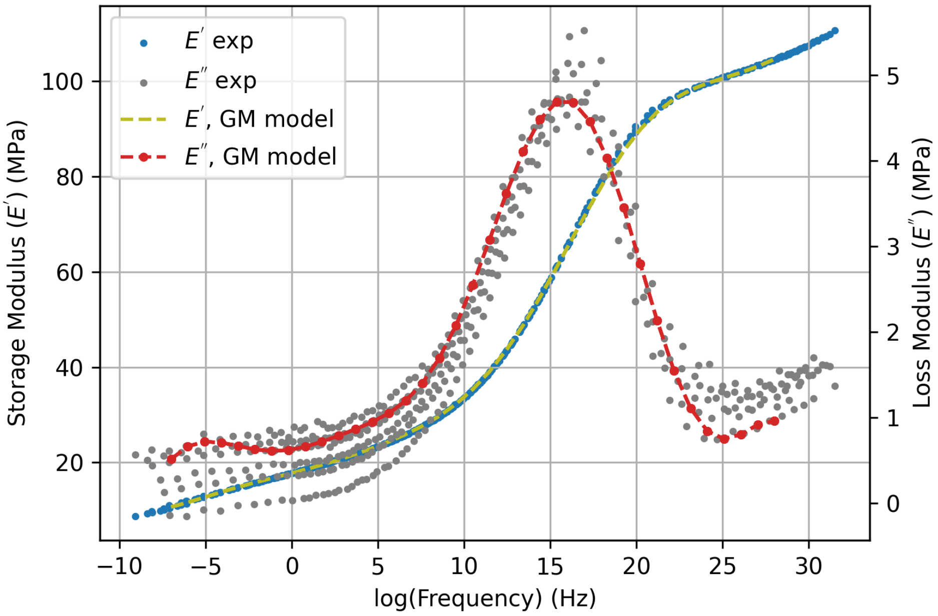

Figure 3.6: Master curves for the storage (E') and loss (E'') modulus as a function of the loading frequency. Experimental master curves are fitted using the Generalised Maxwell (GM) model.

3.3.3 Mechanical Properties

The characteristic stress-strain response of a representative ES PCL filament, tested using bollard grips under loading/unloading conditions at 75 mm min^{-1} is illustrated in Fig. 3.7. The stress-strain profile can be decomposed into i) a linear elastic region and ii) a plastic region with two-stage hardening, until failure which occurred randomly in the gauge region. The linear region is characterised by an apparent elastic modulus of 9.1 ± 1 MPa (here and for other mechanical properties, the average value and standard deviation were calculated based on the response of at least 7 filaments). The filament yields at around 0.9 ± 0.2 MPa. Subsequently, the filament plastically deforms until reaching a nominal strain of 11 ± 1, with maximum nominal stress reaching 2.5 ± 0.2 MPa.

To obtain the loading/unloading response, a single filament was tested in uniaxial tension up to a pre-determined value of nominal strain (ε_n = 1, 2, 4.5, 6.5, and 9), before unloading and reloading. The reversal stress was set to 0.1 MPa because below this value the sample would lose tension, causing the sample to detach from the grips and the software would recognise it as a fractured sample. Loading/unloading results shown in Fig. 3.7 confirm that filaments are subjected to plastic deformation, which increases with the applied strain. Furthermore, each deformation cycle displayed a small hysteresis loop, which progressively increases with the applied strain, indicating that the mechanical response of the filaments is viscoelastic.

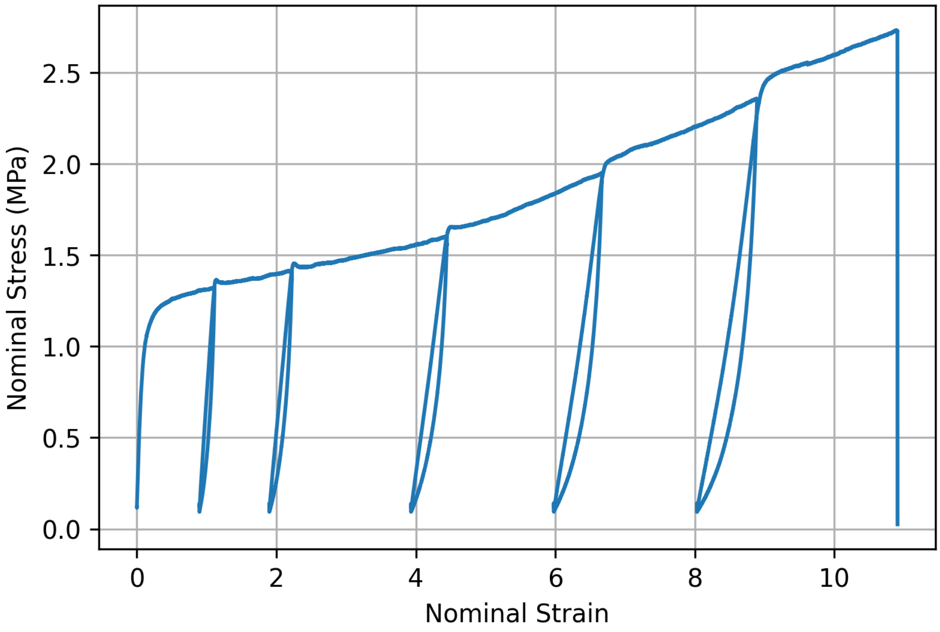

Figure 3.7: Tensile response response of a filament tested using bollard grips at 75 mm min^{-1}. The unloading/reloading sequences were performed at nominal strains of 1, 2, 4.5, 6.5, and 9.

Fig. 3.8 shows the stress relaxation response of six independent samples extended at 75 mm min^{-1} up to a force of 0.6, 0.8, 0.9, 1, 1.2, and 1.4 N, respectively, corresponding to a maximum nominal stress $\sigma_{n,max}$ = 1.1, 1.5, 1.7, 1.9, 2.3 and 2.7 MPa, with displacement kept constant afterwards for five minutes. Results confirm that filaments are viscous and exhibit stress relaxation. The relaxation response can be decomposed into an instantaneous relaxation reaction followed by a long-term plateau. To evaluate differences in relaxation response with deformation, the percentage change in stress during relaxation was recorded, based on the peak stress and the last recorded stress values. The stress drop ranged from 31.88% for $\sigma_{n,max} = 1.1$ MPa to 35.79% for $\sigma_{n,max} = 2.7$ MPa.

3.3.4 Rate Sensitivity and Experimental Variability

Fig. 3.9a illustrates the experimental variability in the stress-strain response measured using bollard grips. The figure shows the stress-strain response of seven independent samples tested at 150 mm min^{-1}. Although filaments demonstrate a similar overall response, they exhibit different yield, ultimate stress and strain values. A similar variability is observed at other loading rates (not shown). The experimental variability may be attributed to several factors. Firstly, the manipulation of filaments during mounting to achieve precise positioning and alignment may lead to pre-stretching and

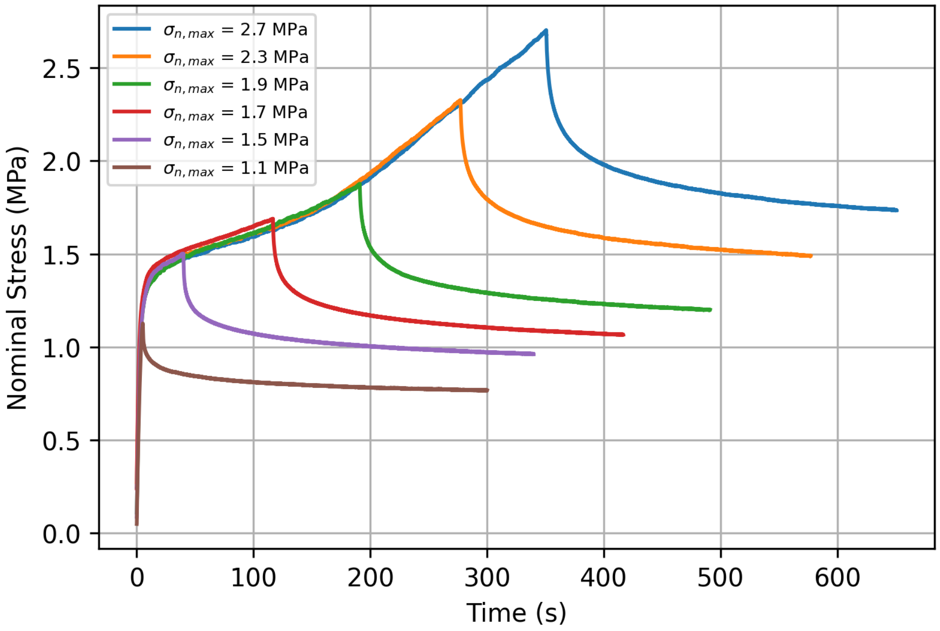

Figure 3.8: Stress relaxation response of filaments stretched using bollard grips at 75 mm min^{-1}, up to maximum stresses 1.1, 1.5, 1.7, 1.9, 2.3, and 2.7 MPa, and let to relax under constant displacement for five minutes.

pre-stresses that may impact the recorded stress-strain values. Secondly, all stress-strain curves use the same averaged reference diameter for nominal stress calculation. Lastly, the mechanisms through which fibres are recruited and activated with the load may vary from sample to sample due to its random nature.

Fig. 3.9b shows the averaged uniaxial response for at least seven filaments at extension rates of 5, 75, and 150 mm min^{-1}. The shadowed region represents the standard deviation at each strain. Corresponding values of apparent elastic modulus, yield stress and maximum tensile stress are reported in Figure 3.10. Although results suggest that the response is rate-dependent, the observed rate-dependency does not follow the expected trend that samples tested at a higher displacement rate experience higher stresses. In particular, samples tested at displacement rates of 5 mm min^{-1} were stiffer and stronger on average than samples tested at the faster rates of 75 and 150 mm min^{-1}. Statistical analysis results shown in Fig. 3.10 show that the measured differences between properties at different displacement rates are statistically significant.

Bollard grips are a commonly utilised for rope testing because they diffuse stress concentration from the clamps by distributing the pulling tension over a larger surface area, enabling samples to be stretched to larger strains. However, the results shown in Fig. 3.9a suggest that they are prone to significant experimental variability. Therefore, we considered screw-side grips as an alternative

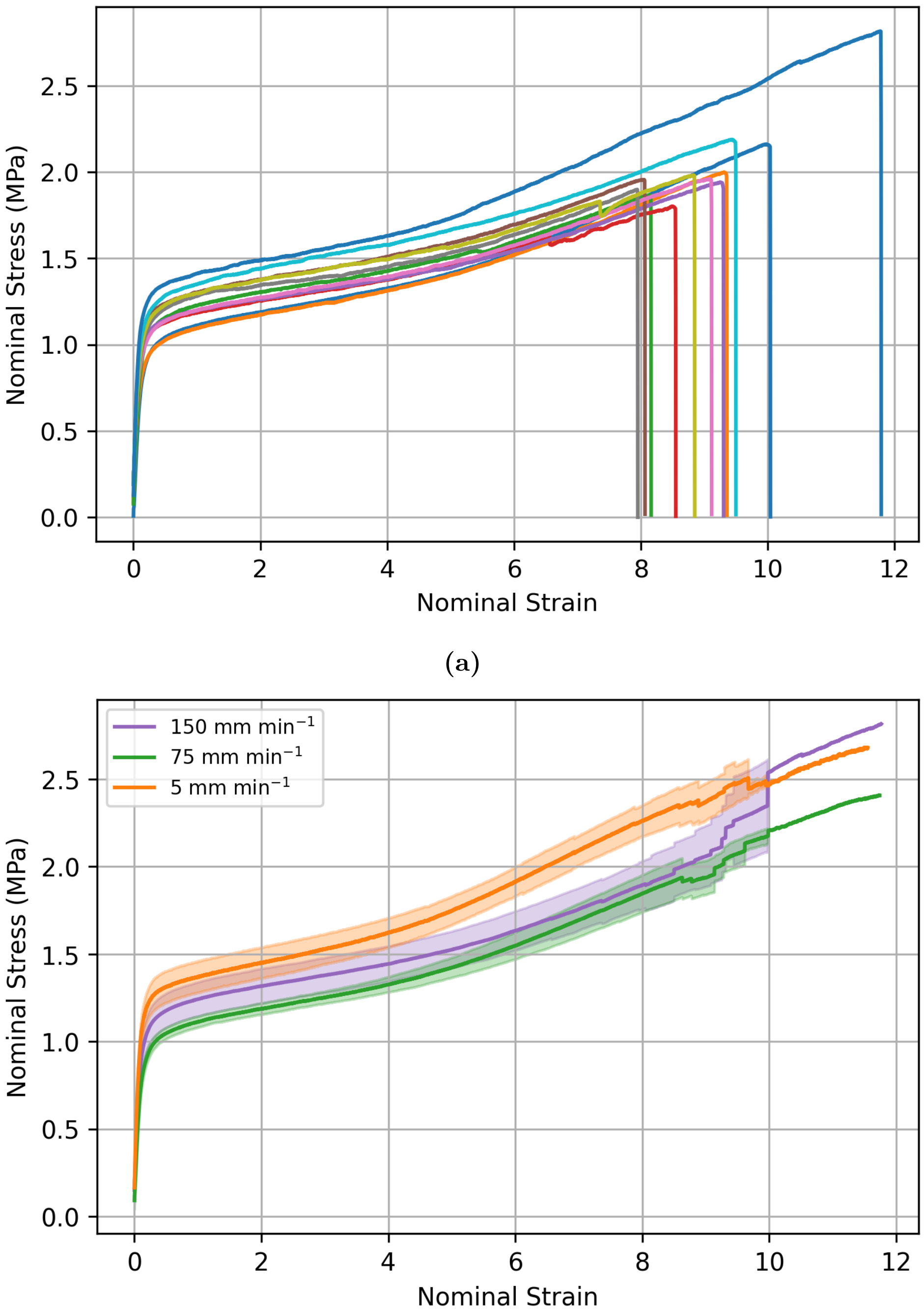

(a)

(b)

Figure 3.9: (a) Illustration of experimental variability in the stress-strain response of electrospun filaments tested at 150 mm min^{-1} using bollard grips. (d) Average response for at least seven filaments tested at extension rates of 5, 75, and 150 mm min^{-1}. Surrounding shadowing represents the standard deviation.

method to bollard grips, and investigated whether they could provide more accurate measurements. Fig. 3.11a illustrates the experimental variability in the measured stress-strain curve for samples tested at 75 mm min^{-1}. Similar to the bollard grips, filaments tested using screw-side grips still exhibit a large variability in the stress-strain response. Different from the response obtained using bollard grips, the stress-strain response is now decomposed into a linear regime followed by a plastic

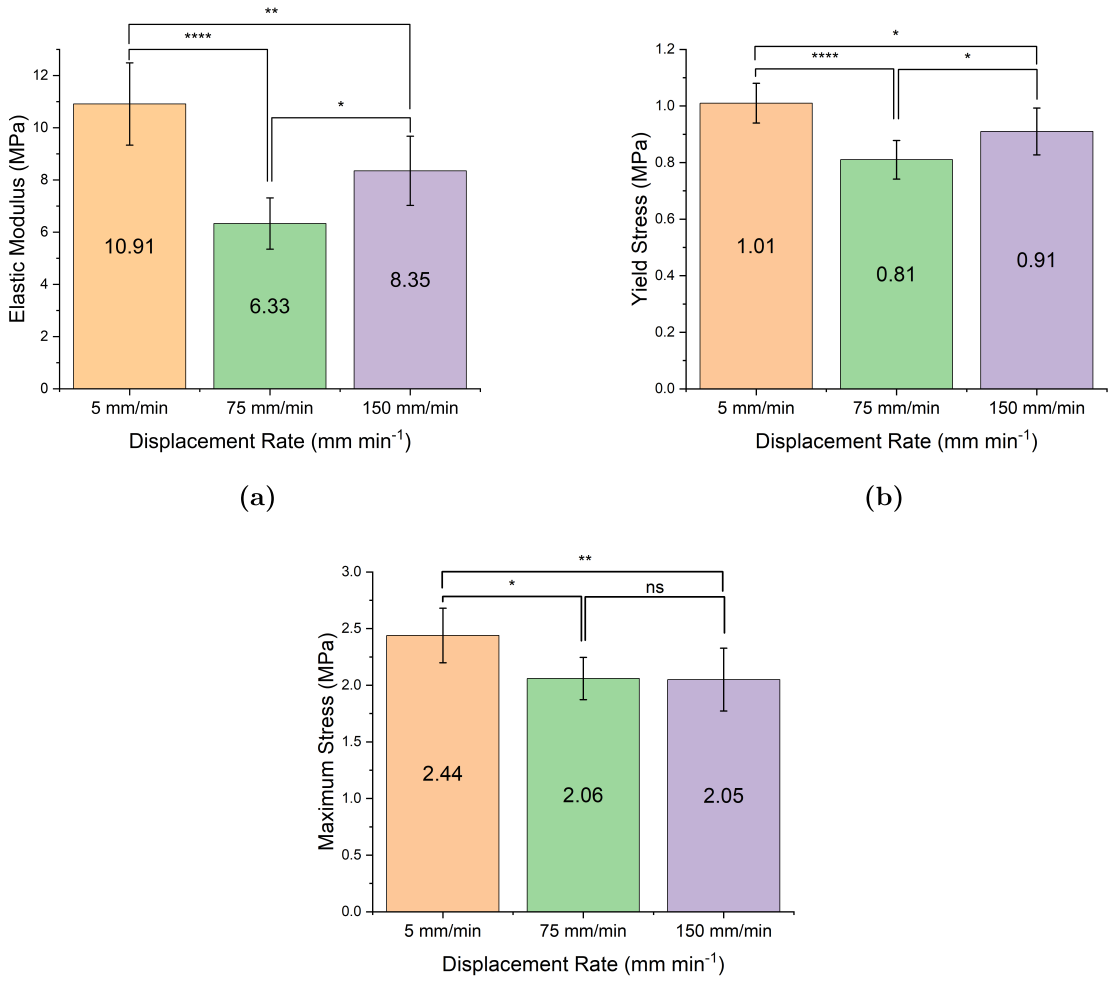

(a) **(b)**

(c)

Figure 3.10: Summary statistics on the effect of displacement rate on the (a) elastic modulus, (b) yield stress (σ_y), and (c) maximum tensile stress (σ_{max}). Error bars represent standard deviation. ns = not significant, $*p < 0.05$, $**p < 0.01$, $***p < 0.001$, $****p < 0.0001$.

regime with moderate linear hardening, without re-hardening at large strains. Filaments are unable to reach the same stresses as bollard grips and fail around strains of about four, which is approximately three times less than the strain obtained with bollard grips. The average response of filaments tested using screw-side grips at different displacement rates is shown in Fig 3.11b, with the shaded regions showing the standard deviation at each strain value. In the early loading stage, the curves suggest a rate-dependent trend, with higher loading rates generally corresponding to slightly higher stresses. However, the differences between rates are small and fall within the experimental variability, making a clear distinction in yield stress and different rates less definitive. We note however that the averaged curve for 75 mm min^{-1} went below the averaged curve for 5 mm min^{-1} at larger strains, which could be due to damage phenomena. Statistical analysis results shown in Fig. 3.12 reveal that the observed difference in stress values between different extension rates are not statistically significant.

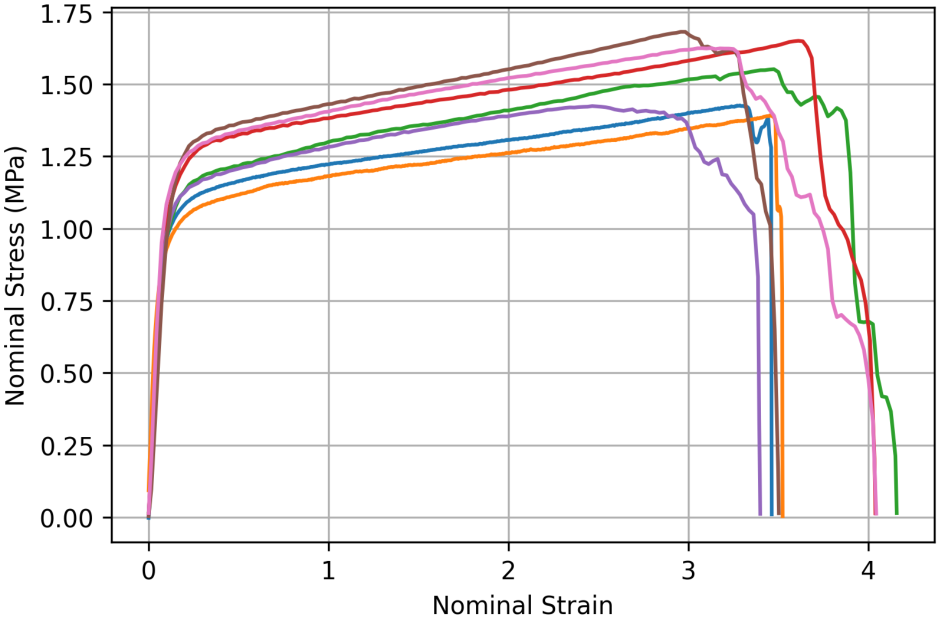

(a)

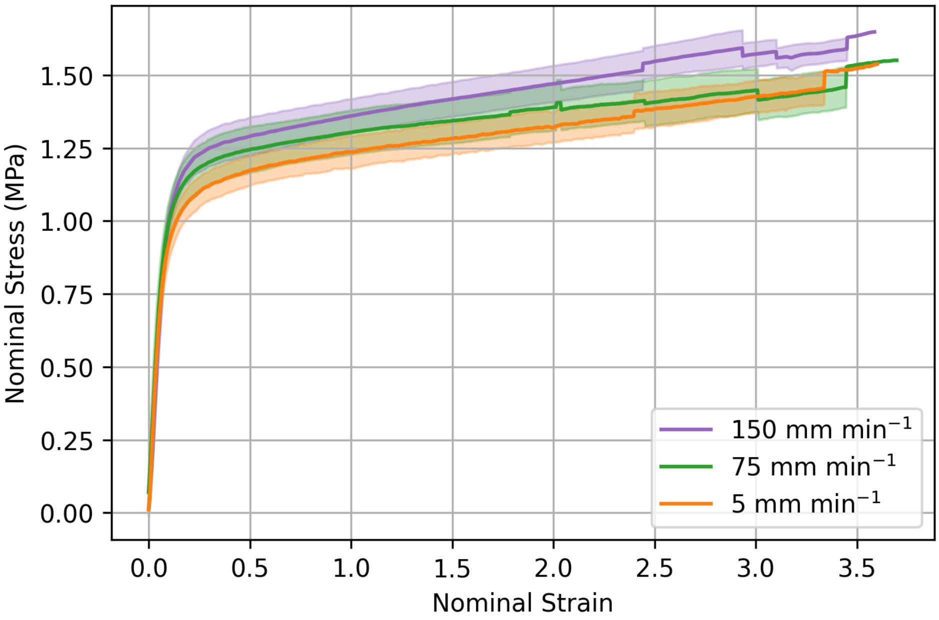

(b)

Figure 3.11: (a) Illustration of experimental variability in the stress-strain response of electrospun filaments tested at 75 mm min^{-1} using screw-side grips. (b) Averaged uniaxial response of filaments tested at extension rates of 5, 75, and 150 mm min^{-1}.

3.3.5 SEM characterisation

SEM of pre-stretched filaments (bollard grips) The morphology of ES filaments in the as-produced and stretched states are shown in Fig. 3.13 for two levels of magnification. During the manufacturing, ES fibres are deposited in a random fashion onto the fine metallic wire. The fibres conglomerate to produce filaments with an isotropic, porous, and tightly packed network structure, shown in Fig. 3.13a. As-produced filaments are free from beads and other imperfections. However,

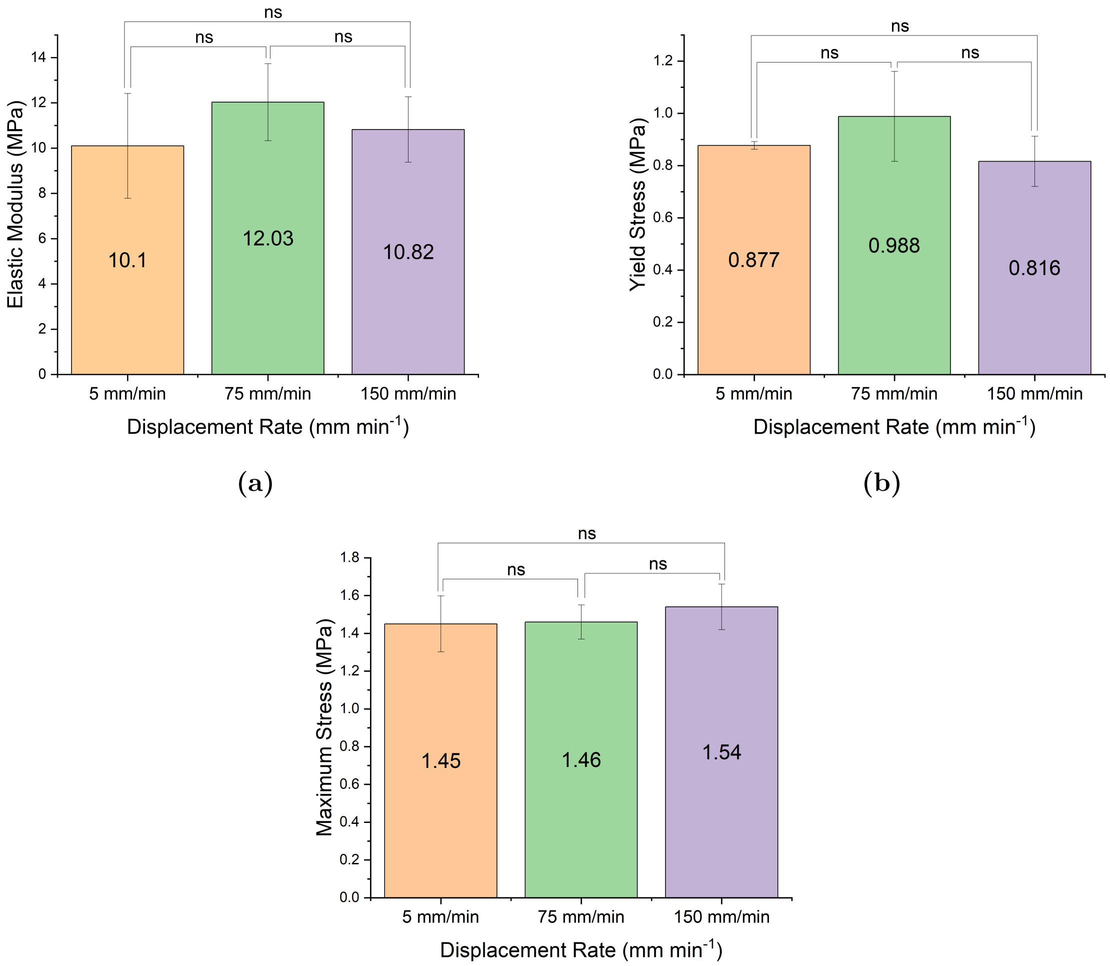

(a) **(b)**

(c)

Figure 3.12: Summary statistics on the effect of strain rate on the (a) elastic modulus, (b) yield stress (σ_y), and (c) maximum stress (σ_{max}). Error bars represent standard deviation. ns = not significant, *$p < 0.05$, **$p < 0.01$, ***$p < 0.001$, ****$p < 0.0001$.

fibre fusion is observed, as highlighted in Fig. 3.13b. Fig. 3.13c shows the micrograph of a filament stretched by ten times its original length. Comparing Figs 3.13a and 3.13c, a significant reduction in filament diameter is observed due to fibre stretching, as well as fibre alignment in the stretching direction. The reduction in overall filament diameter causes fibres to come into contact with each other, leading to fibre fusion and coalescence, shown in Fig. 3.13d. The diameter of the fibres themselves is also reduced. Although not visible from the SEM micrographs, un-stretched and stretched filaments exhibit different optical properties. Un-stretched filaments were opaque white and flexible, whilst stretched filaments displayed shiny optical properties, which can be attributed to strain-induced crystallisation.

We further evaluated the fibre morphology progression at different stages of the stress-strain to better comprehend the key deformation mechanisms influencing the mechanical properties of the

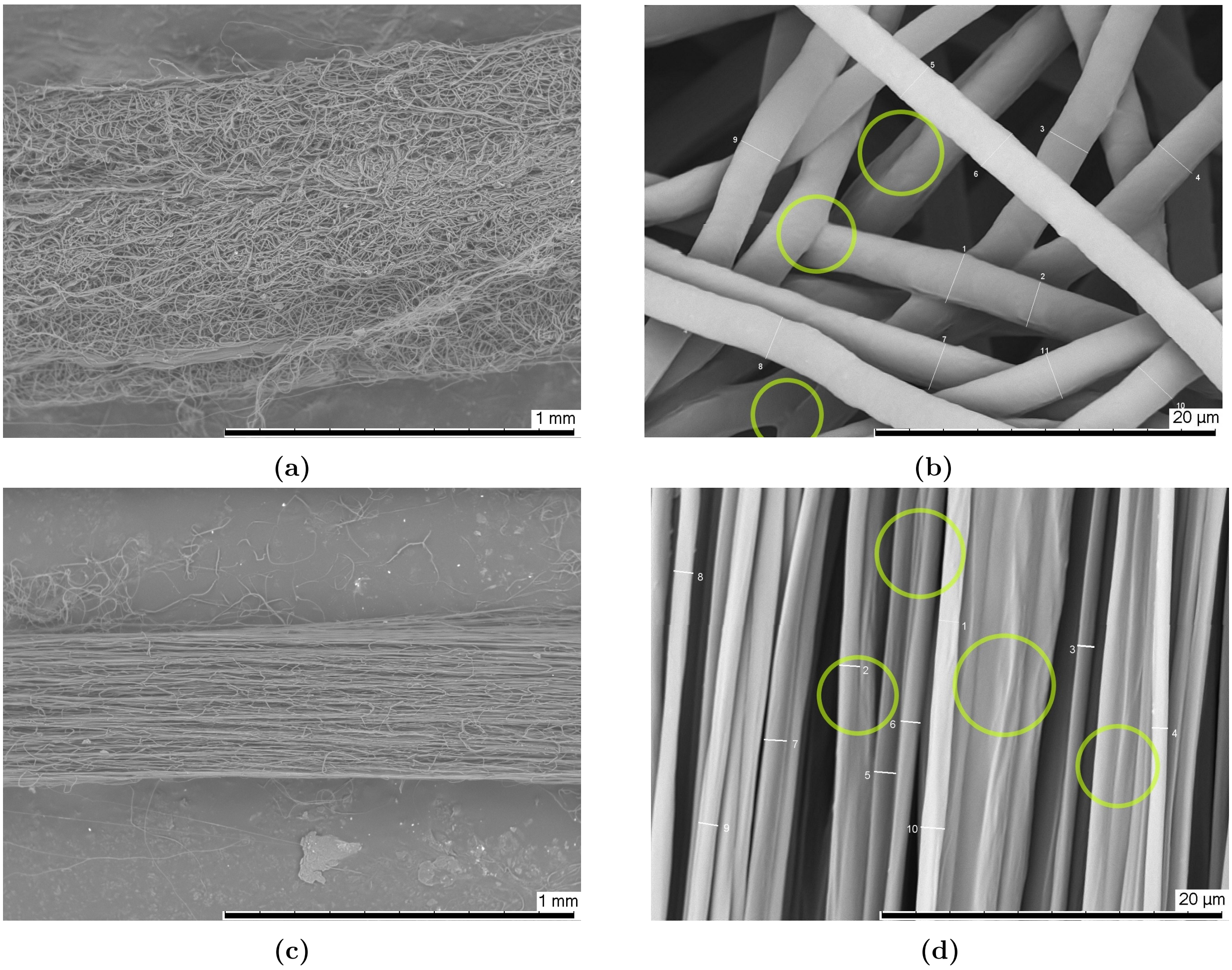

(a) **(b)** **(c)** **(d)**

Figure 3.13: Micrographs showing the surface topology of (a)-(b) un-stretched and (c)-(d) stretched ($\varepsilon_n = 9$) electrospun filaments. Neon yellow circles in figures (b)-(d) highlight fibre fusion.

material. SEM micrographs corresponding to filaments stretched to different strains are shown in Fig. 3.14, alongside the typical stress-strain response. In the as-produced state (Fig. 3.14 (A)), fibres are randomly oriented with a homogeneous diameter size and the topology contains large pores. Upon applying tension and reaching strains of one or two (Fig. 3.14 (B) and 3.14 (C)), the stress-strain curve indicates that the material is plastically deforming. Micrographs reveal that a small numbers fibres are commencing to align in the loading direction, while the microstructure remains mainly isotropic. Comparing micrographs Fig. 3.14 (B) and 3.14 (C), there are more aligned fibres at stage (C) compared to (B). Upon reaching stage (D), the fibre morphology has completely altered with the majority of fibres are aligned in the loading direction, the topological porosity is minimal and fibres appear to coalesce. At stage (E), the fibres remain aligned in the loading direction, but appear to coalesce further. Finally, reaching stage (F), the fibre morphology remains the same, but the fibre diameters reduced relative to stage (E).

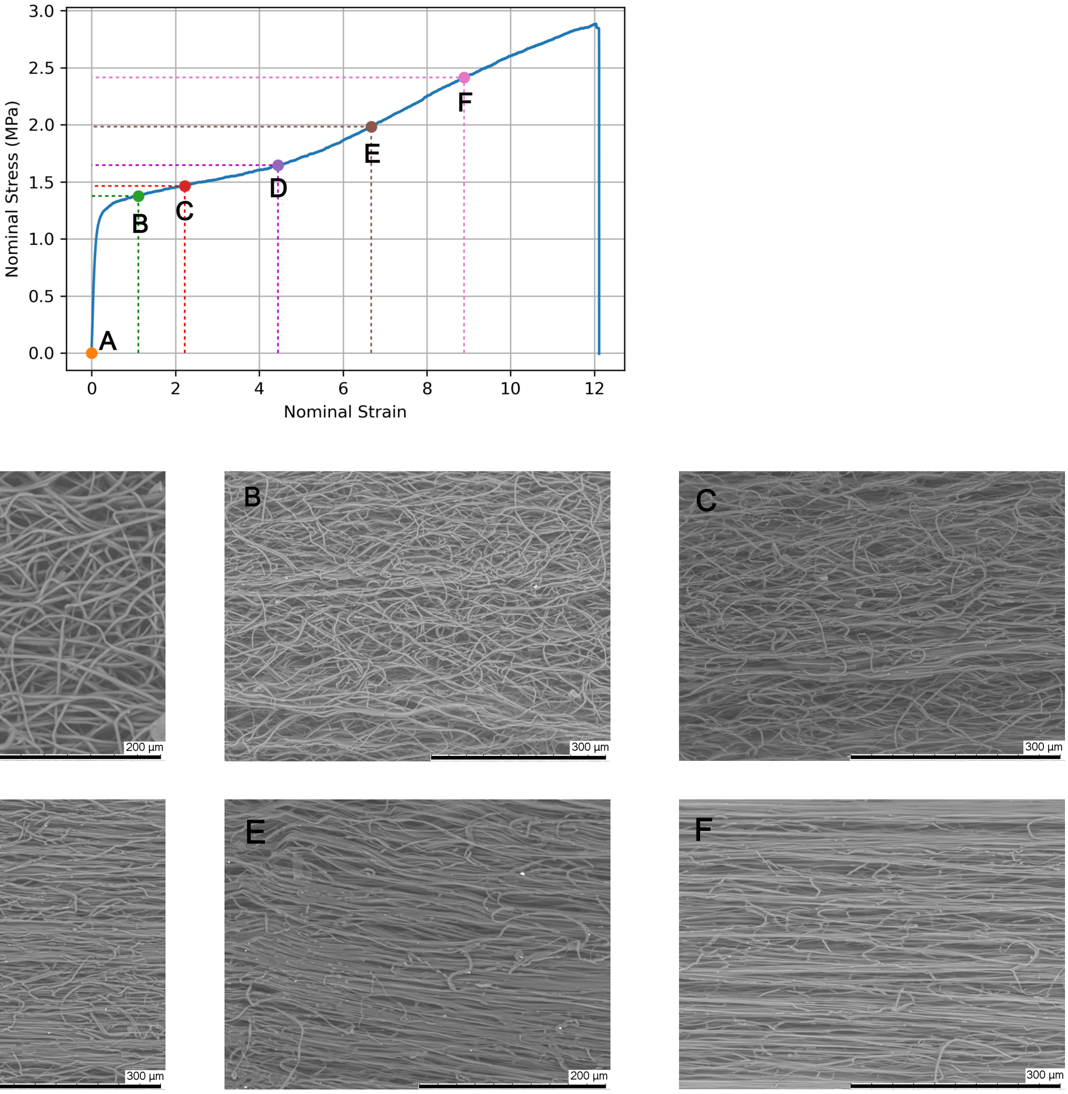

Figure 3.14: SEM micrographs showing the microstructural evolution of filaments stretched with bollard grips.

The porosity, filament diameter, and fibre diameter were measured for every strain and the results are summarised in Table 3.3. Analysing differences between the initial state ($\varepsilon_n = 0$) and the final recorded strain ($\varepsilon_n = 9$), the porosity decreased by 42.7%, the filament diameter by 46.4%, and the fibre diameter by 62.5%. We also calculated the overall volume change of the filament J using the following formula:

$$J = \frac{Ld^2}{L_0 d_0^2} = \lambda \frac{d^2}{d_0^2} \tag{3.4}$$

where d_0 and d respectively refer to the initial and current diameter of the filament. Values are reported in Table 3.3. Calculated values show that the filament undergoes significant volume expansion during stretching, with $J > 1$ despite the reduction in filament diameter during stretching, due to the very large axial stretch. We also estimated the axial stretch of the fibres assuming that they deform under constant volume. The fibre stretch λ_f was calculated as:

$$\lambda_f = \frac{d_{f0}^2}{d_f^2} \tag{3.5}$$

where d_{f0} and d_f respectively refer to the initial and current diameter of the fibres. Fibre stretch values are also reported in Table 3.3. Comparing the fibre stretch λ_f to the filament stretch $\lambda = \varepsilon_n + 1$, it can be observed that fibres deform on average less than the filament as a whole. This indicates that the deformation of the filament is not solely accommodated by the stretching of the fibres, and that other mechanisms are involved as well, such as the untangling and re-alignment of the fibres. The stretching of fibres is particularly prominent in the re-hardening region, where the majority of fibres are aligned in the loading direction: between (B) and (D), the fibre stretch increases by 95%, whereas it increases by 178% between (D) and (F).

An additional important observation is the large standard deviation in measured fibre diameters between stages (A) and (D), indicating that a proportion fibres in the loading direction may have been stretched already, whilst others are only beginning to stretch as they are recruited in the loading direction. The standard deviation is reduced in the re-hardening regions (i.e. (E) and (F)), as fibres are gradually approaching the same value. Once fibres reach their maximum extensibility, filament failure occurs.

SEM of pre-stretched filaments (screw-side grips) SEM micrographs corresponding to filaments stretched to different strains using screw-side grips are shown in Fig. 3.15. The results are similar to corresponding results obtained by pre-stretching the filaments using bollard grips. For un-

Table 3.3: The surface porosity ϕ, filament diameter, fibre diameter, filament volume ratio J and fibre stretch λ_f for samples stretched to various strains $\varepsilon_n = \lambda - 1$ using bollard grips.

λ	Stage	ϕ (%)	Filament diameter (μm)	Fibre diameter (μm)	J	λ_f
1	A	24.19	832.2 ± 10.1	3.2 ± 0.5	1	1
2	B	21.01	761.6 ± 12.3	2.8 ± 0.7	1.68	1.31
3	C	19.51	679.1 ± 14.0	2.3 ± 0.8	2.00	1.94
5	D	17.40	624.7 ± 4.5	2.0 ± 0.8	2.82	2.56
8	E	15.48	574.6 ± 16.4	1.5 ± 0.3	3.81	4.55
10	F	13.85	446.1 ± 2.9	1.2 ± 0.3	2.87	7.11

stretched filaments, fibres initially have uniform diameter and are randomly oriented (Fig. 3.15 (B)). Upon the application of the load, fibres begin to untangle and align in the loading direction, as shown in Figure 3.15 (B and C). At a strain of around 2, the filament texture is clearly anisotropic, with many fibres aligned in the direction of loading (Fig. 3.15 (D) and Fig. 3.15 (E)). However, there are still undulating fibres that are aligned in the loading direction but are tortuous and not fully stretched. Upon reaching a strain of around four (Fig. 3.15 (F)), most tortuous fibres have engaged with the applied tension. Subsequently, fibres contract onto a tightly packed structure, thus reducing the filament diameter. The porosity, filament, and fibre diameters were measured for every strain and the results are summarised in Table 3.4. Results show that surface porosity reduces from 25% ± 1 to 16% ± 1 and the filament diameter reduces by 35.8% between strains of 0 and 4. Furthermore, fibres also reduced in diameter by 54.3%. The filament volume ratio J was computed using Eq. 3.4, and the fibre stretch was computed using Eq. 3.5. Calculated values also reported in Table 3.4.

Table 3.4: The surface porosity ϕ, filament diameter, fibre diameter, filament volume ratio J and fibre stretch λ_f for samples stretched to various strains $\varepsilon_n = \lambda - 1$ using using screw-side grips.

λ	Stage	ϕ (%)	Filament Diameter (μm)	Fibre Diameter (μm)	J	λ_f
1	A	25.34	859.9 ± 23.7	3.5 ± 0.7	1	1
1.5	B	22.07	815.7 ± 19.8	3.1 ± 0.6	1.35	1.27
2	C	21.53	737.5 ± 15.1	2.7 ± 0.7	1.47	1.68
3	D	18.15	611.9 ± 14.9	2.3 ± 0.7	1.52	2.32
4	E	17.46	587.1 ± 13.3	1.7 ± 0.5	1.86	4.24
5	F	16.89	552.2 ± 8.9	1.6 ± 0.5	2.06	4.79

In-situ SEM of stretched filaments *In-situ* SEM was also conducted to investigate microstructural elements that cannot be captured through the previously used SEM method, such as filament failure. Fig. 3.16 shows a series of SEM micrographs which exhibit the sequence of events to filament failure. The imprint of the collecting wire is also visible on these images. In the initial state (Fig. 3.16a) filaments are randomly oriented and gradually begin to align in the loading direction upon the

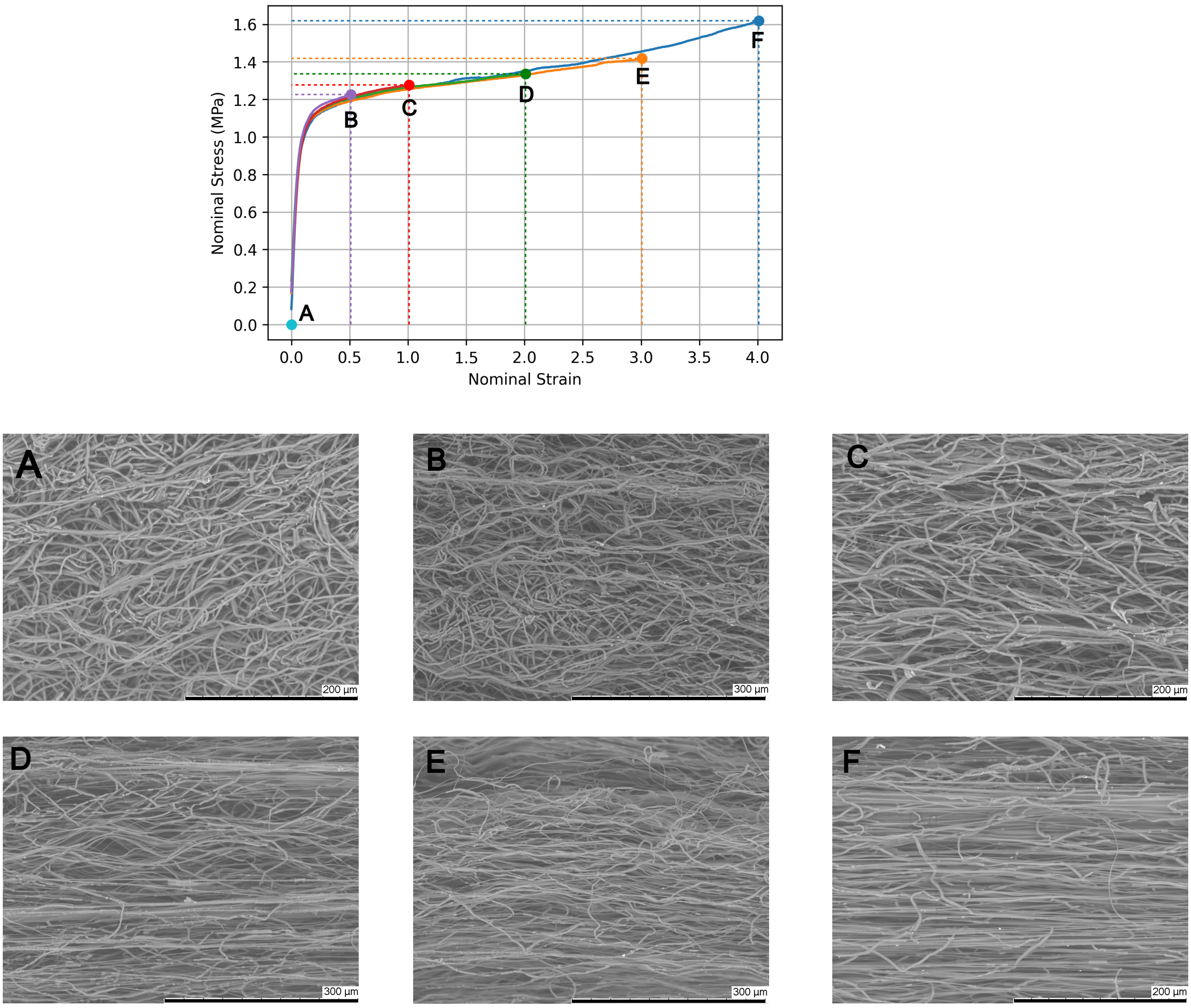

Figure 3.15: SEM micrographs showing the microstructural evolution of filaments with screw-side grips.

application of load alongside contracting in the transverse direction to loading (Fig. 3.16b). Subsequently, fibres in the outer layer rupture (Fig. 3.16c), creating a neck where deformation localises and where fibres are more aligned relative to the rest of the filament. Fibre failure then progresses with increasing strain. The micrographs indicate that rupture predominantly initiates at the outer layers and propagates inwards towards the filament core, as shown in Figs. 3.16d – 3.16f. However, this failure sequence is not necessarily universal; depending on local structural heterogeneity and stress distribution, rupture may also initiate within the interior of the filament and propagate outward.

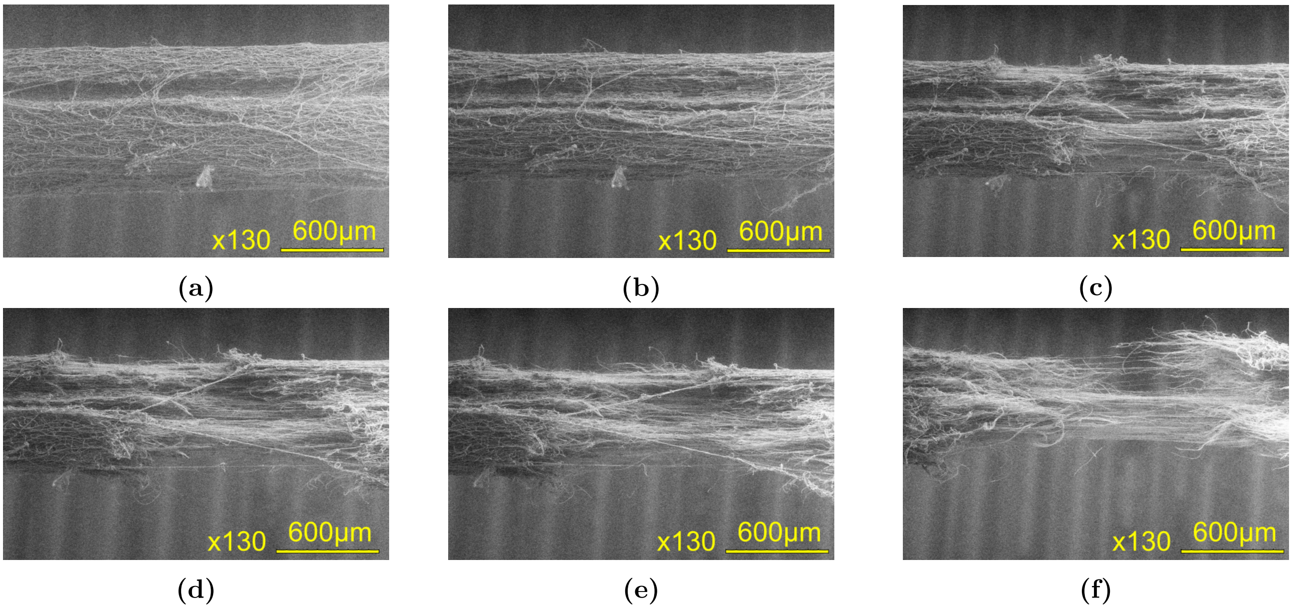

(a) (b) (c) (d) (e) (f)

Figure 3.16: *In-situ* SEM micrographs showing the continuous microstructure evolution of the electrospun filaments stretched with screw-side grips. The fracture process involves the rupture of fibres from the outer layer inwards.

3.4 Phenomenological Model

3.4.1 Model description

We developed a rate-dependent constitutive model to capture the filament response up to large deformations. In the proposed model, the stress response is decomposed into viscoelastic and viscoplastic components. The viscoelastic component aims to describe intermolecular interactions within the fibres, whereas the viscoplastic component aims to capture the inter-fibre interactions and reorganisation of the fibre network during stretching, as well as the re-hardening at large deformations, attributed to the stretching of the individual fibres. A 1D rheological depiction of the model is shown in Fig. 3.17. The framework consists of a generalised Maxwell model in series with a J_2 viscoplastic dashpot. This model was adopted as the simplest possible combination of two standard constitutive models respectively used to represent linear viscoelastic behaviour and elastic-viscoplastic behaviour. The model is versatile, allowing an arbitrary number of relaxation times in the viscoelastic model, as well as general forms of viscoplastic and hardening functions. Furthermore, an efficient algorithm for the numerical implementation of this model was developed by (Miled et al., 2011) and is adopted here.

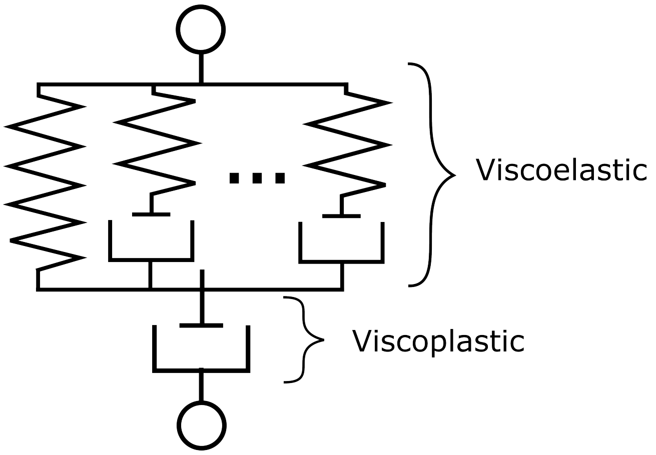

Figure 3.17: 1D representation of the constitutive model, consisting of generalised Maxwell model in series with a viscoplastic dashpot.

We limit the presentation of the model to the one-dimensional case, given the geometry of the filament and the uniaxial tension loading condition. Let λ be the tensile stretch. The logarithmic (true) strain is given by:

$$\varepsilon = \ln(\lambda) \tag{3.6}$$

The true strain is additively decomposed into viscoelastic and viscoplastic components:

$$\varepsilon = \varepsilon^{ve} + \varepsilon^{vp} \tag{3.7}$$

According to the Boltzmann hereditary integral (Bergstrom, 2015; Brinson, 2015), the stress is related to the viscoelastic strain by:

$$\sigma(t) = \int_0^t E(t-\tau)\frac{\partial \varepsilon^{ve}}{\partial \tau} d\tau \tag{3.8}$$

where $E(t)$ is the viscoelastic modulus of the generalised Maxwell model, which can be expressed using Prony series as:

$$E(t) = E_\infty + \sum_{k=1}^{N} E^{(k)} \exp\left(-\frac{t}{\tau^{(k)}}\right) \tag{3.9}$$

where E_∞ is the long-term modulus, $\tau^{(k)}$ are the viscoelastic relaxation times and $E^{(k)}$ the corresponding moduli of the N viscoelastic branches in the generalised Maxwell model. Substituting expression (3.9) into the hereditary integral (3.8), we obtain the stress as:

$$\sigma(t) = E_\infty \varepsilon^{ve} + \sum_{k=1}^{N} \sigma^k(t) \tag{3.10}$$

where

$$\sigma^k(t) = E^{(k)} \exp\left(-\frac{t}{\tau^{(k)}}\right) \int_{-\infty}^{t} \exp\left(\frac{\tau}{\tau^{(k)}}\right) \frac{\partial \varepsilon^{ve}}{\partial \tau} d\tau \tag{3.11}$$

The viscoplastic strain is described using standard J_2 viscoplasticity with isotropic hardening. The yield function is given by:

$$f(\sigma_{eq}, p) = \sigma_{eq} - (\sigma_y + R(p)) \tag{3.12}$$

where $\sigma_{eq} = |\sigma|$ is the equivalent stress (in 1D), σ_y is the yield stress, and $R(p)$ is the hardening function, which depends on the accumulated plastic strain p. Note that the stress is always positive in the loading scenarios considered in the present paper. For uniaxial tension, the accumulated plastic strain is given by:

$$p(t) = \int_0^t \dot{p}(\tau) d\tau \quad \text{with} \quad \dot{p} = |\dot{\varepsilon}^{vp}| \tag{3.13}$$

The uniaxial flow rule for the viscoplastic strain is simply expressed as:

$$\dot{\varepsilon}^{vp} = \dot{p}\text{sign}(\sigma) \tag{3.14}$$

and the plastic multiplier is defined by a viscoplastic function g_v:

$$\begin{cases} \dot{p} = 0, & \text{if } f \leq 0 \text{ (viscoelasticity)} \\ \dot{p} = g_v(\sigma_{eq}, p) > 0, & \text{if } f > 0 \text{ (viscoelasticity + viscoplasticity)} \end{cases} \tag{3.15}$$

To capture rehardening at large deformation, we take the hardening function of an exponential form:

$$R(p) = k \exp(np) \tag{3.16}$$

where k is the hardening coefficient and n the hardening exponent. The viscoplastic function is defined by Norton's power law:

$$g_v(\sigma_{eq}, p) = \begin{cases} \frac{\sigma_y}{\eta} \left(\frac{f}{\sigma_y}\right)^m, & \text{if } f > 0 \\ 0, & \text{otherwise} \end{cases} \tag{3.17}$$

where η and m are the viscoplastic modulus and exponent, respectively.

The numerical implementation of the viscoelastic-viscoplastic model is based on the fully-implicit algorithm proposed by (Miled et al., 2011). In brief, the algorithm involves a viscoelastic predictor step followed by a viscoplastic correction to satisfy the yield condition. The viscoplastic correction step is identical to the classical elasto-viscoplastic return mapping algorithm, which is achieved via the introduction of incremental relaxation moduli. Another advantage of the method is that it does not require the storage of the entire deformation history, but only the state variables at the previous times step. We refer to the paper by (Miled et al., 2011) for details about the time-discretisation algorithm.

3.4.2 Comparison between model predictions and experimental data

We have calibrated the model based on experimental data obtained using the screw-side grips. Experimental and model results are both presented using true stress and strain. In the experiments, the true strain was calculated from the nominal strain ε_n using the relation $\varepsilon = \ln(1 + \varepsilon_n)$, whereas the true stress was calculated from the nominal stress σ_n as $\sigma = \sigma_n \frac{\lambda}{J}$. Here, the volume change J was determined as a function of the stretch by fitting the values reported in Table 3.4 with the empirical formula:

$$J = \lambda^{0.45} \tag{3.18}$$

which satisfies the requirement that $J(1) = 1$. The empirical fitting of the volume ratio as a function of applied stretch is shown in Fig. 3.18.

Model parameters were identified in the following way. The strain rate used in the model was the same as in the experiments. As an initial guess, the instantaneous apparent modulus ($E_0 = E_\infty + \sum E_i$) and yield stress were initially calibrated based on the experimentally measured apparent elastic modulus and yield stress, respectively. For simplicity, we considered $N = 2$ Maxwell elements in the viscoelastic model, which we found sufficient to obtain good agreement with experimental stress-strain curves for the considered strain rates. The remaining viscoelastic and viscoplastic parameters were optimised using least square minimisation using Python scipy optimization algorithm. However, the optimised model initially underestimated the stiffness during elastic unloading and reloading under non-monotonic loading conditions.

To further investigate this, an alternative approach was considered in which the viscoelastic parameters were directly taken from DMA measurements (refer to Table 3.6). Despite the significantly larger number of Maxwell elements ($N = 37$), this approach failed to accurately reproduce the cyclic and stress relaxation behaviour (see Appendix B in Section 3.8). This discrepancy is attributed to non-linear viscoelastic effects, as parameters identified under small-strain, linear viscoelastic conditions are not directly transferable to large-strain loading. In contrast, the reduced-order model with $N = 2$ Maxwell elements and fitted parameters provided good agreement with the experimental stress–strain response. Nevertheless, this approach should be regarded as a phenomenological approximation of the non-linear viscoelastic behaviour over a limited range of strain rates. To assess its consistency with independent DMA data, the storage and loss moduli predicted by the model were compared with experimental master curves (Fig. 3.6). The nominal strain rate in tensile testing was converted to an equivalent frequency using $\dot{\varepsilon}_n \approx 4\varepsilon_0 f$ (Song et al., 2023).

For a displacement rate of 75 mm min^{-1} ($\dot{\varepsilon}_n = 0.125$ s^{-1}), the corresponding frequency is $f = 31.25$ Hz. At this frequency, the experimental storage modulus is approximately 19.5 MPa, with the loss modulus ranging from 0.1 to 0.9 MPa. Using Eqs. (3.2) and (3.3) with $\omega = 2\pi f$, the model predicts a storage modulus of 25 MPa and a loss modulus of 0.022 MPa, which are in reasonable agreement with the experimental data. Similar trends were observed at other loading rates: for 5 mm min^{-1} ($f = 2.1$ Hz), the experimental storage modulus is approximately 18 MPa, while for 150 mm min^{-1} ($f = 62.5$ Hz), it is approximately 21 MPa. In both cases, the model predicts a storage modulus of approximately 25 MPa.

Finally, the apparent modulus was refined to ensure consistency with the stiffness contributions inferred from the DMA data. Specifically, a stiffness value of 25 MPa was adopted, which despite increasing the initial elastic response, it improved the agreement with the unloading and reloading behaviour during non-monotonic loading, as shown below. The final set of parameters used to fit all stress–strain curves is reported in Table 3.5.

Table 3.5: Model parameters used to reproduce the stress-strain response measured using screw-side grips.

Viscoelastic Parameters		
Elastic moduli	$E_\infty = 10$ MPa	
	$E^{(1)} = 8$ MPa	$E^{(2)} = 7$ MPa
Relaxation times	$\tau^{(1)} = 10.00$ s	$\tau^{(2)} = 2.00$ s
Viscoplastic Parameters		
Yield Stress	$\sigma_y = 0.7$ MPa	
Hardening function	$k = 0.5$ MPa	$n = 1.45$
Viscoplastic function	$\eta = 1$ MPa s	$m = 1$

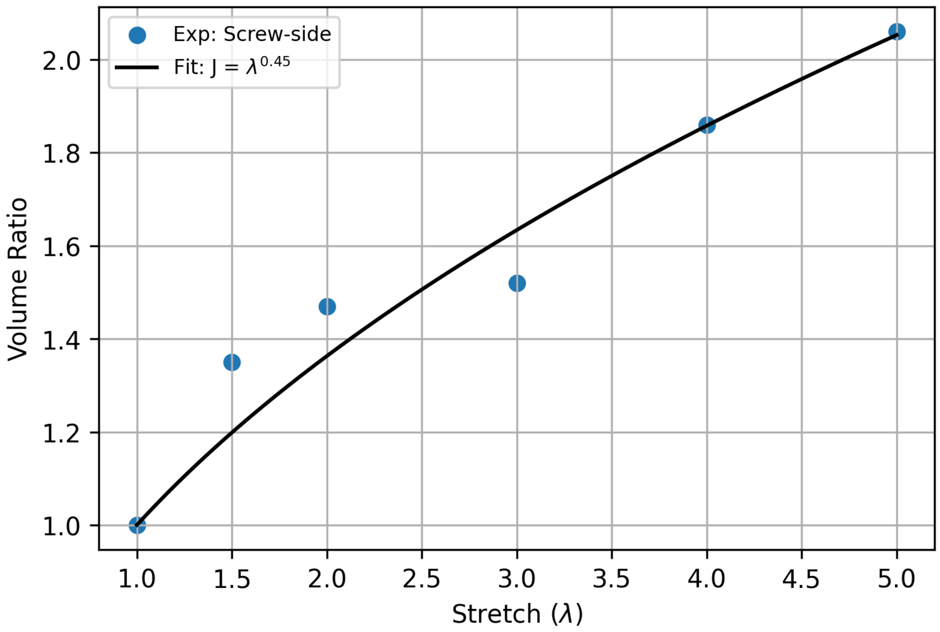

Figure 3.18: Relationship between stretch and volume ratio. The solid black line is the empirical fitting function $J = \lambda^{0.45}$.

Model predictions are compared to experimental data for uniaxial tension at various displacement rates in Fig. 3.19. Consistent with the experimental observations, the model predicts an (apparent) linear elastic response, followed by plastic yielding and hardening. The slope of the initial elastic response is overestimated by the model, which was found necessary to capture the elastic response during the unloading and reloading stages in non-monotonic loading, as shown below.

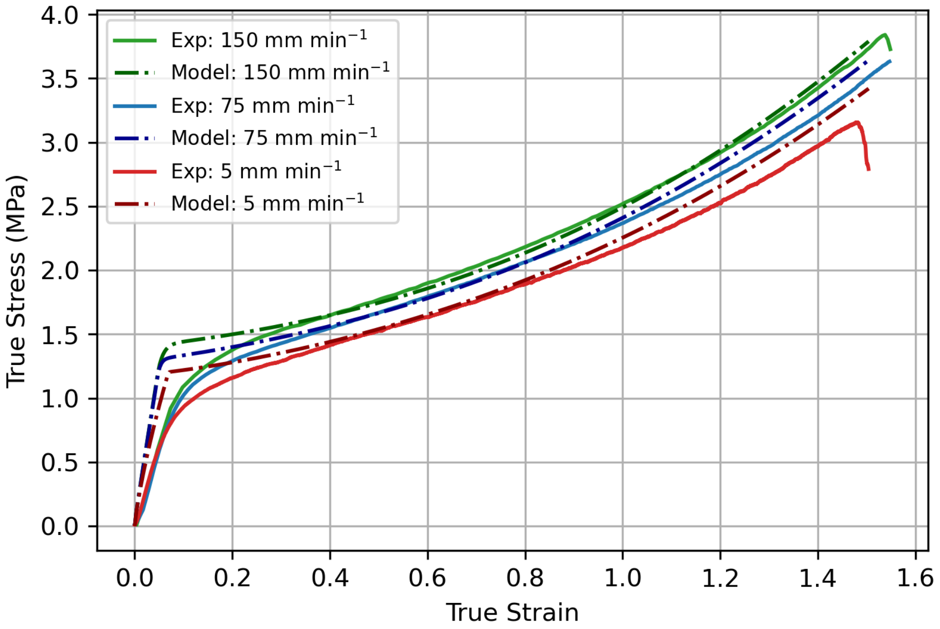

Figure 3.19: Comparison between experimental results and model predictions for the uniaxial tension response of filaments at different extension rates.

The loading/unloading response using screw-side grips is shown in Fig. 3.20 for a displacement rate of 75 mm min^{-1}. The model well predicts the unloading-reloading response at 0.4 and 0.7 strain, with a good prediction of the modulus and hysteresis loop. However, at larger strains of 1.1 and 1.4, the model predictions are less accurate. Nevertheless, the model continues to capture the progressive increase in hysteresis and the overall material response with good agreement.

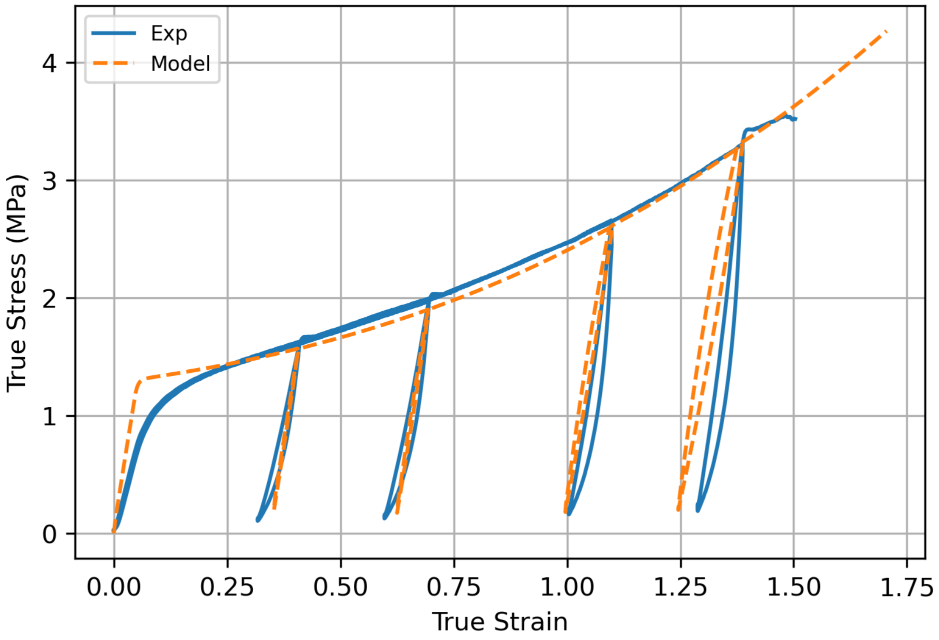

Figure 3.20: Comparison between experimental results and model predictions for the loading/unloading response of filaments at a displacement rate of 75 mm min^{-1}.

Model predictions in relaxation tests are shown in Fig. 3.21, along with experimental data. Different curves correspond to different values of the maximum (true) stress reached during the initial loading stage at 75 mm min^{-1}. The displacement was then held constant while the stress relaxed. The model well captures the experimental response. In particular, the model is able to predict both the short-term and long-term responses for different values of the applied displacement.

3.5 Discussion

3.5.1 Mechanical behaviour

Based on the typical experimental stress-strain curve and the SEM micrographs taken at various deformation stages shown in Fig. 3.14, we decompose and interpret the mechanical response of filaments in four stages. The first stage is the linear (visco)elastic response of the filament, which occurs up to a nominal strain of about 0.08 ± 0.01. During the linear deformation stage, the filament consists

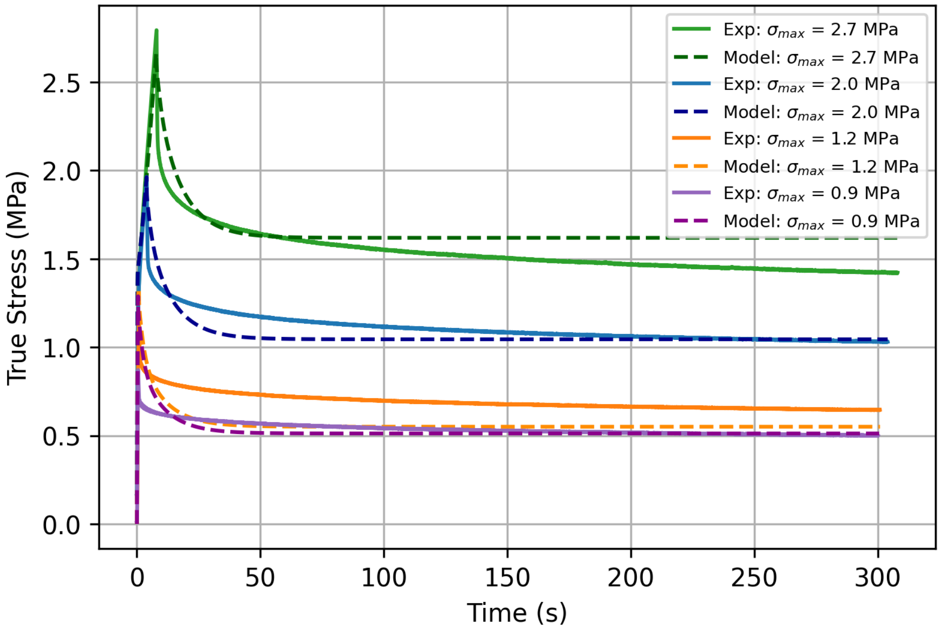

Figure 3.21: Comparison between experimental results and model predictions for the stress relaxation response of filaments loaded to a given maximum stress value σ_{max} at a displacement rate of 75 mm min^{-1}, and held at constant elongation afterwards.

of a network of fibres interconnected through junction points that enable load transfer. Fibres act as the primary load-bearing components, whereas the junctions act as load-transferring elements (Rawal, 2022). These junctions arise from two main mechanisms. First, physical cross-links that consist of fibre entanglements and frictional contacts between individual fibres. Second, additional bonding which may occur at fibre–fibre contact points formed during deposition, where wet fibres come into contact and partially fuse or adhere due to solvent presence and subsequent solidification (Fig. 3.13b) (Bhardwaj and Kundu, 2010; Richard-Lacroix and Pellerin, 2013; Suwantong, 2016). These bonded junctions enhance the structural integrity and interconnectivity of the network. As a result, the filament can be described as an elastic network of fibres, in which the macroscopic mechanical response is governed by both the properties of individual fibres and the characteristics of the junctions. In such networks, the elastic modulus is known to depend on factors including the porosity, the intrinsic modulus of the fibres, the fibre diameter and curvature, and the density of both entanglement-based and bonded junctions (Pai et al., 2011). For example, in a previous study on polyamide-6 mats under tensile loading, (Molnar et al., 2012) found that fibre bonding and friction play an important role in maintaining the structural integrity of the network.

The second stage involves the plastic yielding of the filament, which is attributed to the gradual breaking of the cross-links. The large variability in yield point (Fig. 3.9a) could be related to the variation in density and strength of the cross-link points from sample to sample, as well as to pre-stress introduced when tightening the specimen onto the grips, which could rupture some of the cross-links. During yielding, the overall deformation of the filament is primarily accommodated by progressive fibre alignment in the loading direction, hence the macroscopic stress shows only small hardening. Additional mechanisms that may play a role are layer slippage, considering electrospinning is a layer-by-layer deposition technique, there may be layer slippage concurrently occurring with the re-alignment of fibres.

The third stage involves re-hardening, where the stress-strain gradient steepens at large deformations. We attribute re-hardening to the stretching of individual fibres aligned in the loading direction (Fig. 3.14). The large stretching of individual fibres is evidenced by the reduction in diameter (by 40% between stages (D) and (F)), which implies stretching of the fibres assuming near incompressibility of the polymer. As the fibres are stretched to large deformations, they themselves undergo re-hardening, which is primarily attributed to the limit extensibility of stretched polymer chains in the PCL network. Strain-induced crystallisation probably plays a minor role in the overall rehardening, given the small increase in crystallinity (between stages (E) and (F) the recorded crystallinity value increased only by 3%, cf. Table 3.1). Several groups have studied the evolution of the mechanical properties of fibres in relation to their diameter. For example, (Tan and Lim, 2004) found that a reduction in fibre diameter resulted in an increase in Young's modulus of PLLA nanofibres. (Zussman et al., 2006) showed that ES fibres made of Nylon-6,6 possess a skin-core morphology. The skin consists of oriented layered planes with crystallites, but are misoriented with respect to the core fibre axis. As the fibre diameter is reduced, a critical diameter is reached where the skin and core are similarly oriented, correlating with an increase in molecular orientation. Such results have been further supported by experimental tests conducted by (Lim et al., 2008) and (Arinstein et al., 2007), which showed that the Young's modulus, molecular orientation, and crystallinity increased with smaller fibre diameters due to the greater restriction of polymer conformation.

The final stage is filament failure, corresponding to the sudden stress drop in the stress-strain response (Fig. 3.9). SEM micrographs in Fig. 3.16 reveal that filament rupture occurs in localised regions where fibres are highly aligned in the loading direction and have reached their extensibility limit. It is possible that cross-section inhomogeneities induced by the detachment of the filament from the collecting wire also impact filament failure. However, micrographs do not indicate any localisation of damage near the wire imprint. We hypothesise that failure occurs through a compensation mechanism, whereby failure of an individual fibre involves load redistribution over the remaining fibres. The process is repeated as the macroscopic load in further increased, until catastrophic failure. Similar findings have been reported by (Farukh et al., 2014a,b), who investigated the progressive damage of thermally bonded non-woven networks. These studies reported that network failure often occurred at advanced stages of stretching when fibres have re-oriented and straightened in the loading direction. Fibre failure occurs once their stress or strain threshold was reached. Progressive failure of the fibres would gradually lead to the overall rupture of the network. Fibres can also fail due to the gradual growth of damage through other mechanisms. As an example, (Ridruejo et al., 2011) reported that damage occurs at the very early stages of deformation. Micro-damage in fibres is initially triggered by chemical bond breakage formed at wet contact points and further develops due to frictional slippage between fibres during plastic deformation. This has phenomena has been confirmed by (Chidambaram et al., 2000) and (Farukh et al., 2014a), who argue that bonding process changes the molecular orientation of fibres in the chemical bond periphery, leading to a decrease in elastic modulus and strength of the fibres.

Our experimental results show that the mechanical response of ES PCL filaments is rate dependent. This is most clearly seen from the stress relaxation tests, Fig. 3.8, as well as from the presence of hysteresis during loading/unloading sequences. A strain rate effect is also observed on the yield stress (Figs 3.9b and 3.11b), although definitive conclusions are made difficult by the experimental variability. Predictions of the phenomenological model show that a viscoelastic–viscoplastic formulation is able to reproduce the key features of the material response, including rate-dependent yield stress, hysteresis, and stress relaxation. Rate-dependent behaviour of ES PCL has also been reported in the literature in the context of ES mats (Baker et al., 2015; Duling et al., 2008). Several mechanisms can influence the rate-dependent behaviour of filaments at both the fibre and polymer chain scale. At fibre level, mechanisms include the debonding of chemical and physical cross-link points, disentanglement, and slippage of fibres onto each other. The intrinsic response of the PCL chains constituting the fibres is also rate-dependent. The precise interplay between these mechanisms is still ambiguous and require further investigation.

The impact of moisture and wet conditions is an important factor to consider when evaluating the performance of electrospun (ES) filaments. The mechanical properties of ES filaments can vary significantly depending on the environment in which they are used. In this study, PCL ES filaments were produced in a controlled environment and stored in a desiccator prior to testing. However, all mechanical tests were conducted in environmental humidity conditions. In a recent work, Alharbi and Guthold (2024) compared the mechanical properties of hydrated and dry ES PCL nanofibers. Results showed that hydrated samples stretched slightly more and failed at earlier stresses, however, the differences were small. Further investigation is needed to fully understand the effects of hydration on ES filaments.

3.5.2 Reliability of mechanical testing

ES filaments were characterised utilising two types of mechanical grips, namely screw-side grips and bollard grips, in order to evaluate the impact of the testing method on the measured properties of filaments prepared in the exact same conditions. Indeed, difficulties in comparing experimental measurements for non-woven textiles with similar preparation conditions but tested following different protocols were recently highlighted by (Rashid et al., 2021). Our results show that measured properties are strongly impacted by the type of grips. In particular, filaments tested using screw-side grips failed at much smaller strains, which prevented us to observe the re-hardening behaviour at large deformation with this method. We hypothesise that gluing filaments to the cardboard (Fig. 3.2) locally prevents the untangling and alignment of the fibres during stretching, leading to stress concentration within the fibres near the grips and hence to premature failure. In an attempt to alleviate the local pressure at the grips, square rubber sheets were inserted between the cardboard and the grip face, however, no difference was noted. Another difference is that specimens tested using screw-side grips (Fig. 3.11a) suggest a rate-dependent trend, with higher strain rates generally corresponding to slightly higher stresses, consistent with typical PCL behaviour (Duling et al., 2008). However, the differences between strain rates are small and fall within the experimental variability, and therefore a statistically significant trend cannot be established.

A key limitation associated with bollard grips tensile tests is that it is difficult to measure strain accurately. This could partially explain the large experimental variability and unexpected rate-dependency observed using these grips. First, the defined gauge length did not take into account the excess filament wrapped around the bollard, which can also be stretched and contribute to the prescribed cross-head displacement. Second, the axial strain was not homogeneous within the gauge region with some regions showing delayed activation. Strain delocalisation is attributed to hardening (possibly assisted by strain-induced recrystallisation) in the highly stretched regions, preventing necking. As a result, reported measures of strains should be seen as average values. To address this, we have attempted to measure the local axial strain using digital image correlation (DIC). However, we encountered several obstacles. First, creating a micron- to nano-sized speckle pattern on the porous structure proved difficult, as the paint seeped into the pores. Second, our available equipment (a Point Grey camera paired with a Nikkor 105 mm lens) did not offer sufficient magnification to capture the nano-sized speckle pattern clearly. Third, due to the high strain experienced by the filaments, the tracking pattern often moved out of the camera's field of view. For these reasons, strain characterization using image-based methods was not included in the scope of this study, and further investigations are required.

In addition to these measurement challenges, the conversion of force–displacement data into stress–strain response introduces a further source of uncertainty. Rather than measuring the dimensions of each individual specimen, an averaged cross-sectional area was used. Given the inherent variability in filament geometry, both along the length and between samples, this assumption may lead to systematic over- or underestimation of the calculated stress and corresponding modulus. Since the cross-sectional area scales with the square of the filament radius, even small diameter variations can result in appreciable differences in the derived mechanical properties, thereby contributing to the observed experimental variability. Nevertheless, adopting a consistent reference dimension ensures internal consistency across the dataset, such that relative trends remain robust despite uncertainty in absolute values.

3.5.3 Implications for biomedical application

Continuous ES filaments as studied in this work offer great promises as tissue engineering scaffolds for tendon and ligament repair, thanks to their porous architecture and ability to be braided into yarns with customisable mechanical properties (Abhari et al., 2018a,b). The natural anterior cruciate ligament bears an average daily load in the range 0-300 N, with rupture typically occurring at forces around 2300 N in healthy adults (Marieswaran et al., 2018). While a single ES filament has an average maximum tensile force of the order of 1.5 N (based on the tensile response shown in Fig. 3.7), previous work by Mouthuy and coworkers (Mouthuy et al., 2015; Savić et al., 2021) has shown that the strength of yarns increases almost linearly with the number of filaments. In particular, (Savić et al., 2021) showed that PCL yarns can achieve ultimate tensile forces up to 270 N.

(Mouthuy et al., 2015) also highlighted the benefit of pre-stretching the filaments prior to further assembly into braided structures. Pre-stretching the filaments increases their apparent stiffness and yield strength while reducing the ability of the material to deform plastically, which could compromise material performance. Furthermore, stretched filaments possess a highly aligned microfibrous structure, closely mimicking the extracellular matrix (ECM) of natural ligaments, as also demonstrated in the present work, see Fig. 3.14. Fig. 3.22a shows the representative response of a filament that has been previously pre-stretched by a factor of eight using bollard grips, following the procedure described in Section 3.2.4. The apparent modulus of the pre-stretched filament is 9.5 MPa, which is slightly higher than the un-stretched average value of 9.1 MPa reported in Section 3.3.3. However, the yield stress raised to 1.8 MPa which is twice the yield stress of the un-stretched samples, also reported in Section 3.3.3. Fig. 3.22b shows the typical response of a pre-streched filament during 10 loading/unloading cycles with the maximum force set to 0.7 N, corresponding to a nominal stress of 1.3 MPa. While the specimen still exhibits some residual plastic deformation after the first unloading, the plastic deformation did not increase significantly in subsequent cycles and the hysteresis loop stabilised to a steady shape. In other words, pre-stretched filaments exhibit nearly viscoelastic behaviour in a strain range 0-12 %. This apparent viscoelastic behaviour is attributed to the disentanglement and reorientation of the fibres, which was completed during the pre-stretching stage, exhausting the capability of further plastic deformation in the pre-stretched specimen.

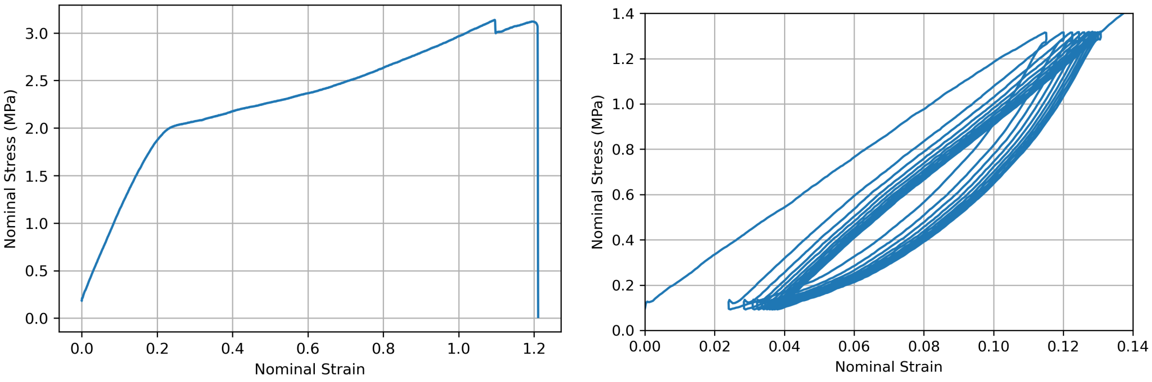

(a) **(b)**

Figure 3.22: Representative nominal stress-strain response of filament pre-stretched by a factor of eight during (a) monotonic loading and (b) cyclic loading up to a nominal stress of 1.3 MPa. All mechanical tests were conducted at 75 mm min^{-1} using bollard grips. Nominal strains reported in the figure were calculated using the pre-stretched state as the reference state.

Fatigue response of ES filaments is also critical for tendon and ligament repair applications. While a complete fatigue characterisation of the ES filaments is beyond the scope of thie work, we did conduct some preliminary tests on pre-stretched filaments. Specifically, pre-stretched filaments were tested using the DMA instrument at 1 and 5 Hz at 1% strain for 18 hours. For each tested frequency, the filament was able to withstand 324,000 cycles and exhibited minimal changes in dimension, storage and loss modulus over time. These preliminary results suggest that ES filaments are able to maintain mechanical stability for extended periods of time.

3.6 Conclusion

Mechanical properties of novel electrospun poly-(ε-caprolactone) filaments were characterised and correlated with microstructural evolutions at the fibre network level. Thermal characterisation using DSC showed that the fibres are semi-crystalline, and that the degree of crystallinity slightly increases with the degree of pre-stretch. The small-strain viscoelastic behaviour of the filament was characterised by DMA, revealing a very broad transition region in the frequency domain for both the storage and loss moduli. The large deformation behaviour of the filament was characterised in tensile tests at various displacement rates. Results show that the filaments are viscoelastic-viscoplastic, involving rate-dependent plastic yielding followed by hardening at large deformations. The mechanical response is attributed to progressive fibre engagement and alignment, involving crosslink debonding and disentanglement, followed by stretching of individual fibres in the ES network as the deformation increases. These results support the idea of pre-stretching the filaments prior to their assembly into braided structures, in order to exhaust the plastic deformation capability of the filaments, effectively making them viscoelastic.

Our study highlights the importance of the testing method, by comparing responses measured using screw-side grips and bollard grips. While bollard grips enable the filaments to be stretched to larger strains and to exhibit significant re-hardening, they also cause inhomogeneous stretching of the filaments, which prevents accurate strain measurements. Variable degree of pre-stress introduced while mounting the specimens on the bollard grips might also contribute to the experimental variability.

A 1D phenomenological model was proposed to capture the viscoelastic-viscoplastic behaviour of electrospun filaments up to large strains. The model is able to capture the key features of the response, including the rate-dependent, loading/unloading response and stress relaxation with good agreement. However, the model is purely phenomenological. Future work includes the development of a micromechanical model, starting from a description of the individual fibres and their interaction in the non-woven network. This will provide further insight into the deformation behaviour of the filaments, which is critical to predict failure mechanisms in future medical textiles made of ES materials.

Acknowledgements

This work was supported by a Future Leaders Fellowship of UK Research and Innovation [MR/W006995/1] and by the Norman Collisson Foundation. The authors would like to thank Mr Gordon Kumar and

Dr Huanming Chen for experimental and modelling support, Dr Nicholas Hawkins for DSC and DMA support, Dr Igor Dyson for mechanical testing and electron microscopy support, Dr Kalin Dragnevski for electron microscopy support, and Dr Meng Liang for the production of electrospun filaments.

Conflicts of Interest

Dr. P.-A. Mouthuy is the inventor on a patent application (WO20150403999A1) related to the filament fabrication technology.

3.7 Appendix A: Fitting of DMA master curves

Table 3.6: Moduli $E^{(i)}$ (MPa) and relaxation times $\tau^{(i)}$ (s) used to fit the experimental master curves in Fig. 3.6 using the Generalised Maxwell model. The relaxed modulus is $E_\infty = 10$ MPa.

$E^{(1)} = 0.66$	$\tau^{(1)} = 3.2 \times 10^{7}$	$E^{(14)} = 1.46$	$\tau^{(14)} = 3.2 \times 10^{-6}$	$E^{(27)} = 5.78$	$\tau^{(27)} = 3.2 \times 10^{-19}$
$E^{(2)} = 0.99$	$\tau^{(2)} = 3.2 \times 10^{6}$	$E^{(15)} = 1.64$	$\tau^{(15)} = 3.2 \times 10^{-7}$	$E^{(28)} = 4.91$	$\tau^{(28)} = 3.2 \times 10^{-20}$
$E^{(3)} = 1.12$	$\tau^{(3)} = 3.2 \times 10^{5}$	$E^{(16)} = 1.91$	$\tau^{(16)} = 3.2 \times 10^{-8}$	$E^{(29)} = 3.90$	$\tau^{(29)} = 3.2 \times 10^{-21}$
$E^{(4)} = 1.12$	$\tau^{(4)} = 3.2 \times 10^{4}$	$E^{(17)} = 2.31$	$\tau^{(17)} = 3.2 \times 10^{-9}$	$E^{(30)} = 2.90$	$\tau^{(30)} = 3.2 \times 10^{-22}$
$E^{(5)} = 1.05$	$\tau^{(5)} = 3.2 \times 10^{3}$	$E^{(18)} = 2.85$	$\tau^{(18)} = 3.2 \times 10^{-10}$	$E^{(31)} = 2.05$	$\tau^{(31)} = 3.2 \times 10^{-23}$
$E^{(6)} = 0.97$	$\tau^{(6)} = 3.2 \times 10^{2}$	$E^{(19)} = 3.52$	$\tau^{(19)} = 3.2 \times 10^{-11}$	$E^{(32)} = 1.44$	$\tau^{(32)} = 3.2 \times 10^{-24}$
$E^{(7)} = 0.91$	$\tau^{(7)} = 3.2 \times 10^{1}$	$E^{(20)} = 4.28$	$\tau^{(20)} = 3.2 \times 10^{-12}$	$E^{(33)} = 1.14$	$\tau^{(33)} = 3.2 \times 10^{-25}$
$E^{(8)} = 0.91$	$\tau^{(8)} = 3.2 \times 10^{0}$	$E^{(21)} = 5.08$	$\tau^{(21)} = 3.2 \times 10^{-13}$	$E^{(34)} = 1.12$	$\tau^{(34)} = 3.2 \times 10^{-26}$
$E^{(9)} = 0.95$	$\tau^{(9)} = 3.2 \times 10^{-1}$	$E^{(22)} = 5.82$	$\tau^{(22)} = 3.2 \times 10^{-14}$	$E^{(35)} = 1.30$	$\tau^{(35)} = 3.2 \times 10^{-27}$
$E^{(10)} = 1.03$	$\tau^{(10)} = 3.2 \times 10^{-2}$	$E^{(23)} = 6.93$	$\tau^{(23)} = 3.2 \times 10^{-15}$	$E^{(36)} = 1.55$	$\tau^{(36)} = 3.2 \times 10^{-28}$
$E^{(11)} = 1.13$	$\tau^{(11)} = 3.2 \times 10^{-3}$	$E^{(24)} = 6.71$	$\tau^{(24)} = 3.2 \times 10^{-16}$	$E^{(37)} = 1.65$	$\tau^{(37)} = 3.2 \times 10^{-29}$
$E^{(12)} = 1.23$	$\tau^{(12)} = 3.2 \times 10^{-4}$	$E^{(25)} = 6.73$	$\tau^{(25)} = 3.2 \times 10^{-17}$		
$E^{(13)} = 1.33$	$\tau^{(13)} = 3.2 \times 10^{-5}$	$E^{(26)} = 6.41$	$\tau^{(26)} = 3.2 \times 10^{-18}$		

3.8 Appendix B: VE–VP Model Using 37 Maxwell Elements

The VE-VP model was implemented using the 37 Maxwell elements listed in Table 3.6. Accordingly, the parameters reported in Table 3.5 were updated so that the values of $E^{(i)}$ and $\tau^{(i)}$ correspond directly to those identified in Table 3.6. To preserve the same instantaneous modulus, E_0, as in the proposed VE model, the sum of the Maxwell spring moduli satisfies $\sum E^{(i)} = 97$ MPa. Consequently, E_∞ must take a negative value in order to enforce $E_0 = 25$ MPa. Model predictions are presented in Figure 3.23.

Figure 3.23a presents the predicted uniaxial tensile response of the filaments using the 37-element Maxwell representation. The model overestimates the initial stiffness, leading to a steeper linear elastic response compared to the experimental data. While a degree of rate dependence is captured immediately beyond the elastic regime, this effect diminishes rapidly with increasing strain, such that the model responses at different strain rates converge towards a single curve at larger deformations. This convergence is not observed experimentally and indicates that the viscoelastic spectrum defined by the 37-element Prony series does not translate meaningfully into the VE-VP framework. In particular, the large number of elements suppresses the ability of the model to preserve distinct rate-dependent behaviour under finite deformation.

Under cyclic loading (Fig. 3.23b), the limitations of the model become more evident. While the loading paths approximately follow the experimental trends, the unloading response is poorly captured, resulting in a near absence of hysteresis. Experimentally, energy dissipation is observed, reflected by the increasing hysteresis loops across higher applied strain. In contrast, the model predicts almost reversible behaviour, suggesting that the internal dissipation mechanisms are not adequately represented. This deficiency arises because the relaxation spectrum is dominated by short relaxation times, which relax too rapidly to contribute to energy dissipation over the duration of the loading cycle.

The discrepancies are further highlighted in the stress relaxation response (Fig. 3.23c). The model exhibits an almost instantaneous drop to a constant stress level, significantly underestimating both the magnitude and the time-dependent evolution of relaxation observed experimentally. In contrast, the experimental data show a gradual decay over the full duration of the test, indicating the presence of longer relaxation processes. The inability of the model to capture this behaviour is again attributed to the excessive number of short relaxation times in the fitted Prony series, which leads to an unrealistic redistribution of stiffness towards rapidly relaxing modes.

These results demonstrate that, although a 37-element Prony series can provide an excellent numerical fit to the frequency-domain data, it lacks physical interpretability and fails to produce realistic predictions when embedded within a finite-strain VE-VP framework. The resulting parameter set is therefore better understood as a high-dimensional curve-fitting exercise rather than a physically meaningful representation of the material behaviour. This highlights the need for a reduced and physically motivated set of viscoelastic elements that balances fitting accuracy with predictive capability across different loading conditions.

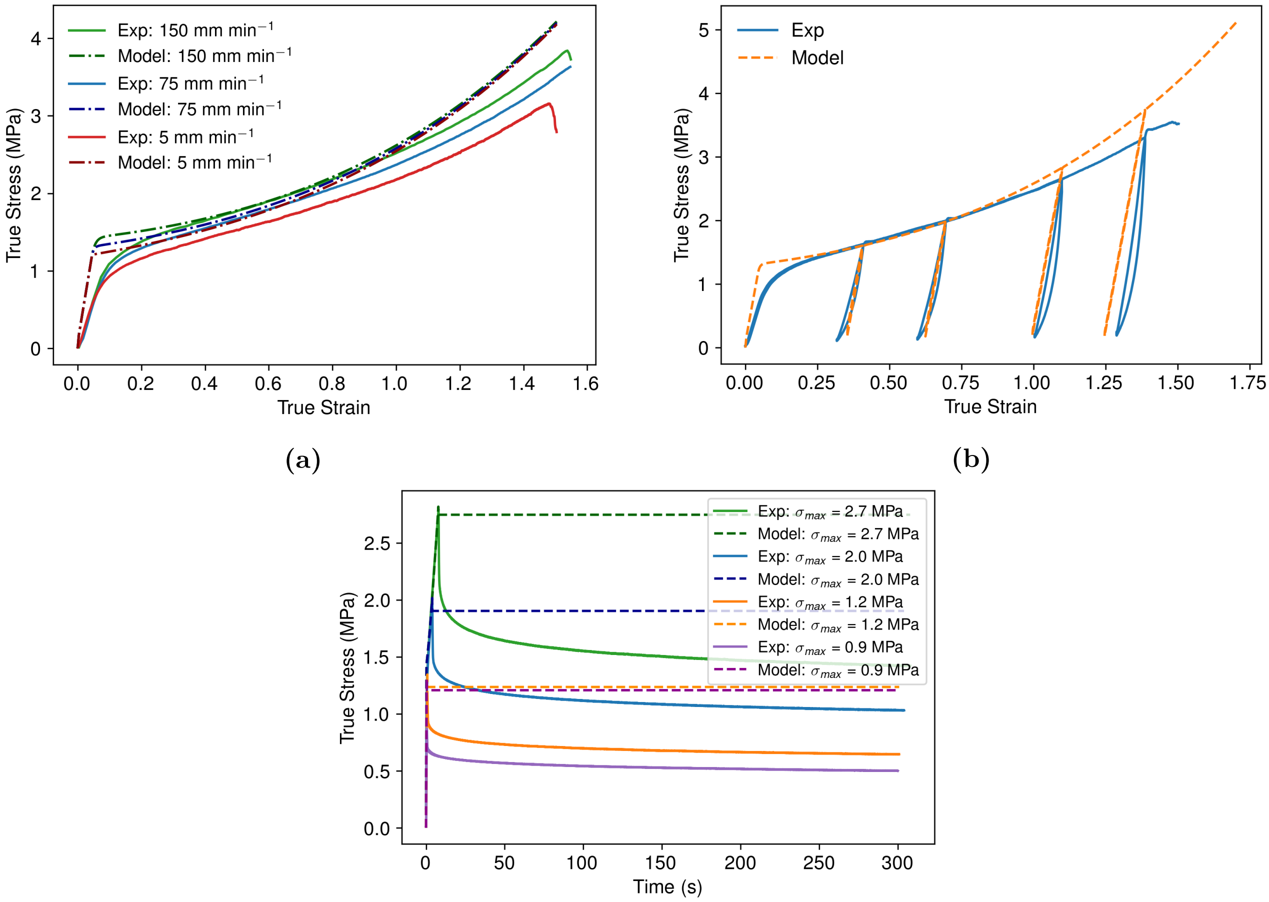

(a) **(b)**

(c)

Figure 3.23: Comparison between experimental measurements and VE–VP model predictions using a 37-element Maxwell representation for (a) uniaxial tension at varying extension rates, (b) cyclic loading, and (c) stress relaxation at different maximum stress levels, $\sigma_{\max}$.

Chapter 4

Hydrolytic degradation of electrospun poly(ε-caprolactone) filaments for biological tissue repair

This chapter presents an investigation into the degradation behaviour of electrospun PCL filaments under both loaded and unloaded conditions. The experimental methods and data discussed herein are based on the work published in: Zanetti Ferreira, T., Chen, H., Chen, K., Mouthuy, P. A., & Brassart, L. (2026). Hydrolytic degradation behaviour of electrospun poly(ε-caprolactone) filaments for biological tissue repair. *Journal of the Mechanical Behavior of Biomedical Materials*, 175, 107308. https://doi.org/10.1016/j.jmbbm.2025.107308.

Each author contributed to the article as follows:

- **Thales Zanetti Ferreira**: Writing - review & editing, Writing - original draft, Software, Methodology, Investigation, Formal analysis, Conceptualization.
- **Huanming Chen**: Resources.
- **Kaili Chen**: Resources.
- **Pierre-Alexis Mouthuy**: Writing - review & editing, Supervision, Resources, Methodology, Funding acquisition, Formal analysis, Conceptualization.
- **Laurence Brassart**: Writing - review & editing, Writing - original draft, Supervision, Methodology, Funding acquisition, Formal analysis, Conceptualization.

4.1 Introduction

Electrospinning (ES) is an attractive technique for the processing of biomaterials, owing to its ability to produce lightweight, fibrous structures that closely mimic the extracellular matrix. Applications of ES constructs for biomedical applications include scaffolds for tissue engineering, wound healing devices, and drug delivery systems (Guo et al., 2022; Ibrahim and Klingner, 2020; Stace et al., 2019). Various polymers have been successfully electrospun to date, including biodegradable polymers such as poly(lactic acid) (PLA), poly(lactic-co-glycolic acid) (PLGA) and poly(ε-caprolactone) (PCL), as well as natural polymers such as collagen and gelatin (Stace et al., 2019).

In recent years, continuous ES filaments consisting of aligned microfibers have been proposed as a promising biomaterial for ligament and tendon repair (Mouthuy et al., 2015; Savić et al., 2021). Continuous ES filaments can be stretched and processed into braided yarns, which can in turn be used to create biomedical implants with tailored mechanical properties. In our recent work, we have characterised the mechanical properties of PCL ES filaments, focusing on their large deformation, rate-dependent response (Ferreira et al., 2025). Another recent study investigated the microstructural changes within the microfibers of ES PCL filaments during stretching (Chandler et al., 2025). However, the degradation behaviour of this material has not yet been investigated.

PCL is a semi-crystalline polymer with low glass transition temperature ($T_g \approx -60°\text{C}$) and low melting temperature ($T_m \approx 60°\text{C}$). It has been extensively used for biomedical applications, owing to its biodegradabilility, biocompatibility and ease of processing (Bartnikowski et al., 2019; Woodruff and Hutmacher, 2010). In physiological conditions, the degradation of PCL primarily occurs by bulk erosion through hydrolytic cleavage of ester groups. Compared to other polyesters, it exhibits significantly slower degradation (approximately 2–4 years to full breakdown) due to the presence of five hydrophobic $-\text{CH}_2$ moieties in its repeating units, which increases its resistance to hydrolysis (Dwivedi et al., 2020). The slow degradation of PCL is also due to its high degree of crystallinity (up to 70% depending on the molecular weight, (Sisson et al., 2013)), since the dense packing of polymer chains in the crystalline regions hinders water penetration, resulting in a much slower degradation of the crystalline domains (Hakkarainen, 2002; Jenkins and Harrison, 2008).

Over the past decades, numerous studies have investigated the degradation of PCL in both physiological (Coombes et al., 2004; Domingos et al., 2010; Lam et al., 2009; Pitt et al., 1981a; Tsuji et al., 2005; Yavuz et al., 2002) and accelerated degradation conditions (Chung et al., 2012; Lam et al., 2008; Little et al., 2009; Sailema-Palate et al., 2016). However, studies focusing on the degradation behaviour of PCL ES fibers remain limited (Bazgir et al. (2021); Bolgen et al. (2005); Johnson et al. (2009); Limbert et al. (2016); Vieira et al. (2011)). The degradation mechanisms and kinetics of ES networks are expected to differ from those of bulk PCL, primarily due to differences in surface area-to-volume ratio, as well as changes in hydrophobicity and crystallinity induced by the electrospinning process (Cipitria et al., 2011; Dong et al., 2009). For example, Bolgen et al. (2005) observed a greater degradation rate in ES construct with thinner fibers, which was attributed to their higher surface-to-volume ratio, enabling higher water penetration.

Another important factor that could impact the degradation behaviour of ES constructs is the presence of applied loads. To date, there have been only limited attempts at characterising the degradation behaviour of polyesters degrading under applied loads, and findings have been somewhat contradictory. For example, Deng et al. (2005) investigated the degradation response of PLGA multifilament braids under tensile loads, but found that the loads did not affect the degradation rate (measured by the reduction in molecular weight) significantly. Samanta et al. (2025) reported that applied tensile loads reduced the degradation rate of PLGA specimens, and further impacted their degradation mechanism. In contrast, other studies found that tensile loads accelerate the degradation of PLGA electrospun scaffolds Li et al. (2010) and PLGA membranes (Guo et al., 2016). Recently, Chen et al. (2026) found that both tensile and compressive loads accelerate the degradation of PLA below a certain molecular weight threshold. However, these materials are typically in their glassy state upon implantation, and therefore the mechanisms for force-assisted degradation may be different than in PCL. To the best of our knowledge, the effect of tensile loads on the hydrolytic degradation of PCL ES constructs has not been investigated before.

The objective of this study is to investigate the effect of mechanical loads on the hydrolytic degradation behaviour of PCL ES filaments. Accelerated degradation tests were conducted in Phosphate Buffer Saline (PBS) solution at 45 °C for up to 5 weeks, and filaments were subjected to a tensile weight during degradation using a custom-designed rig. Characterisation of the degraded filaments include measurements of the molecular weight by Gel Permeation Chromatography (GPC), thermal analysis by Differential Scanning Calorimetry (DSC), morphological evaluation by Scanning Electron Microscopy (SEM), and uniaxial tensile tests. Our results show a significant effect of mechanical loads on the degradation rate of the filaments, accompanied by reduction in strain at break but an increase in modulus and strength. Results are discussed in light of possible mechanisms for microstructure evolution in filaments degrading under load.

4.2 Experimental Methods

4.2.1 Polymer Solution Preparation

Electrospinning solutions were prepared by dissolving PCL with initial weight average molecular weight of approximately $M_w = 175$ kg mol^{-1} according to the manufacturer (Ashland Specialities, Ireland) in 1,1,1,3,3,3-hexafluoroisopropanol (HFIP) (Apollo Scientific Ltd, UK). The polymer was dissolved at a 10% weight-to-volume (w/v) ratio by dissolving 10 g of PCL in 100 mL of HFIP. The solutions were agitated at room temperature using a roller mixer (Stuart SRT9D, UK) set to 21 rpm for a minimum of 24 hours to ensure complete dissolution.

4.2.2 Electrospinning

Electrospun filaments were fabricated by depositing a continuous fibre onto a thin guided wire, forming a dense and narrow mesh that could be detached as a long, continuous thread, as illustrated in Fig. 1.1. A detailed description of the production method is provided by Mouthuy et al. (2015). The electrospinning process utilised a single-nozzle setup with a continuous metallic wire (100 μm diameter) (Goodfellow, UK), an SL30P30/230 high-voltage power supply (30 kV) (Spellman, UK), and a syringe pump (World Precision Instruments Limited, US). The metallic wire was cleaned with 70% ethanol prior to setup. Electrospinning was conducted within a glove box under constant airflow. The room temperature was maintained at 22 ± 3°C and the relative humidity at 40 ± 3%. The polymer solution was delivered at a rate of 1 mL hr^{-1}, with the nozzle tip positioned 20 cm from the wire and an applied voltage between 7 kV and 10.5 kV. The wire moved perpendicularly to the nozzle tip at a speed of 0.4 mm s^{-1}. The resulting product was a metallic wire coated with a continuous ES mesh. Upon exiting the glovebox, the ES filament was detached from the wire and automatically collected on a rotating spool. Upon completion of electrospinning, spools were placed in grip-sealed bags and stored in a vacuum desiccator at room temperature to remove residual solvent and moisture, ensuring that the filaments remained dry. Filaments were stored under these conditions for periods of up to three months before post-processing stretching.

Dry ES continuous filaments were stretched to an average of seven times their original length using an industrial drawing machine (Retech, Switzerland). Initially, a spool containing 5 meters of unstretched material was loaded onto the drawing machine. The filament was then fed through a series of bollards, incrementally stretching it to produce a continuous filament approximately 35 meters in length. An illustration of this stretching process is provided in Fig. 4.1. Pre-stretching of the filaments serves two primary purposes: i) it increases the stiffness of the filaments and reduces the risk of plastic deformation after implantation, and ii) it promotes alignment of the fibres in the primary loading direction, mimicking the structure of native fibrous tissue such as tendons and ligaments (Chandler et al., 2025; Ferreira et al., 2025; Mouthuy et al., 2015). Pre-stretched ES filament spools were stored in a desiccator to prevent environmental degradation and mechanical damage.

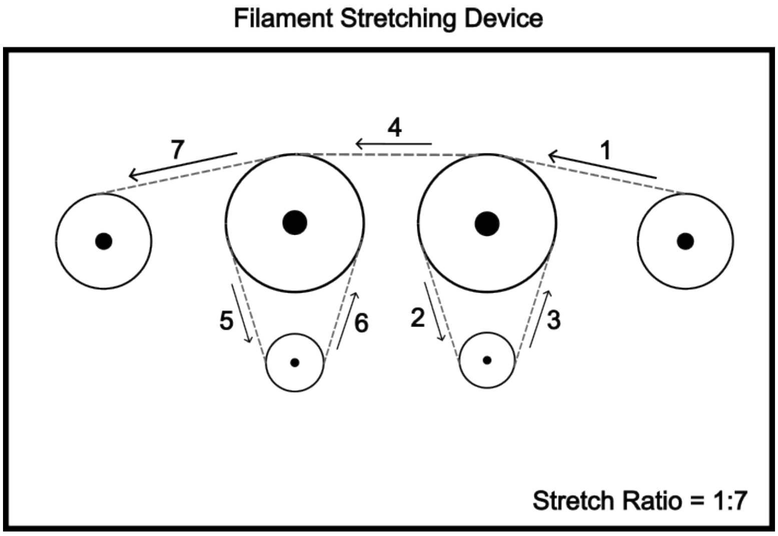

Figure 4.1: Schematic of the post-processing filament stretching device. The filament is routed through a series of driven and guide rollers, following the path indicated by the dashed line, to impose a controlled stretch ratio of 1:7. Numbered sections denote the filament stretching path order.

4.2.3 Degradation Tests

ES filaments were degraded in PBS (Merck, UK) solution with pH 7.4 at constant temperature of 45 °C up to 5 weeks, and under different applied loads (0, 25, and 50 g). The temperature of 45 °C was identified as the upper limit for accelerated degradation without altering the fundamental degradation mechanism. This temperature is lower than the main melting temperature of PCL (around 60 °C). It also corresponds to the onset of the endothermic peak in DSC tests of pre-stretched filaments (Chandler et al., 2025), indicating a destabilisation of the crystalline structure and which could impact the hydrolytic degradation mechanism. It is important to note that the crystallisation temperature of PCL is typically in the range of 30–34 °C. Operating at 45 °C therefore places the material above this range, where chain mobility is increased, particularly in the presence of water. Under these conditions, secondary crystallisation or lamellar reorganisation may occur during degradation, potentially leading to changes in crystallinity over time. Such morphological evolution can influence water diffusion and hydrolysis rates. Nevertheless, Chung et al. (2012) showed that the temperature-dependence of the hydrolysis reaction kinetics of PCL-based electrospun scaffolds was well described by an Arrhenius relation, based on degradation tests at three temperatures (25 °C, 37 °C and 45 °C) and pH of 7.4. These results suggest that the degradation mechanism does not change within this temperature range.

Regarding the choice of mechanical loading, the braided implant is estimated to experience a maximum force of 300 N distributed across 216 filaments (Lin et al., 2025; Savić et al., 2021). Assuming a linear relationship between the number of filaments, this corresponds to a force of approximately 1.38 N per filament, equivalent to a suspended mass of approximately 138 g under gravity. The degradation experiments were conducted at substantially lower loads, selected to remain within the initial linear elastic region of the stress-strain response of the unstretched filaments. The applied masses of 25 g and 50 g correspond to forces of approximately 0.25 N and 0.49 N, respectively. Assuming a circular filament cross-section with diameter 832.2 μm, these loads correspond to approximate nominal stresses of 0.45 MPa and 0.90 MPa. These stress levels are below the onset of yielding (see Fig. 3.9b and Fig. 3.11b) in the unstretched filaments and therefore provide a relevant basis for assessing degradation under sustained sub-yield loading. Filaments degraded under no load served as controls.

Degradation of the filaments under load was conducted in a custom-designed testing rig, consisting of an aluminium frame equipped with 3D-printed bollard grips made of thermoset resin (Formlabs, US), as shown in Fig. 4.2. Details about the design of the testing rig are provided in Section 4.7. The frame was submerged in a 30 x 30 x 30 cm PBS tank, kept at constant temperature using silicone heating mats (RS Pro, UK) attached to its base and sides. The setup could accommodate up to 72 loaded ES PCL filaments simultaneously. In parallel, degradation studies on non-loaded samples were conducted using 50 mL test tube vials. Each filament was cut to a standardised length of 25 cm, and at least twelve ES filaments were degraded per time point, with six filaments placed in each vial. The vials were filled with PBS solution and then submerged in a shared water bath to ensure uniform thermal exposure throughout the testing period. The temperature and pH were continuously monitored using an Arduino Mega 2560 with a Ramps 1.4 board, equipped with a DS3231 real-time clock, three NTC temperature probes, a DF Robot pH sensor, and a micro-SD module for data logging. The Arduino also operated as a PID controller to regulate the heating mats and maintain precise water temperature. We have verified that the pH remained stable, averaging 7.5 ± 0.6 throughout the 5-week testing period.

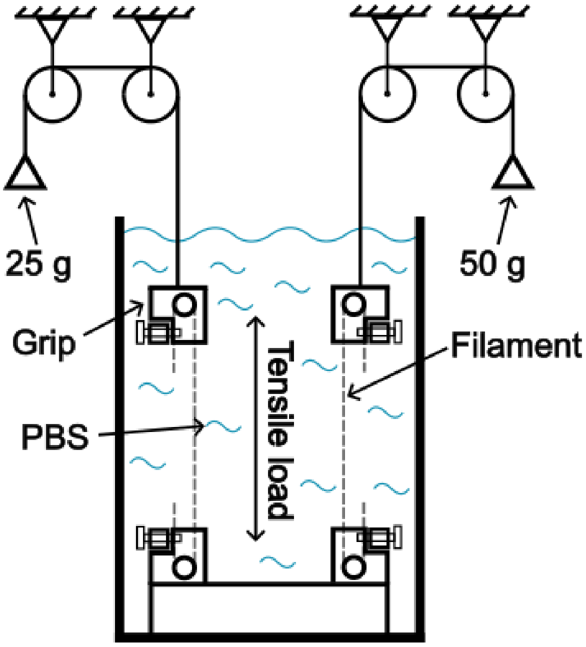

Figure 4.2: Schematic of the custom-designed degradation rig.

Filaments were weighed before submersion, and in their wet and dry states following a predefined degradation period using a digital balance (Sartorius, Germany) with a 0.01 mg precision. After removal from the bath, wet samples were laid on a paper towel to remove excess water and weighed immediately, dried for 72 hours at environmental temperature (i.e. 22 ± 2°C) and re-weighed. The water uptake w and mass change f were determined as:

$$w = \frac{m_w - m_d}{w_d}, \quad f = \frac{m_i - m_d}{m_i}, \tag{4.1}$$

where m_i, m_w and m_d respectively represent the initial, wet and dry weights of the filaments. Due to the rapid drying of the filaments (approximately 10 minutes at room temperature), it was not possible to unmount and weigh the loaded specimens sufficiently fast to obtain accurate water uptake measurements for samples degraded under load. After weighing, the filaments were cleaned using an ultrasonic cleaning bath (Ultrawave, UK) to remove excess salt, dried, and stored for further characterisation.

4.2.4 Gel Permeation Chromatography

The molecular weight of the filaments was measured using an HPLC gel permeation chromatography (GPC) system (Shimadzu, UK). Samples of approximately 2.5 mg were dissolved in tetrahydrofuran (THF) solvent at a concentration of 10 mg ml^{-1}. GPC analysis was conducted at an average flow rate of 1.0 mL min^{-1} at room temperature, with the system column calibrated using polystyrene standards of known molecular weights. The number average molecular weight M_n, weight average molecular weight M_w, and dispersity $Đ = M_w/M_n$ were calculated. Only one measure was taken for each degradation duration and load.

The evolution of number-average molecular weight with degradation time was fitted using two kinetic models from the literature. Both models are based on the assumption that the concentrations of ester bonds and water are constant during degradation, and neglect mass loss. The first model further neglects autocatalysis, giving (Pitt and Gu, 1987):

$$\frac{1}{M_n} = \frac{1}{M_{n_0}} + k_1 t \tag{4.2}$$

where M_{n_0} is the initial number average molecular weight and k_1 is the rate constant. In contrast, the second model assumes that hydrolysis is autocatalysed by the acidic end groups produced by chain scission, leading to (Pitt et al., 1981a; Pitt and Gu, 1987):

$$M_n = M_{n_0} \exp(-k_2 t) \tag{4.3}$$

where k_2 is the rate constant in the model accounting for autocatalysis. Derivation details of these two models can be found for example in (Lyu et al., 2007). Fitting of the experimental degradation curves was based on linear regressions of $1/M_n$ (Model 1) and $\ln(M_n)$ (Model 2) as a function of time, setting M_{n_0} to the value for the undegraded polymer.

4.2.5 Thermal Properties

Differential scanning calorimetry (DSC) tests were conducted with a DSC Q2000 differential scanning calorimeter (TA Instruments, US) in a nitrogen atmosphere with a flow rate of 50 mL min^{-1} and aluminium hermetic cups with lid. Samples were first cooled to reach a thermal equilibrium of -90 °C, then heated at 10 °C min^{-1} up to 80°C. Samples were then cooled at 10 °C min^{-1} down to -30 °C. The heat flow per unit mass (W g^{-1}) was recorded to identify any phase transformations. DSC thermographs were analysed using TA Universal Analysis software. The enthalpy of fusion from solid to liquid ($\Delta H_{S \to L}$) and recrystallisation enthalpy ($\Delta H_{L \to S}$) were calculated from the areas under the respective peaks to determine the degree of crystallinity (K), using the following formula:

$$K(\%) = \frac{\Delta H}{\Delta H_0} \times 100 \tag{4.4}$$

where ΔH is the experimentally-measured melting enthalpy ($\Delta H_{S\rightarrow L}$ or $\Delta H_{L\rightarrow S}$), and ΔH_0 is the reference value for 100% crystalline material, reported as 139.5 J g^{-1} (Lam et al., 2008; Pitt and Gu, 1987). Only one measurement was taken for each degradation duration and load.

4.2.6 Microstructural Characterisation

The microstructure of the pre-stretched, undegraded specimens and dried, degraded specimens was examined using a TM3030Plus tabletop Scanning Electron Microscope (SEM, Hitashi, Japan). Specimens were mounted onto an aluminium stub using carbon adhesive disk. The SEM operated under variable pressure with a 15 kV acceleration voltage and 4.4-4.8 mm working distance. Micrographs were obtained from randomly selected regions at magnifications between x100 and x1000 to examine the mechanisms of degradation at both the fibre and filament scale. The filament and fibre apparent diameters were measured using ImageJ software. The reported average diameter values are based on micrographs corresponding to three different samples and at least eight recordings were taken for each sample.

4.2.7 Mechanical Testing

The mechanical response of dried degraded ES PCL filaments was characterised using an Instron 5582 electromechanical tensile tester (Instron, UK) with a 100 N load cell. Filaments were cut to a standardised length of 120 mm as this was the minimum length required to wrap the filaments around the grips. Filaments were first wrapped around the top bollard and clamped. Wrapping around the lower component was carefully conducted to ensure vertical alignment and prevent any torsion of the filament. A 45 mm gauge length was defined by the two contact points at which the filament tangentially contact the grips. Mounting the filaments introduced some pre-load in the range 0.05-0.2 N. Uniaxial tensile tests were conducted at room temperature (22 ± 2°C) and environmental humidity conditions (38 ± 5 %).

Filaments were tested at an extension rate 75 mm min^{-1} until failure. This extension rate was selected for consistency with our previous work (Ferreira et al., 2025), where we characterised the behaviour of the unstretched, undegraded filaments at three extension rates, 5, 75 and 150 mm min^{-1}. The value of 75 mm min^{-1} was adopted in the present work as a representative value. The nominal strain was defined as $\varepsilon_n = \frac{L-L_0}{L_0}$, with L_0 and L the initial and deformed gauge lengths. The nominal stress was calculated by dividing the measured force by the cross-sectional area of the filament, assuming a circular geometry. The filament cross-section is in practice slightly non-circular, exhibiting a mild

U-shaped morphology resulting from detachment from the collection wire. Diameter measurements were therefore taken consistently from the flatter (deposition) side of the filament. The diameter was obtained from SEM images (see Section 4.3.3) by averaging multiple measurements taken along the filament length from at least three samples. For filaments degraded without applied load, the diameter of the undegraded, pre-stretched filaments was used ($d_0 = 467.08$ μm). For the filaments degraded under applied loads, the average diameters (in μm) calculated from SEM images were 359.84 ± 13.24, 335.22 ± 10.87, 302.73 ± 17.11, and 314.09 ± 35.7 after 1, 2, 3 and 5 weeks of degradation under 25 g load, and 294.92 ± 19.72, 286.05 ± 24.19 and 256.36 ± 19.85 after 1, 2 and 3 weeks of degradation under 50 g load.

It should be noted that this approach provides an apparent stress, as the calculation is based on the external filament diameter and does not account for internal porosity. Consequently, the effective load-bearing area is smaller than assumed, leading to an underestimation of the intrinsic material modulus. In addition, the assumption of a constant circular cross-section may not strictly hold, as heterogeneous stretching can lead to inconsistent filament geometry and internal structure. These factors introduce some uncertainty in the absolute values of stress and modulus. Despite these limitations, increasing stretch reduces porosity and promotes fibre alignment, thereby improving load transfer within the filament and reducing uncertainties associated with internal structure and geometry. Nevertheless, the measured stresses remain lower than those of bulk PCL due to residual porosity. As all samples were analysed using a consistent methodology, the observed trends remain valid for comparative purposes.

The apparent elastic modulus was calculated by fitting a linear regression in the linear elastic regime of the nominal stress-strain response. At least four samples were tested for each degradation condition. Statistical analysis was performed in Python using statsmodels and pingouin packages. Pairwise comparisons between independent groups with unequal sample sizes were evaluated using two-way ANOVA and the Games–Howell tests. Results were considered significant at $p \leq 0.05$.

4.3 Results

4.3.1 Degradation Tests

Fig. 4.3a shows the evolution of M_n with degradation time, for specimens degraded with and without applied loads. In the initial, undegraded state, the molecular weight is $M_n = 123$ kg mol^{-1}

with Đ = 1.42. The molecular weight then decreases with time over the considered time period. Despite the relatively short degradation period, the reduction in molecular weight is significant. This contrasts with previous findings by Chung et al. (2012), who did not observe any noticeable reduction in molecular weight in ES PCL sheets degraded in PBS at the same temperature for up to 42 days. Fig. 4.3a also shows that the molecular weight decreases faster under applied loads. For degradation without load, the molecular weight shows a 21.1% reduction by Week 5. In comparison, samples subjected to a 25 g load show a reduction of 33.2% after 5 weeks, and samples subjected to 50 g load show a molecular weight reduction of 35.4% after only 3 weeks (these samples broke before reaching 5 weeks of degradation). The evolution of the dispersity is shown in Fig. 4.3b. Under no load, Đ shows minimal variation during degradation, remaining between 1.42 and 1.55 over the study period. In contrast, the dispersity under a 25 g load increases from 1.42 to 1.72 by Week 5, and the dispersity under a 50 g load increases to 1.95 by Week 3.

Fig. 4.3a also shows the fitting of the experimental curves using Eqs (4.2) and (4.3), respectively. Fitted experimental constants and R^2 values are provided in Table 4.1. Overall, both models fit the experimental reasonably well over the considered time period, with and without applied loads. However, the autocatalytic model provides a slightly better fit. A linear decrease of $\ln(M_n)$ with time was previously reported by Pitt et al. (1981a) and Pitt and Gu (1987) in both *in vitro* and *in vivo* degradation of PCL at 37 °C. Other studies have reported similar degradation kinetics at 37 °C and neutral pH, e.g. (Fernández et al., 2015; Larrañaga et al., 2014; Tsuji and Ikada, 1998; Zhang et al., 2013).

Table 4.1: Rate constants of Model 1 (Eq. (4.2)) and Model 2 (Eq. (4.3)) fitted on the experimental data.

	k_1 (mol kg^{-1} weeks^{-1})	R^2(%) (Model 1)	k_2 (weeks^{-1})	R^2(%) (Model 2)
0 g	4.15×10^{-4}	99.0	0.0468	99.6
25 g	6.55×10^{-4}	91.0	0.0728	93.1
50 g	1.33×10^{-3}	98.0	0.1386	98.9

The water uptake during degradation of specimens degraded without load is reported in Table 4.2, showing an increase in water uptake with degradation time. The mass change of the filaments after a given degradation period and for each applied load is also reported in Table 4.2, showing an increase in weight. This is attributed to the deposition of salt from the PBS solution, which was observed in SEM images for unwashed filaments (images not shown). Similar mass increase was previously reported during degradation of porous PCL membrane (Gaona et al., 2012). The mass change appears to

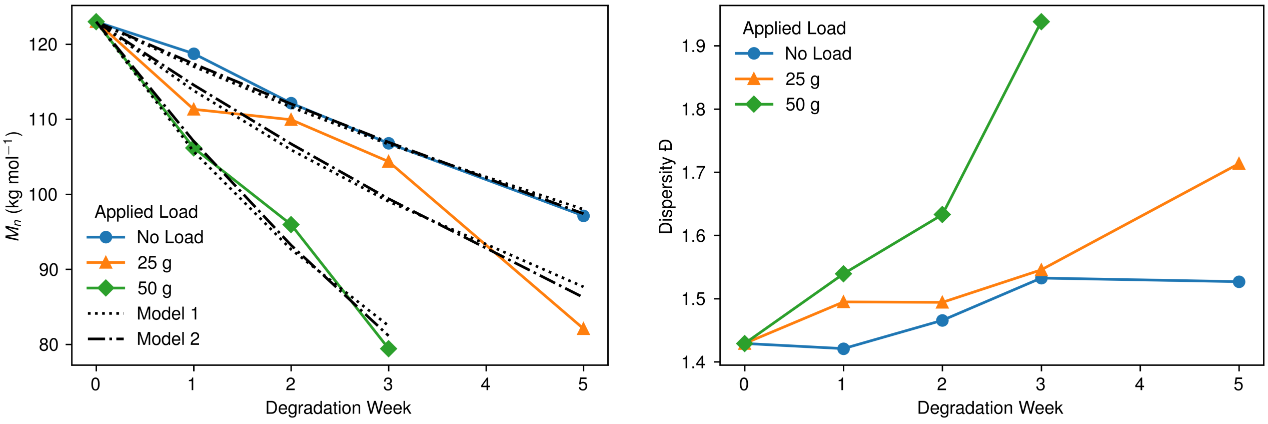

(a) **(b)**

Figure 4.3: (a) Number-average molecular weight M_n as a function of degradation time for specimens degrading with and without applied loads. Dashed lines are fits using two different models: Model 1 corresponds to the non-autocatalytic Anderson model, while Model 2 corresponds to the autocatalytic Pitt model. (b) Dispersity (Đ) as a function of degradation time. Colourful lines connecting the data points are included as a guide to the eye only and do not represent a fitted model.

increase with the applied load. However, no consistent pattern is observed across different degradation periods.

Table 4.2: Water uptake and mass change of degraded filaments. The results are the average reported values using at least six filaments for the mass change and only two for water uptake.

	Water uptake, w (%)	*Mass change, f* (%)		
	No Load	No Load	25 g	50 g
Week 1	68.1	34.6 ± 22.6	52.7 ± 32.3	65.7 ± 53.9
Week 2	137.1	18.1 ± 5.1	105.7 ± 57.5	183.9 ± 123.1
Week 3	172.2	5.1 ± 10.3	72.0 ± 54.4	91.9 ± 62.2
Week 5	226.2	11.49 ± 22.1	258.6 ± 119.8	-

4.3.2 Thermal Properties

The DSC thermograph of an undegraded ES PCL filament is shown as the black-solid line in Fig. 4.4. Melting starts at 54.3°C, with a peak at 59.0°C (Fig. 4.4a), followed by a recrystallisation peak during cooling at approximately 30.7°C (Fig. 4.4b). Fig. 4.4 also shows DSC thermographs for the filaments degraded under non-loaded and loaded conditions. Compared to the undegraded case, the endothermic (melting) and exothermic (recrystallisation) peaks show an increase in height, reduction in width, and slight shift of their positions to higher temperature with increasing degradation time. Mechanical loads applied during degradation appear to reduce the peak height.

The evolution of the degree of crystallinity with degradation time calculated based on $\Delta H_{S\to L}$ in Eq. (4.4) is shown in Fig. 4.5a. The degree of crystallinity is 51.4 % in the initial, undegraded state,

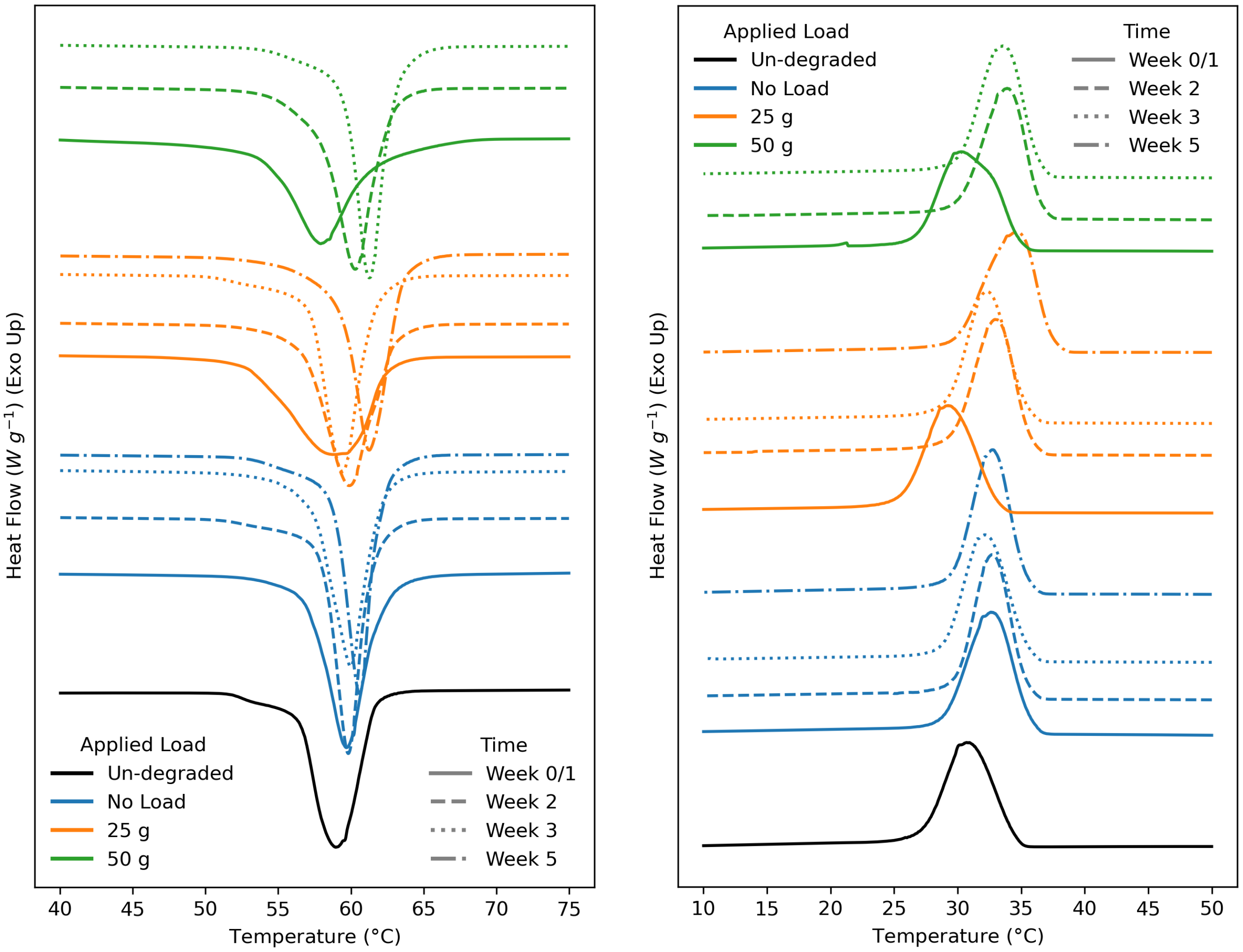

(a) Melting Peaks **(b)** Recrystallization Peaks

Figure 4.4: DSC thermographs of electrospun PCL filaments after different exposure time periods and applied loads, showing (a) melting peaks during heating and (b) recrystallisation peaks during cooling.

and increases with both during exposure time and the applied load. The crystallinity of samples degrading under no applied load increases by approximately 18% between Week 0 and Week 5, whereas the degree of crystallinity of samples subjected to a 25 g load shows a 22% increase over the same time period. Samples degrading under a 50 g load show a 17% increase in crystallinity within just three weeks. Fig. 4.5b shows the degree of crystallinity of pre-degraded samples following a heating and cooling cycle, calculated based on $\Delta H_{L \to S}$. Undegraded samples reach a degree of crystallinity of about 35.6 % when cooled from the melt, which is significantly lower than the initial degree of crystallinity. The crystallinity degree increases with the degradation time, and is enhanced in samples degraded under load.

Fig. 4.6 shows the evolution of the melting and recrystallisation temperatures as a function of degradation time, for different applied loads. For a given applied load, both temperatures increase

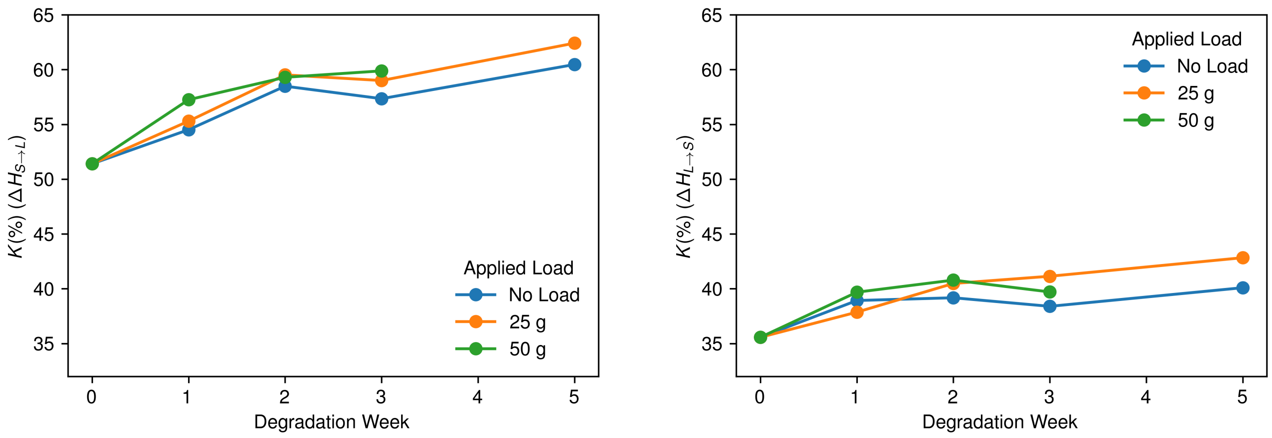

(a) **(b)**

Figure 4.5: Degree of crystallinity calculated based on (a) $\Delta H_{S\to L}$ and (b) $\Delta H_{L\to}S$ in samples pre-degraded with and without applied loads. Lines connecting the data points are included as a guide to the eye only and do not represent a fitted model.

overall with the degradation time, whereas the effect of the applied load for a given degradation period is less clear.

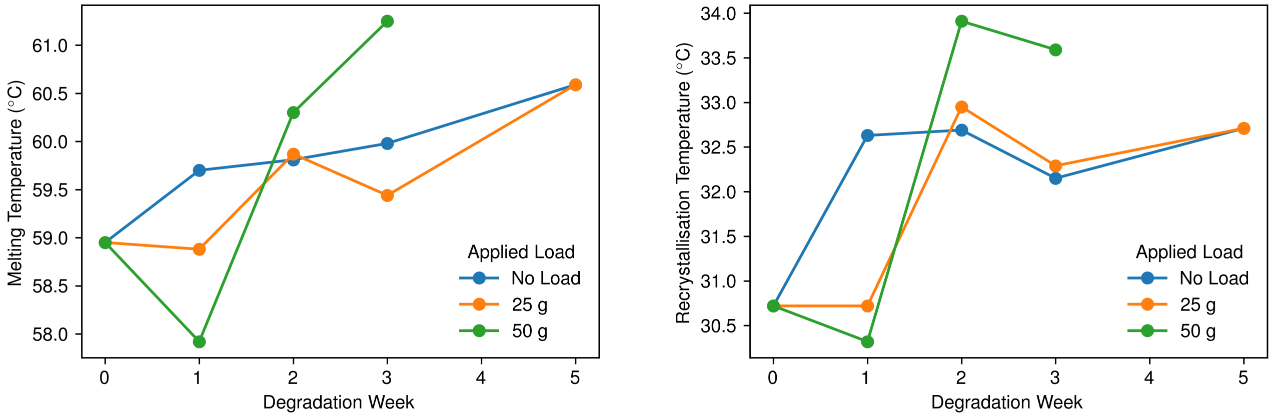

(a) **(b)**

Figure 4.6: Evolution of (a) melting temperature and (b) recrystallisation temperature as a function of degradation time and for different applied loads. Lines connecting the data points are included as a guide to the eye only and do not represent a fitted model.

4.3.3 Microstructural Characterisation

Fig. 4.7 shows SEM micrographs of filaments subjected to varying degradation durations and applied loads. Across all samples, the ES morphology is characterised by an anisotropic, porous, and densely packed fibrous network. For the same exposure time, the apparent diameter of the filament decreases with the applied load. The filament diameter also decreases with the exposure time for filaments degraded under load. Additionally, filaments subjected to a 50 g load show early signs of structural deterioration by localised fibre rupture.

Filament and fibre diameters measured across all degradation conditions are shown in Fig. 4.8 as a function of the degradation time. Numerical data are reported in Table 4.3. It should be noted that electrospun filaments are not perfectly cylindrical; their cross-sections are often flattened due to the electrospinning collection and stretching processes. Measurements correspond more to the width of the flatter side of the filament rather than a true diameter of a circular cross-section. For samples degraded under no applied load, the apparent filament and fibre diameters remain relatively constant over time, with variations falling within the bounds of standard deviation. In contrast, samples subjected to applied loads during degradation exhibit a progressive decrease in filament and fibre diameter during degradation, with a larger applied load causing a larger decrease in diameter for a given exposure time. The reduction in filament diameter indicates the occurrence of creep deformation during degradation under load, involving axial elongation of the filaments along with lateral contraction. The concurrent reduction in fibre diameter further indicates that filament creep involves fibre creep as well. These observations are consistent with our previous observations that stretching of ES filaments causes a reduction in both filament and fibre diameters (Ferreira et al., 2025). A more detailed discussion of the creep behaviour observed during degradation under load is provided in the Appendix B (Section 4.8).

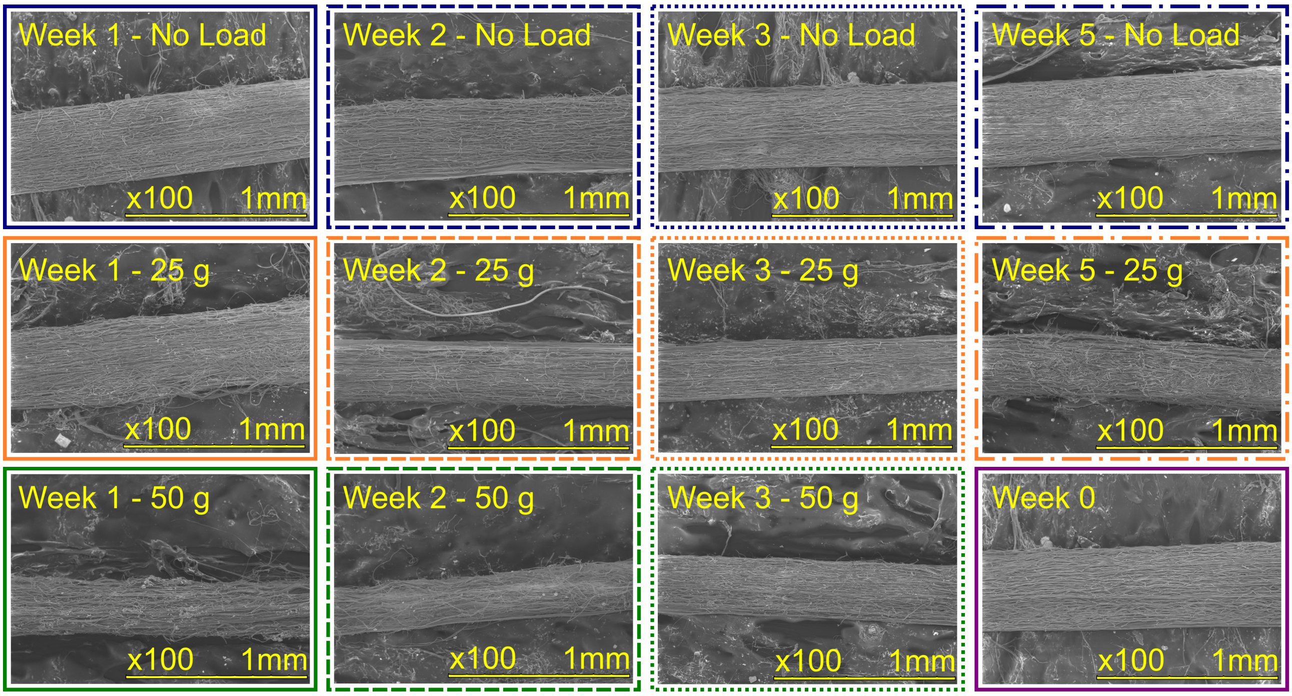

Figure 4.7: Representative SEM micrographs for each degradation time and applied load.

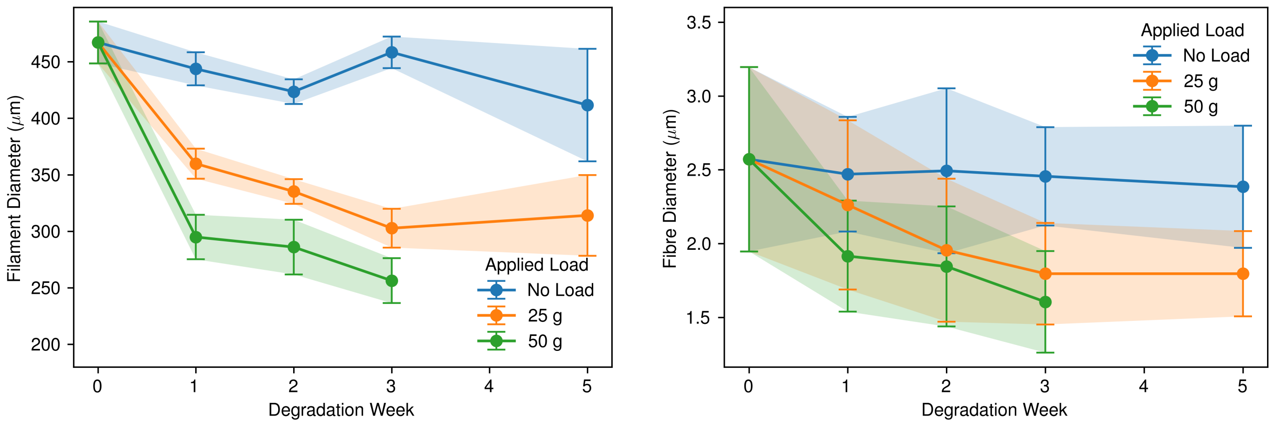

(a) **(b)**

Figure 4.8: Evolution of the (a) filament and (b) fibre diameter with degradation time and for different applied loads. Diameters were calculated based on SEM micrographs. Data points represent mean values, with shaded regions representing a linear interpolation between the standard deviation for each averaged value. Lines connecting the data points are included as a guide to the eye only and do not represent a fitted model.

Table 4.3: Filament and fibre diameter.

	Filament Diameter (μm)			**Fibre Diameter** (μm)		
	0g	25g	50g	0g	25g	50g
Week 0	467.08 ± 18.54	-	-	2.57 ± 0.62	-	-
Week 1	443.68 ± 14.64	359.84 ± 13.24	294.92 ± 19.72	2.60 ± 0.39	2.26 ± 0.57	1.92 ± 0.38
Week 2	423.52 ± 10.85	335.22 ± 10.87	286.05 ± 24.19	2.49 ± 0.56	1.96 ± 0.48	1.85 ± 0.41
Week 3	458.35 ± 13.97	302.73 ± 17.11	256.36 ± 19.85	2.40 ± 0.30	1.80 ± 0.34	1.61 ± 0.34
Week 5	411.62 ± 49.72	314.09 ± 35.71	-	2.39 ± 0.41	1.79 ± 0.29	-

4.3.4 Mechanical Properties

Representative stress-strain curves of filaments degraded under no applied load are shown in Fig. 4.9a (refer to Section 4.9 for complete dataset). The response of the undegraded specimen is characterised by an initial linear elastic regime, followed by plastic deformation with mild strain hardening, until failure. The average apparent yield stress of the undegraded specimens is 4.7 ± 0.95 MPa, where the yield stress was measured using the 0.2% offset strain. A 50 g load corresponds to a 2.7 MPa stress based on a filament diameter of 467.1 μm (Table 4.3) so that the loads applied during degradation were lower than the yield stress of the undegraded filament. The response of the degraded samples also exhibits elasto-plastic characteristics, with a lower apparent elastic modulus, lower yield stress and reduced hardening capacity. The most significant effect of degradation is the reduction in plastic deformation (ductility), causing a major reduction in the strain at break. Compared to samples degraded under no load, filaments degraded under 25 g load show an increase in elastic modulus and apparent yield stress, but a reduced ductility resulting in a smaller strain at break. In particular, some specimens degraded for more than 2 weeks show brittle-like behaviour and fail before yielding. (Fig.

4.9b). Degradation under a 50 g load causes a further increase in elastic modulus with degradation time. However, all these specimens fail before the yield point in a brittle-like manner and the strain at overall decreases with the degradation time (Fig. 4.9c). Note that specimens broke in the bath before reaching 5 weeks of degradation, so that no data could be collected at this time point. Figure 4.10 shows the same representative stress-strain curves at each time point, for all three loading conditions. At each time point, increasing the applied load corresponds to higher initial stiffness and a lower strain at break.

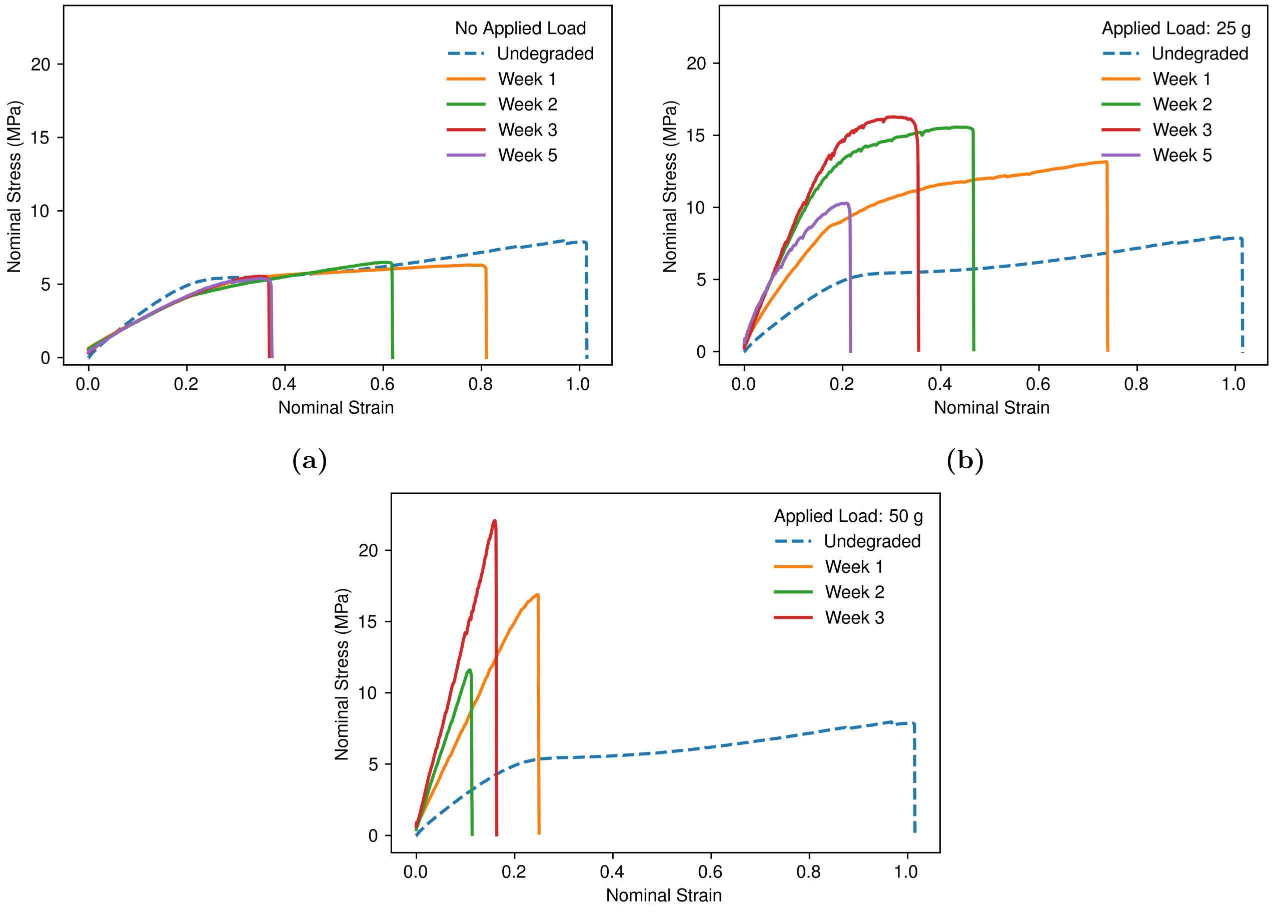

(a)

(b)

(c)

Figure 4.9: Representative stress-strain curves of filaments degraded under (a) no load, (b) 25 g, and (c) 50 g applied load. The extension rate was 75 mm min^{-1}.

The evolution of average elastic modulus is shown in Fig. 4.11a, along with the standard deviation over four specimens. The undegraded samples have an apparent elastic modulus of approximately 22.8 ± 2.4 MPa. Samples degraded under no applied load show a small reduction in elastic modulus after the first week of exposure, and the modulus appears to remain constant afterwards, at least during the considered degradation period. In contrast, samples degraded under applied load show an increase in apparent modulus with both degradation time and applied load. The evolution of elastic

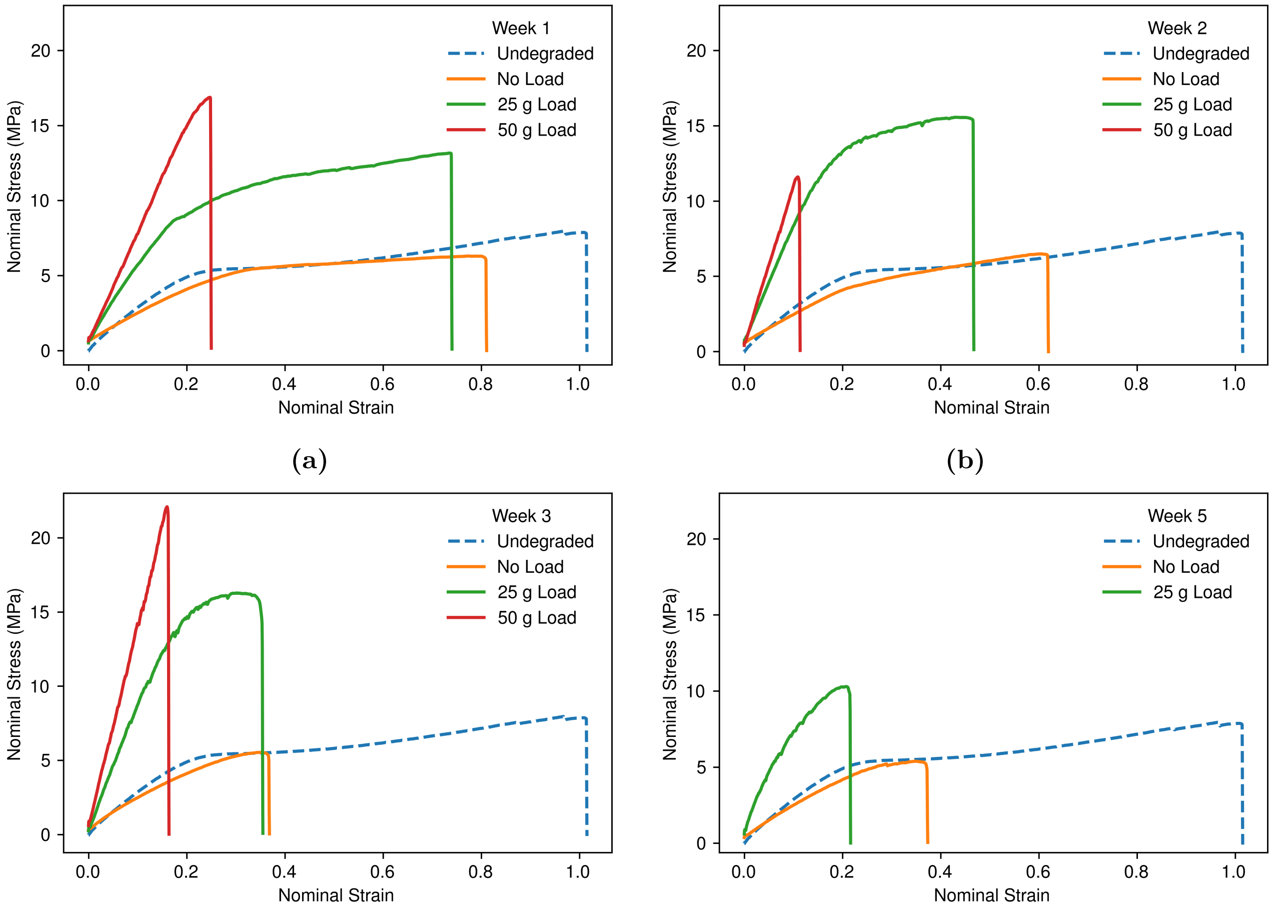

(a)

(b)

(c)

(d)

Figure 4.10: Representative stress-strain curves of filaments degraded for (a) 1 week , (b) 2 weeks, (c) 3 weeks and (d) 5 weeks and for different applied loads. The extension rate was 75 mm min^{-1}.

modulus with degradation time contrasts with the corresponding evolution of the overall degree of crystallinity (Fig. 4.5a), which show comparable increase in degrees of crystallinity with time for all three loading conditions, with a mild positive effect of the load. This suggests that the change in overall degree of crystallinity alone cannot explain the change in elastic modulus during degradation under load. The evolution of the maximum stress is shown in Fig. 4.11b. While the maximum stress decreased with degradation time in non-loaded specimens, a non-monotonous evolution is observed in filaments degraded under a 25 g load, with an initial increase in maximum stress followed by a drop. In filaments degraded under a 50 g load, the maximum stress increases with exposure time overall. However, we recall no data point could be collected after 5 weeks. In contrast, the elongation at break decreases with exposure time in all loading conditions, and decreases as the applied load increases (Fig. 4.11c). For samples degraded under no load, a 40% reduction in strain at break is observed by Week 1, while for samples under 50 g load, the reduction reaches approximately 80%.

Measured mechanical properties show substantial variation across specimens (Fig. 4.11). Variability in the mechanical response of undegraded and unstretched ES filaments has previously been reported (Ferreira et al., 2025), reflecting inherent heterogeneity in the electrospinning process and manifesting particularly in the maximum stress and strain at break. Our earlier work also demonstrated that these filaments are prone to inhomogeneous axial deformation (i.e., necking). In the present study, additional differences may arise from post-processing filament drawing, which can alter the degree of pre-stretch and further increase specimen-to-specimen variability. Nevertheless, Fig. 4.11 indicates that the degradation process itself introduces further variability, especially in the measured elastic modulus, for which the undegraded specimens initially exhibited excellent reproducibility.

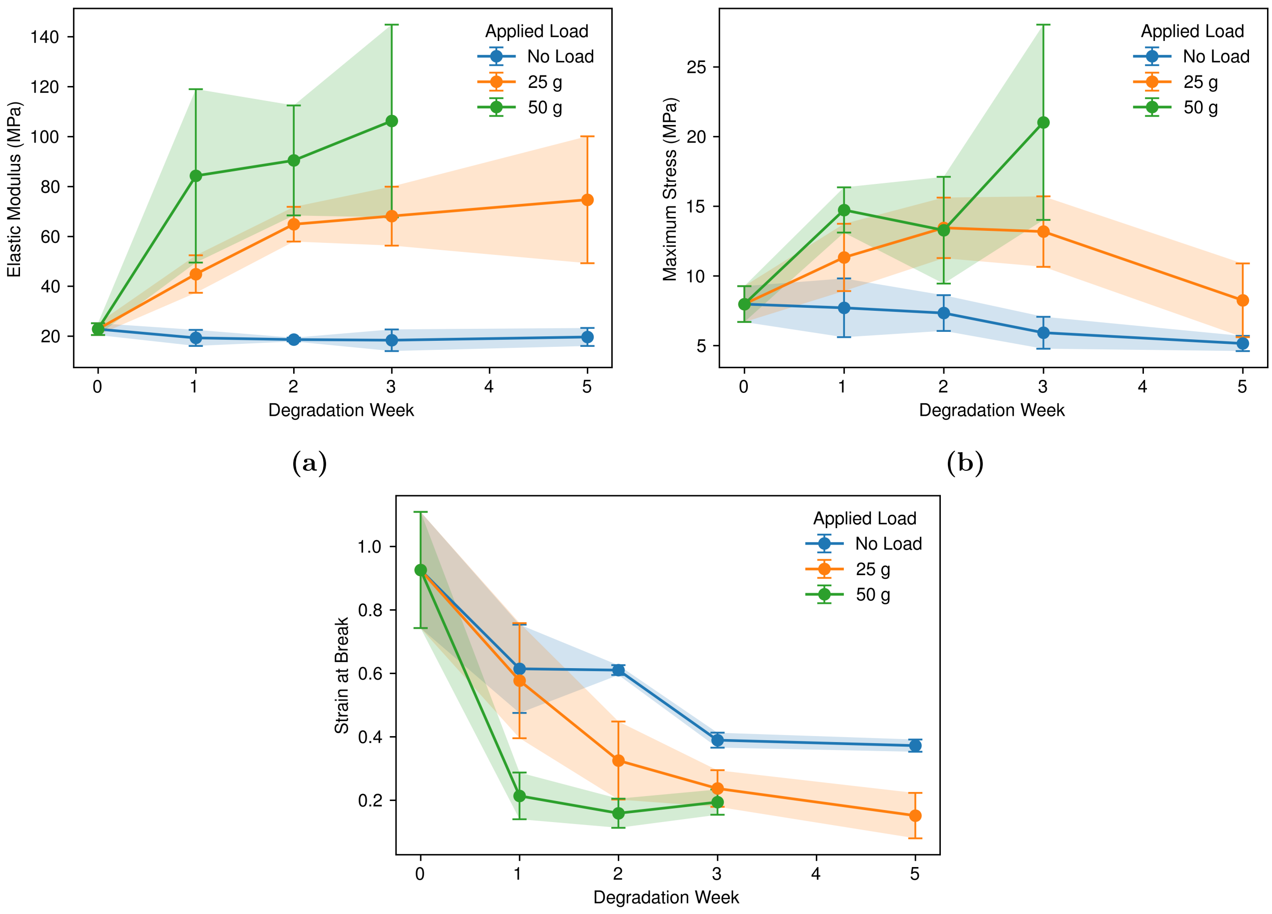

(a)

(b)

(c)

Figure 4.11: (a) Average elastic modulus (E), (b) maximum stress (σ_{max}) and (c) strain at break (ε_{break}). At least 4 filaments were tested per each degradation condition. Data points represent mean values, with shaded regions representing a linear interpolation between the standard deviation for each averaged value. Lines connecting the data points are included as a guide to the eye only and do not represent a fitted model.

Games–Howell post-hoc tests were performed to assess the effect of loading conditions within each degradation time point for elastic modulus, maximum stress, and strain at break, with pairwise comparisons shown in Fig. 4.12. Significant differences were observed only at selected weeks. For the elastic modulus, differences were most consistently detected between unloaded and loaded filaments: no load versus 25 g was significant at all time points, while no load versus 50 g reached significance only in Week 3. No differences were found between 25 g and 50 g at any week. For maximum stress, significant effects were limited to Weeks 1 and 3, with Week 1 showing a difference between no load and 50 g, and Week 3 showing differences between no load and both 25 g and 50 g, while 25 g versus 50 g remained non-significant. For strain at break, no significant load-dependent differences were observed in Weeks 1 or 2, whereas Week 3 showed clear differences between no load and both loaded conditions, with again no significant contrasts between 25 g and 50 g across all weeks.

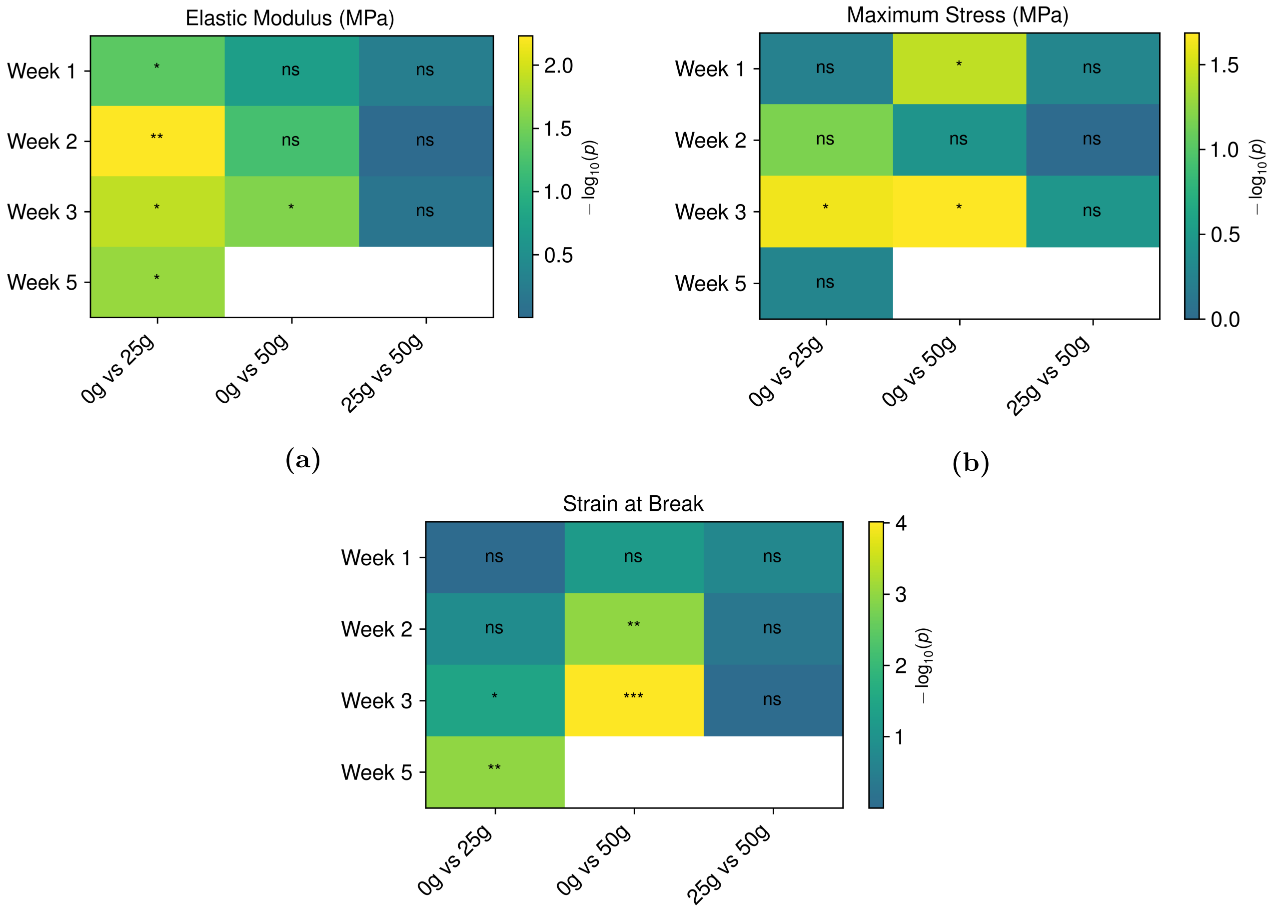

(a)

(b)

(c)

Figure 4.12: Games-Howell pairwise statistical comparison between applied loads at each degradation time point for (a) elastic modulus, (b) maximum stress, and (c) strain at break. Each cell indicates the significance level of each comparison: ns = not significant, *p<0.05, **p<0.01, ***p<0.001.

4.4 Discussion

4.4.1 Microstructure Evolution During Degradation

ES filaments considered in this study were subjected to a pre-stretch ratio of 7 prior to degradation. In our previous work (Ferreira et al., 2025), we have characterised the mechanical behaviour and concurrent microstructure evolution of undegraded, unstretched filaments stretched using bollard grips for nominal strains up to about 11. The filaments were shown to exhibit a viscoelastic-viscoplastic response, with an initial modulus of 6.3 MPa and initial yield stress of 0.8 MPa at 75 mm min^{-1} extension rate, and an increase in hardening rate with the applied stretch. Deformation of the unstretched, undegraded ES filaments involved the progressive alignment of the fibres and the inelastic deformation of the individual fibres themselves, as evidenced by the reduction in fibre diameter measured by SEM at different stretching stages. We attribute the hardening response of the filament to the intrinsic response of the fibres as they align with the loading, involving molecular processes such as plasticity of the crystalline domains, alignment of the polymer chains in the amorphous regions and recrystallisation. In the present work, the filaments were pre-stretched to a nominal strain of approximately 7 before further testing, which is well into the plastic region of the unstretched filaments. As a result, the initial microstructure is already highly anisotropic, consisting of a densely packed network of ES fibres mainly aligned and pre-stretched in the loading direction (Fig. 4.7). As compared to the corresponding unstretched filament, pre-stretching thus increases the apparent modulus, apparent yield stress and hardening capacity.

The microstructure of ES fibres of the same material was recently characterised by Chandler et al. (2025) using a combination of DSC, X-Ray Diffraction (XRD) and Dynamic Mechanical Thermal Analysis (DMTA). These authors proposed that semi-crystalline fibres consist of chain-folded crystals (CFCs) and chain-extended crystals (CECs), whose relative proportions depend on the degree of pre-stretch. A high degree of pre-stretch would increase the proportion of CECs by unfolding of the CFCs and recrystallisation of extended chains in the amorphous domain and unfolded CFC. As a guide for our discussion, we assume in the following that the fibre microstructure of the pre-stretched filaments mainly consists of CEC crystals aligned in the stretching direction, and connected by the pre-extended chains in the amorphous phase (Fig. 4.13).

Based on Fig. 4.13, the mechanical response of the pre-stretched, undegraded filaments (blue curves in Fig. 4.9) can be interpreted as follows. The initially linear response is attributed to the

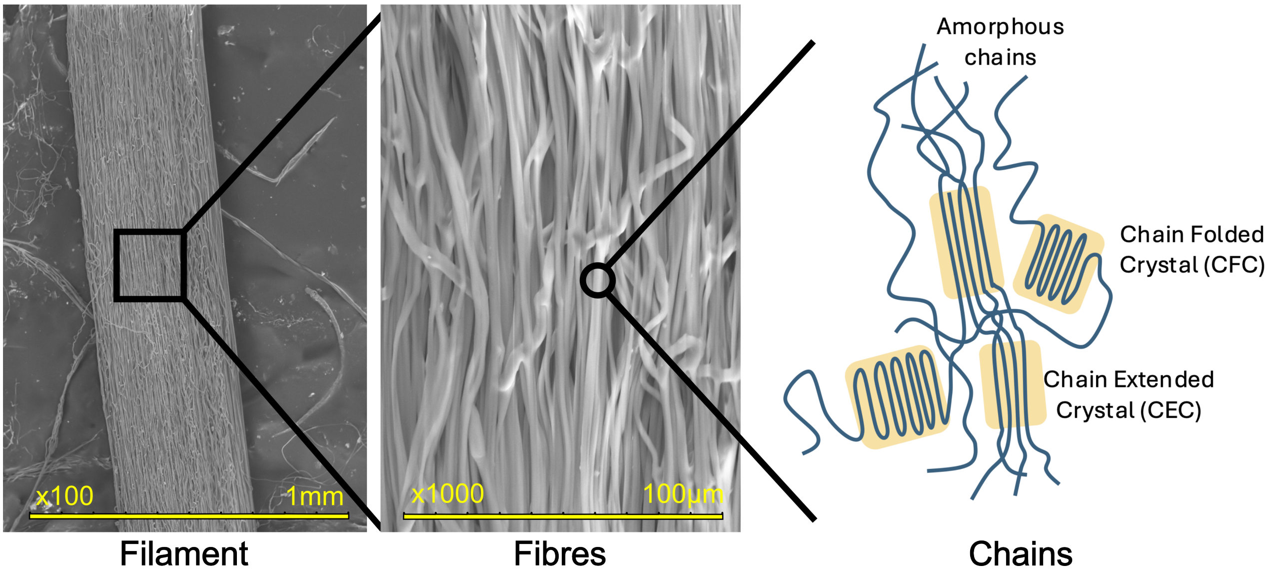

Figure 4.13: Schematic of the semi-crystalline microstructure of the PCL fibres, based on (Chandler et al., 2025).

elastic deformation of the crystalline domains and amorphous regions. The apparent plastic yielding may then be due to the fragmentation or unfolding of CFCs (as proposed by Chandler et al. (2025)) and possibly the plastic deformation by crystallographic slip of the CECs. The moderate hardening could be attributed to the stretching of the chains in the amorphous regions, as they approach their extensibility limit, until failure by chain scission.

Hydrolytic degradation of PCL is generally considered to proceed by bulk erosion at body temperature and neutral pH conditions (Bartnikowski et al., 2019; Pitt et al., 1981a). In particular, Bartnikowski et al. (2019) collected degradation data at physiological conditions from a large number of studies and found that the degradation rate was independent of the construct geometry, indicative of a bulk erosion process. In the present study at 45 °C, the highly porous structure of the ES filaments would promote the fast transport of water into the fibre structure, favouring bulk degradation. Water uptake into the filament involves two physically distinct processes operating on different timescales. First, water floods the open inter-fibre pore network by capillary action, a process that is effectively instantaneous on the timescale of the degradation experiments and ensures that all fibres are rapidly exposed to the aqueous environment. Second, water molecules must diffuse into the solid polymer fibre itself. The timescale for this process can be estimated from the characteristic diffusion time $t \sim r^2/D$, where r is the fibre radius and D is the diffusion coefficient of water in the polymer (Burkersroda et al., 2002). For hydrophobic aliphatic polyesters such as PCL, reported water diffusion coefficients at temperatures in the range 40–50°C are of the order $D \sim 10^{-12} - 10^{-11}$ m^2 s^{-1} (Siparsky et al., 1997). Taking a representative pre-stretched fibre radius of $r \approx 2$ μm, the characteristic time for water to diffuse through the fibre cross-section is estimated at $t \sim r^2/D \approx 4$ s to 40 s. This is many orders of magnitude shorter than the weekly sampling intervals of the degradation experiments, confirming that the fibres are effectively water-saturated at all measurement points, and that water availability within the fibre is not a rate-limiting factor for hydrolytic chain scission. The same argument applies to sample drying prior to testing: water desorption from individual fibres is similarly rapid, though water retained within the pore structure of the filament may require longer to evacuate depending on pore geometry and connectivity. To minimise residual moisture and ensure consistent sample mass, specimens were gently dried with absorbent paper towel and subsequently dried at room temperature for at least one week prior to characterisation.

Consistent with these transport considerations, a significant reduction in molecular weight is observed while both filament and fibre diameters remain approximately constant for samples degraded under no applied load (Fig. 4.8). This behaviour provides further support for a bulk erosion mechanism, although a minor contribution from surface erosion cannot be completely excluded. Furthermore, although both degradation models provide a good description of the experimental data, the improved agreement obtained with Model 2 suggests that the degradation process may involve a degree of autocatalysis (Fig. 4.3a), in line with previous reports in the literature (Pitt et al., 1981a; Pitt and Gu, 1987).

The relatively rapid degradation observed in our study, compared to previous findings on PCL ES sheets by Chung et al. (2012), may be explained by the pre-stretching of the ES filaments. Bolgen et al. (2005) reported that reducing the filament diameter of ES PCL scaffolds increased their degradation rate, owing to enhanced water penetration and a higher surface-area-to-volume ratio. In our case, both pre-stretching and mechanical loading reduce filament diameter and increase the surface-area-to-volume ratio. Stretching of the filament may also promote partial uncoiling of polymer chains, exposing more amorphous regions and facilitating water accessibility to hydrolysable sites along the chains, thereby accelerating the degradation process.

Our DSC results show that degradation is accompanied by an increase in the apparent degree of crystallinity from approximately 50% in the pre-stretched, undegraded state to 60% after 5 weeks of exposure (Fig. 4.5a). It is important, however, to consider the extent to which the degree of crystallinity and ΔH represent the same quantity, particularly in a system where crystallite size and perfection, molecular weight, sample mass, and water content may all be changing simultaneously. The degree of crystallinity is calculated as $K(\%) = \Delta H/\Delta H_0$, where ΔH_0 is the theoretical enthalpy of fusion for a fully crystalline specimen. This ratio is a reliable measure of crystalline fraction only when the sample mass is accurately known, water content is negligible, and crystallite perfection is comparable across conditions. During hydrolytic degradation, each of these assumptions may be violated: preferential loss of amorphous polymer reduces the denominator of the mass-normalised enthalpy; absorbed water contributes to sample mass without contributing to the thermal signal, suppressing the apparent ΔH. Consequently, the observed increase in crystallinity is most reliably interpreted as an increase in the proportion of crystalline material relative to the remaining polymer, rather than a definitive increase in the absolute amount of crystalline phase. Without complementary techniques such as SAXS or WAXS, or gravimetric correction for mass loss and water uptake, it is not possible from DSC data alone to determine whether the total mass of crystalline material increases, remains constant, or decreases during degradation. The increase in melting temperature observed with degradation (Fig. 4.6a) does, however, support the interpretation that ΔH is at least partly associated with the formation of thicker or more thermodynamically stable crystallites, consistent with crystal perfection rather than solely an artefact of mass changes. The more rapid increase in apparent crystallinity during the first two weeks is consistent with preferential degradation of amorphous regions and possible annealing in the presence of water (Lam et al., 2008; Pitt et al., 1981a), while the subsequent slower increase may reflect chain scission enhanced mobility facilitating crystal thickening rather than substantial nucleation of new crystalline domains (Little et al., 2009). Fig. 4.5a also suggests that applied tensile loads enhance recrystallisation, likely through strain-induced chain alignment, with CEC acting as nucleation sites (Chandler et al., 2025).

Overall, the melting temperature increases with degradation time (Fig. 4.6a), which is indicative of recrystallisation into more thermodynamically stable domains (Gaona et al., 2012; Tsuji and Ikada, 1998). This is consistent with an increase in proportion of CEC crystalline domains (Chandler et al., 2025). However, the evolution of melting temperature with degradation under applied loads is non-monotonic, showing an initial decrease after one week of exposure (Fig. 4.6a). The effect is particularly significant for degradation under 50 g load, where the melting temperature drops after one week, before sharply increasing afterwards. It is possible that applied loads initially disrupt the existing crystalline domains, for example by breaking or unfolding of the CFCs, leading to the formation of a less stable and more heterogeneous crystalline structure. Over time, due to a combination of annealing and degradation, mobile chains are able to recrystallise into more stable crystalline domains, as reflected by the sharp rise in both melting and recrystallisation temperatures. However, it is worth noting that only one DSC test was carried out per condition. Further repeats need to be carried out to support these hypotheses.

4.4.2 Effect of Mechanical Loads on Degradation Kinetics

A key finding of this study is that degradation of ES PCL filaments is significantly accelerated in the presence of tensile loads (Fig. 4.3a). Load-enhanced degradation has been reported in other degradable polymers, including poly(lactic acid) (Chen et al., 2026; Vieira et al., 2011) and poly(glycolic acid) (Deng et al., 2005; Guo et al., 2016; Li et al., 2010; Samanta et al., 2025), though direct evidence in PCL remains limited. The acceleration observed here may reflect several concurrent phenomena. The applied tensile load increases the stored elastic energy in the polymer chains, which can lower the activation energy for hydrolytic chain scission, a mechanism described within the framework of mechanochemistry (Akbulatov and Boulatov, 2017; Dong et al., 2024). This effect is expected to be more pronounced in pre-stretched filaments, where loads are more efficiently transferred to the amorphous regions between crystalline domains, where hydrolysis preferentially occurs. Furthermore, mechanical loading may promote water uptake and ingress by increasing free volume within the amorphous phase, thereby increasing the local concentration of water at reaction sites. However, it remains unclear whether the polymer chains are sufficiently stretched to induce bond-level configurational changes, such as bond elongation or angle distortion, required for a force-assisted hydrolysis mechanism to be fully operative.

Regardless of the actual physical mechanism(s) underpinning force-assisted degradation, the effect of applied loads on the reaction rate can be described phenomenologically using an Eyring-type equation (Bell, 1978; Kauzmann and Eyring, 1940):

$$k_\sigma = k \exp\left(\frac{\alpha W}{k_B T}\right) \tag{4.5}$$

where k_σ is the reaction rate in the presence of applied loads, k is the reaction rate in the absence of applied loads, k_B is the Boltzmann constant, T is the absolute temperature, W is the applied load in grams, and α is an empirical parameter. The evolution of the rate constants of Model 2 are represented as a function of the applied load in Fig. 4.14, showing that they follow Eq. (4.5) with $\alpha = 9.6 \times 10^{-23}$ J g^{-1}. Additional degradation studies involving a broader range of applied loads and temperature are however needed to determine the predictive capability of the empirical equation (4.5).

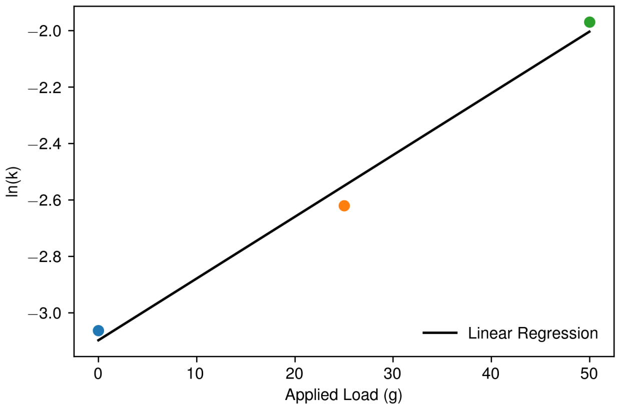

Figure 4.14: Dependence of the reaction rate constant k_2 on the applied load. The continuous line represents the fitting of experimental data with an Eyring-type equation.

4.4.3 Effect of Degradation on Mechanical Properties

For specimens degraded without applied loads, the small initial drop in elastic modulus observed after one week of exposure (Fig. 4.11a) is likely due to the plasticisation effect of water, rather than hydrolytic degradation. For longer exposure times, a slight increase in modulus is observed, which could be the result of recrystallisation and associated change in proportion of CFC to CEC crystalline domains, balancing the effect of degradation in the amorphous phase. The reduction in strain and stress at break (Figs 4.11b and 4.11c) with degradation time may be explained in the following way. As hydrolysis proceeds and long polymer chains are cut in the amorphous regions, the mechanical force transmitted along the fibre concentrates over a smaller number of chains, causing high stretch and premature failure of highly loaded chains by chain scission.

Specimens degrading under an applied load show a clear increase in elastic modulus with the exposure time. We attribute this effect to creep-induced microstructural changes during degradation under load. While the applied loads are smaller than the filament yield stress at room temperature, these loads are sufficient to cause significant creep deformation during degradation at elevated temperature. This can be seen from the reduction in filament diameter in Fig. 4.8a, which suggests that the fibres continue to align in the loading direction during degradation under load, causing a further reduction in the filament porosity. Likewise, the reduction in fibre diameter shown in Fig. 4.8b (see also Table 4.3) indicates that the fibres themselves undergo significant creep deformations during degradation under load. For example, fibres in specimens degraded under a 25 g load for 5 weeks exhibit an average fibre stretch of about 2, as calculated from the reduction in fibre diameters and assuming incompressibility. We hypothesise that fibre creep involves the alignment and stretching of the polymer chains between the amorphous regions, increasing the fibre stiffness. Applied loads could also change the nature of crystallinity, with CECs enabling a more efficient load transfer from extended amorphous chains to the crystalline domains. On the other hand, the increase in overall degree of crystallinity during degradation (Fig. 4.5a) cannot explain the increase in modulus in specimens degraded under load, since it is similar for all three considered loading conditions, and therefore cannot explain the difference in apparent elastic modulus at a given degradation time point (Fig. 4.11a). An increase in CEC fraction could also explain the increase in yield stress, since CECs have a higher resistance to flow. The reduced strain at break and ductile-brittle transition during degradation under load (Fig. 4.11c) could be due to forces concentrating highly-stretched chains between the crystalline domains, causing chain scission. These microstructural changes could themselves be accelerated by force-assisted hydrolytic degradation.

4.5 Conclusion

This work investigated the degradation behaviour of ES PCL filaments, with particular attention to the interplay between hydrolytic degradation and applied loads. In the absence of applied load, a significant reduction in molecular weight is observed after 5 weeks of degradation in PBS at 45 °C, which translates into a reduction in mechanical properties. Tensile loads applied during degradation accelerate the reduction in molecular weight, which is primarily attributed to the uncoiling of the polymer chains under load, facilitating access of water to the reaction sites. Degradation under loads also leads to an increase in elastic modulus and the maximum stress, and to a significant decrease in the elongation at break. These effects are attributed to changes in the semi-crystalline morphology during degradation enabled by the increased mobility of the chains in the amorphous regions. It is also likely that the coupled effects of stress and degradation are amplified by filament pre-stretching after manufacturing. However, the underlying fundamental mechanisms could also be relevant to other polymers and manufacturing processes.

Overall, our findings highlight the need to consider mechanical loads in degradation studies, which impact both the reaction kinetics and the evolution of mechanical properties themselves. Such studies would enable more reliable predictions of mechanical performance and lifetime, which are critical for the design of biomedical implants in load-bearing applications. Future studies are needed to consider cyclic loading conditions over longer exposure times. Degradation studies at other (lower) temperatures are also needed to characterise the temperature-dependence of the rate constants, necessary for the extrapolation of accelerated degradation tests. Mechanistic models with predictive capability are also needed to guide the design of these materials.

4.6 Acknowledgements

The authors acknowledge the support of an EPSRC DPhil studentship at the University of Oxford (TZF), a Future Leaders Fellowship of UK Research and Innovation [MR/W006995/1] (LB, HC) and the Norman Collisson Foundation (PAM). The authors would like to thank Dr Nicholas Hawkins for DSC support, Dr Igor Dyson for mechanical testing and electron microscopy support, and Daisy Crouch for the production of electrospun filaments. The authors are also grateful to Prof. Charlotte Williams from the Department of Chemistry at the University of Oxford for providing access to GPC equipment.

4.7 Appendix A: Experimental Rig

A custom-designed degradation testing rig was developed to simultaneously apply static loads to a large number of ES filaments during degradation in aqueous media. The rig was designed to prevent mechanical interference between samples and maintain central alignment of the loading. Additional motivations included ease of assembly, cost-efficiency through 3D printing, and adaptability for various loading conditions.

Computer-aided design (CAD) illustrations of the rig are shown in Fig. 4.15. The rig features a compact layout (the rig base measures 28 x 28 cm) and includes four peripheral walls and two additional internal pillars. Four vertical pillars, each 36 cm in length, connect the base to the top plate providing ample vertical clearance for each filament elongation within the water bath and weight suspension. The top section mirrors the base in layout but also incorporates an extended outer frame to house the pulley system.

The pulley system transmits load from the static weights to the upper grips via a two-point rolling element setup. This system uses nylon sewing thread, selected for its flexibility, mechanical strength, and resistance to aqueous degradation. The two-point configuration ensures vertical alignment of both the grips and weights, while integrated roller bearings minimise friction and ensure consistent force application throughout the degradation process.

Each side of the rig supports 12 filaments, using 3D-printed, bollard-style grips that were fabricated in two parts due to size limitations of the stereolithography printer. These grips provide secure filament fixation, maintain central loading alignment, and prevent tangling or twisting during testing. Combined with two centrally located support beams, the rig accommodates up to 72 filaments simultaneously. The central beams utilize an overhead pulley system, which spatially separates the weights, avoiding interference between pulley systems.

Mounting the filaments involved the following steps. ES filaments were cut to a standard length of 250 mm and mounted to the bottom bollard-style fixed grips. The free end of each filament was then attached to the unrestricted upper grip. The nylon sewing wire, was carefully looped around the roller-bearings system to prevent inducing any pre-stretching or damage to the filaments. Finally, a 25 g or 50 g weight hook was attached to an open-loop knot at the end of the nylon thread to apply the desired static load.

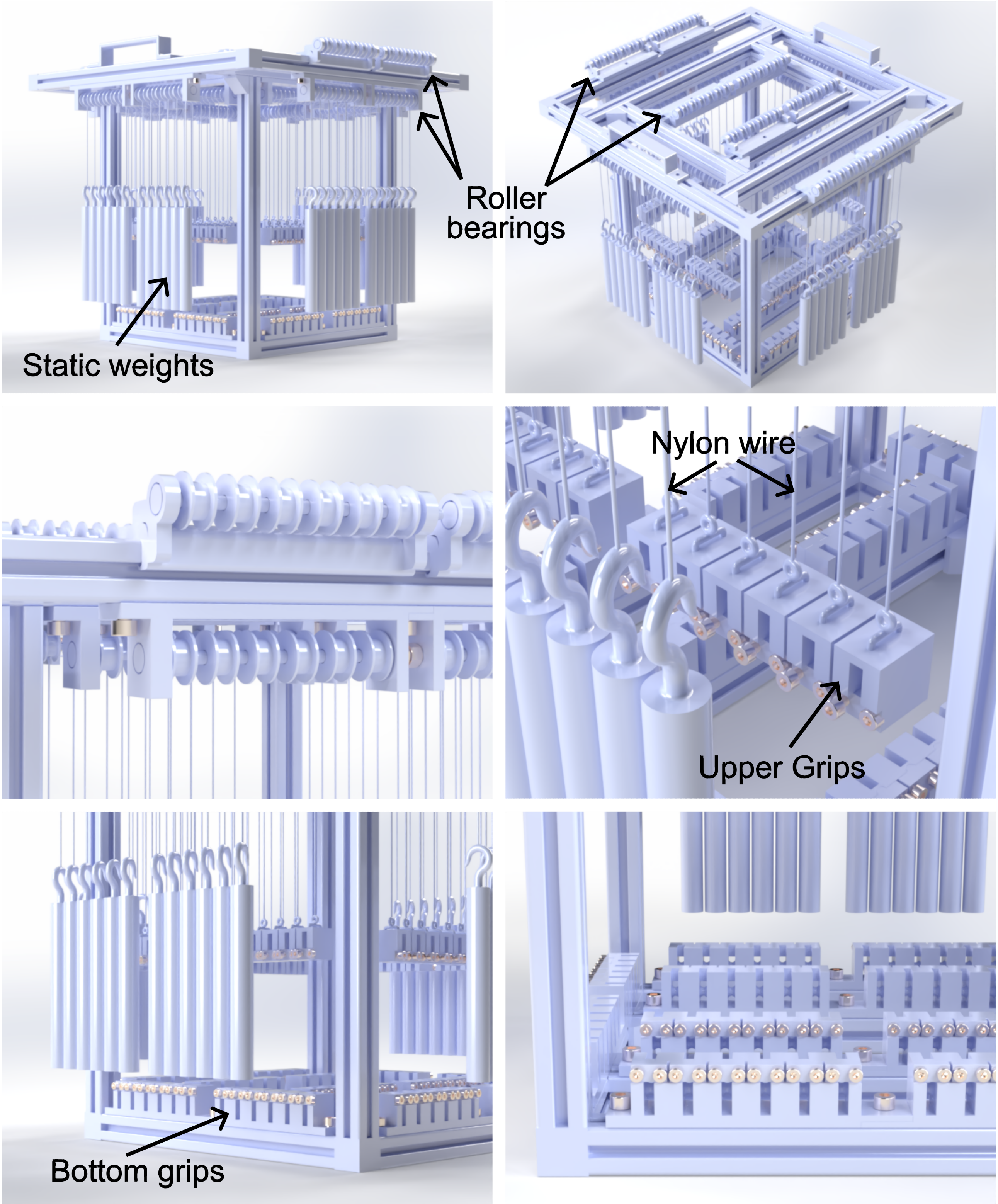

Figure 4.15: Computer-aided design (CAD) illustrations of the custom-designed degradation testing rig for ES filaments.

4.8 Appendix B: Contextualisation of Creep Behaviour Under Applied Load

To interpret the observed creep behaviour during degradation, particularly in relation to the reduction in filament and fibre diameter (Fig. 4.8), it is first necessary to consider the expected mechanical response of the material under comparable loading conditions in the absence of degradation. The applied engineering stresses in the present experiments were estimated as 1.46 MPa and 2.86 MPa for the 25 g and 50 g loads, respectively, assuming an initial filament diameter of 467.08 μm for stress calculations. These stresses remain well below the yield stress of the pre-stretched filament (Fig. 4.9).

Using the linear elastic relation $\varepsilon = \sigma/E$, the instantaneous strain upon loading can be approximated by considering two distinct contributions: filament-scale structural compliance and fibre-scale material deformation. At the filament level, an apparent strain may arise from the straightening, reorientation, and progressive load transfer of initially loose or misaligned fibres within the filament architecture. Approximating this response using the measured apparent elastic modulus of undegraded samples ($E \approx 22.8$ MPa) gives estimated strains of 0.064–0.125 (6.4–12.5%). This suggests that a substantial portion of the initial extension may originate from structural rearrangement rather than intrinsic polymer stretching. At the level of individual fibres, deformation is governed by the bulk mechanical properties of PCL. For dry PCL, the elastic modulus is typically reported in the range $E \approx 210$–440 MPa (Bartnikowski et al., 2019; Labet and Thielemans, 2009), corresponding to an estimated instantaneous strain of approximately 0.007–0.015 (0.7–1.5%) under the applied stresses. This indicates that only limited elastic deformation would be expected within the fibres themselves at these load levels. Extending this analysis using the VE-VP model developed earlier in this thesis (Section 3.4), the predicted creep strains increase to approximately 0.14 and 0.29 for the 25 g and 50 g loads, respectively. These values exceed the purely elastic estimates because the model incorporates time-dependent viscoelastic deformation mechanisms.

The fibres used in this study were pre-stretched by a factor of seven during manufacture, which is expected to reduce subsequent creep through fibre orientation and strain hardening effects (Martins et al., 2015). As shown in the earlier chapter, nominal strains of up to 1100% were sustained during processing from the unstretched state, indicating that further deformation of 10–20% is mechanically plausible through continued structural relaxation and progressive disentanglement within the filament architecture.

Nevertheless, the experimentally observed continuous reduction in both filament and fibre diameter indicates that the measured creep response cannot be attributed to intrinsic viscoelasticity alone. Rather, it reflects the progressive effects of hydrolytic degradation, which reduce molecular weight through chain scission, increase chain mobility, and lower the effective stiffness of the polymer network. In combination with water-induced plasticisation and elevated temperature, these mechanisms promote sustained deformation under constant load. Similar behaviour has been reported in related aliphatic polyesters, where significant strain develops under sub-yield stresses during degradation due to the coupled effects of mechanical loading and hydrolysis (Samanta et al., 2025).

4.9 Appendix C: Stress-strain Curves

Stress-strain curves of undegraded and degraded filaments for each degradation condition and degradation time are presented in Fig. 4.16, including all repeats.

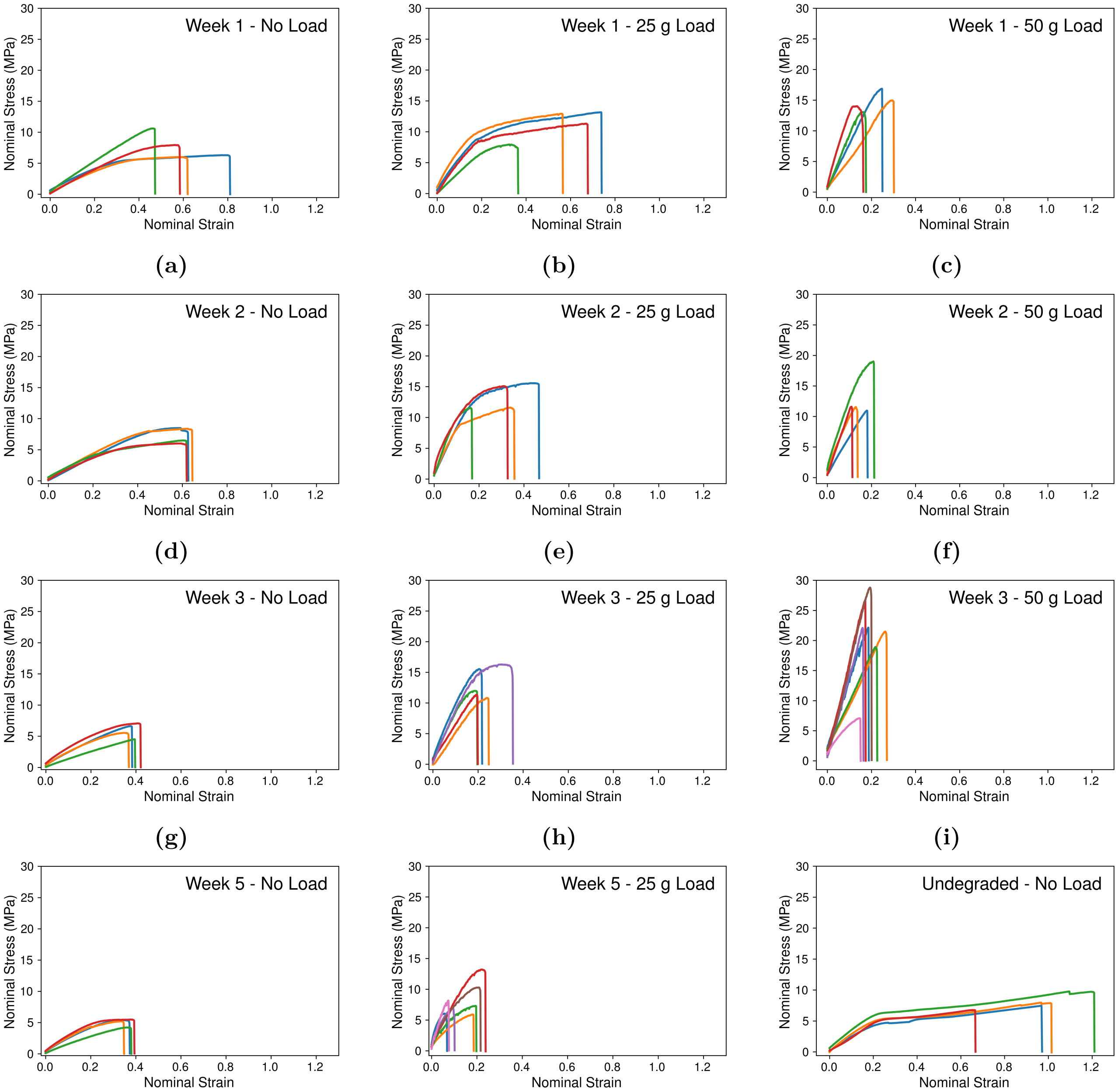

(a) (b) (c)

(d) (e) (f)

(g) (h) (i)

(j) (k) (l)

Figure 4.16: Complete dataset of all mechanical tensile tests conducted at an extension rate of 75 mm min^{-1}. The first column corresponds to filaments degraded under no applied load, the second column corresponds to filaments degraded under a 25 g load, and the third column corresponds to filaments degraded under a 50 g load. Each row corresponds to a different degradation time point (Weeks 1–5). The response of undegraded filaments (Week 0) is shown in Figure 4.16l.

4.10 Appendix D: Experimental Rig Limitations

The testing device is an innovative apparatus designed to evaluate the effect of load on the degradation rate of electrospun filaments. As with any new design, there are several limitations that should be addressed in future iterations to enhance functionality and efficiency.

A primary objective of the design was to maximize the number of samples tested while minimizing spatial requirements and cost. The use of 3D printing enabled innovative configurations that efficiently utilized available space to accommodate multiple filaments. However, this design approach introduced several challenges. For example, the close proximity between samples, particularly at the free-ended grips and weights, increased the risk of sample fracture due to components rubbing against or becoming entangled with one another. This occasionally resulted in combined weights being applied to a single filament. To mitigate this issue, a recommended design improvement is to increase spacing between filaments and reduce the number of samples tested simultaneously.

The process of mounting and dismounting filaments proved to be highly tedious and inefficient. Requiring the removal and reinsertion of 488 bolts significantly prolonged the process, while the delicate positioning of each filament increased the risk of disturbing adjacent samples. Additionally, the design's wiring system posed further complications. Routing the wire connecting the loose-grip to the static weight through narrow gaps demanded careful hand manoeuvring, further reducing efficiency. To improve this, a quick-release or clip mechanism is recommended to enable faster and easier filament handling. Furthermore, designing a modular framework that allows independent access to different sections would greatly enhance usability.

Another limitation involved the need to manage all samples for the entire testing period simultaneously. When removing samples from week one, for example, the entire rig had to be lifted from the tank, samples extracted, and the rig repositioned. This process inadvertently introduced additional stresses to the remaining filaments. Furthermore, each time the rig was re-immersed, the sudden pressure changes caused additional mechanical stresses. To resolve this, future designs should allow for individual sample retrieval on a staggered schedule, enabling samples to be removed without disturbing others.

The device's compact dimensions, with minimal tolerances for space, posed another challenge: the hanging weights obstructed the installation of a surrounding enclosure to minimize water evaporation.

Consequently, water levels required frequent refilling. This process further stressed the filaments, as pouring water into the tank created ripples and cyclic loading conditions. To address this issue, a revised design should incorporate a surrounding box or sealed chamber to reduce evaporation. Alternatively, a drip-feed refill system could be implemented to maintain consistent water levels without causing disruptive fluctuations.

An important enhancement to the current experimental rig would be the integration of a system capable of accurately detecting and quantifying creep in electrospun filaments. Several approaches were considered during the course of this study. One option involved employing a tracking camera system to monitor filament displacement in real time; however, implementing a multi-camera setup capable of independently tracking all 72 filaments was deemed prohibitively expensive and logistically complex. Another approach involved measuring the initial and final lengths of the filaments and calculating creep as the net extension. However, this method was found to be insufficiently accurate, as creep deformation occurs predominantly within the gauge length and may not be reflected in the overall sample length due to grip slippage or unmeasured displacement at the ends. These challenges underscore the need for a more robust and precise creep measurement technique that can be scaled for high-throughput degradation studies without compromising accuracy. Future work should explore digital image correlation (DIC) systems or laser extensometry with automated optical tracking as potential solutions for reliable creep quantification in ES scaffolds.

Addressing these design challenges in future iterations will significantly improve the device's functionality, efficiency, and reliability in testing electrospun filaments.

Chapter 5

Thermo-mechanical characterisation and modelling of hydrolytically degraded electrospun poly(ε-caprolactone) filaments for biological tissue repair.

5.1 Introduction

The long-term performance of biodegradable polymer scaffolds is governed by a delicate balance between mechanical function and progressive molecular degradation under physiological conditions. In Chapter 4, electrospun poly(ε-caprolactone) (PCL) filaments were shown to undergo bulk hydrolytic degradation, manifested by reductions in molecular weight and changes in mechanical behaviour, when exposed to an elevated temperature of 45 °C over a five-week period. While this accelerated study provided evidence that applied tensile loading enhances degradation kinetics and alters mechanical response, several fundamental questions remain unresolved. In particular, it is not yet clear whether similarly measurable hydrolytic degradation occurs under physiological conditions, nor how the viscoelastic properties of electrospun PCL evolve during degradation. Moreover, the previous results revealed an apparent reduction in mechanical stiffness in unloaded filaments despite an increase in crystallinity, an observation that cannot be explained by crystallinity alone and points to a more complex interplay between amorphous degradation and crystalline reorganisation.

These unresolved observations motivated a more detailed investigation into the distinct roles of the amorphous and crystalline phases and their evolving interactions during degradation. Addressing this requires not only extending the degradation study to physiological temperature but also refining the mechanical characterisation methodology to ensure that intrinsic material behaviour is accurately captured. Building on the findings established in Chapter 3, where screw-side grips were shown to provide a more reliable and intrinsic measurement of filament mechanics than bollard-style grips, the present study adopts this improved testing configuration. This approach minimises geometric artefacts during uniaxial deformation, enabling a clearer assessment of degradation-induced changes in viscoelastic and elastic behaviour.

Accordingly, this chapter investigates the hydrolytic degradation of ES PCL filaments under both unloaded and tensile-loaded conditions in phosphate-buffered saline (PBS) at 37°C for up to eight weeks. Experimental characterisation includes molecular weight analysis by gel permeation chromatography (GPC), thermal analysis using differential scanning calorimetry (DSC), morphological assessment by scanning electron microscopy (SEM), and uniaxial tensile testing. The mechanical behaviour is interpreted using an equivalent Maxwell-type viscoelastic model, and the experimental results are further analysed through a micromechanical framework based on the Reuss rule of mixtures to elucidate the evolving contributions of the amorphous and crystalline phases.

5.2 Experimental Methods

The experimental methodology largely follows the protocol established in Chapter 4, with only key deviations and additional procedures specific to the present study highlighted here. First, the polymer solution was prepared using poly(ε-caprolactone) (PCL) resin with a higher weight-average molecular weight, $M_w = 270$ kg mol^{-1} (Ashland Specialities, Ireland), compared to the 175 kg mol^{-1} used previously. Second, electrospun filaments were degraded in phosphate-buffered saline (PBS; Merck, UK) at pH 7.3 and a constant temperature of 37.5°C for up to 8 weeks, under both unloaded conditions and a sustained applied load of 25 g. Prior to characterisation, all samples were dried at room temperature for at least one week to minimise the influence of residual moisture on the measured properties. For thermal analysis, the DSC protocol incorporated a second heating cycle to erase prior thermal history, enabling consistent comparison of thermal behaviour across different degradation times and levels of stretch.

Compared to the methodology described in Chapter 4, the degradation of unloaded filaments was conducted in a separate PBS tank. For each degradation time point, at least twelve electrospun filaments, each cut to a standardised length of 25 cm, were placed inside a petri dish. Each dish was filled with PBS and sealed by nesting it within a slightly larger petri dish, ensuring that the filaments remained fully submerged and stationary during incubation. The interlocked petri dishes were then immersed in the secondary PBS tank, which was maintained at 37.5°C using a commercial temperature controller (Inkbird ITC-308, China). The pH within the petri dishes was not monitored during the degradation period.

The mechanical response of dried electrospun PCL filaments was characterised using an Instron 5582 electromechanical tensile tester (Instron, UK) equipped with a 100 N load cell. In contrast to our previous work in Chapter 4, screw-side grips were used instead of bollard-style grips. This modification introduces several important differences in the measured mechanical response, discussed in Chapter 3. The shorter gauge length associated with screw-side grips reduces the extent of heterogeneous deformation and promotes more rapid engagement of the fibre network during loading, resulting in a more uniform deformation of the microstructure. Moreover, eliminating filament wrapping around a bollard removes geometrically induced stretching, leading to lower measurable strains and a reduced apparent hardening response. Finally, this gripping configuration enables a more direct and accurate assessment of strain-rate dependency, as the measured deformation corresponds purely to axial stretching rather than a combination of stretching, bending, and grip-induced effects. Collectively, these factors provide a more intrinsic characterisation of filament mechanics and allow clearer interpretation of the coupled effects of degradation and strain rate.

For mechanical testing, individual filaments were mounted onto custom cardboard frames using superglue adhesive gel (Loctite, US), with an additional cardboard layer applied to stabilise the specimen and prevent slippage during loading (details of the frame design are provided in Section 3.2.4). The frames were then mounted in the testing apparatus, with a gauge length of 10 mm. Prior to testing, filaments were pre-loaded to 0.1 N to ensure consistent alignment and removal of slack. Uniaxial tensile tests were conducted at room temperature (22 ± 2°C) and environmental humidity conditions (38 ± 5 %). Filaments were tested at three different nominal strain rates (i.e. 0.5, 0.05, and 0.005 s^{-1}) to understand the rate-dependent behaviour of ES PCL. These are equivalent to an extension rate of 300, 30 and 3 mm min^{-1}, respectively. These strain rates were selected to cover a broad range of deformation speeds while remaining within the displacement velocity limits of the testing machine. The nominal strain was defined as $\varepsilon_n = \frac{L-L_0}{L_0} = \lambda - 1$, with L_0 and L the initial and deformed gauge lengths, respectively, and λ the filament stretch. For the filaments degraded without any applied load, the pre-stretched filament diameter was used ($d_0 = 397.67\ \mu m$). For filaments degraded under a 25 g load, the average diameters for Weeks 1, 2, 4, 6, and 8 were 286.35, 273.29, 264.03, 242.18, and 243.93 µm, respectively (Table 5.2). For each loading condition and time period, a minimum of four samples were tested, and the force (N), elongation (mm) were recorded as a function of time. The apparent elastic modulus was calculated by fitting a linear regression to the initial linear portion of each stress-strain curve. To ensure consistency across strain rates, a minimum number of data points was required to define the linear region (x_{min} = 10, 100, and 400 points for 0.5, 0.05, and 0.005 s^{-1}, respectively). Within this window, the linear region was iteratively optimised until a coefficient of determination of at least $R^2 = 0.90$ was achieved, ensuring a robust and reproducible estimate of the apparent elastic modulus.

5.3 Experimental Results

5.3.1 Degradation Tests

Figure 5.1a shows the evolution of the number-average molecular weight (M_n) of ES PCL filaments over the 8-week degradation period under both unloaded and loaded conditions. In the undegraded state, the filaments exhibit an initial molecular weight of $M_n = 192$ kg mol^{-1} with a dispersity Đ of 1.39. As degradation progresses, M_n decreases steadily with time. Despite the relatively short exposure duration, the reduction in molecular weight is substantial at 37.5°C in PBS. The rate of molecular weight loss is higher in samples degraded under load: after 8 weeks, unloaded specimens show a 10.5% reduction in M_n, while those subjected to a 25 g tensile load show a 14.4% decrease. Figure 5.1a also includes model fits obtained using Eqn. (4.3). The fitted rate constants and corresponding R^2 values are summarised in Table 5.1. Overall, the model provides a good representation of the experimental data for both loading conditions, capturing an exponential decay trend in the hydrolytic degradation in PCL. The evolution of dispersity is shown in Fig. 5.1b. For the unloaded condition, the dispersity increases gradually, whilst under applied load, the dispersity increases more rapidly.

Table 5.1: Rate constants for model (Eqn. (4.3)) fitted on the experimental data.

	k (weeks^{-1})	R^2(%) of k
0 g	0.0137	95.8
25 g	0.0205	98.6

5.3.2 Thermal Properties

The DSC thermograph of an undegraded ES PCL filament is shown as the solid black line in Fig. 5.2a. Melting initiates at 55.4°C, with a peak at 59.0°C, followed by a recrystallisation event upon

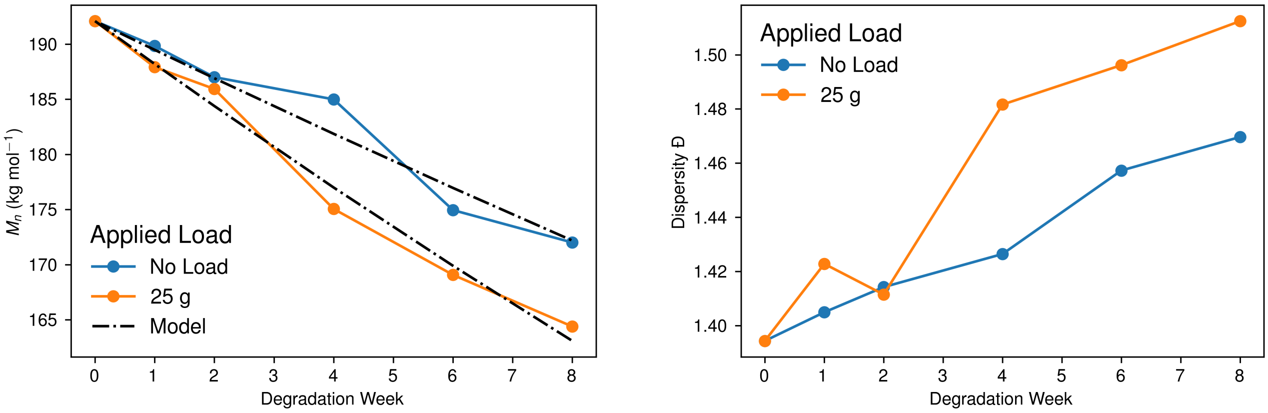

(a) **(b)**

Figure 5.1: (a) Evolution of the number-average molecular weight (M_n) of electrospun PCL filaments as a function of degradation time under unloaded and loaded conditions. Dashed-dot line represents model fit. (b) Evolution of the dispersity (Đ) over the same degradation period. Colourful lines connecting the data points are included as a guide to the eye only and do not represent a fitted model.

cooling at approximately 33.4°C (data not shown). Figure 5.2a also presents the melting behaviour of filaments subjected to degradation under both unloaded and mechanically loaded conditions. Compared to the undegraded sample, the degraded filaments exhibit melting peaks with varying shapes and magnitudes. However, a general trend is observed: the endothermic melting peaks tend to increase in height, narrow in width, and shift slightly to higher temperatures with increasing degradation time.

All samples underwent a double melt–recrystallisation cycle. The melting response during the second heating cycle is shown in Fig. 5.2b. For the undegraded sample, the second-cycle melting peak is noticeably reduced, occurring at 55.7°C. Correspondingly, the degree of crystallinity decreases from 51.6% in the first cycle to 30.8% in the second. Following the first melt, effectively erasing the thermal history of the polymer, all samples display similar thermal behaviour: a gradual increase in heat flow, a sharp melting peak, followed by a decline in heat flow and steady plateau.

Figure 5.3 presents the evolution of crystallinity and melting temperature as a function of degradation time, under different applied loads and heating cycles. For the melting crystallinity (Fig. 5.3a), the results from the first heating cycle show a clear increase in crystallinity with increasing degradation time. Furthermore, applied load enhances this effect, with loaded filaments exhibiting higher crystallinity compared to unloaded controls. In contrast, after erasing the material history in the second heating cycle, crystallinity also increases over time (from approximately 30% to 40%), but the effect of applied load is no longer apparent. A similar trend is observed for the melting temperature (Fig. 5.3b). During the first cycle, the melting temperature increases from 59°C to 59.6°C over 8 weeks of

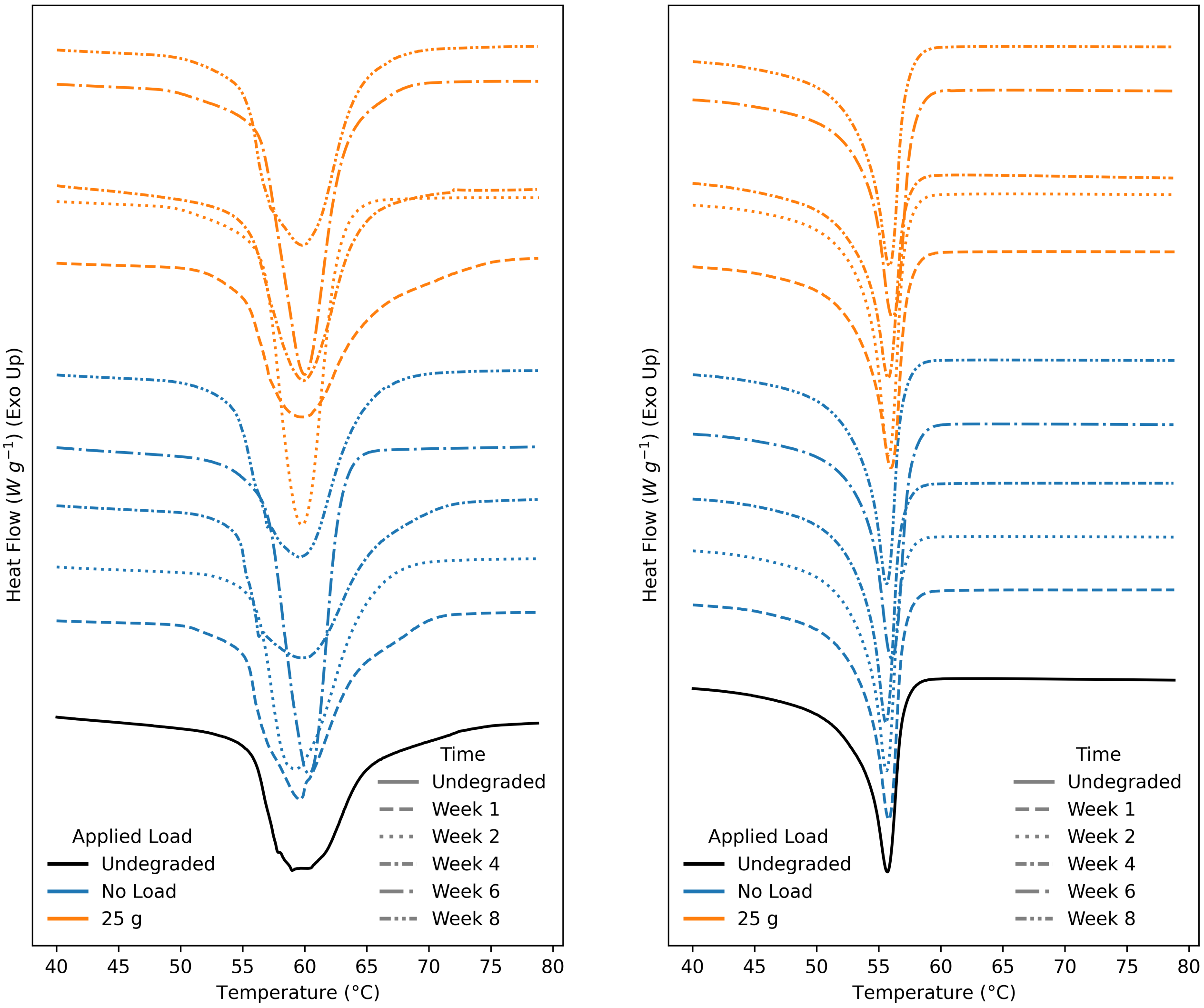

(a) **(b)**

Figure 5.2: DSC thermographs of electrospun PCL filaments after different exposure times and applied loads, showing: (a) melting peaks during the first heating cycle and (b) melting peaks during the second heating cycle.

degradation, although reaching a maximum of 60.3°C at Week 6. Applied load further elevates the melting temperature relative to unloaded samples, reaching a maximum of 60.4°C. However, during the second cycle, the melting temperature remains relatively stable across the degradation period.

5.3.3 Microstructural Characterisation

Figure 5.4 presents representative SEM micrographs of undegraded filaments, alongside a higher-magnification image detailing the fibre morphology. The low-magnification micrograph (Fig. 5.4a) shows a uniform, continuous filament composed of fibres tightly aligned along the longitudinal axis, with no visible defects or surface irregularities. The high-magnification image (Fig. 5.4b) reveals smooth and continuous fibres with consistent diameters, forming a densely packed and interconnected network with small pore sizes. No evidence of fractured or flattened fibres is observed; however, occa-

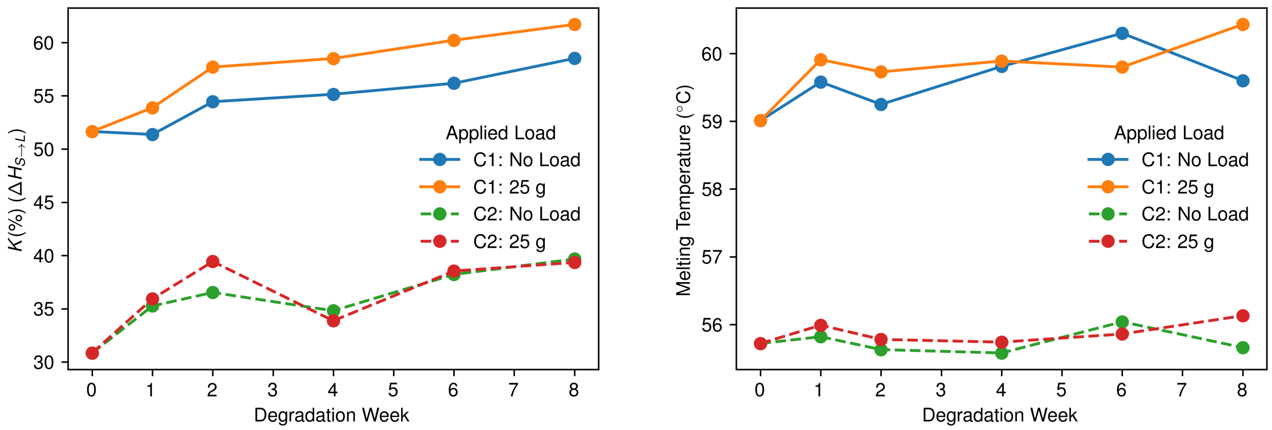

(a) **(b)**

Figure 5.3: (a) Degree of crystallinity calculated based on $\Delta H_{S\to L}$ and (b) evolution of melting temperature as a function of degradation time and for different applied loads. C1 and C2 refer to cycles 1 and 2, respectively.

sional fibre necking and limited fibre fusion are apparent, arising from the drawing process (Chandler et al., 2025).

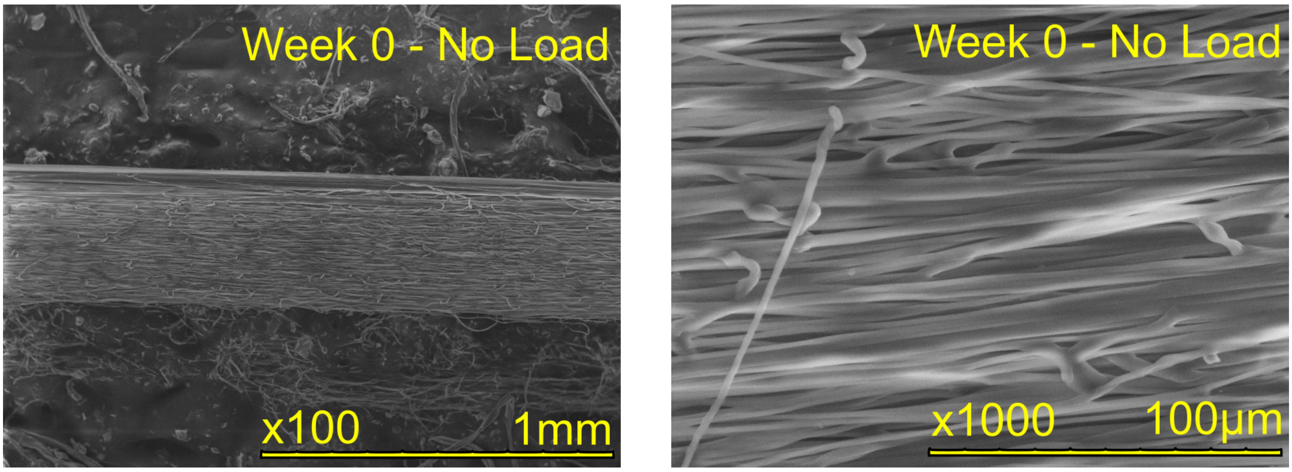

(a) **(b)**

Figure 5.4: SEM micrographs exhibiting the surface topology of pre-stretched undegraded filaments.

Figure 5.5 presents SEM micrographs of filaments subjected to different degradation durations and applied loads. Across all conditions, the electrospun morphology largely retains its characteristic anisotropic, porous, and densely packed fibrous architecture. With increasing degradation time, fibre coalescence becomes progressively more evident in both unloaded and loaded samples. However, distinct morphological differences emerge between the two conditions. In the unloaded filaments, degradation is accompanied by the appearance of surface cracks in sections of the filament surface, first noticeable at Week 4. In contrast, filaments degraded under applied load exhibit early fibre fusion, visible from Week 1, resulting in a denser and more continuous morphology.

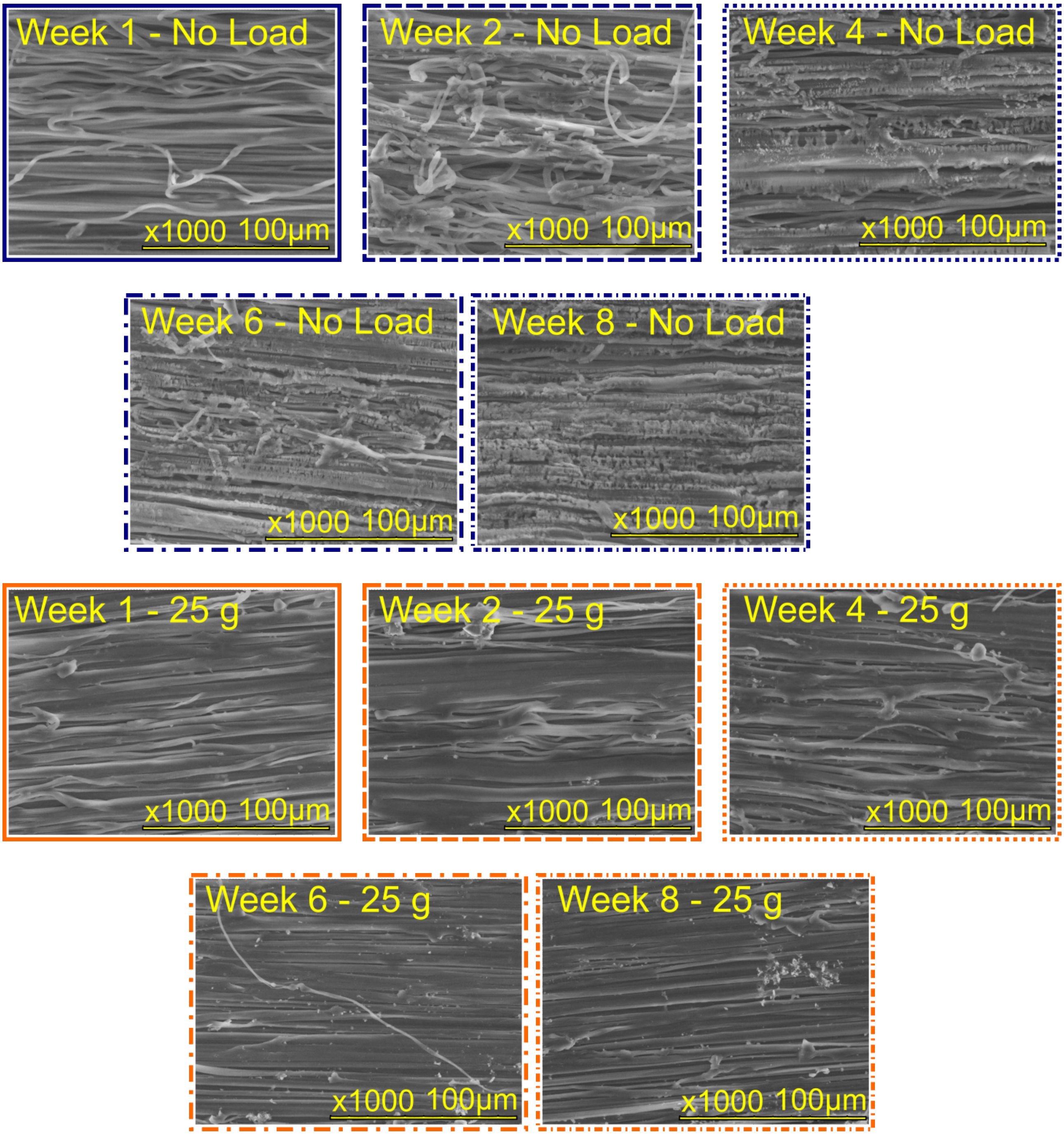

Figure 5.5: Representative SEM micrographs for each degradation time and applied load. Applied load colour scheme: blue is no applied load and orange is 25 g applied load.

Filament diameters were measured across all degradation conditions are presented in Fig. 5.6, with the corresponding numerical data summarised in Table 5.2. It should be noted that ES filaments are not perfectly cylindrical; their cross-section are often flattened due to the electrospinning collection and stretching process. Measurements correspond to the width of the flatter side of the filament rather than a true diameter of a circular cross-section. For samples degraded under no applied load, the apparent filament diameter gradually decreased over time while maintaining a relatively constant standard deviation throughout the degradation period. In contrast, samples subjected to constant mechanical loading exhibited a more pronounced and progressive reduction in filament diameter with increasing degradation time. This reduction is indicative of creep deformation occurring under load, characterised by axial elongation of the filaments accompanied by lateral contraction. These findings are consistent with our previous observations that mechanical stretching of electrospun PCL filaments results in a decrease in filament diameter (refer to Section 3.3.5).

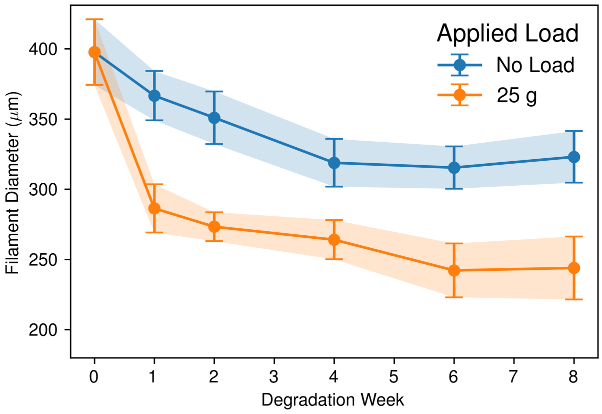

(a)

Figure 5.6: Evolution of the filament diameter with degradation time and for different applied loads. Diameters were calculated based on SEM micrographs. Shaded area represents a linear interpolation between the standard deviation for each averaged value.

Table 5.2: Filament diameter.

	Filament Diameter (μm)	
	No Load	25 g
Week 0	397.67 ± 23.45	-
Week 1	366.60 ± 17.54	286.35 ± 17.22
Week 2	350.94 ± 18.74	273.29 ± 10.31
Week 4	318.82 ± 17.01	264.03 ± 13.97
Week 6	315.38 ± 15.08	242.18 ± 19.14
Week 8	323.04 ± 18.34	243.93 ± 22.43

5.3.4 Mechanical Properties

Representative stress–strain curves of electrospun PCL filaments degraded under no applied load are shown in Fig. 5.7a. Each curve corresponds to a representative specimen tested at a strain rate of 0.05 s^{-1}, selected from four independent tensile tests (refer to Section 5.7 for complete stress–strain data). The undegraded filament (Week 0) exhibits an initial linear elastic region, followed by plastic deformation with mild strain hardening prior to fracture, consistent with previous findings in Chapter 3. In contrast, degraded samples (Weeks 1–8) display a mixed linear-nonlinear response with no evident plateau. With the exception of Week 1, the curves show a decrease in the elastic modulus relative to the undegraded state, while both the maximum stress and strain at break progressively decline with increasing degradation time. Under an applied static load of 25 g (Fig. 5.7b), the filaments exhibit a higher elastic modulus and maximum stress but a reduced strain at break with increasing degradation time.

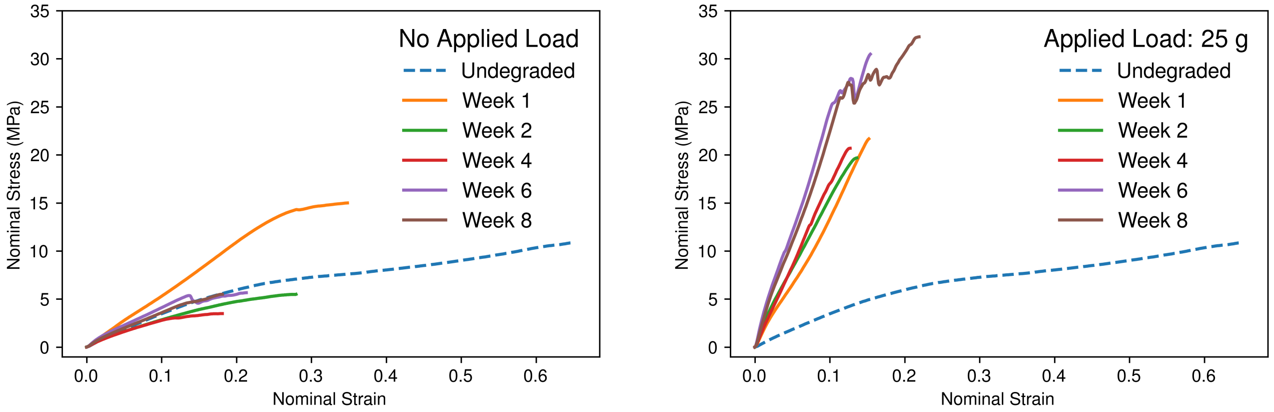

(a) **(b)**

Figure 5.7: Representative nominal stress–strain curves of electrospun PCL filaments degraded for different durations under (a) no applied load and (b) a constant 25 g load. Tests were performed at an extension rate of 30 mm min^{-1} (equivalent to a strain rate of 0.05 s^{-1}). The dashed line represents the undegraded (Week 0) sample.

The evolution of the average elastic modulus is shown in Figs. 5.8a and 5.8b, together with the standard deviation calculated from at least four specimens for each strain rate (i.e. 0.005, 0.05, 0.5 s^{-1}). For filaments degraded under no applied load, the modulus increases slightly after the first week of exposure, followed by a modest decrease in subsequent weeks; however, the overall variation remains relatively small. By contrast, filaments degraded under applied load show a clear and continuous increase in apparent modulus with degradation time. The evolution of the maximum stress is presented in Figs. 5.8c and 5.8d. For unloaded specimens, the maximum stress decreases with degradation time. By comparison, filaments degraded under a 25 g load exhibit a different trend: an initial sharp increase in maximum stress, followed by a gradual rise and then a slight decrease in the final week. The elongation at break is shown in Figs. 5.8e and 5.8f. In both loading conditions, the strain at break decreases with increasing exposure time. The effect of applied load accelerates this reduction; however, the values appear to plateau between 0.1 and 0.2 strain after extended degradation.

Figure 5.8a shows strain rate dependence: higher strain rates correspond to higher modulus values, while lower strain rates result in lower modulus values. For loaded samples (Fig. 5.8b), the same general trend is evident, although an exception arises at the intermediate strain rate (0.05 s^{-1}), where the average elastic modulus exceeds that of samples tested at 0.5 s^{-1} strain rate. For the maximum stress (Figs. 5.8c and 5.8d), the strain rate hierarchy follows the expected trend, with higher strain rates leading to higher maximum stress. In contrast, for strain at break (Fig. 5.8e), specimens tested at higher strain rates fractured earlier than those tested at lower strain rates. For loaded filaments (Fig. 5.8f), however, the viscous effect is less clear, as the averaged results overlap considerably. Nonetheless, in all cases, the results remain within the range of one standard deviation.

To further examine rate-dependent behaviour, the mechanical properties are plotted as a function of strain rate for each degradation week, as shown in Fig. 5.9. Under no load (Fig. 5.9a), the elastic modulus exhibits an increasing trend with greater strain rates. In contrast, for the applied load condition (Fig. 5.9b), the modulus remains comparatively insensitive to strain rate, with only minor variations and some scatter across weeks. For the maximum stress, the no-load condition (Fig. 5.9c) shows a slight increase with strain rate at early degradation stages, although this trend becomes less distinct at later weeks, where increased variability is observed. Under applied load (Fig. 5.9d), the maximum stress exhibits only a weak dependence on strain rate. A similar trend is observed for the strain at break (Figs. 5.9e and 5.9f), which generally decreases slightly with increasing strain rate for both loading conditions, suggesting a transition towards more brittle behaviour at higher rates.

The mechanical properties show increasing variability with degradation time. Variability in the mechanical response of the undegraded and unstretched ES filaments has been previously reported in Section 3.3.4 in Chapter 3, reflecting inherent heterogeneity in the electrospinning process and manifesting particularly in the maximum stress and strain at break. Our earlier work demonstrated that filaments are prone to inhomogenous axial deformations (i.e. necking). In the present study, additional differences may arise from the post-processing filament drawing, which can alter the degree of pre-stretch and further increase specimen-to-specimen variability. Nevertheless, Fig. 5.8 shows little variability in unloaded samples, but in the case of loaded samples, the variability progressively increases with degradation time.

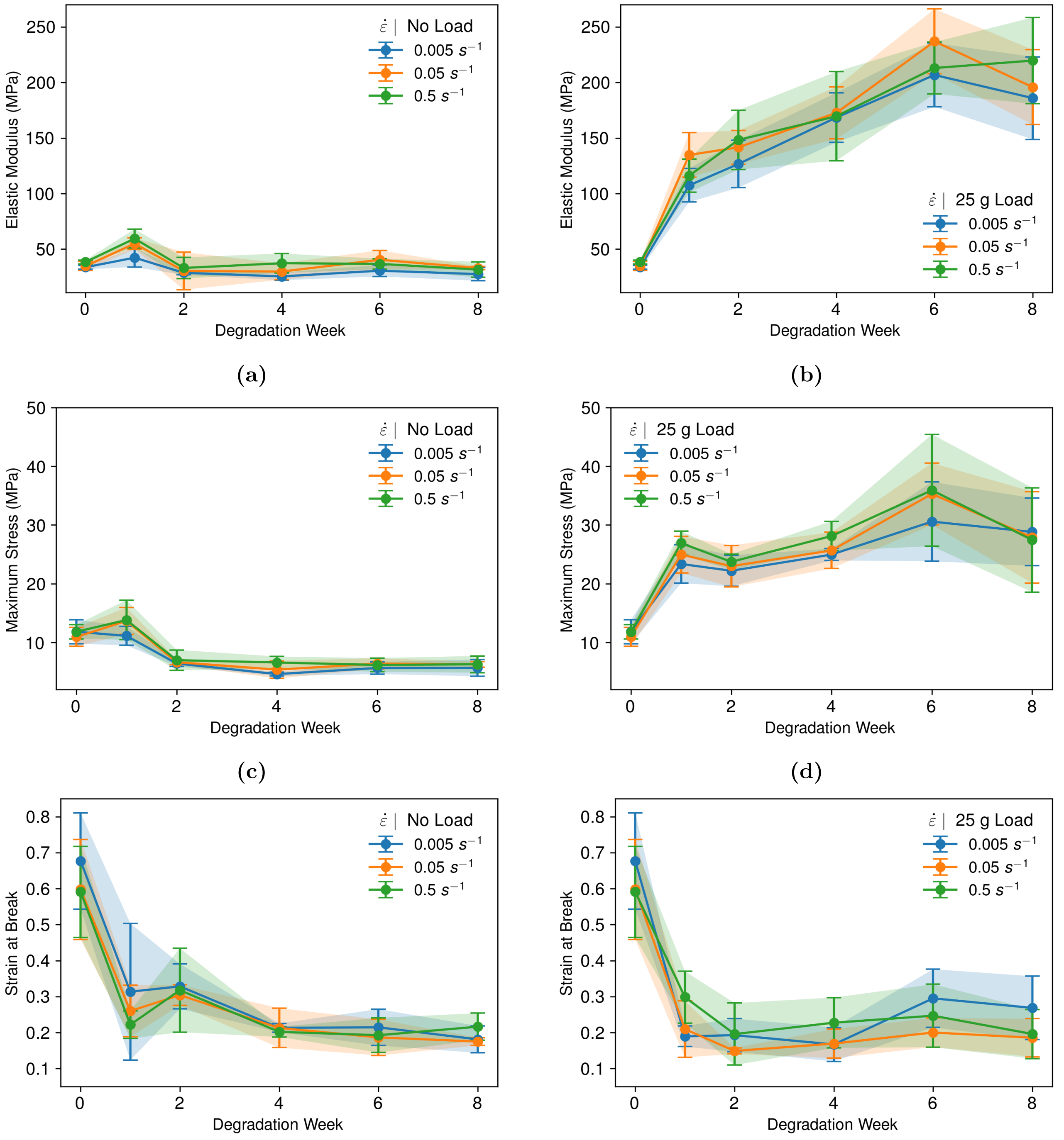

(a) (b) (c) (d) (e) (f)

Figure 5.8: Row 1: Average apparent elastic modulus (a) no load and (b) 25 g applied load. Row 2: Average maximum stress (σ_{max}) for (c) no load and (d) 25 g applied load. Row 3: Average strain at break (ε_{break}) for (e) no load and (f) 25 g applied load. At least 4 filaments were tested for each degradation condition. All values are derived from nominal stress–strain measurements.

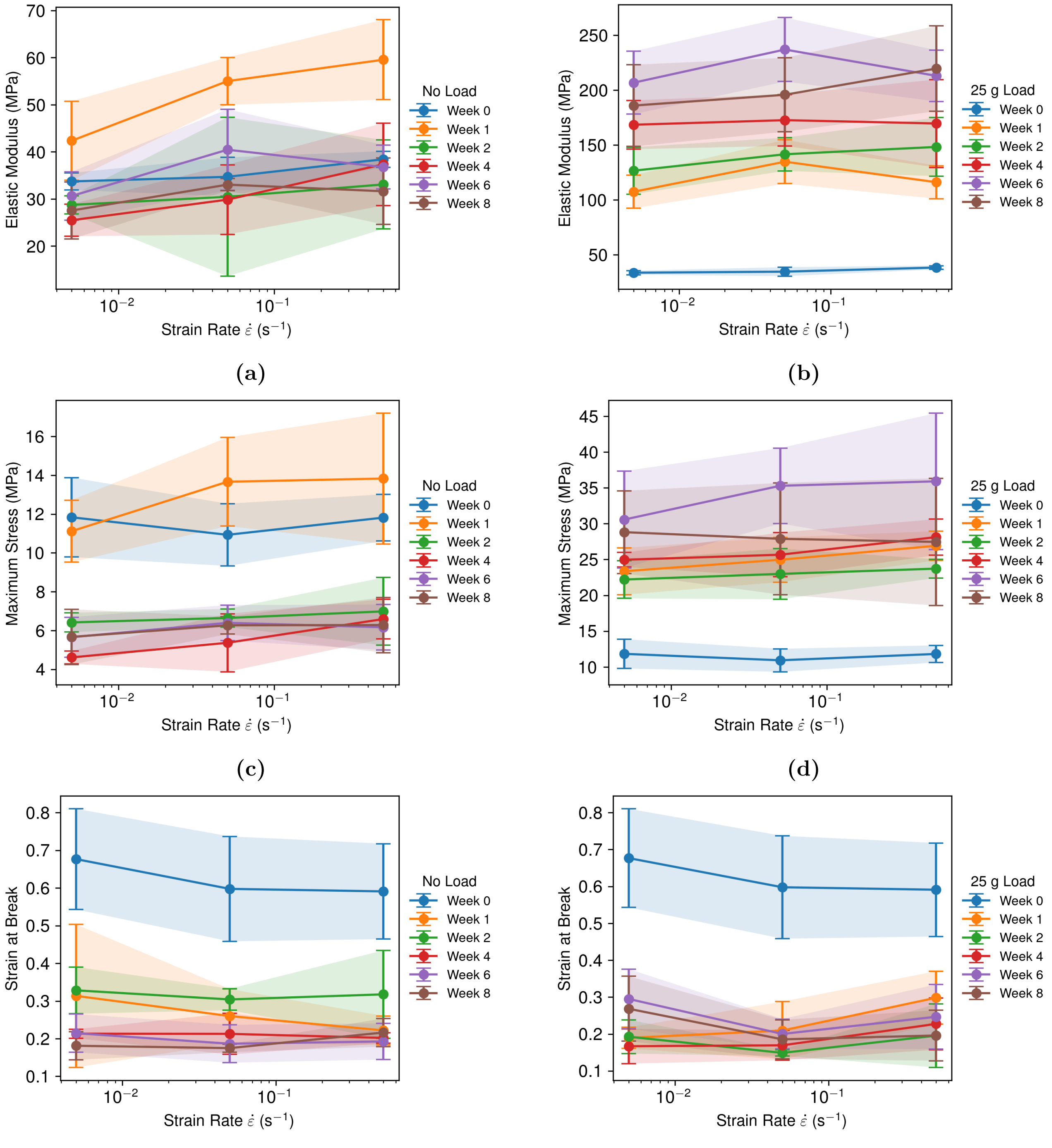

(a) (b) (c) (d) (e) (f)

Figure 5.9: Mechanical properties as a function of strain rate for electrospun PCL filaments at different degradation weeks. Elastic modulus (a, b), maximum stress (c, d), and strain at break (e, f) are shown for unloaded (left) and 25 g loaded (right) conditions. Markers indicate mean values and shaded regions represent a linear interpolation between the standard deviation of each value.

5.4 Phenomenological model

5.4.1 Viscoelastic Constitutive Framework

In this work, we propose a rate-dependent constitutive model to describe the mechanical response of electrospun PCL filaments. A pre-stretched filament may be idealised as a bundle of highly aligned individual fibres, such that, under applied stress, load is efficiently transferred along the filament axis. At the microscale, the mechanical response of these fibres is governed by the semi-crystalline morphology of PCL, in which load-bearing crystalline domains are interconnected by deformable amorphous regions. The relative contributions of these phases, together with their distinct deformation and relaxation mechanisms, collectively determine the macroscopic stress–strain behaviour of the filament. Consistent with this microstructural interpretation, the stress–strain curves in Fig. 5.7 exhibit mixed linear–nonlinear characteristics that reflect both instantaneous elastic deformation and time-dependent relaxation. To capture this combined response in a minimal yet physically motivated manner, a simple viscoelastic framework consisting of a Maxwell-type element is adopted, as illustrated in Fig. 5.10.

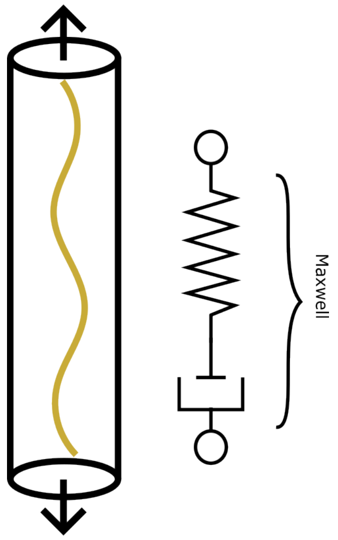

Figure 5.10: 1D representation of fibre as a constitutive model represented as one equivalent Maxwell element.

For simplicity, the model is formulated in one dimension, consistent with the filament geometry and uniaxial loading conditions. Since the individual moduli of the amorphous and crystalline phases are not directly known, their combined elastic response is represented by a single effective spring. The Maxwell element obeys the following constitutive relations:

$$\sigma_s = E\varepsilon_s, \quad \sigma_d = \eta_d \dot{\varepsilon}_d \tag{5.1}$$

where σ_s and σ_d are the stresses in the spring and dashpot, respectively, E is the effective elastic modulus, ε_s is the spring strain, η_d is the dashpot viscosity, and $\dot{\varepsilon}_d$ is the dashpot strain rate. In the Maxwell configuration, both elements experience the same stress ($\sigma = \sigma_s = \sigma_d$), while the total strain is the sum of the spring and dashpot contributions ($\varepsilon = \varepsilon_s + \varepsilon_d$). Differentiating this relationship yields the governing equation for the Maxwell model:

$$\dot{\varepsilon} = \frac{\dot{\sigma}}{E} + \frac{\sigma}{\eta_d} \tag{5.2}$$

5.4.2 Model Validation and Calibration

All results are presented in terms of true stress and strain rather than nominal values. The experimental data was corrected such that the true strain, ε, was calculated from the nominal strain, ε_n, using $\varepsilon = \ln(1 + \varepsilon_n)$, while the true stress, σ, was obtained from the nominal stress, σ_n, through $\sigma = \sigma_n \frac{\lambda}{J}$, where λ is the stretch and J represents the volume change. The latter was determined from an empirical relationship previously derived for electrospun PCL filaments in the unstretched configuration in Section 3.4.2, expressed as $J = \lambda^{0.45}$. This power-law formulation is multiplicatively homogeneous, meaning that the same $J(\lambda)$ expression remains valid for pre-stretched filaments, as the deformation gradient and its determinant compose multiplicatively across configurations. The nominal strain rate was also converted to the true strain rate using $\dot{\varepsilon} = \dot{\varepsilon}_n/(1 + \varepsilon_n)$, ensuring that both stress–strain and rate-dependent analyses were performed within a fully consistent true kinematic framework.

Model predictions were compared to a representative experimental true stress–strain curve selected for each strain rates of 0.5, 0.05, and 0.005 s^{-1} for each degradation week and loading condition, shown in Figs. 5.11 and 5.12. For the undegraded, unloaded filaments in Fig. 5.11a, the single Maxwell element underestimates the initial elastic modulus and overestimates the relaxation contribution, resulting in a mismatch between the predicted and experimental curve shapes. In this case, the model reproduces the overall trend of increasing stress with strain but does not reproduce the non-linearity observed experimentally. At Week 1 (Fig. 5.11b) under no applied load, the agreement between model and experiment improves. The Maxwell model reproduces both the rate dependency and the general shape of the stress–strain curves, with particularly good agreement at the lowest strain rate of 0.005 s^{-1}. For subsequent degradation weeks (Weeks 2, 4, 6, and 8), the unloaded filaments exhibit increasingly linear stress–strain responses. Consistent with this behaviour, the Maxwell model reproduces the dominant linear trend and provides a reasonable approximation across all strain rates.

Small deviations are observed, with the response being occasionally under- or over-estimated relative to the experimental curves. Across these weeks, the model predictions remain largely linear and do not exhibit pronounced curvature or a relaxation plateau within the strain range tested.

For filaments degraded under a 25 g applied load shown in Fig. 5.12, a similar overall level of agreement is observed between model predictions and experimental data. The model reproduces the increased stiffness and maintains consistency across strain rates for most degradation weeks. At Weeks 6 and 8 (Figs. 5.12d - 5.12e), the experimental curves at lower strain rates exhibit more noticeable stress relaxation, which manifests as increased curvature relative to earlier weeks. While the single Maxwell element does not fully reproduce this curvature, the optimised parameters allow the model to approximate the experimental response within the tested strain range. Overall, the model provides a consistent representation of the early elastic response and reproduces the monotonic tensile behaviour observed across degradation time, strain rate, and loading condition.

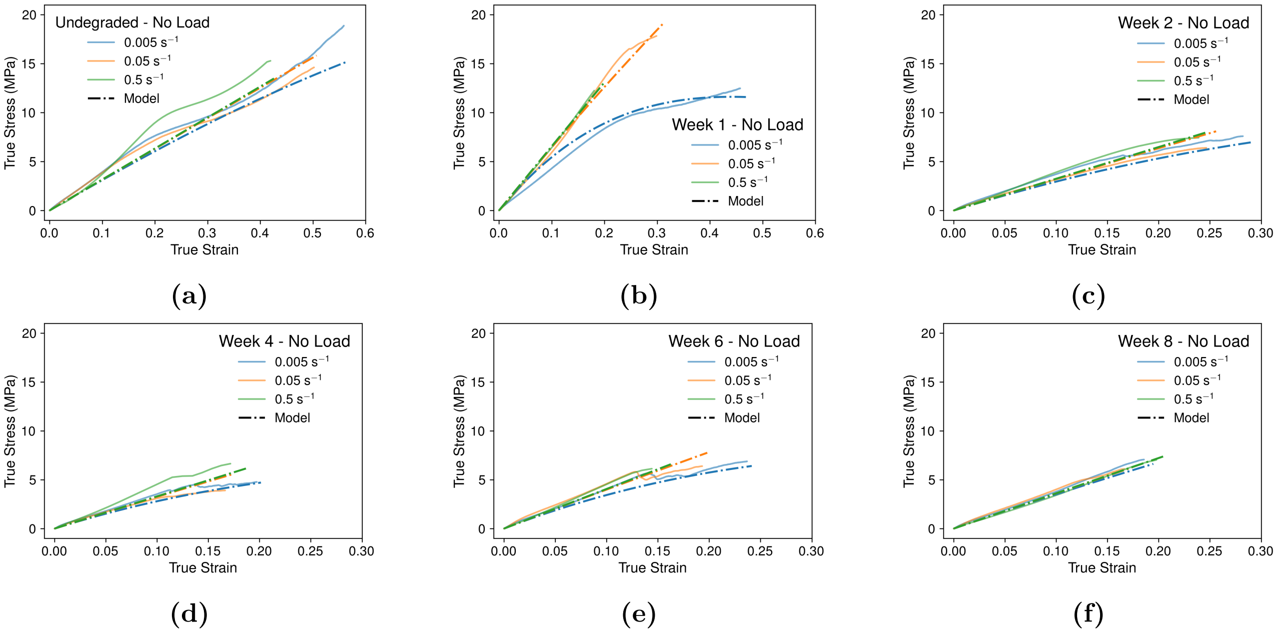

Figure 5.11: Maxwell element model fit to true stress–strain responses of unloaded filament specimens tested at strain rates of 0.005, 0.05, and 0.5 s^{-1}. Each subplot presents representative experimental curves and corresponding model predictions for degradation times of Weeks 0, 1, 2, 4, 6, and 8.

The Maxwell model was implicitly calibrated using the true stress–strain data, with the elastic modulus (E) and viscosity parameter (η_d) optimised via a non-linear least-squares routine in Python (SciPy) across all experimental repeats for each degradation week and loading condition. More specifically, for a given week, the Maxwell model was evaluated for each dataset using a forward integration scheme, generating a predicted stress response for an initial pair of parameters (E, η). The residuals were defined as the point-wise differences between the modelled and experimental stresses for every

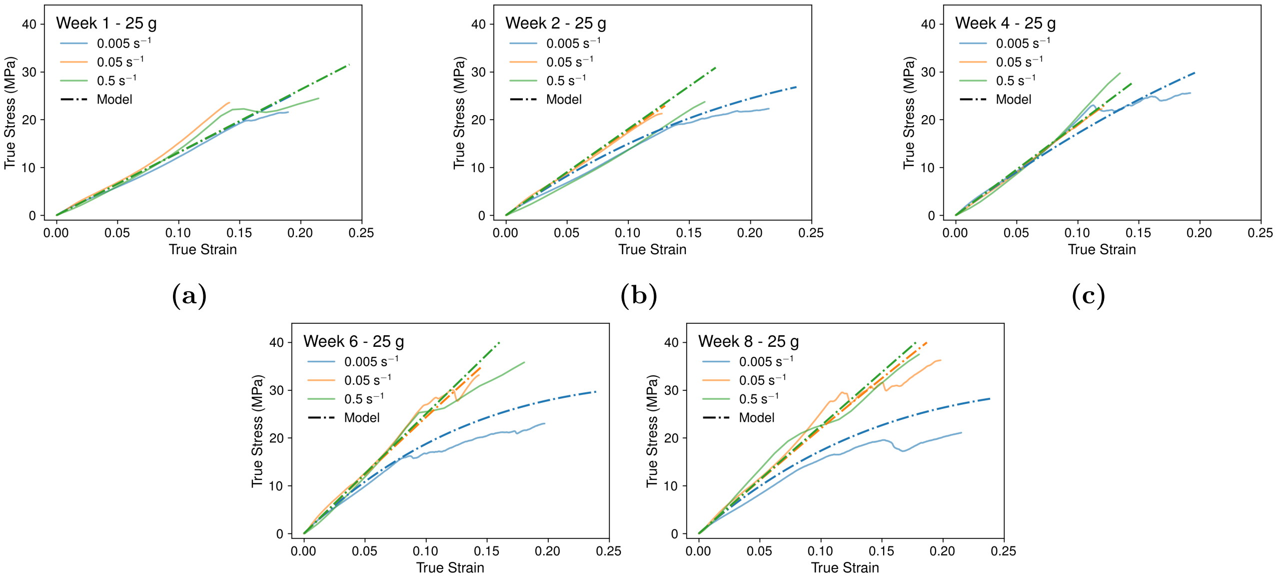

(a) (b) (c)

(d) (e)

Figure 5.12: Maxwell element model fit to true stress–strain responses of 25 g applied load filament specimens tested at strain rates of 0.005, 0.05, and 0.5 s^{-1}. Each subplot presents representative experimental curves and corresponding model predictions for degradation times of Weeks 1, 2, 4, 6, and 8.

data point across all curves. These residuals were concatenated into a single vector, and the non-linear least-squares algorithm iteratively adjusted E and η to minimise the total sum of squared residuals across the entire dataset for that condition. To illustrate the parameter identification procedure, the full set of experimental stress–strain curves used in the optimisation is provided in Section 5.8 (Appendix B) (Figs. 5.18 – 5.19). The resulting optimised elastic moduli and relaxation times are summarised in Figs. 5.13a and 5.13b, respectively. Although standard deviations are included in the analysis, they are small relative to the mean values and therefore not visually prominent in the plotted results. Numerical values are provided in Table 5.3. The elastic moduli extracted from the Maxwell model closely resembles the trends observed in the experimentally averaged nominal stress–strain data for both unloaded and loaded filaments in Figs. 5.8a - 5.8b. The corresponding relaxation times are presented in 5.13b. In the unloaded condition, the relaxation time decreases sharply relative to the undegraded state, followed by moderate fluctuations between Weeks 1 and 6, before increasing again at Week 8. In contrast, filaments degraded under sustained load exhibit a maximum in relaxation time at Week 1, after which the relaxation time decreases and remains comparatively low for the remainder of the degradation period.

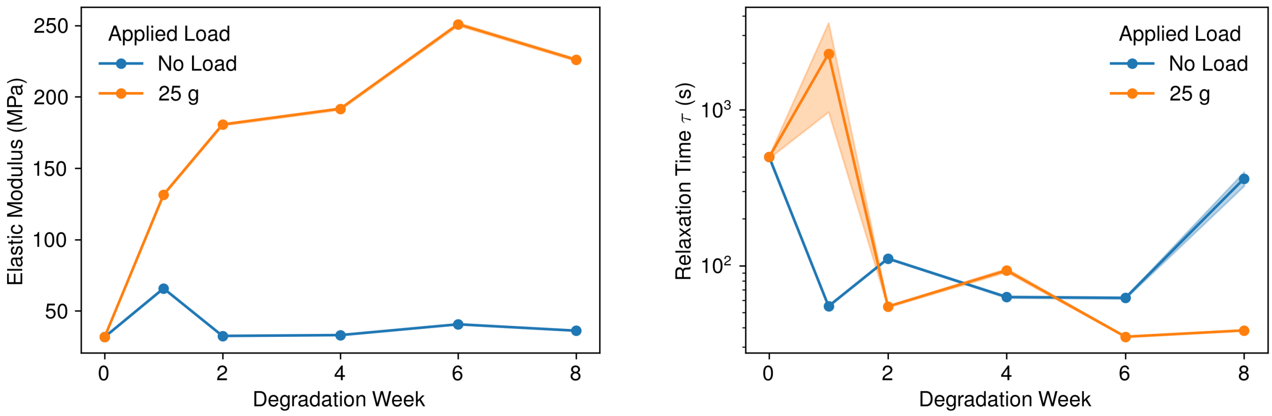

(a) **(b)**

Figure 5.13: Optimised (a) elastic modulus and (b) relaxation times ($\tau = \eta_d/E$) for both no load and 25 g applied load in the true stress-strain space. Shaded regions represent a linear interpolation between the standard deviation for each optimised value.

Table 5.3: Optimised values of the elastic modulus (E) and relaxation time ($\tau = \eta_d/E$) for each degradation week and loading condition. The coefficient of determination (R^2) quantifies the goodness-of-fit between the model predictions and experimental data. Reported values represent the mean ± standard deviation.

	Elastic Modulus (MPa)		Relaxation Time (τ)		R^2 (%)	
	No Load	25 g	No Load	25 g	No Load	25 g
Week 0	31.68 ± 0.07	–	497.49 ± 8.81	–	88.8	–
Week 1	65.75 ± 0.20	131.44 ± 0.45	54.91 ± 0.26	2291.36 ± 1322.33	90.8	89.6
Week 2	32.46 ± 0.06	180.60 ± 0.61	111.04 ± 0.83	54.67 ± 0.59	91.7	90.5
Week 4	33.04 ± 0.10	191.65 ± 0.71	62.86 ± 0.75	93.28 ± 2.32	91.4	89.5
Week 6	40.61 ± 0.15	250.89 ± 0.96	62.07 ± 0.77	34.98 ± 0.20	88.6	74.2
Week 8	36.13 ± 0.16	225.95 ± 0.84	362.27 ± 37.12	38.42 ± 0.18	89.8	73.6

5.5 Discussion

5.5.1 Hydrolytic Degradation: Unloaded vs Loaded Conditions

GPC results shown in Fig. 5.1a demonstrate that degradation of electrospun PCL filaments is characterised by a progressive reduction in number-average molecular weight, consistent with bulk degradation governed by random chain scission (Pitt et al., 1981a; Pitt and Gu, 1987). Over the 8-week degradation period, unloaded filaments exhibited a 10.5% decrease in M_n, whereas filaments subjected to a sustained tensile load showed a larger reduction of 14.4%, indicating that mechanical loading accelerates molecular degradation. When placed in the context of existing literature, these findings align with a subset of reported observations. Studies have reported negligible changes in molecular weight for PCL scaffolds degraded at physiological temperatures over comparable timeframes, including porous constructs (Larrañaga et al., 2014; Little et al., 2009) and electrospun materials (Chung et al., 2012). In contrast, other investigations have demonstrated a clear and measurable reduction in molecular weight during the degradation of electrospun PCL (Bosworth and Downes, 2010; Natu et al., 2013), consistent with the trends observed here. Such discrepancies are attributed to differences in scaffold morphology, fibre diameter, molecular orientation, and post-processing history, all of which strongly influence water uptake and the accessibility of hydrolysable ester bonds (Bartnikowski et al., 2019; Bolgen et al., 2005).

In Chapter 4, we proposed that the pre-stretch inherent to electrospinning and subsequent drawing increases exposure of ester linkages in amorphous regions and promotes bulk hydrolysis, with this effect further amplified under applied load. The present results further support this hypothesis by showing that sustained tensile loading also accelerates degradation at physiological temperatures through creep-assisted chain alignment and stress localisation along amorphous tie chains, which enhances water accessibility and lowers the energetic barrier for hydrolysis, consistent with mechanochemical degradation of polyesters (Li et al., 2010; Zanetti Ferreira et al., 2026). Consistent with this interpretation, similar trends were observed in Chapter 4 at 45°C, where autocatalytic-model degradation constants of 0.0468 (unloaded) and 0.0728 (25 g load) were obtained. These values exceed those fitted in the present study at 37.5°C (Table 5.1), indicating a temperature dependence of hydrolytic degradation kinetics in electrospun PCL filaments.

SEM observations in Fig. 5.5 suggest that localised degradation phenomena coexist with the overall bulk-degradation behaviour, giving rise to distinct surface morphologies. Unlike in Section 4.3.3 in Chapter 4, where no discernible surface modification was observed apart from isolated rupture damage, unloaded filaments in the present study exhibit the formation of microcracks in sections of the filament surface during degradation. This behaviour suggests the presence of localised degradation mechanisms superimposed on bulk hydrolysis. An autocatalytic contribution is plausible, as the slower convective removal of acidic degradation products can lead to a local pH drop, promoting further hydrolysis and localised damage that manifests as cracks (Chlanda et al., 2020; Pitt et al., 1981a; Zhang et al., 2013). Although surface erosion cannot be excluded as the confined degradation environment likely favoured acidic build-up and the development of local pH gradients, which would further accelerate chain scission near the surface leading to the formation of cracks (Chung et al., 2012; Lam et al., 2008). Filaments degraded under sustained tensile load exhibit no surface cracking. We hypothesise that the faster chain scission and free volume increases the mobility and recrystallisation in inter-lamellar regions leading to denser, more homogenous surfaces (Flamini et al., 2022).

5.5.2 Microstructural Evolution with Degradation

DSC results (Fig. 5.3a) show that degradation is accompanied by a progressive increase in crystallinity, rising from 51% in the pre-stretched, undegraded state to 56% after 8 weeks. This increase is most pronounced during the first two weeks, followed by a more gradual, steady growth of crystalline domains. Crystallinity development is further enhanced in filaments degraded under applied load. These trends are consistent with our results in Section 4.3.2, both in terms of magnitude and temporal evolution. The accelerated increase observed during the initial two weeks has been attributed to annealing-driven crystallisation, enabled by enhanced chain mobility early in degradation (Lam et al., 2008; Pitt et al., 1981a). The subsequent steady increase in crystallinity is commonly associated with continued annealing as degradation progresses, where ongoing chain scission further increases molecular mobility and facilitates crystal thickening and perfection (Chlanda et al., 2020; Little et al., 2009; Tan and Lim, 2006). Under applied load, additional crystallinity growth is attributed to strain-induced chain alignment, where chain-extended crystals act as effective nucleation sites and facilitate incorporation of amorphous chains into larger crystalline domains (Chandler et al., 2025). Overall, the close agreement between the present results and earlier observations further strengthens the previously established hypothesis regarding the coupled roles of degradation, annealing, and mechanical loading in driving crystallinity evolution in electrospun PCL filaments.

The melting temperature shown in Fig. 5.3b varies within a narrow range (approximately 59 – 60 °C for C1 and 55.5 – 56.2 °C for C2) over the 8-week degradation period. No clear monotonic evolution with degradation time is observed, and the fluctuations are comparable to the experimental scatter, indicating that the effect of degradation time on melting temperature is relatively weak. However, a consistent offset between conditions is evident, with filaments degraded under applied load exhibiting slightly higher melting temperatures than unloaded samples. This suggests that the presence of mechanical load promotes subtle structural reorganisation, even though the overall changes remain small.

Consistent with this behaviour, Fig. 5.2a shows a slight shift of the melting endotherm towards higher temperatures with degradation time and applied load. Changes in peak width are relatively subtle and not always clearly distinguishable, indicating that any narrowing of the endotherm is modest. These observations are indicative of water-induced plasticisation and thermal annealing, which enhance chain mobility and facilitate the rearrangement of amorphous segments and less stable crystalline domains into more thermodynamically stable structures (Chlanda et al., 2020; Tan and Lim, 2006). It should be noted that Fig. 5.2a presents representative DSC curves. Variability between samples is expected due to intrinsic material heterogeneity, including local differences in crystalline fraction, degree of pre-stretch, and fibre cross-sectional area, which influence water penetration and structural reorganisation kinetics.

To decouple these effects from the initial thermal history and isolate degradation-induced changes in crystal structure, the second heating cycle provides further insight. By erasing the thermal history and allowing sufficient time for the polymer to recrystallise, the material exhibits a nearly identical melting peak response across all samples, regardless of their prior degradation or loading history. Despite this similarity in peak shape, degradation continues to influence the thermal behaviour. As shown in Fig. 5.3a, the degree of crystallinity increases progressively with degradation time. This trend can be attributed to chain scission processes: as degradation advances, polymer chains become shorter, which enhances chain mobility in the molten state and facilitates their rearrangement into more ordered crystalline regions (Castilla-Cortázar et al., 2012). Although the overall degree of crystallinity remains comparable between unloaded and loaded samples, the evolution of melting temperature with degradation time (Fig. 5.3b) reveals a subtle but consistent increase under loading. Since applied load accelerates chain scission, we hypothesise the resulting shorter polymer chains likely promote the formation of a greater number of crystalline lamellae with a broader size distribution. This microstructural diversification leads to slightly higher melting temperatures in the loaded samples, reflecting the presence of multiple lamellar populations with varying thermal stability.

In addition to driving changes in crystalline structure and thermal stability, degradation-induced chain mobility and recrystallisation also influence the mesoscale morphology of the electrospun fibre network. Both unloaded and loaded filaments exhibited fibre coalescence (Fig. 5.5), a phenomenon also reported in previous studies (Castilla-Cortázar et al., 2012; Chandler et al., 2025; Flamini et al., 2022; Natu et al., 2013). Unlike our earlier work in Chapter 4, where fibre coalescence was not observed, the filaments used in the present study were approximately 70 μm smaller in diameter, indicating that they experienced a greater degree of pre-stretch during post-processing. In addition, the polymer solution employed here possessed a molecular weight approximately 100 kg mol^{-1} higher than previously, which would be expected to increase chain entanglement density and enhance drawability during filament formation. Under such conditions, mechanical drawing is more likely to induce high levels of chain orientation and to generate a heterogeneous crystalline microstructure comprising coexisting lamellar populations, including a larger fraction of thin, imperfect, or metastable crystalline domains. The greater presence of these metastable crystalline regions alongside a shorter inter-fibre distance due to greater drawing may predispose the fibres to coalescence during subsequent degradation.

Chandler et al. (2025) attributed fibre coalescence to local heating generated by mechanical work during plastic deformation, leading to the fusion of unstable crystalline regions between adjacent fibres. In the present study, we propose that fibre coalescence arises from the combined action of thermal, chemical, and molecular mechanisms. First, localised heating generated during mechanical drawing increases the surface temperature of the polymer, creating initial sites of contact and partial fusion between neighbouring fibres (Fig. 5.4b). Upon immersion in water, water-induced plasticisation further enhances molecular mobility by expanding the free volume, which facilitates segmental reptation and diffusion of cleaved polymer chains, allowing them to reorganise and crystallise at interfacial regions. As degradation proceeds as shown in Fig. 5.5, these fused contact points grow progressively, driven by the migration of short-chain segments from surrounding fibres that re-attach to and reinforce existing crystalline junctions. Moreover, since degradation occurs under favourable annealing conditions, the elevated thermal energy promotes lamellar thickening and crystal coalescence, further consolidating the fused regions.

Interestingly, Zhang et al. (2015) reported that hydrolytic degradation increases the surface wettability of electrospun PCL fibres, indicating a progressive rise in surface polarity. The introduction of hydrophilic end groups and increased surface energy promote thermodynamic driving forces for interfacial minimisation. When neighbouring fibres come into contact under thermally softened conditions, this elevated surface energy, together with enhanced molecular mobility, facilitates inter-diffusion across interfaces and increases the likelihood of coalescence. Collectively, these processes promote local "welding" of fibres, giving rise to the coalesced morphologies observed in both unloaded and loaded samples. Fibre coalescence may also explain the gradual reduction in apparent filament diameter for unloaded filaments, as adjacent fibres merge into a denser and more uniform structure.

5.5.3 Mechanical Behaviour: Microstructure to Macroscopic Response

Mechanical results in Fig. 5.8a reveal that samples degraded without any applied load, apart from Week 1, exhibited little to negligible change in elastic modulus relative to the undegraded filaments. The modest stiffer response observed at Week 1 is likely attributed to early-stage secondary crystallisation and annealing-like structural relaxation: initial hydrolytic scission produces shorter, more mobile chain segments that can reorganise and recrystallise, leading to lamellar thickening and increased crystal perfection. As degradation progresses, however, the elastic modulus, maximum stress, and strain at break all decline. This progressive loss of mechanical integrity arises because water preferentially cleaves chains within the amorphous regions, reducing the number of effective load-bearing tie-chains that bridge crystalline lamellae. With fewer tie-chains available to distribute load, stress transfer between lamellar domains becomes increasingly inefficient, causing stiffness to fall while stress and strain at failure diminish.

Similar overall trends were observed in Fig. 4.11, though two key differences emerge. First, the apparent elastic modulus in the present work is consistently higher across all degradation weeks. This discrepancy is attributed to the use of screw-side grips rather than bollard grips, which suppresses geometric slack and induces more uniform fibre engagement, thereby yielding a stiffer intrinsic response. Second, while our earlier study showed an immediate drop in modulus after one week, attributed to water-induced plasticisation, in the present work we observe the opposite: an initial increase. We hypothesise that this difference arises from the lower degradation temperature used here, which lies closer to the recrystallisation onset for electrospun PCL rather than the melting onset. Under these conditions, mild hydrolysis combined with water plasticisation enhances chain mobility sufficiently to promote secondary crystallisation rather than softening. In contrast, the higher temperature used previously may have accelerated chain relaxation and disrupted lamellar stability, favouring plasticisation over recrystallisation during early degradation. Additionally, because the filaments in this study were more drawn, even small temperature shifts can influence the relaxation behaviour of extended-chain lamellae, altering the relative degradation rates of different microstructural populations and contributing to the distinct mechanical trends observed.

In contrast, filaments degraded under sustained tensile loading (Fig. 5.8b) display a progressive increase in elastic modulus with degradation time. A similar stiffening trend was observed in Fig. 4.11, which was attributed to creep-induced microstructural evolution during degradation under load. The applied tensile stress promotes stress-assisted chain alignment and facilitates degradation-induced recrystallisation, leading to a progressive stiffening response of load-bearing domains. Under these conditions, newly formed crystalline domains are expected to consist predominantly of chain-extended crystals (CECs), rather than folded-chain crystals (CFCs), resulting in higher intrinsic stiffness and more efficient load transfer along the filament axis. This hypothesis could be verified using techniques sensitive to crystalline morphology and orientation, such as wide-angle X-ray scattering (WAXS) or small-angle X-ray scattering (SAXS) to assess lamellar structure and crystal orientation.

In both unloaded and loaded cases, the improved load engagement provided by screw-sided grips further elucidates the mechanical response by minimising grip-induced artefacts such as rotation, bending, and delayed fibre recruitment. Consequently, the measured stress–strain response in Figs. 5.11 and 5.12 evolve from an initially non-linear form towards a progressively more linear behaviour, allowing clearer insight into the intrinsic mechanical response of the filament. We therefore hypothesise that, as degradation proceeds, the mechanical behaviour becomes increasingly governed by deformation and bending of the crystalline framework, rather than by cooperative deformation of amorphous and crystalline phases. The concurrent reduction in strain at break observed in Figs. 5.8e – 5.8f is directly linked to this microstructural evolution. Progressive recrystallisation promotes crystal growth and coalescence, and in the case of loaded fibres, additional crystal alignment, which localises stress at crystal–amorphous interfaces and reduces the density of effective load-bearing tie chains (Seguela, 2005; Tan and Lim, 2006). The resulting loss of amorphous connectivity limits molecular mobility, restricts available deformation pathways, and promotes premature failure. Together, these effects explain the transition from ductile to increasingly brittle behaviour and the emergence of a more linear, predominantly elastic response, which is further amplified under sustained tensile loading.

The evolution of relaxation time shown in Fig. 5.13b indicates a degradation-dependent shift in the characteristic time scale of the viscoelastic response, together with a strong dependence on applied load. In both unloaded and loaded filaments, relaxation times decrease during the early stages of degradation, indicating a progressive reduction in long-time viscoelastic processes. This behaviour is consistent with the preferential degradation of amorphous domains, which are primarily responsible for time-dependent deformation through chain mobility and segmental relaxation. As degradation proceeds, the reduction in elastically active amorphous chains limits the filament's capacity to sustain delayed stress relaxation, leading to shorter characteristic relaxation times.

During the first week of degradation, a divergence between the two loading conditions is observed. While the unloaded filaments exhibit a substantial reduction in relaxation time, the loaded filaments show a transient increase, reaching relaxation times exceeding 10^3 s. This suggests that the presence of an applied load stabilises long-lived viscoelastic mechanisms in the early stages of degradation. Such behaviour may arise from load-induced chain alignment and constrained amorphous regions adjacent to crystalline lamellae, which can temporarily enhance stress transfer efficiency and delay relaxation. In this regime, the applied load appears to counteract the initial effects of chain scission by promoting mechanically stabilised amorphous domains. Beyond Week 1, relaxation times in both conditions decrease and converge toward the order of 10^1–10^2 s, indicating a transition to a degradation-dominated regime. From Weeks 2 to 6, the relaxation times under load remain consistently lower than those of the unloaded filaments. This inversion suggests that sustained loading accelerates the loss of long-time relaxation modes, potentially due to enhanced hydrolytic accessibility or stress-assisted chain scission within the amorphous phase. The combined effects of degradation and mechanical constraint may therefore suppress slow viscoelastic processes more efficiently under load than in the unloaded condition.

5.5.4 Micromechanical Insights: Contribution of Phases

The overall mechanical response of electrospun PCL filaments can be decomposed into the respective contributions of the amorphous and crystalline phases. As illustrated schematically in Fig. 5.14, the filament response was initially represented by a single equivalent spring within the Maxwell framework; however, resolving the individual phase contributions is necessary to understand how degradation alters the tensile modulus at the microscale. For a two-phase semi-crystalline system, the effective fibre modulus can be estimated using classical rule-of-mixtures formulations, which interpolate the moduli of the amorphous and crystalline domains according to their evolving volume fractions. In the present case, a series representation was adopted, consistent with a Reuss-type approximation, to reflect the underlying microstructure of electrospun PCL filaments, in which load is transmitted sequentially through alternating amorphous and crystalline regions along the fibre axis. Under this assumption, both phases experience the same stress while the total strain is partitioned between them, yielding a lower-bound estimate of the effective modulus. Physically, this implies that the amorphous phase acts as the more compliant region that accommodates most of the deformation, whereas the crystalline domains function as comparatively stiff, load-bearing elements distributed along the load path. This representation is particularly appropriate for a highly oriented fibrillar structure, for which a parallel (Voigt) approximation, assuming equal strain in both phases, would likely overpredict the stiffness, as it implicitly assumes that the crystalline phase governs the deformation, which is not representative of a system where a compliant amorphous phase mediates the mechanical response.

To examine the evolution of the phase moduli during degradation, two physically motivated assumptions are introduced. First, the crystalline phase is treated as a quasi-inert, load-bearing domain whose stiffness remains approximately constant over the degradation timescale (Struik, 1987). Second, hydrolytic degradation is assumed to occur preferentially within the amorphous regions, such that reductions in amorphous stiffness are directly linked to molecular-weight loss arising from chain scission.

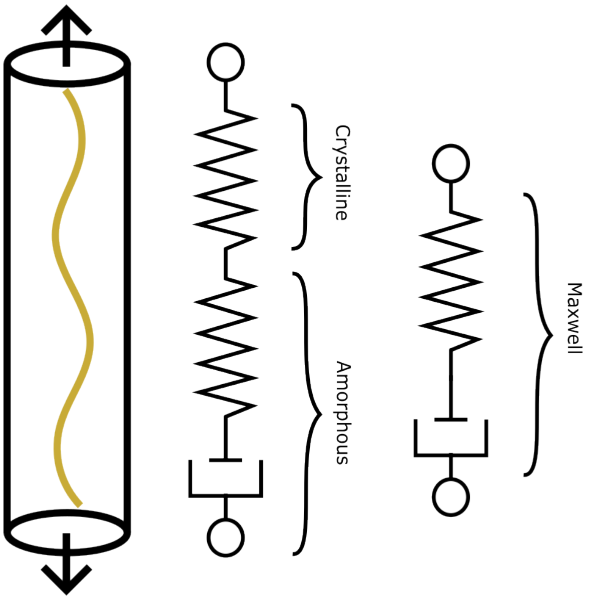

Figure 5.14: Decomposing crystalline and amorphous contributions, which are combined together as one equivalent Maxwell model.

Under these assumptions, the effective fibre modulus (E_f) may be expressed using the Reuss rule of mixtures,

$$E_f(t) = \left(\frac{V_a(t)}{E_a(t)} + \frac{V_c(t)}{E_c(t)} \right)^{-1}, \qquad V_a(t) + V_c(t) = 1, \tag{5.3}$$

where V_a and V_c denote the amorphous and crystalline volume fractions, respectively, and E_a and E_c are the corresponding phase moduli. This formulation is appropriate when the phases are assumed to experience equal stress and deform in series.

To identify how temporal changes in phase properties influence the overall fibre response, Eqn. 5.3 is differentiated with respect to time, yielding

$$\frac{dE_f}{dt} = -E_f(t)^2 \left[\frac{1}{E_a} \frac{dV_a}{dt} - \frac{V_a}{E_a^2} \frac{dE_a}{dt} + \frac{1}{E_c} \frac{dV_c}{dt} - \frac{V_c}{E_c^2} \frac{dE_c}{dt} \right]. \tag{5.4}$$

Invoking the assumption of a time-invariant crystalline modulus ($dE_c/dt = 0$) and recognising that changes in phase fractions must satisfy $dV_c/dt = -dV_a/dt$, the above expression simplifies to

$$\frac{dE_f}{dt} = -E_f(t)^2 \left[\left(\frac{1}{E_c} - \frac{1}{E_a} \right) \frac{dV_c}{dt} - \frac{V_a}{E_a^2} \frac{dE_a}{dt} \right]. \tag{5.5}$$

Amorphous-phase degradation kinetics

To interpret this condition physically, the degradation mechanism within the amorphous domains must be considered. Hydrolysis of ester bonds proceeds according to

$$\mathrm{RCOOR'} + \mathrm{H_2O} \rightarrow \mathrm{RCOOH} + \mathrm{R'OH}, \tag{5.6}$$

producing shorter chain segments terminated by carboxyl and hydroxyl groups. In an autocatalytic reaction, the acidic end group can further increase the hydrolysis rate because $-\mathrm{COOH}$ can dissociate into $-\mathrm{COO^-}$ and $\mathrm{H^+}$ that further catalyses the reaction (Lyu et al., 2007; Pitt et al., 1981a). As a result, the rate of change of concentration of acidic (COOH) end groups is expressed as follows:

$$\frac{dC_a}{dt} = kC_a, \tag{5.7}$$

where C_a is the concentration of acidic end groups (mol kg^{-1}), such that $C_a = 1/M_n$. Integration of Eqn. 5.7 in terms of molecular weight yields the following expression,

$$C_a = C_{a_0} \exp(kt), \tag{5.8}$$

where C_{a_0} is the initial concentration of acidic end groups. Differentiating this expression,

$$\frac{dC_a}{dt} = kC_{a_0} \exp(kt). \tag{5.9}$$

The production rate of acidic end groups dC_a/dt is the same as the rate of chain scission. Therefore, it is possible to assume that the density of elastically effective chains N within the amorphous network decreases at the same rate as the density of chain scission, such that

$$\frac{dN}{dt} = -\rho N_A \frac{dC_a}{dt}, \tag{5.10}$$

where ρ is the polymer density and N_A is Avogadro's constant. The pre-factor ρN_A converts concentrations expressed per unit mass into number densities per unit volume. Treating the amorphous regions as an entangled, rubber-like network of macromolecules that is approximately incompressible, the elastic modulus is related to the shear modulus G through $E_a = 3G$. Classical rubber elasticity theory then gives

$$E_a = 3G = 3Nk_BT, \tag{5.11}$$

where N is the number density of elastically active chains, k_B is the Boltzmann constant, and T is the absolute temperature. Differentiating Eqn. 5.11 with respect to time and substituting for dN/dt yields

$$\frac{dE_a}{dt} = -3\rho N_A k_B T \frac{dC_a}{dt}. \tag{5.12}$$

Substitution of the acidic end-group production rate (Eqn. 5.7) into Eqn. 5.12, followed by integration, leads to

$$E_a = E_{a_0} + K(1 - \exp(kt)); \quad K = 3\rho N_A k_B T C_{a_0} = \frac{3\rho N_A k_B T}{M_{n_0}} \tag{5.13}$$

where E_{a_0} and M_{n_0} are the initial amorphous modulus and number-average molecular weight, respectively. Importantly, Eqn. 5.13 is valid only at early stages of degradation, as it assumes that each chain scission event removes one elastically effective chain. At longer times, this assumption breaks down because an increasing fraction of scission events occurs along elastically inactive segments. In addition, as the molecular weight decreases, the growing population of shorter, elastically inactive chains leads to a dilution of the load-bearing network, effectively increasing the molecular weight between entanglements (M_e). This further reduces the sensitivity of the amorphous modulus to continued chain scission.

To assess the practical relevance of amorphous modulus decay over the experimental timeframe considered here, the initial magnitude of the amorphous modulus was estimated independently using an equivalent form of rubber elasticity theory expressed in terms of the entanglement molecular weight,

$$E_a = 3\frac{\rho R T}{M_e}, \tag{5.14}$$

where R is the universal gas constant and M_e is the molecular weight between entanglements. Equation 5.14 is fully consistent with Eqn. 5.11, noting that $N = \rho N_A / M_e$. Using representative values for PCL ($\rho = 1140$ kg m^{-3} (Ketelaars et al., 1997), $R = 8.314$ J mol^{-1} K^{-1}, $T = 310$ K, and $M_e = 2.5$ kg mol^{-1} (Kurz et al., 2018)), Eqn. 5.11 yields an intrinsic amorphous modulus of approximately $E_a \approx 3.5$ MPa. Substituting this value into Eqn. 5.13 indicates that the predicted reduction in E_a over an 8-week degradation period is negligible ($\ll 1\%$). Consequently, within the experimentally relevant timescales considered here, the amorphous modulus may be treated as effectively constant, such that $dE_a/dt \approx 0$.

Governing condition for fibre-modulus evolution

Under this approximation, Eqn. 5.5 reduces to

$$-\frac{1}{E_f^2}\frac{dE_f}{dt} = \left(\frac{1}{E_c} - \frac{1}{E_a}\right)\frac{dV_c}{dt}. \tag{5.15}$$

To assess whether crystallinity evolution alone can yield no net change in the fibre modulus over the degradation period, we linearised the initial fibre modulus by assuming $E_f \approx E_{f_0}$. This approximation treats the fibre modulus as a quasi-constant over the time increment of interest and enables direct evaluation of the sign and magnitude of dE_f/dt. Furthermore, assuming $E_c \gg E_a$, the term $1/E_c$ is neglected relative to $1/E_a$, yielding

$$\frac{d(E_f/E_{f_0})}{dt} = \frac{E_{f_0}}{E_{a_0}}\frac{dV_c}{dt}. \tag{5.16}$$

Kawai et al. (2022) reported an average crystalline modulus of $E_c = 10.7$ GPa for PCL crystals, with comparable values reported for other aliphatic polyesters, such as, PLLA (Jariyavidyanont et al., 2023; Lee et al., 2018; Wasanasuk and Tashiro, 2012). Since the amorphous modulus was estimated as $E_{a_0} \approx 3.5$ MPa, resulting in the following ratio, $E_{f_0}/E_{a_0} = 2.04$. The remaining model parameter, dV_c/dt, can be obtained directly from experimental measurements. The rate of change of crystallinity was determined from a linear fit to Fig. 5.3a, which for the unloaded condition yields

$$V_c(t) = 0.00852t + 0.516, \tag{5.17}$$

such that $dV_c/dt = 0.00852$ week^{-1}. Therefore,

$$\frac{d(E_f/E_{f_0})}{dt} = (2.04)(0.00852) = 0.0174 \text{ week}^{-1}. \tag{5.18}$$

This result indicates that crystallinity evolution alone predicts an increase in the normalised fibre modulus of approximately 1.7% per week, corresponding to a cumulative increase of about 13.9% over an 8-week period. In contrast, the experimental measurements indicate no significant change in the fibre modulus over this period, highlighting a non-negligible discrepancy between the crystallinity-driven prediction and the observed mechanical response.

One possible explanation is that the kinetic evolution of the amorphous modulus proposed in Eqn. 5.13 is incomplete. In particular, maintaining an approximately constant fibre modulus, as observed experimentally, would require a concurrent reduction in the amorphous modulus sufficient to offset the stiffening associated with the increasing crystalline volume fraction. To examine this hypothesis, we return to the expression for the fibre modulus given in Eqn. 5.5. Both the crystalline volume fraction, V_c, and the amorphous modulus, E_a, are assumed to evolve linearly with time, while the effective fibre modulus remains approximately constant over the degradation period ($dE_f/dt \approx 0$). Enforcing this condition yields the following expression for the minimum rate of amorphous softening required to counterbalance crystallinity-driven stiffening:

$$\frac{dE_a}{dt} = \frac{E_a^2}{V_a}\left(\frac{1}{E_c} - \frac{1}{E_a}\right)\frac{dV_c}{dt}. \tag{5.19}$$

Inspection of Eqn. 5.19 reveals that the amorphous modulus E_a is a key parameter governing the magnitude of the required softening rate dE_a/dt, while all other quantities are either fixed or independently measured. For the purpose of this analysis, the initial amorphous modulus E_{a_0} is used, as it provides the upper bound on the required softening rate. This observation motivates closer scrutiny of the assumptions underlying the estimation of E_{a_0}. In the present formulation, the fibre modulus has been approximated using a two-phase description comprising single scalar crystalline and amorphous moduli. However, this representation is a substantial oversimplification of the ES filament morphology. For example, the amorphous phase is mechanically heterogeneous, consisting of both bulk amorphous regions and inter-lamellar tie-chain networks. The latter can exhibit significantly higher effective stiffness due to constrained chain mobility and enhanced load-bearing connectivity (Polińska et al., 2021). In addition, electrospinning and post-processing drawing induce strong molecular orientation within the amorphous domains, giving rise to an anisotropic mechanical response that is not captured by an isotropic modulus derived from bulk rubber elasticity. This anisotropy affects both the magnitude of E_{a_0} and the efficiency of load transfer between crystalline and amorphous phases during deformation.

In light of these considerations, a range of initial amorphous moduli was explored by logarithmically scaling the initially estimated value of E_{a_0} to assess the sensitivity of the model predictions to its assumed magnitude. This approach implicitly accounts for potential contributions from amorphous anisotropy and tie-chain-induced stiffening. For each assumed value of E_{a_0}, the fibre modulus E_f was evaluated at the initial and final time points using the Reuss formulation (Eqn. 5.3), allowing both the crystalline volume fraction V_c and the amorphous modulus E_a to evolve. In contrast, the normalised rate of fibre stiffening, $d(E_f/E_{f_0})/dt$ (Eqn. 5.16), and the corresponding rate of amorphous softening, dE_a/dt (Eqn. 5.19), were evaluated with the crystalline volume fraction and modulus held constant at $V_c = 0.516$ and $E_c = 10.7$ GPa, respectively. The results, summarised in Table 5.4, show that the predicted normalised rate of fibre stiffening remains nearly invariant across all values of E_{a_0}, indicating that the crystallinity-driven stiffening contribution is largely insensitive to the assumed initial amorphous modulus. In contrast, both the absolute change in fibre modulus, ΔE_f, and the rate of amorphous softening required to offset crystallinity-induced stiffening depend strongly on E_{a_0}. Specifically, higher initial amorphous moduli require proportionally larger rates of amorphous softening to maintain $dE_f/dt \approx 0$, whereas lower values of E_{a_0} permit a more balanced compensation between crystalline stiffening and amorphous degradation.

Table 5.4: Influence of the assumed initial amorphous modulus E_{a_0} on fibre modulus evolution and amorphous softening rate.

E_a (MPa)	E_{f_0} (MPa)	$E_f(t=8)$ (MPa)	ΔE_f	$\frac{d(E_f/E_{f_0})}{dt}$	$\frac{dE_a}{dt}$
0.35	0.72	0.83	0.11	0.0174	-0.0061
3.5	7.2	8.4	1.2	0.0174	-0.061
35	72.1	83.9	11.8	0.0173	-0.607
350	699.4	806.5	107.1	0.0168	-5.886

To further interpret this sensitivity to E_{a_0}, it is also necessary to examine the amorphous degradation law itself. Referring to Eqn. 5.13, the evolution of the amorphous modulus is governed by the initial value E_{a_0} and the kinetic term $K(1 - \exp(kt))$, which together constrain the maximum attainable reduction in stiffness. As a result, the adopted kinetic law cannot generate the level of amorphous softening required when E_{a_0} is large, since the term $K(1 - \exp(kt))$ remains too small to significantly reduce a highly stiff amorphous phase. This limitation warrants further consideration, as the initial amorphous modulus in electrospun fibres is expected to be relatively high due to molecular orientation and tie-chain morphology. The inability of the proposed kinetic law to accommodate substantial softening at physically realistic values of E_{a_0} therefore exposes a fundamental shortcoming of the current modelling framework.

Overall, these discrepancies underscore the limitations of describing the mechanical response of degrading electrospun PCL fibres using a simple two-phase Reuss-type approximation with homogeneous amorphous and crystalline moduli. Such a framework is insufficient to explain the experimentally observed invariance of the fibre modulus during degradation. The present analysis suggests that additional mechanisms, neglected in the current formulation, are likely to play a critical role. These include mechanically heterogeneous amorphous behaviour, preferential degradation of load-bearing tie-chain networks, anisotropic amorphous response induced by electrospinning and drawing, and potentially evolving inefficiencies in load transfer between phases as degradation progresses. Collectively, these effects may moderate the effective fibre-scale stiffness, counterbalancing crystallinity-driven stiffening.

Future modelling efforts should therefore move beyond a single scalar amorphous modulus and incorporate microstructure-informed descriptions of phase heterogeneity and evolving load transfer to achieve closer quantitative and mechanistic agreement with experimental observations.

5.6 Conclusion

This study investigated the hydrolytic degradation of electrospun poly(ε-caprolactone) filaments under unloaded and tensile-loaded conditions, integrating experimental characterisation with a simple viscoelastic Maxwell model to establish a direct link between molecular degradation, microstructural evolution, and macroscopic mechanical behaviour. Across 8 weeks of degradation in PBS at 37.5 °C, molecular weight decreased in all samples, with applied load accelerating chain scission. Thermal analysis revealed progressive lamellar reorganisation and an overall increase in crystallinity. Mechanical testing demonstrated a transition from elastic–plastic behaviour in undegraded filaments to predominantly elastic and brittle responses after immersion. Under static tensile load, filaments displayed higher stiffness and strength than unloaded counterparts throughout degradation, despite both experiencing molecular weight loss and increasing crystallinity. Time-dependent mechanical testing further demonstrated that degradation is accompanied by a progressive reduction in viscoelastic dissipation, with stress relaxation becoming less pronounced and the response increasingly dominated by elastic mechanisms at slow loading rates. This evolution is consistent with a loss of load-bearing amorphous connectivity, alongside increased crystalline constraint. Attempts to rationalise these trends using a Reuss-type two-phase mixture model revealed that classical composite descriptions cannot simultaneously account for crystallinity-driven stiffening, and amorphous softening under coupled mechanical and chemical stimuli.

Overall, the results demonstrate that degradation of electrospun PCL is governed not solely by hydrolytic chain scission, but by a strong coupling between applied mechanical load, microstructural reorganisation, and evolving viscoelastic processes. These findings highlight that the *in vivo* mechanical performance of electrospun PCL scaffolds cannot be inferred from hydrolysis-driven degradation alone. Instead, the local mechanical environment plays a decisive role in controlling degradation kinetics, phase connectivity, and the retention of mechanical integrity. While the present framework remains simplified, it provides a microstructure-informed foundation for the development of more physically grounded models incorporating microstructural elements, enabling more predictive design of electrospun scaffolds and other biodegradable polymers with tailored degradation and mechanically adaptive behaviour.

5.7 Appendix A: Stress-strain Plots

Stress–strain curves of undegraded and degraded filaments for each degradation condition and degradation time are presented in Figs. 5.15 - 5.17, including all repeats.

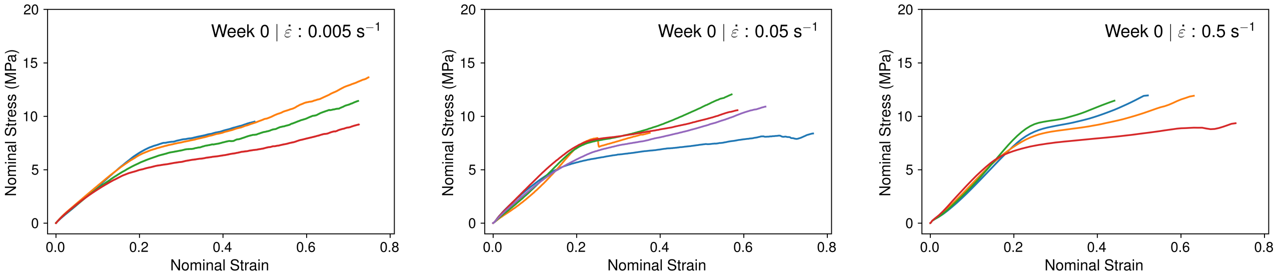

Figure 5.15: Nominal stress–strain curves for unloaded filament specimens tested at an strain rates of 0.005, 0.05, and 0.5 s^{-1}. Results are shown for undegraded (Week 0) samples. Each subplot contains multiple replicate specimens, illustrating sample-to-sample variability within each group.

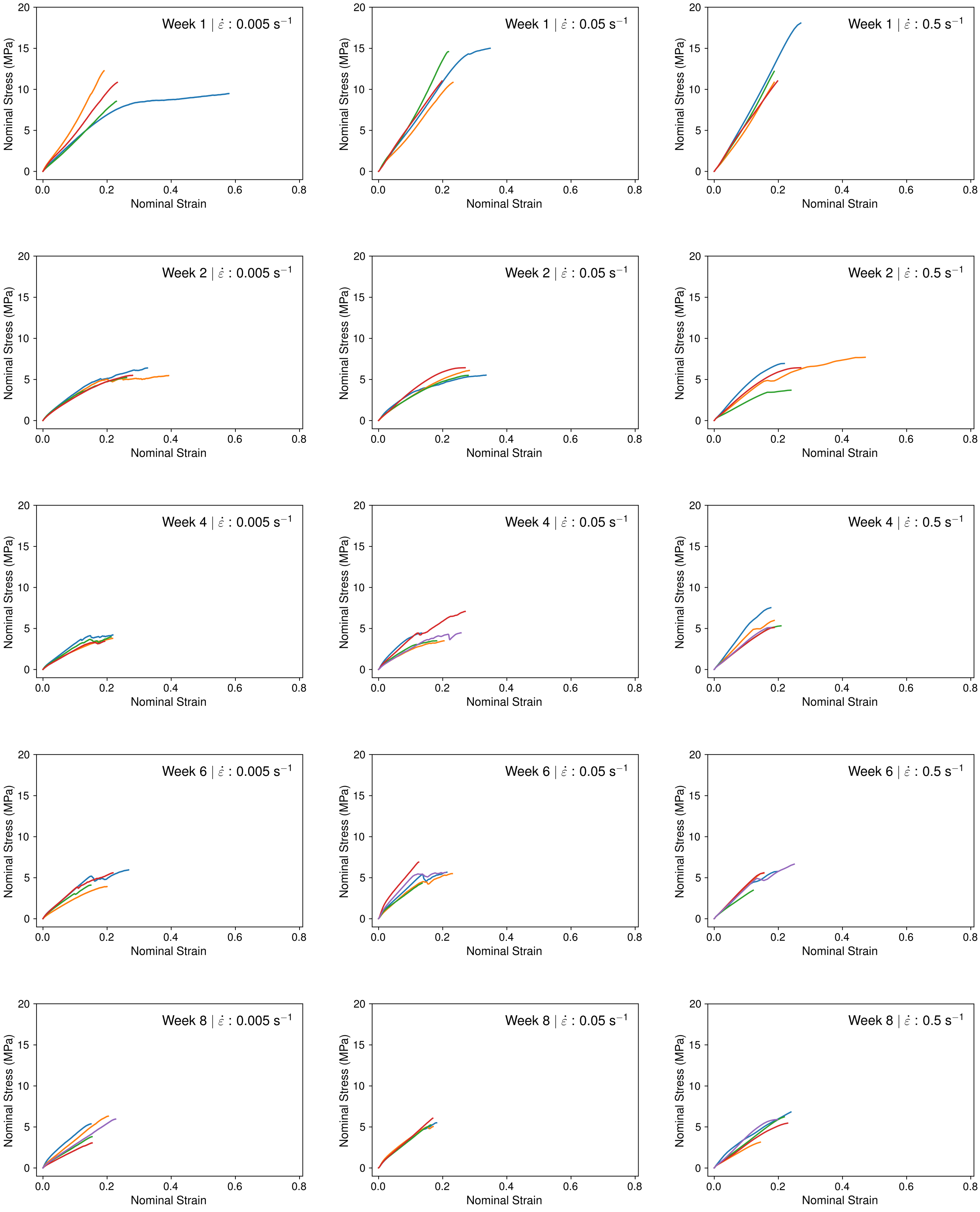

Figure 5.16: Nominal stress–strain curves for unloaded filament specimens tested at an strain rates of 0.005, 0.05, and 0.5 s^{-1}. Results are shown for degradation time points of Weeks 1, 2, 4, 6, and 8. Each subplot contains multiple replicate specimens, illustrating sample-to-sample variability within each group.

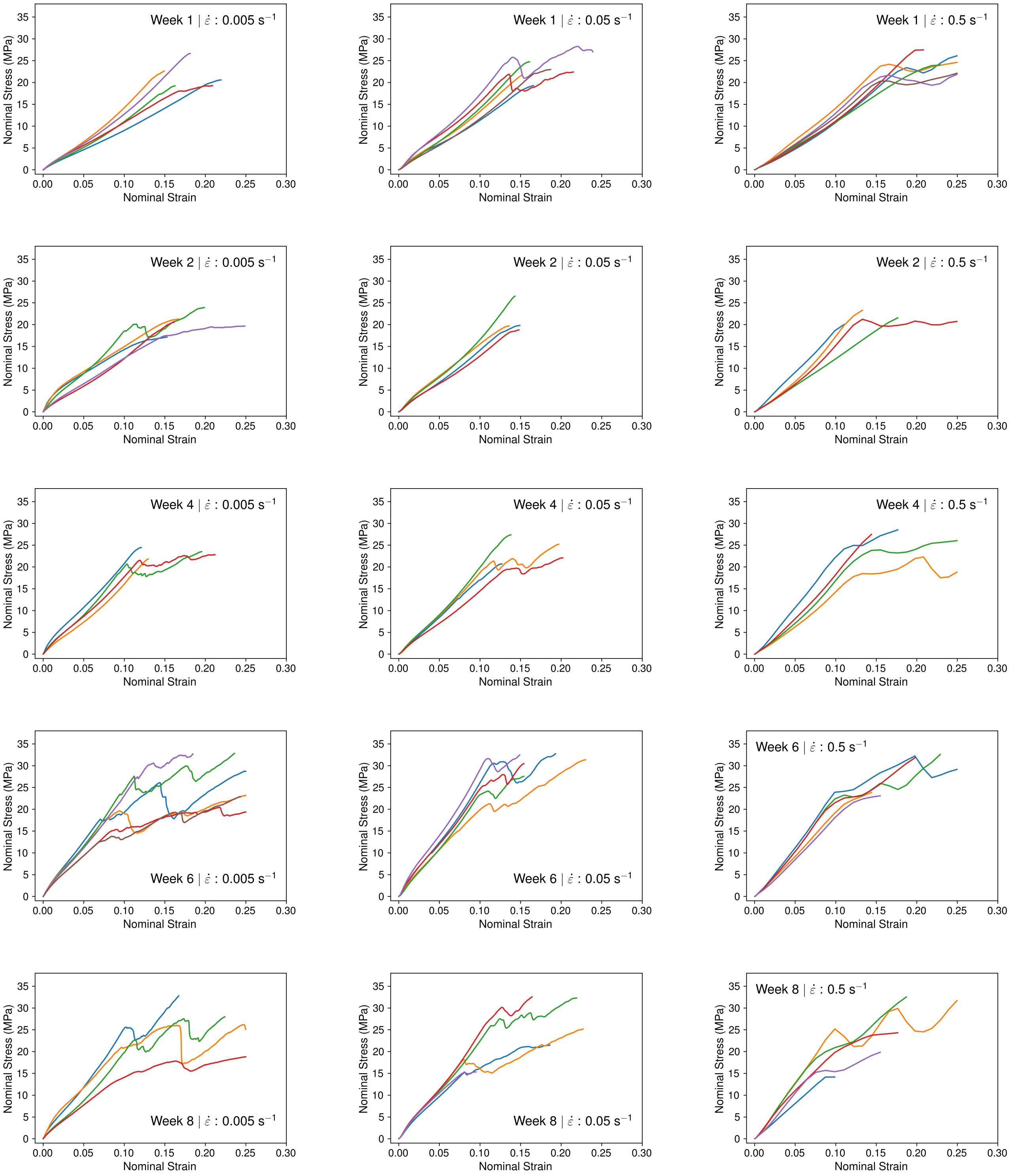

Figure 5.17: Nominal stress–strain curves for 25 g applied load filament specimens tested at an strain rates of 0.005, 0.05, and 0.5 s^{-1}. Results are shown for degradation time points of Weeks 1, 2, 4, 6, and 8. Each subplot contains multiple replicate specimens, illustrating sample-to-sample variability within each group.

5.8 Appendix B: Model Optimisation Results

Figures 5.18 and 5.19 show the full set of experimental curves for unloaded and loaded specimens, used to iteratively optimise the single Maxwell element parameters. This process identifies the optimal elastic modulus (E) and relaxation time (τ) for each degradation week, as presented in Figs. 5.13a and 5.13b. Following optimisation, the model response is evaluated using the same fitted parameters at three different strain rates (0.005, 0.05, and 0.5 s^{-1}), and overlaid on the experimental data.

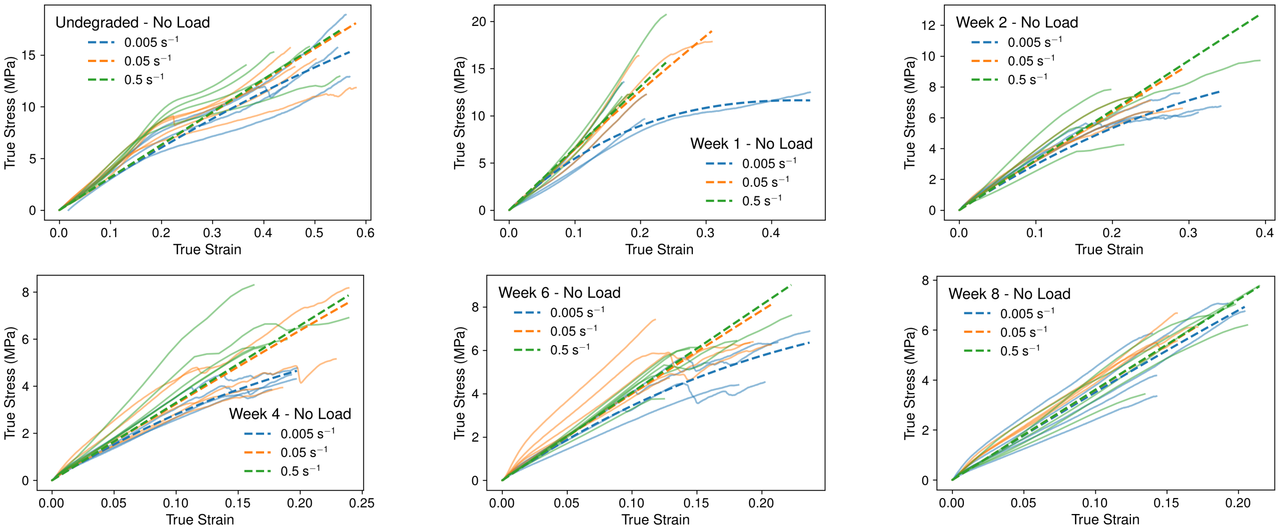

Figure 5.18: Stress–strain curves for unloaded filament specimens across different degradation weeks. Fitted Maxwell model responses (E, τ) are shown for three strain rates (0.005, 0.05, and 0.5 s^{-1}).

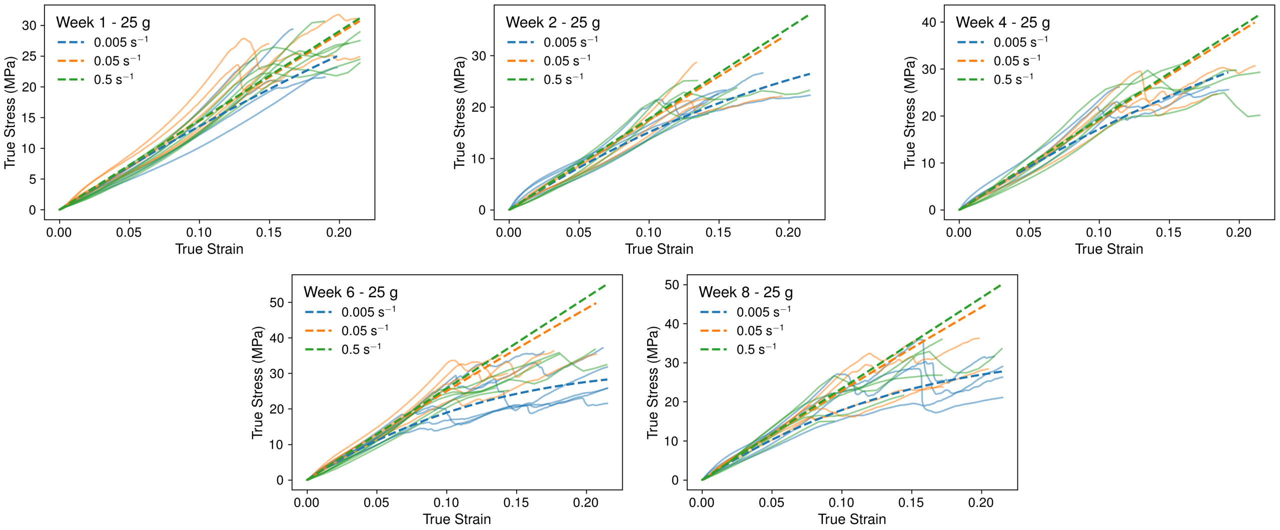

Figure 5.19: Stress–strain curves for loaded filament specimens across different degradation weeks. Fitted Maxwell model responses (E, τ) are shown for three strain rates (0.005, 0.05, and 0.5 s^{-1}).

Chapter 6

Conclusions

6.1 Overview

This thesis has presented a comprehensive body of research aimed at characterising the thermo-mechanical behaviour and degradation response of electrospun poly(ε-caprolactone) filaments, combining experimental investigation with constitutive modelling to support their future application in tendon and ligament reconstruction. A systematic experimental programme was conducted, encompassing thermal analysis, mechanical testing under monotonic and cyclic loading, and detailed morphological and topographical characterisation. Together, these approaches enabled a deeper understanding of how processing history, microstructural evolution, and environmental exposure govern the functional performance of electrospun PCL filaments over time. The findings presented in this thesis contribute to the broader fields of non-woven fibrous networks, biodegradable polymer systems, and biomedical implant design by providing new insight into the coupled thermo-mechanical–degradation behaviour of electrospun scaffolds at the filament and fibre scales. In particular, this work advances understanding on electrospun scaffold mechanics and time-dependent polymer behaviour, and how they interact to control strength, stiffness, and durability properties that are critical for load-bearing soft-tissue applications. The outcomes also provide a mechanistic foundation for predictive modelling of electrospun architectures, bridging the gap between material characterisation and scaffold-level performance.

The thermo-mechanical behaviour of electrospun PCL filaments was first investigated in Chapter 3. Experimental results demonstrated that the mechanical response is non-linear and exhibits combined viscoelastic–viscoplastic behaviour with pronounced strain hardening up to large nominal strains of approximately 12. This response was shown to be closely linked to microstructural evolution within the filament, including progressive fibre recruitment and engagement, fibre debonding and chain disentanglement, followed by stretching of individual fibres. A key methodological outcome of this chapter was the identification of significant differences in measured stress–strain behaviour arising from the choice of gripping system; comparison between screw-sided and bollard grips revealed substantial discrepancies in stress-strain response, highlighting the importance of appropriate testing protocols for highly compliant fibrous materials. Finally, a one-dimensional phenomenological constitutive model was developed to capture the observed viscoelastic–viscoplastic behaviour. The model demonstrated good predictive capability under uniaxial loading as well as under non-monotonic loading conditions, providing a robust framework for the material response.

Subsequently, Chapter 4 investigated the degradation mechanisms and kinetics of electrospun PCL filaments at temperatures above physiological conditions, under both free (unloaded) and mechanically loaded conditions. A central finding of this chapter is that electrospun PCL filaments undergo continuous degradation even over relatively short exposure times, with degradation manifested primarily through a reduction in number-average molecular weight. Importantly, the results demonstrated that the application of mechanical load accelerates this degradation process, indicating a strong coupling between mechanical stress and hydrolytic chain scission. Mechanical loading was also found to influence the evolving mechanical properties of the filaments during degradation. In the early stages of exposure, an increase in elastic modulus and tensile strength was observed, followed by a pronounced reduction in strain at break with increasing degradation time. This behaviour was attributed to stress-assisted microstructural reorganisation within the semi-crystalline polymer, including preferential scission in amorphous regions, stress-induced chain alignment, and secondary crystallisation. These processes increase the relative crystalline fraction and restrict molecular mobility, leading to transient stiffening and strengthening, but at the expense of ductility. Altogether, these findings highlight the role of mechanical loading in modulating both the kinetics and mechanical consequences of degradation in electrospun PCL filaments, underscoring the need to account for coupled chemo-mechanical effects when designing and evaluating biodegradable fibrous scaffolds for load-bearing biomedical applications.

Finally, Chapter 5 extended the findings of the previous studies to physiologically relevant temperatures, demonstrating that although degradation kinetics are slower, the underlying mechanisms governing molecular degradation and mechanical property evolution remain consistent. Mechanical testing using screw-side grips enabled reliable characterisation of time- and rate-dependent behaviour, revealing a progressive reduction in relaxation time with increasing degradation time. This response was attributed to microstructural evolution within the filaments, particularly the preferential degradation of amorphous regions and the associated increase in relative crystallinity, which constrained molecular mobility and shortened relaxation times. Collectively, these results confirm that even under physiological conditions, degradation induces changes in both instantaneous and viscoelastic mechanical behaviour, highlighting the strong coupling between degradation, microstructure, and mechanical performance in electrospun PCL filaments intended for load-bearing biomedical applications.

6.2 Scope and Limitations

Despite the novel insights gained into the thermo–mechanical and degradation behaviour of electrospun networks from both experimental and modelling perspectives, research limitations remain in the present body of work. From an experimental standpoint, the intrinsic complexity of non-woven fibrous networks continues to pose significant challenges for reliable characterisation. Key microstructural features, such as fibre diameter distributions, porosity, inter-fibre interactions, network fusion, fibre recruitment, multi-scale deformation, and fracture mechanisms, are inherently heterogeneous and difficult to quantify in a controlled and repeatable manner. Moreover, characterising the mechanical response of these materials under complex or non-uniform loading conditions remains challenging, as individual fibres and local interactions cannot be readily isolated for direct experimental interrogation. This limitation complicates the interpretation of macroscopic measurements and their linkage to underlying microstructural mechanisms. In this study, some of these challenges were explored by employing different gripping systems to quantify heterogeneous strain fields and by attempting the use of digital image correlation (DIC) to capture multi-scale deformation behaviour. However, due to difficulties associated with speckle pattern stability, resolution limits, and non-affine deformation at the fibre level, reliable DIC calibration proved challenging. As a result, microstructural deformation was primarily assessed through post-deformation analysis of SEM micrographs. Accurately measuring strain in electrospun networks proved to be a critical obstacle, particularly due to the non-affine deformation and evolving load paths within the fibrous architecture. While our proposed methodology improved insights in the reported mechanical measurements, they also highlight the need for further methodological development to fully resolve the complex, multi-scale mechanics of electrospun fibre networks.

The degradation experiments conducted on the role of mechano-chemical interactions in accelerating or modifying degradation pathways has gained increasing traction in the literature (Chen et al., 2026; Guo et al., 2016), yet experimental methods capable of systematically probing these effects in electrospun architectures are still scarce. This research contributes to addressing this gap through the development of a bespoke experimental rig designed to investigate the degradation behaviour of ES filaments under controlled mechanical loading conditions. The rig enabled the simultaneous application of sustained load and elevated temperature exposure, providing new insight into how mechanical constraints influence molecular degradation and mechanical property evolution. Nevertheless, the bespoke nature of the experimental setup introduces several limitations, which are discussed in Section 4.10. These include constraints related to load uniformity, environmental control, and long-term testing stability, which may influence the reproducibility and scalability of the results. In addition, the experimental campaign was necessarily limited in sample number due to the time-intensive nature of degradation studies and the complexity of specimen preparation and testing. A larger sample population would have improved statistical robustness and enabled clearer differentiation between degradation-driven variability and intrinsic material heterogeneity. Despite these limitations, the experimental framework established in this work provides a valuable platform for future investigations into load-assisted degradation of electrospun networks. Further refinement of the rig, combined with expanded testing campaigns and integration with microscopic characterisation techniques, would allow more comprehensive assessment of mechano-chemical degradation mechanisms and strengthen the predictive understanding required for the design of durable, load-bearing biodegradable scaffolds.

Two phenomenological constitutive models were proposed in this thesis to describe the mechanical behaviour of electrospun PCL filaments under different material states. While these models provide a useful descriptive framework, their limitations must be acknowledged. The first model, presented in Chapter 3, adopts a combined viscoelastic–viscoplastic framework to represent the experimentally characterised mechanical response of pristine filaments. This formulation was shown to reproduce both monotonic and non-monotonic stress–strain responses with good qualitative and quantitative agreement across the tested loading regimes. In particular, the model effectively captures rate-dependent stiffening, stress relaxation, and the transition between elastic and plastic deformation. Nevertheless, as a phenomenological representation, the model does not explicitly account for the underlying microstructural mechanisms governing deformation. Furthermore, parameter identification is sensitive to the selected filament design, loading protocol, and the model assumes material homogeneity and isotropy, which may not be strictly valid for electrospun filaments with spatial variations in morphology and residual stresses. As a result, the predictive capability of the model outside of filament design and calibrated deformation regimes remains limited.

The second modelling approach, presented in Chapter 5, aimed to characterise the mechanical response of degraded PCL filaments using a single Maxwell element. While this simplified representation was able to capture the general trend of the stress–strain response and provided some insight into the time-dependent softening behaviour induced by degradation, its descriptive power is inherently constrained. The use of a single relaxation mechanism neglects the spectrum of relaxation times and competing deformation processes that arise from heterogeneous degradation, evolving crystallinity, and chain scission. Consequently, the model is unable to reproduce non-linearities or progressive damage effects (i.e. ductile to brittle) observed experimentally. To partially address these shortcomings, a two-phase Reuss model was explored in an attempt to relate macroscopic behaviour to microstructural heterogeneity. However, the assumptions of iso-stress conditions and sharply defined phases render this approach overly simplistic, preventing a meaningful interpretation of the complex, spatially evolving microstructural phenomena occurring during degradation. A potential improvement to address this limitation would be to extend the current two-phase representation into a three-phase model that explicitly distinguishes between crystalline regions, mobile amorphous domains, and a rigid amorphous fraction associated with tie chains. In such a formulation, the crystalline phase would continue to act as a stiff, load-bearing component, while the mobile amorphous phase governs short-term viscoelastic relaxation through segmental mobility. The rigid amorphous fraction, characterised by constrained chain dynamics, would contribute an intermediate response with longer relaxation times. A key challenge would be to explore the interplay between these three phases and quantify their respective contributions, which could provide deeper insight into the complex and spatially evolving microstructural changes occurring during degradation.

Overall, while the proposed models provide a preliminary phenomenological description of the mechanical response of electrospun PCL filaments, they fall short of capturing the coupled, multi-scale, and evolving nature of deformation and degradation in these systems. These shortcomings underscore the need for more physically grounded constitutive models that explicitly incorporate microstructural evolution, damage, and spatial heterogeneity, potentially through multi-mechanism viscoelastic formulations or multi-scale modelling approaches.

6.3 Future Research Directions

This thesis has contributed new insights to the understanding of polymer behaviour and electrospun fibrous filaments. Building on the findings presented, promising directions for future research emerge from this work. A critical next step is the accurate characterisation of strain and microstructural evolution in electrospun networks across multiple length scales. Given the inherently heterogeneous and non-affine deformation of these materials, future studies should aim to capture deformation simultaneously at the fibre and network levels. A potential approach is the use of a multi-camera experimental setup. At the micro-scale, a high-magnification imaging system could be employed to track local mechanisms such as fibre unwrinkling, realignment, diameter evolution, fibre–fibre debonding, frictional sliding, entanglement dynamics, and network fracture. Concurrently, a second imaging system operating at a lower magnification could capture the macroscopic deformation of the filament, including spatial variations in strain localisation and load redistribution along its length. Coupling these multi-scale deformation measurements with the global stress–strain response obtained from mechanical testing would enable a more complete and physically grounded description of network mechanics. Such an approach would provide critical experimental validation for discrete and continuum network models, which are often based on simplifying assumptions due to the lack of direct microstructural data. Improved experimental insight would therefore facilitate the development of more robust and predictive models for electrospun networks. In addition, complementary methodological developments could include the integration of machine learning techniques for automated fibre tracking, enabling continuous measurement of fibre diameter evolution, orientation changes, and interaction events during deformation. These approaches could be further extended to infer the dominant loading modes experienced by individual fibres, such as axial tension, bending, or buckling, thereby providing unprecedented insight into force transmission within fibrous networks. Such developments would represent a natural extension of current digital image correlation techniques and offer a powerful framework for advancing the experimental mechanics of non-woven fibrous materials.

Future work on degradation testing should focus on both refining the experimental methodology and redesigning the bespoke degradation rig to enable more robust and informative measurements. The rig developed in this thesis provides a solid foundation for future design iterations; however, further improvements can be conceptualised based on the limitations outlined in Section 4.10 and the resources available to subsequent researchers. These refinements may include enhanced load control, improved environmental stability, and increased testing capacity to allow for a greater number of repeat experiments, thereby improving statistical confidence. In parallel, future studies should adopt a more comprehensive characterisation strategy that extends beyond macroscale mechanical measurements. While the present work primarily inferred polymer-level degradation mechanisms from bulk mechanical and thermal responses, future research should incorporate direct polymer-scale characterisation techniques, to more explicitly link degradation-induced molecular changes with evolving mechanical behaviour. Such an integrated, multi-scale approach would significantly improve understanding of degradation mechanisms in electrospun networks and strengthen the predictive capability of degradation models for biomedical applications. Following these refinements and a more in-depth experimental characterisation of electrospun PCL filaments, a natural next step would be to extend static loading protocols to dynamic or cyclic loading conditions, thereby better simulating the mechanical environment experienced in real-life load-bearing applications.

Future modelling efforts should focus on capturing the complex, multi-scale interactions that govern the mechanics of fibrous networks. In the present work, a phenomenological modelling approach was adopted, providing a high-level description of the material response using a generic framework with a limited number of parameters. While effective for capturing global trends, such as non-linear viscoelastic–viscoplastic behaviour and stress relaxation, this approach necessarily abstracts away the underlying microstructural mechanisms. Electrospun networks are inherently more complex, and predictive modelling of their behaviour requires tools that explicitly account for fibre-level interactions, network topology, and evolving connectivity. Progress in this area will require close integration of experimental and theoretical efforts. In particular, comprehensive experimental characterisation, such as multi-scale imaging and tracking of fibre recruitment, reorientation, and junction evolution, should precede model development to provide the necessary physical grounding. While phenomenological models are valuable for interpreting overall behaviour, a more robust framework would involve micromechanical modelling based on representative volume elements (RVEs). Building on existing approaches in the literature (Domaschke et al., 2019; Zündel et al., 2019, 2017), future work should develop RVE-based models tailored to experimentally observed mechanisms. Such models would enable explicit representation of inter-fibre mechanics, fibre engagement and disengagement, junction behaviour, and the individual evolution of fibres, ultimately leading to improved predictive capability for the mechanical response of electrospun fibrous networks.

A natural next step, following the development of a robust micromechanical modelling framework, would be to extend the mechanical description to explicitly incorporate degradation mechanisms. This would involve coupling the network mechanics with degradation-driven weakening of individual fibres and fibre–fibre junctions within an RVE-based framework. In such a model, degradation could be represented through the progressive evolution of fibre-level properties, including reductions in stiffness, strength, and failure strain, as well as changes in junction integrity and load-transfer efficiency. The governing laws for degradation would be informed directly by insights obtained from extended experimental characterisation at the polymer scale. This would enable the model to distinguish between competing degradation pathways, and to capture load-assisted degradation effects arising from mechano-chemical coupling. By embedding these degradation laws within an RVE framework, it would become possible to predict how local molecular-level damage accumulates and propagates through the fibrous network, ultimately leading to macroscopic stiffness loss, strength reduction, and failure. Such a coupled mechanical–degradation model would offer a powerful predictive tool for assessing long-term performance of electrospun scaffolds under physiological conditions and mechanical loading, and would significantly enhance the ability to design biodegradable fibrous constructs with controlled degradation rates and reliable mechanical function over their intended service life.

Appendix A

Mathematical Framework for VE-VP Model

This chapter presents the mathematical derivation of the analytical solution that underpins the return mapping algorithm for the viscoelastic(VE)-viscoplastic(VP) model proposed in Chapter 3.

A.1 Mathematical Derivation

The constitutive model is based on the assumption that the total strain can be decomposed into VE and VP components:

$$\varepsilon = \varepsilon^{ve} + \varepsilon^{vp} \tag{A.1}$$

According to the Boltzmann hereditary integral (Bergstrom, 2015; Brinson, 2015), the stress is related to the viscoelastic strain by:

$$\sigma(t) = \int_0^t E(t-\tau)\frac{\partial \varepsilon^{ve}}{\partial \tau} d\tau \tag{A.2}$$

where $E(t)$ is the viscoelastic modulus of the generalised Maxwell model, which can be expressed using Prony series as:

$$E(t) = E_\infty + \sum_{i=1}^{N} E_i \exp\left(-\frac{t}{\tau_i}\right) \tag{A.3}$$

where E_∞ is the long-term modulus, τ_i are the viscoelastic relaxation times and E_i the corresponding moduli of the N viscoelastic branches in the generalised Maxwell model. Substituting expression (A.3) into the hereditary integral (A.2), we obtain the stress as:

$$\sigma(t) = E_\infty \varepsilon^{ve} + \sum_{i=1}^{N} \sigma_i(t) \tag{A.4}$$

where σ_i is the stress for each elastic spring in the Maxwell model and can be expressed in the following mathematical form:

$$\sigma_i(t) = E_i \exp\left(-\frac{t}{\tau_i}\right) \int_{-\infty}^{t} \exp\left(\frac{\tau}{\tau_i}\right) \frac{\partial \varepsilon^{ve}}{\partial \tau} d\tau \tag{A.5}$$

To solve equation A.5 analytically, we decompose the solution into discrete time steps and predict the stress at the next time step. This can be expressed as follows:

$$\sigma_i(t_{n+1}) = E_i \cdot \exp\biggl(\frac{-t_n - \Delta t}{\tau_i}\biggr) \left[\int_{-\infty}^{t_n} \exp\biggl(\frac{\tau}{\tau_i}\biggr) \frac{\partial \varepsilon^{ve}}{\partial \tau} d\tau + \int_{t_n}^{t_{n+1}} \exp\biggl(\frac{\tau}{\tau_i}\biggr) \frac{\partial \varepsilon^{ve}}{\partial \tau} d\tau\right] \tag{A.6}$$

$$\begin{aligned} \sigma_i(t_{n+1}) = E_i \cdot \exp\biggl(-\frac{t_n}{\tau_i}\biggr) \exp\biggl(-\frac{\Delta t}{\tau_i}\biggr) \int_{-\infty}^{t_n} \exp\biggl(\frac{\tau}{\tau_i}\biggr) \frac{\partial \varepsilon^{ve}}{\partial \tau} d\tau \\ + E_i \cdot \exp\biggl(-\frac{t_{n+1}}{\tau_i}\biggr) \int_{t_n}^{t_{n+1}} \exp\biggl(\frac{\tau}{\tau_i}\biggr) \frac{\partial \varepsilon^{ve}}{\partial \tau} d\tau \end{aligned} \tag{A.7}$$

$$\sigma_i(t_{n+1}) = \sigma_i(t_n) \cdot \exp\biggl(-\frac{\Delta t}{\tau_i}\biggr) + E_i \int_{t_n}^{t_{n+1}} \exp\biggl(\frac{\tau - t_{n+1}}{\tau_i}\biggr) \frac{\partial \varepsilon^{ve}}{\partial \tau} d\tau \tag{A.8}$$

Assuming the viscoelastic strain rate ($\frac{\partial \varepsilon^{ve}}{\partial \tau}$) is approximately constant, it can be approximated such that $\frac{\partial \varepsilon^{ve}}{\partial \tau} \approx \frac{\Delta \varepsilon^{ve}}{\Delta t}$. Therefore,

$$\sigma_i(t_{n+1}) = \sigma_i(t_n) \cdot \exp\biggl(-\frac{\Delta t}{\tau_i}\biggr) + E_i \left[\tau_i \cdot \exp\biggl(\frac{\tau - t_{n+1}}{\tau_i}\biggr)\right]_{t_n}^{t_{n+1}} \frac{\Delta \varepsilon^{ve}}{\Delta t} \tag{A.9}$$

$$\sigma_i(t_{n+1}) = \sigma_i(t_n) \cdot \exp\biggl(-\frac{\Delta t}{\tau_i}\biggr) + E_i \left(1 - \exp\biggl(-\frac{\Delta t}{\tau_i}\biggr)\right) \frac{\tau_i}{\Delta t} \cdot \Delta \varepsilon^{ve} \tag{A.10}$$

Returning to equation A.4, replacing the analytical solution derived in equation A.10, we would obtain the following:

$$\sigma(t_{n+1}) = E_\infty \underbrace{\varepsilon^{ve}(t_{n+1})}_{\varepsilon^{ve}(t_{n+1}) = \Delta \varepsilon^{ve} + \varepsilon^{ve}(t_n)} + \sum_{i=1}^{N} \sigma_i(t_{n+1}) \tag{A.11}$$

$$\sigma(t_{n+1}) = E_\infty \Delta \varepsilon^{ve} + E_\infty \varepsilon^{ve}(t_n) + \sum_{i=1}^{N} \sigma_i(t_{n+1}) \tag{A.12}$$

Writing the full equation:

$$\sigma(t_{n+1}) \;=\; E_\infty \Delta\varepsilon^{ve} + E_\infty \varepsilon^{ve}(t_n) + \sum_{i=1}^{N} E_i \left(1 - \exp\!\left(-\frac{\Delta t}{\tau_i}\right)\right) \frac{\tau_i}{\Delta t} \cdot \Delta\varepsilon^{ve} + \sum_{i=1}^{N} \sigma_i(t_n) \cdot \exp\!\left(-\frac{\Delta t}{\tau_i}\right) \tag{A.13}$$

$$\sigma(t_{n+1}) = E_\infty \varepsilon^{ve}(t_n) + \underbrace{\left[E_\infty + \sum_{i=1}^{N} E_i \left(1 - \exp\!\left(-\frac{\Delta t}{\tau_i}\right)\right) \frac{\tau_i}{\Delta t}\right]}_{\tilde{E}} \Delta\varepsilon^{ve} + \sum_{i=1}^{N} \sigma_i(t_n) \cdot \exp\!\left(-\frac{\Delta t}{\tau_i}\right) \tag{A.14}$$

The change in viscoelastic strain is unknown ($\Delta\varepsilon^{ve} = \Delta\varepsilon - \Delta\varepsilon^{vp}$) and is the parameter that needs to determined from each time step in order to estimate the viscoelastic stress. The final solution becomes,

$$\sigma(t_{n+1}) = E_\infty \varepsilon^{ve}(t_n) + \tilde{E}\Delta\varepsilon^{ve} + \sum_{i=1}^{N} \sigma_i(t_n) \cdot \exp\!\left(-\frac{\Delta t}{\tau_i}\right) \tag{A.15}$$

A.2 Return Mapping Algorithm

The return mapping algorithm is developed for the following purpose: given the state of internal variables at time (t_n), and a prescribed total strain increment ($\Delta\varepsilon$), the algorithm enables computation of the stress and internal variables at time (t_{n+1}).

The increment of a variable (stress, strain, etc.) will be denoted by:

$$\Delta(\bullet) \equiv (\bullet)_{n+1} - (\bullet)_n \tag{A.16}$$

The stress-elastic strain relationship at the future time step (t_{n+1}) can be written as:

$$\sigma_{n+1} = \tilde{E} \cdot [(\varepsilon_n + \Delta\varepsilon) - (\varepsilon_n^{vp} + \Delta\varepsilon^{vp})] \tag{A.17}$$

The first step of the return mapping algorithm is to determine the trial viscoelastic stress assuming that no plastic deformation occurs during the increment ($\Delta p = 0, \Delta\varepsilon^{vp} = 0$). Using the analytical formulation derived from the Boltzmann superposition principle (Eqn. A.15), the trial (or predicted) stress at time (t_{n+1}) is given by:

$$\sigma^{pred}(t_{n+1}) = E_\infty \cdot \varepsilon_n^{ve} + \tilde{E} \cdot \Delta\varepsilon + \sum_{i=1}^{N} \exp\left(-\frac{\Delta t}{\tau_i}\right) \cdot \sigma_i(t_n) \tag{A.18}$$

where the effective viscoelastic modulus is:

$$\tilde{E} = E_\infty + \sum_{i=1}^{N} E_i \left(1 - \exp\left(-\frac{\Delta t}{\tau_i}\right)\right) \cdot \left(\frac{\tau_i}{\Delta t}\right) \tag{A.19}$$

In this algorithm, we use a rate-dependent J_2 VP model with isotropic hardening function. In this model, we use a yield function to evaluate the predicted stress and check for the onset of plasticity:

$$f(\sigma^{pred}, p_n) = \left|\sigma^{pred}\right| - \sigma_y - R(p_n) \tag{A.20}$$

where σ^{pred} is the viscoelastic predicted stress, σ_y is the yield stress, $R(p_n)$ is the hardening stress, and p_n the accumulated plasticity at the current time step. The accumulation of plastic strain p is an internal variable which keeps track of the history of the VP strain:

$$p(t) = \int_0^t \dot{p}(\tau)\, d\tau \quad \text{with} \quad \dot{p} = |\dot{\varepsilon}^{vp}| \tag{A.21}$$

The uniaxial flow rule for the viscoplastic strain is expressed as:

$$\dot{\varepsilon}^{vp} = \dot{p}\, \mathrm{sign}(\sigma) \tag{A.22}$$

The hardening stress function is written in an exponential form:

$$R(p_n) = k \cdot \exp(n \cdot p_n) \tag{A.23}$$

where k is the hardening coefficient, n the hardening exponent.

If the predictor stress satisfies the yield condition ($f_{n+1} \leq 0$), then the assumption is true and predicted viscoelastic stress is the solution to the constitutive equations, such that:

$$\begin{cases} \Delta\varepsilon^{ve} = \Delta\varepsilon,\ \Delta\varepsilon^{vp} = 0 \\ p = p_n,\ \varepsilon^{vp}(t_{n+1}) = \varepsilon^{vp}(t_n) \\ \sigma_i(t_{n+1}) = \sum_{i=1}^{N} \left(\sigma_i(t_n) \cdot \exp\left(-\frac{\Delta t}{\tau_i}\right) + E_i \cdot \left(1 - \exp\left(-\frac{\Delta t}{\tau_i}\right)\right) \left(\frac{\tau_i}{\Delta t}\right) \Delta\varepsilon\right) \\ \sigma(t_{n+1}) = \sigma(t_n) \end{cases} \tag{A.24}$$

Alternatively, if the yield condition is violated ($f_{n+1} > 0$), plasticity has developed during the increment. The stress must be corrected such that it satisfied the consistency condition ($f_{n+1} = 0$), as well as the flow rule and hardening law. In this step, we use a plastic corrector algorithm to adjust the stress.

$$\begin{aligned} \sigma(t_{n+1}) &= \sigma^{pred}(t_{n+1}) - \tilde{E} \cdot \Delta\varepsilon^{vp} && \text{(A.25)} \\ &= \sigma^{pred}(t_{n+1}) - \tilde{E} \cdot \Delta p \, \mathrm{sign}(\sigma) && \text{(A.26)} \end{aligned}$$

We can isolate the change in stress

$$(\sigma^{pred} - \sigma) = \tilde{E} \cdot \Delta p \cdot \mathrm{sign}(\sigma) \tag{A.27}$$

Since we want to write this in scalar form, we multiply both sides by $\mathrm{sign}(\sigma)$:

$$(\sigma^{pred} - \sigma) \, \mathrm{sign}(\sigma) = \tilde{E}\Delta p > 0 \tag{A.28}$$

Since $\tilde{E} > 0$ and $\Delta p > 0$, this term is strictly positive. This implies the stress has decreased in the direction of loading and that plastic strain increment reduces the predicted stress so that it lies on the yield surface. To ensure direction of stress does not change in the corrector step and that plastic flow only reduces in magnitude and not direction, we have the following assumption:

$$\mathrm{sign}(\sigma) = \mathrm{sign}(\sigma^{pred}) \tag{A.29}$$

To ensure plastic correction reduces stress magnitude without changing its direction, the corrected stress lies on the same branch of the stress-strain curve. Using this assumption, we can express the stress as:

$$|\sigma| = \left|\sigma^{pred}\right| - \tilde{E} \cdot \Delta p \tag{A.30}$$

In order to determine the total change in plasticity, we begin with an initial guess and say that plasticity has changed by Δp, and we relate this value to a rate-dependent viscoplastic flow rule:

$$\Delta p = g_v(f) \cdot \Delta t \tag{A.31}$$

where $g_v(f)$ is a viscoplastic flow function, commonly following the Norton-type law:

$$g_v(\sigma_{eq}, p) = \begin{cases} \frac{\sigma_y}{\eta}\left(\frac{f}{\sigma_y}\right)^m, & \text{if } f > 0 \\ 0, & \text{otherwise} \end{cases} \tag{A.32}$$

where η is the viscoplastic modulus and m is the viscoplastic exponent.

In order to solve for the plastic multiplier $\Delta p = p_{n+1} - p_n$, we apply the Newton-Raphson method to enforce both the flow rule and stress equilibrium. We begin by solving for a non-linear residual system:

$$\begin{cases} k_p = \Delta p - g_v(f)\Delta t \\ k_\sigma = \sigma + \tilde{E}\Delta p - \sigma^{pred} \end{cases} \tag{A.33}$$

We will solve these values through a local iteration scheme because they are defined at the (Gauss) point level. At each iteration, we are solving the following corrections:

$$\begin{cases} c_p = -\frac{1}{h_v} \cdot \left(\frac{k_p}{(dg_v/df) \cdot \Delta t} + k_\sigma\right) \\ c_\sigma = -(k_\sigma + H_{alg} \cdot c_p) \end{cases} \tag{A.34}$$

where h_v is the effective viscoplastic tangent modulus, given by:

$$h_v \equiv \frac{1}{(dg_v/df) \cdot \Delta t} + H_{alg} + \frac{dR}{dp} \tag{A.35}$$

where H_{alg} is the consistent tangent operator, which for the 1D case, is considered as the total modulus $E = E_\infty + E_i$ calculated for the viscoelastic modulus. We update the accumulated plasticity and stress at that given time step through the following functions.

$$\begin{cases} p_{n+1} = p_n + c_p \\ \sigma_{n+1} = \sigma_n + c_\sigma \end{cases} \tag{A.36}$$

The iterations stopped once a convergence criterion was satisfied:

$$\sqrt{(k_p)^2 + \left(\frac{k_\sigma}{\sigma_y}\right)^2} \leq \text{tolerance, e.g., } 10^{-6} \tag{A.37}$$

After convergence, all of the internal variables at t_{n+1} can then be updated consistently:

$$
\begin{aligned}
p &= p_n + \Delta p && \text{(A.38)}\\
\varepsilon^{vp} &= \varepsilon_n^{vp} + \Delta p \,\mathrm{sign}(\sigma^{pred}) && \text{(A.39)}\\
\sigma &= \sigma^{pred} - \tilde{E}\Delta\varepsilon^{vp} && \text{(A.40)}\\
\Delta\varepsilon^{ve} &= \Delta\varepsilon - \Delta\varepsilon^{vp} && \text{(A.41)}\\
\sigma_i &= \sum_{i=1}^{N} \exp\left(-\frac{\Delta t}{\tau_i}\right)\sigma_i(t_n) + \sum_{i=1}^{N} E_i \left(1 - \exp\left(-\frac{\Delta t}{\tau_i}\right)\right) \frac{\tau_i}{\Delta t}\Delta\varepsilon^{ve} && \text{(A.42)}
\end{aligned}
$$

This completes the return mapping update for a single time increment.

Bibliography

Abdullah, K. and Molnár, K. (2024). The Influence of In Vitro Degradation on the Properties of Polylactic Acid Electrospun Fiber Mats. *Fibers*, 13(1).

Abhari, R. E., Carr, A. J., and Mouthuy, P.-A. (2018a). *15 - Multifilament electrospun scaffolds for soft tissue reconstruction*, pages 295–328. Woodhead Publishing.

Abhari, R. E., Mouthuy, P. A., Vernet, A., Schneider, J. E., Brown, C. P., and Carr, A. J. (2018b). Using an industrial braiding machine to upscale the production and modulate the design of electrospun medical yarns. *Polymer Testing*, 69:188–198.

Abhari, R. E., Mouthuy, P.-A., Zargar, N., Brown, C., and Carr, A. (2017). Effect of annealing on the mechanical properties and the degradation of electrospun polydioxanone filaments. *Journal of the Mechanical Behavior of Biomedical Materials*, 67:127–134.

Akbulatov, S. and Boulatov, R. (2017). Experimental Polymer Mechanochemistry and its Interpretational Frameworks. *Chemphyschem*, 18(11):1422–1450.

Alexeev, D., Goedecke, N., Snedeker, J., and Ferguson, S. (2020). Mechanical evaluation of electrospun poly(ε-caprolactone) single fibers. *Materials Today Communications*, 24:101211.

Alfaro De Prá, M. A., Ribeiro-do Valle, R. M., Maraschin, M., and Veleirinho, B. (2017). Effect of collector design on the morphological properties of polycaprolactone electrospun fibers. *Materials Letters*, 193:154–157.

Alharbi, N., Daraei, A., Lee, H., and Guthold, M. (2023). The effect of molecular weight and fiber diameter on the mechanical properties of single, electrospun PCL nanofibers. *Materials Today Communications*, 35.

Alharbi, N. and Guthold, M. (2024). Mechanical properties of hydrated electrospun polycaprolactone (PCL) nanofibers. *Journal of the Mechanical Behavior of Biomedical Materials*, 155:106564.

Ali, S. A. M., Zhong, S. P., Doherty, P. J., and Williams, D. F. (1993). Mechanisms of polymer degradation in implantable devices: I. Poly(caprolactone). *Biomaterials*, 14(9):648–656.

Ali, U., Zhou, Y., Wang, X., and Lin, T. (2012). Direct electrospinning of highly twisted, continuous nanofiber yarns. *Journal of the Textile Institute*, 103(1):80–88.

Ameer, Pr, and Kasoju (2019). Strategies to Tune Electrospun Scaffold Porosity for Effective Cell Response in Tissue Engineering. *Journal of Functional Biomaterials*, 10(3):30.

Amjad, S. N. and Picu, R. C. (2022). Stress relaxation in network materials: the contribution of the network. *Soft Matter*, 18(2):446–454.

Amoroso, N. J., D'Amore, A., Hong, Y., Wagner, W. R., and Sacks, M. S. (2011). Elastomeric Electrospun Polyurethane Scaffolds: The Interrelationship Between Fabrication Conditions, Fiber Topology, and Mechanical Properties. *Advanced Materials*, 23(1):106–111.

Andersson, R. L., Ström, V., Gedde, U. W., Mallon, P. E., Hedenqvist, M. S., and Olsson, R. T. (2015). Micromechanics of ultra-toughened electrospun PMMA/PEO fibres as revealed by in-situ tensile testing in an electron microscope. *Scientific Reports*, 4(1):6335.

Argento, G., Simonet, M., Oomens, C. W. J., and Baaijens, F. P. T. (2012). Multi-scale mechanical characterization of scaffolds for heart valve tissue engineering. *Journal of Biomechanics*, 45(16):2893–2898.

Arinstein, A., Burman, M., Gendelman, O., and Zussman, E. (2007). Effect of supramolecular structure on polymer nanofibre elasticity. *Nature Nanotechnology*, 2(1):59–62.

Arruda, E. M. and Boyce, M. C. (1993). A three-dimensional constitutive model for the large stretch behavior of rubber elastic materials. *Journal of the Mechanics and Physics of Solids*, 41(2):389–412.

Arslan, M. and Boyce, M. C. (2006). Constitutive Modeling of the Finite Deformation Behavior of Membranes Possessing a Triangulated Network Microstructure. *Journal of Applied Mechanics*, 73(4):536–543.

Baji, A., Mai, Y.-W., Wong, S.-C., Abtahi, M., and Chen, P. (2010). Electrospinning of polymer nanofibers: Effects on oriented morphology, structures and tensile properties. *Composites Science and Technology*, 70(5):703–718.

Baker, S., Sigley, J., Helms, C. C., Stitzel, J., Berry, J., Bonin, K., and Guthold, M. (2012). The mechanical properties of dry, electrospun fibrinogen fibers. *Materials Science and Engineering: C*, 32(2):215–221.

Baker, S. R., Banerjee, S., Bonin, K., and Guthold, M. (2015). Determining the mechanical properties of electrospun poly-ε-caprolactone (PCL) nanofibers using AFM and a novel fiber anchoring technique. *Materials Science and Engineering: C*, 59:203–212.

Barrett, G. R., Line, L. L., Shelton, W. R., Manning, J. O., and Phelps, R. (1993). The Dacron ligament prosthesis in anterior cruciate ligament reconstruction: A four-year review. *The American Journal of Sports Medicine*, 21(3):367–373.

Bartnikowski, M., Dargaville, T. R., Ivanovski, S., and Hutmacher, D. W. (2019). Degradation mechanisms of polycaprolactone in the context of chemistry, geometry and environment. *Progress in Polymer Science*, 96:1–20.

Bazgir, M., Zhang, W., Zhang, X., Elies, J., Saeinasab, M., Coates, P., Youseffi, M., and Sefat, F. (2021). Degradation and Characterisation of Electrospun Polycaprolactone (PCL) and Poly(lactic-co-glycolic acid) (PLGA) Scaffolds for Vascular Tissue Engineering. *Materials*, 14(17):4773.

Bell, G. I. (1978). Models for the Specific Adhesion of Cells to Cells. *Science*, 200(4342):618–627.

Bellincampi, L. D., Closkey, R. F., Prasad, R., Zawadsky, J. P., and Dunn, M. G. (1998). Viability of fibroblast-seeded ligament analogs after autogenous implantation. *Journal of Orthopaedic Research*, 16(4):414–420.

Bergstrom, J. (2015). *Mechanics of solid polymers : theory and computational modeling*. William Andrew is an imprint of Elsevier, Amsterdam, first edition.

Bhardwaj, N. and Kundu, S. C. (2010). Electrospinning: A fascinating fiber fabrication technique. *Biotechnology Advances*, 28(3):325–347.

Bolgen, N., Menceloglu, Y. Z., Acatay, K., Vargel, I., and Piskin, E. (2005). In vitro and in vivo degradation of non-woven materials made of poly(ε-caprolactone) nanofibers prepared by electrospinning under different conditions. *Journal of Biomaterials Science, Polymer Edition*, 16(12):1537–1555.

Bosworth, L. A. (2014). Travelling along the Clinical Roadmap: Developing Electrospun Scaffolds for Tendon Repair. *Conference Papers in Science*, 2014:1–6.

Bosworth, L. A. and Downes, S. (2010). Physicochemical characterisation of degrading polycaprolactone scaffolds. *Polymer Degradation and Stability*, 95(12):2269–2276.

Boyce, M. C. and Arruda, E. M. (2000). Constitutive models of rubber elasticity: A review. *Rubber chemistry and technology*, 73(3):504–523.

Brinson, H. F. (2015). *Polymer Engineering Science and Viscoelasticity: An Introduction.* Springer Nature, Netherlands, 2nd 2015 edition.

Burkersroda, F. v., Schedl, L., and Göpferich, A. (2002). Why degradable polymers undergo surface erosion or bulk erosion. *Biomaterials*, 23(21):4221–4231.

Caballero, D. E., Montini-Ballarin, F., Gimenez, J. M., Biocca, N., Rull, N., Frontini, P., and Urquiza, S. A. (2022). Reduced kinematic multiscale model for tissue engineering electrospun scaffolds. *Mechanics of Materials*, 166:104214.

Caballero, D. E., Montini-Ballarin, F., Gimenez, J. M., and Urquiza, S. A. (2019). Multiscale constitutive model with progressive recruitment for nanofibrous scaffolds. *Journal of the Mechanical Behavior of Biomedical Materials*, 98:225–234.

Cai, Y. Z., Zhang, G. R., Wang, L. L., Jiang, Y. Z., Ouyang, H. W., and Zou, X. H. (2012). Novel biodegradable three-dimensional macroporous scaffold using aligned electrospun nanofibrous yarns for bone tissue engineering. *J Biomed Mater Res A*, 100(5):1187–94.

Callister, W. (2005). *Fundamentals of Materials Science and Engineering: An Integrated Approach.* Wiley.

Carleton, J. B., Rodin, G. J., and Sacks, M. S. (2017). Layered Elastomeric Fibrous Scaffolds: An In-Silico Study of the Achievable Range of Mechanical Behaviors. *ACS Biomaterials Science & Engineering*, 3(11):2907–2921.

Carlisle, C. R., Coulais, C., Namboothiry, M., Carroll, D. L., Hantgan, R. R., and Guthold, M. (2009). The mechanical properties of individual, electrospun fibrinogen fibers. *Biomaterials*, 30(6):1205–1213.

Carniel, T. A., De Castro, P. B., Santos, A. L. G., De Mello Roesler, C. R., Breitenbach, E. R., Salmoria, G. V., Morozo, M. A., Colaco, P. A., Fiori, M. A., and Fancello, E. A. (2021). Mechanical characterization of hydrolysis effects on the stiffness of bioabsorbable polymeric filaments: An experimental and modeling approach based on a simple constitutive damage model. *Polymers and Polymer Composites*, 29(9):S262–S273.

Casalini, T. (2017). *3 - Bioresorbability of polymers: Chemistry, mechanisms, and modeling*, pages 65–83. Woodhead Publishing.

Castilla-Cortázar, I., Más-Estellés, J., Meseguer-Dueñas, J. M., Escobar Ivirico, J. L., Marí, B., and Vidaurre, A. (2012). Hydrolytic and enzymatic degradation of a poly(ε-caprolactone) network. *Polymer Degradation and Stability*, 97(8):1241–1248.

Chainani, A., Hippensteel, K. J., Kishan, A., Garrigues, N. W., Ruch, D. S., Guilak, F., and Little, D. (2013). Multilayered electrospun scaffolds for tendon tissue engineering. *Tissue Eng Part A*, 19(23-24):2594–604.

Chandler, A., Schofield, R. M., Mouthuy, P.-A., and Assender, H. E. (2025). Stretch-Induced Microstructural Evolution of Electrospun Polycaprolactone Microfibers for Biomedical Applications. *ACS Applied Polymer Materials*, 7(13):8504–8518.

Chandra, R. and Rustgi, R. (1998). Biodegradable polymers. *Progress in Polymer Science*, 23(7).

Chavoshnejad, P. and Razavi, M. J. (2020). Effect of the Interfiber Bonding on the Mechanical Behavior of Electrospun Fibrous Mats. *Sci Rep*, 10(1):7709.

Chen, H., Pan, Z., Sulley, G. S., Williams, C. K., and Brassart, L. (2026). Hydrolytic degradation of amorphous PLA: Effect of mechanical loads. *Polymer Degradation and Stability*, 243.

Chen, N., Koker, M. K. A., Uzun, S., and Silberstein, M. N. (2016). In-situ X-ray study of the deformation mechanisms of non-woven polypropylene. *International Journal of Solids and Structures*, 97-98:200–208.

Chen, N. and Silberstein, M. N. (2018). Determination of Bond Strengths in Non-woven Fabrics: a Combined Experimental and Computational Approach. *Experimental Mechanics*, 58(2):343–355.

Chen, N. and Silberstein, M. N. (2019). A micromechanics-based damage model for non-woven fiber networks. *International Journal of Solids and Structures*, 160:18–31.

Chidambaram, A., Davis, H., and Batra, S. K. (2000). Strength loss in thermally bonded polypropylene fibers. *International Nonwovens Journal*, 9(3):27–35.

Chlanda, A., Kijenska-Gawronska, E., Zdunek, J., and Swieszkowski, W. (2020). Internal nanocrystalline structure and stiffness alterations of electrospun polycaprolactone-based mats after six months of in vitro degradation. An atomic force microscopy assay. *J Mech Behav Biomed Mater*, 101:103437.

Chung, A. S., Hwang, H. S., Das, D., Zuk, P., McAllister, D. R., and Wu, B. M. (2012). Lamellar stack formation and degradative behaviors of hydrolytically degraded poly(ε-caprolactone) and poly(glycolide-ε-caprolactone) blended fibers. *Journal of Biomedical Materials Research Part B: Applied Biomaterials*, 100B(1):274–284.

Cipitria, A., Skelton, A., Dargaville, T. R., Dalton, P. D., and Hutmacher, D. W. (2011). Design, fabrication and characterization of PCL electrospun scaffolds—a review. *Journal of Materials Chemistry*, 21(26):9419.

Coombes, A. G., Rizzi, S. C., Williamson, M., Barralet, J. E., Downes, S., and Wallace, W. A. (2004). Precipitation casting of polycaprolactone for applications in tissue engineering and drug delivery. *Biomaterials*, 25(2):315–25.

Courtney, T., Sacks, M., Stankus, J., Guan, J., and Wagner, W. (2006). Design and analysis of tissue engineering scaffolds that mimic soft tissue mechanical anisotropy. *Biomaterials*.

Croisier, F., Duwez, A. S., Jérôme, C., Léonard, A. F., Van Der Werf, K. O., Dijkstra, P. J., and Bennink, M. L. (2012). Mechanical testing of electrospun PCL fibers. *Acta Biomaterialia*, 8(1):218–224.

Dahlstedt, L., Dalén, N., and Jonsson, U. (1990). Goretex prosthetic ligament vs. Kennedy ligament augmentation device in anterior cruciate ligament reconstruction: A prospective randomized 3-year follow-up of 41 cases. *Acta Orthopaedica Scandinavica*, 61(3):217–224.

Delp, A., Becker, A., Hülsbusch, D., Scholz, R., Müller, M., Glasmacher, B., and Walther, F. (2021). In Situ Characterization of Polycaprolactone Fiber Response to Quasi-Static Tensile Loading in Scanning Electron Microscopy. *Polymers*, 13(13):2090.

Deng, M., Zhou, J., Chen, G., Burkley, D., Xu, Y., Jamiolkowski, D., and Barbolt, T. (2005). Effect of load and temperature on in vitro degradation of poly(glycolide-co-l-lactide) multifilament braids. *Biomaterials*, 26(20):4327–4336.

Dhanasekaran, N. P. D., Muthuvelu, K. S., and Arumugasamy, S. K. (2022). *Recent Advancement in Biomedical Applications of Polycaprolactone and Polycaprolactone-Based Materials*, pages 795–809. Elsevier, Oxford.

Domaschke, S. and Ehret, A. E. (2020). On the homogeneity and isotropy of planar long fibre network computational models. *SN Applied Sciences*, 2(4).

Domaschke, S., Morel, A., Kaufmann, R., Hofmann, J., Rossi, R. M., Mazza, E., Fortunato, G., and Ehret, A. E. (2020). Predicting the macroscopic response of electrospun membranes based on microstructure and single fibre properties. *Journal of the Mechanical Behavior of Biomedical Materials*, 104:103634.

Domaschke, S., Zündel, M., Mazza, E., and Ehret, A. E. (2019). A 3D computational model of electrospun networks and its application to inform a reduced modelling approach. *International Journal of Solids and Structures*, 158:76–89.

Domingos, M., Chiellini, F., Cometa, S., De Giglio, E., Grillo-Fernandes, E., Bártolo, P., and Chiellini, E. (2010). Evaluation ofin vitrodegradation of PCL scaffolds fabricated via BioExtrusion. Part 1: Influence of the degradation environment. *Virtual and Physical Prototyping*, 5(2):65–73.

Dong, L., Li, L., Chen, H., Cao, Y., and Lei, H. (2024). Mechanochemistry: Fundamental Principles and Applications. *Adv Sci (Weinh)*, page e2403949.

Dong, Y., Liao, S., Ngiam, M., Chan, C. K., and Ramakrishna, S. (2009). Degradation Behaviors of Electrospun Resorbable Polyester Nanofibers. *Tissue Engineering Part B: Reviews*, 15(3):333–351.

Duling, R. R., Dupaix, R. B., Katsube, N., and Lannutti, J. (2008). Mechanical Characterization of Electrospun Polycaprolactone (PCL): A Potential Scaffold for Tissue Engineering. *Journal of Biomechanical Engineering*, 130(1).

Dunn, M. G., Liesch, J. B., Tiku, M. L., and Zawadsky, J. P. (1995). Development of fibroblast-seeded ligament analogs for ACL reconstruction. *Journal of Biomedical Materials Research*, 29(11):1363–1371.

Dwivedi, R., Kumar, S., Pandey, R., Mahajan, A., Nandana, D., Katti, D. S., and Mehrotra, D. (2020). Polycaprolactone as biomaterial for bone scaffolds: Review of literature. *J Oral Biol Craniofac Res*, 10(1):381–388.

D'Amore, A., Amoroso, N., Gottardi, R., Hobson, C., Carruthers, C., Watkins, S., Wagner, W. R., and Sacks, M. S. (2014). From single fiber to macro-level mechanics: A structural finite-element model for elastomeric fibrous biomaterials. *Journal of the Mechanical Behavior of Biomedical Materials*, 39:146–161.

Eda, G. and Shivkumar, S. (2007). Bead-to-fiber transition in electrospun polystyrene. *Journal of Applied Polymer Science*, 106(1):475–487.

Edlund, U. and Albertsson, A. C. (2003). Polyesters based on diacid monomers. *Adv Drug Deliv Rev*, 55(4):585–609.

Engelmayr, George C., J. and Sacks, M. S. (2006). A Structural Model for the Flexural Mechanics of Nonwoven Tissue Engineering Scaffolds. *Journal of Biomechanical Engineering*, 128(4):610–622.

Fang, J., Niu, H., Lin, T., and Wang, X. (2008). Applications of electrospun nanofibers. *Science Bulletin*, 53(15):2265–2286.

Farukh, F., Demirci, E., Sabuncuoglu, B., Acar, M., Pourdeyhimi, B., and Silberschmidt, V. V. (2014a). Mechanical behaviour of nonwovens: Analysis of effect of manufacturing parameters with parametric computational model. *Computational Materials Science*, 94:8–16.

Farukh, F., Demirci, E., Sabuncuoglu, B., Acar, M., Pourdeyhimi, B., and Silberschmidt, V. V. (2014b). Numerical analysis of progressive damage in nonwoven fibrous networks under tension. *International Journal of Solids and Structures*, 51(9):1670–1685.

Fennessey, S. F. and Farris, R. J. (2004). Fabrication of aligned and molecularly oriented electrospun polyacrylonitrile nanofibers and the mechanical behavior of their twisted yarns. *Polymer*, 45(12):4217–4225.

Fernández, J., Etxeberria, A., and Sarasua, J.-R. (2015). In vitro degradation studies and mechanical behavior of poly(ε-caprolactone-co-δ-valerolactone) and poly(ε-caprolactone-co-L-lactide) with random and semi-alternating chain microstructures. *European Polymer Journal*, 71:585–595.

Fernández, J., Etxeberria, A., Ugartemendia, J. M., Petisco, S., and Sarasua, J.-R. (2012). Effects of chain microstructures on mechanical behavior and aging of a poly(L-lactide-co-ε-caprolactone) biomedical thermoplastic-elastomer. *Journal of the Mechanical Behavior of Biomedical Materials*, 12:29–38.

Fernández, J., Larrañaga, A., Etxeberría, A., and Sarasua, J. R. (2013). Effects of chain microstructures and derived crystallization capability on hydrolytic degradation of poly(l-lactide/ε-caprolactone) copolymers. *Polymer Degradation and Stability*, 98(2):481–489.

Ferreira, T. Z., Pan, Z., Mouthuy, P.-A., and Brassart, L. (2025). Characterisation and modelling of continuous electrospun poly(ε- caprolactone) filaments for biological tissue repair. *Journal of the Mechanical Behavior of Biomedical Materials*, 161:106810.

Flamini, M. D., Lima, T., Corkum, K., Alvarez, N. J., and Beachley, V. (2022). Annealing post-drawn polycaprolactone (PCL) nanofibers optimizes crystallinity and molecular alignment and enhances mechanical properties and drug release profiles. *Materials Advances*, 3(7):3303–3315.

Fung, Y. C., Perrone, N., and Anliker, M. (1972). *Biomechanics, its foundations and objectives.* Prentice-Hall, Englewood Cliffs, N.J.

Gabr, A. and Haddad, F. (2022). The National Ligament Registry: The Seventh Annual Report. Report.

Galeski, A. (2003). Strength and toughness of crystalline polymer systems. *Progress in Polymer Science*, 28(12):1643–1699.

Gaona, L. A., Gómez Ribelles, J. L., Perilla, J. E., and Lebourg, M. (2012). Hydrolytic degradation of PLLA/PCL microporous membranes prepared by freeze extraction. *Polymer Degradation and Stability*, 97(9):1621–1632.

Garg, K. and Bowlin, G. L. (2011). Electrospinning jets and nanofibrous structures. *Biomicrofluidics*, 5(1):013403.

Gaumer, J., Prasad, A., Lee, D., and Lannutti, J. (2009). Structure–function relationships and source-to-ground distance in electrospun polycaprolactone. *Acta Biomaterialia*, 5(5):1552–1561.

Gleadall, A. (2015). *Mechanical properties of biodegradable polymers for medical applications*, pages 163–199.

Goutianos, S., Mao, R., and Peijs, T. (2018). Effect of inter-fibre bonding on the fracture of fibrous networks with strong interactions. *International Journal of Solids and Structures*, 136-137:271–278.

Greiner, A. and Wendorff, J. H. (2007). Electrospinning: A Fascinating Method for the Preparation of Ultrathin Fibers. *Angewandte Chemie International Edition*, 46(30):5670–5703.

Guo, M., Chu, Z., Yao, J., Feng, W., Wang, Y., Wang, L., and Fan, Y. (2016). The effects of tensile stress on degradation of biodegradable PLGA membranes: A quantitative study. *Polymer Degradation and Stability*, 124:95–100.

Guo, Y., Wang, X., Shen, Y., Dong, K., Shen, L., and Alzalab, A. A. A. (2022). Research progress, models and simulation of electrospinning technology: a review. *Journal of Materials Science*, 57(1):58–104.

Gupta, B. S. and Moghe, A. K. (2013). *Nanofiber structures for medical biotextiles*, pages 48–90.

Göpferich, A. (1996). Mechanisms of polymer degradation and erosion. *Biomaterials*, 17(2):103–114.

Hagen, R., Salmén, L., Lavebratt, H., and Stenberg, B. (1994). Comparison of dynamic mechanical measurements and Tg determinations with two different instruments. *Polymer Testing*, 13(2):113–128.

Hakkarainen, M. (2002). *Aliphatic Polyesters: Abiotic and Biotic Degradation and Degradation Products*, pages 113–138. Springer Berlin Heidelberg, Berlin, Heidelberg.

Holzapfel, G. A. (2005). Similarities between soft biological tissues and rubberlike materials. In *Constitutive Models for Rubber IV*, pages 607–617, Leiden. A.A. Balkema.

Hu, W., Huang, Z. M., and Liu, X. Y. (2010). Development of braided drug-loaded nanofiber sutures. *Nanotechnology*, 21(31):315104.

Huang, F., Li, K., and Kulachenko, A. (2009). Measurement of interfiber friction force for pulp fibers by atomic force microscopy. *Journal of Materials Science*, 44(14):3770–3776.

Huang, X., Wen, D., Zhao, Y., Wang, Q., Zhou, W., and Deng, D. (2016). Skeleton-based tracing of curved fibers from 3D X-ray microtomographic imaging. *Results in Physics*, 6:170–177.

Huang, Z.-M., Zhang, Y. Z., Ramakrishna, S., and Lim, C. T. (2004). Electrospinning and mechanical characterization of gelatin nanofibers. *Polymer*, 45(15):5361–5368.

Ibrahim, H. M. and Klingner, A. (2020). A review on electrospun polymeric nanofibers: Production parameters and potential applications. *Polymer Testing*, 90:106647.

Indelicato, P. A., Pascale, M. S., and Huegel, M. O. (1989). Early experience with the GORE-TEX polytetrafluoroethylene anterior cruciate ligament prosthesis. *Am J Sports Med*, 17(1):55–2.

Iordanskii, A. L., Zaikov, G. E., and Berlin, A. A. (2015). Diffusion kinetics of hydrolysis of biodegradable polymers. Weight loss and control of the release of low molecular weight substances. *Polymer Science Series D*, 8(3):211–218.

ISO (2019). ISO 2307:2019 - Fibre ropes - Determination of certain physical and mechanical properties.

Jariyavidyanont, K., Yu, Q., Petzold, A., Thurn-Albrecht, T., Gluge, R., Altenbach, H., and Androsch, R. (2023). Young's modulus of the different crystalline phases of poly (l-lactic acid). *J Mech Behav Biomed Mater*, 137:105546.

Jenkins, M. J. and Harrison, K. L. (2008). The effect of crystalline morphology on the degradation of polycaprolactone in a solution of phosphate buffer and lipase. *Polymers for Advanced Technologies*, 19(12):1901–1906.

Ji, Y., Li, B., Ge, S., Sokolov, J. C., and Rafailovich, M. H. (2006). Structure and Nanomechanical Characterization of Electrospun PS/Clay Nanocomposite Fibers. *Langmuir*, 22(3):1321–1328.

Ji, Y., Li, C., Wang, G., Koo, J., Ge, S., Li, B., Jiang, J., Herzberg, B., Klein, T., Chen, S., Sokolov, J. C., and Rafailovich, M. H. (2008). Confinement-induced super strong PS/MWNT composite nanofibers. *EPL (Europhysics Letters)*, 84(5).

Johnson, J., Niehaus, A., Nichols, S., Lee, D., Koepsel, J., Anderson, D., and Lannutti, J. (2009). Electrospun PCL in Vitro: a Microstructural Basis for Mechanical Property Changes. *Journal of Biomaterials Science, Polymer Edition*, 20(4):467–481.

Jubera, R., Ridruejo, A., González, C., and Llorca, J. (2014). Mechanical behavior and deformation micromechanisms of polypropylene nonwoven fabrics as a function of temperature and strain rate. *Mechanics of Materials*, 74:14–25.

Jung, J. H., Ree, M., and Kim, H. (2006). Acid- and base-catalyzed hydrolyses of aliphatic polycarbonates and polyesters. *Catalysis Today*, 115(1-4):283–287.

Kartus, J., Movin, T., and Karlsson, J. (2001). Donor-site morbidity and anterior knee problems after anterior cruciate ligament reconstruction using autografts. *Arthroscopy: The Journal of Arthroscopic & Related Surgery*, 17(9):971–980.

Kauzmann, W. and Eyring, H. (1940). The Viscous Flow of Large Molecules. *Journal of the American Chemical Society*, 62(11):3113–3125.

Kawai, A., Hamamoto, N., and Sasanuma, Y. (2022). Conformational characteristics and conformation-dependent properties of poly(ε-caprolactone). *Physical Chemistry Chemical Physics*, 24(18):11382–11394.

Ketelaars, A. A. J., Papantoniou, Y., and Nakayama, K. (1997). Analysis of the density and the enthalpy of poly(ε-caprolactone)-polycarbonate blends: Amorphous phase compatibility and the effect of secondary crystallization. *Journal of Applied Polymer Science*, 66(5):921–927.

Khiste, S. V., Ranganath, V., and Nichani, A. S. (2013). Evaluation of tensile strength of surgical synthetic absorbable suture materials: an *in vitro* study. *Journal of Periodontal & Implant Science*, 43(3):130.

Khodadadi, M., Alijani, S., Montazeri, M., Esmaeilizadeh, N., Sadeghi-Soureh, S., and Pilehvar-Soltanahmadi, Y. (2020). Recent advances in electrospun nanofiber-mediated drug delivery strategies for localized cancer chemotherapy. *Journal of Biomedical Materials Research Part A*, 108(7):1444–1458.

Kim, K., Yu, M., Zong, X., Chiu, J., Fang, D., Seo, Y. S., Hsiao, B. S., Chu, B., and Hadjiargyrou, M. (2003). Control of degradation rate and hydrophilicity in electrospun non-woven poly(D,L-lactide) nanofiber scaffolds for biomedical applications. *Biomaterials*, 24(27):4977–85.

Kim, K. W., Lee, K. H., Khil, M. S., Ho, Y. S., and Kim, H. Y. (2004). The effect of molecular weight and the linear velocity of drum surface on the properties of electrospun poly(ethylene terephthalate) nonwovens. *Fibers and Polymers*, 5(2):122–127.

Kohane, D. S. and Langer, R. (2008). Polymeric Biomaterials in Tissue Engineering. *Pediatric Research*, 63(5):487–491.

Kongkhlang, T., Tashiro, K., Kotaki, M., and Chirachanchai, S. (2008). Electrospinning as a New Technique To Control the Crystal Morphology and Molecular Orientation of Polyoxymethylene Nanofibers. *Journal of the American Chemical Society*, 130(46):15460–15466.

Kulachenko, A. and Uesaka, T. (2012). Direct simulations of fiber network deformation and failure. *Mechanics of Materials*, 51:1–14.

Kumar, V. and Rawal, A. (2017). Elastic moduli of electrospun mats: Importance of fiber curvature and specimen dimensions. *Journal of the Mechanical Behavior of Biomedical Materials*, 72:6–13.

Kurz, R., Schulz, M., Scheliga, F., Men, Y., Seidlitz, A., Thurn-Albrecht, T., and Saalwächter, K. (2018). Interplay between Crystallization and Entanglements in the Amorphous Phase of the Crystal-Fixed Polymer Poly(ε-Caprolactone). *Macromolecules*, 51:5831.

Labet, M. and Thielemans, W. (2009). Synthesis of Polycaprolactone: A Review. *Chem. Soc. Rev.*, 38:3484.

Lach, A. A., Morris, H. L., Martins, J. A., Stace, E. T., Carr, A. J., and Mouthuy, P.-A. (2019). Pyridine as an additive to improve the deposition of continuous electrospun filaments. *PLOS ONE*, 14(4):e0214419.

Lam, C. X., Hutmacher, D. W., Schantz, J. T., Woodruff, M. A., and Teoh, S. H. (2009). Evaluation of polycaprolactone scaffold degradation for 6 months in vitro and in vivo. *J Biomed Mater Res A*, 90(3):906–19.

Lam, C. X. F., Savalani, M. M., Teoh, S.-H., and Hutmacher, D. W. (2008). Dynamics of in vitro polymer degradation of polycaprolactone-based scaffolds: accelerated versus simulated physiological conditions. *Biomedical Materials*, 3(3):034108.

Lanza, R., Langer, R., Vacanti, J. P., and Atala, A. (2020). *Principles of tissue engineering.* Academic Press, London, fifth edition.

Larrañaga, A., Aldazabal, P., Martin, F. J., and Sarasua, J. R. (2014). Hydrolytic degradation and bioactivity of lactide and caprolactone based sponge-like scaffolds loaded with bioactive glass particles. *Polymer Degradation and Stability*, 110:121–128.

Lasprilla-Botero, J., Álvarez Láinez, M., and Lagaron, J. M. (2018). The influence of electrospinning parameters and solvent selection on the morphology and diameter of polyimide nanofibers. *Materials Today Communications*, 14:1–9.

Laycock, B., Nikolić, M., Colwell, J. M., Gauthier, E., Halley, P., Bottle, S., and George, G. (2017). Lifetime prediction of biodegradable polymers. *Progress in polymer science*, 71:144–189.

Lee, K., Lee, B., Kim, C., Kim, H., Kim, K., and Nah, C. (2005). Stress-strain behavior of the electrospun thermoplastic polyurethane elastomer fiber mats. *Macromolecular Research*, 13(5):441–445.

Lee, K. H., Kim, H. Y., Khil, M. S., Ra, Y. M., and Lee, D. R. (2003). Characterization of nano-structured poly(ε-caprolactone) nonwoven mats via electrospinning. *Polymer*, 44(4):1287–1294.

Lee, S., Kimoto, M., Tanaka, M., Tsuji, H., and Nishino, T. (2018). Crystal modulus of poly (lactic acid)s, and their stereocomplex. *Polymer*, 138:124–131.

Legnani, C., Ventura, A., Terzaghi, C., Borgo, E., and Albisetti, W. (2010). Anterior cruciate ligament reconstruction with synthetic grafts. A review of literature. *International Orthopaedics*, 34(4):465–471.

Li, C., Guo, C., Fitzpatrick, V., Ibrahim, A., Zwierstra, M. J., Hanna, P., Lechtig, A., Nazarian, A., Lin, S. J., and Kaplan, D. L. (2020). Design of biodegradable, implantable devices towards clinical translation. *Nature Reviews Materials*, 5(1):61–81.

Li, P., Feng, X., Jia, X., and Fan, Y. (2010). Influences of tensile load on in vitro degradation of an electrospun poly(L-lactide-co-glycolide) scaffold. *Acta Biomater*, 6(8):2991–6.

Li, S. (1999). Hydrolytic degradation characteristics of aliphatic polyesters derived from lactic and glycolic acids. *Journal of Biomedical Materials Research*, 48(3):342–353.

Lim, C. T., Tan, E. P. S., and Ng, S. Y. (2008). Effects of crystalline morphology on the tensile properties of electrospun polymer nanofibers. *Applied Physics Letters*, 92(14):141908.

Limbert, G., Omar, R., Krynauw, H., Bezuidenhout, D., and Franz, T. (2016). The anisotropic mechanical behaviour of electro-spun biodegradable polymer scaffolds: Experimental characterisation and constitutive formulation. *Journal of the Mechanical Behavior of Biomedical Materials*, 53:21–39.

Lin, C.-C. and Anseth, K. S. (2013). *The Biodegradation of Biodegradable Polymeric Biomaterials*, pages 716–728.

Lin, J., Chen, K., Liang, M., Machain, T. C., Crouch, D., Mengoli, S., Exley, G., Zaplluzha, A., Baldwin, M., Jackson, W., Cosker, T., Snelling, S., Carr, A., Blunn, G., Price, A., and Mouthuy, P.-A. (2025). Translational Potential of an Electrospun Polycaprolactone Scaffold for Anterior Cruciate Ligament Reconstruction. *Advanced Fiber Materials.*

Lin, L. and Argon, A. S. (1994). Structure and plastic deformation of polyethylene. *Journal of Materials Science*, 29(2):294–323.

Little, D., Guilak, F., and Ruch, D. S. (2010). Ligament-derived matrix stimulates a ligamentous phenotype in human adipose-derived stem cells. *Tissue Eng Part A*, 16(7):2307–19.

Little, U., Buchanan, F., Harkin-Jones, E., McCaigue, M., Farrar, D., and Dickson, G. (2009). Accelerated degradation behaviour of poly(ε-caprolactone) via melt blending with poly(aspartic acid-co-lactide) (PAL). *Polymer Degradation and Stability*, 94(2):213–220.

Liu, L., Xu, W., Ding, Y., Agarwal, S., Greiner, A., and Duan, G. (2020). A review of smart electrospun fibers toward textiles. *Composites Communications*, 22:100506.

Liu, X., Xu, H., Zhang, M., and Yu, D.-G. (2021). Electrospun Medicated Nanofibers for Wound Healing: Review. *Membranes*, 11(10):770.

Liu, Y., Li, K., M. Mohideen, M., and Ramakrishna, S. (2019). *Chapter 8 - Three-dimensional (3D) printing based on controlled melt electrospinning in polymeric biomedical materials*, pages 159–172. Academic Press.

Lohmander, L. S., Östenberg, A., Englund, M., and Roos, H. (2004). High prevalence of knee osteoarthritis, pain, and functional limitations in female soccer players twelve years after anterior cruciate ligament injury. *Arthritis & Rheumatism*, 50(10):3145–3152.

Lucas, N., Bienaime, C., Belloy, C., Queneudec, M., Silvestre, F., and Nava-Saucedo, J. E. (2008). Polymer biodegradation: mechanisms and estimation techniques. *Chemosphere*, 73(4):429–42.

Luciani, A., Coccoli, V., Orsi, S., Ambrosio, L., and Netti, P. A. (2008). PCL microspheres based functional scaffolds by bottom-up approach with predefined microstructural properties and release profiles. *Biomaterials*, 29(36):4800–7.

Lukianov, A. V., Richmond, J. C., Barrett, G. R., and Gillquist, J. (1989). A multicenter study on the results of anterior cruciate ligament reconstruction using a Dacron ligament prosthesis in "salvage" cases. *The American Journal of Sports Medicine*, 17(3):380–386.

Lustiger, A. and Markham, R. L. (1983). Importance of tie molecules in preventing polyethylene fracture under long-term loading conditions. *Polymer*, 24(12):1647–1654.

Lyu, Schley, J., Loy, B., Lind, D., Hobot, C., Sparer, R., and Untereker, D. (2007). Kinetics and Time-Temperature Equivalence of Polymer Degradation. *Biomacromolecules*, 8(7):2301–2310.

Majima, T., Funakosi, T., Iwasaki, N., Yamane, S.-T., Harada, K., Nonaka, S., Minami, A., and Nishimura, S.-I. (2005). Alginate and chitosan polyion complex hybrid fibers for scaffolds in ligament and tendon tissue engineering. *Journal of Orthopaedic Science*, 10(3):302–307.

Malikmammadov, E., Tanir, T. E., Kiziltay, A., Hasirci, V., and Hasirci, N. (2018). PCL and PCL-based materials in biomedical applications. *Journal of Biomaterials Science, Polymer Edition*, 29(7-9):863–893.

Manoukian, O. S., Sardashti, N., Stedman, T., Gailiunas, K., Ojha, A., Penalosa, A., Mancuso, C., Hobert, M., and Kumbar, S. G. (2019). *Biomaterials for Tissue Engineering and Regenerative Medicine*, pages 462–482. Elsevier, Oxford.

Marieswaran, M., Jain, I., Garg, B., Sharma, V., and Kalyanasundaram, D. (2018). A Review on Biomechanics of Anterior Cruciate Ligament and Materials for Reconstruction. *Applied Bionics and Biomechanics*, 2018(1):4657824.

Martins, C., Pinto, V., Guedes, R. M., and Marques, A. T. (2015). Creep and Stress Relaxation Behaviour of PLA-PCL Fibres – A Linear Modelling Approach. *Procedia Engineering*, 114:768–775.

Mazza, E. and Ehret, A. E. (2015). Mechanical biocompatibility of highly deformable biomedical materials. *Journal of the Mechanical Behavior of Biomedical Materials*, 48:100–124.

Megelski, S., Stephens, J. S., Chase, D. B., and Rabolt, J. F. (2002). Micro- and Nanostructured Surface Morphology on Electrospun Polymer Fibers. *Macromolecules*, 35(22):8456–8466.

Men, Y. (2020). Critical Strains Determine the Tensile Deformation Mechanism in Semicrystalline Polymers. *Macromolecules*, 53(21):9155–9157.

Menczel, J. D. and Prime, R. B. (2009). Thermal analysis of polymers.

Miled, B., Doghri, I., and Delannay, L. (2011). Coupled viscoelastic–viscoplastic modeling of homogeneous and isotropic polymers: Numerical algorithm and analytical solutions. *Computer Methods in Applied Mechanics and Engineering*, 200(47):3381–3394.

Mirkhalaf, M. and Vadizadeh, R. (2024). Micro-mechanical modeling of semi-crystalline polymers: A review. *International Journal of Solids and Structures*, 290.

Molnar, K., Vas, L. M., and Czigany, T. (2012). Determination of tensile strength of electrospun single nanofibers through modeling tensile behavior of the nanofibrous mat. *Composites Part B: Engineering*, 43(1):15–21.

Mondesert, H. (2020). *Anisotropic PCL electrospun scaffolds for soft tissue engineering: Elaboration, morphological and mechanical properties.* Thesis.

Mouthuy, P. A., Zargar, N., Hakimi, O., Lostis, E., and Carr, A. (2015). Fabrication of continuous electrospun filaments with potential for use as medical fibres. *Biofabrication*, 7(2):025006.

Nangare, S., Jadhav, N., Ghagare, P., and Muthane, T. (2020). Pharmaceutical applications of electrospinning. *Annales Pharmaceutiques Françaises*, 78(1):1–11.

Natta, F. J. v., Hill, J. W., and Carothers, W. H. (1934). Studies of Polymerization and Ring Formation. XXIII.1 ε-Caprolactone and its Polymers. *Journal of the American Chemical Society*, 56:455–457.

Natu, M. V., de Sousa, H. C., and Gil, M. H. (2013). Influence of polymer processing technique on long term degradation of poly(ε-caprolactone) constructs. *Polymer Degradation and Stability*, 98(1):44–51.

Natu, M. V., Sousa, H. C. d., and Gil, M. H. (2011). *Electrospun Drug-Eluting Fibers for Biomedical Applications*, pages 57–85. Studies in Mechanobiology, Tissue Engineering and Biomaterials. Springer Berlin Heidelberg.

Nau, T. and Teuschl, A. (2015). Regeneration of the anterior cruciate ligament: Current strategies in tissue engineering. *World J Orthop*, 6(1):127–36.

Negi, V. and Picu, R. C. (2019). Mechanical behavior of nonwoven non-crosslinked fibrous mats with adhesion and friction. *Soft Matter*, 15(29):5951–5964.

Nerurkar, N. L., Elliott, D. M., and Mauck, R. L. (2007). Mechanics of oriented electrospun nanofibrous scaffolds for annulus fibrosus tissue engineering. *Journal of Orthopaedic Research*, 25(8):1018–1028.

Nikolova, M. P. and Chavali, M. S. (2019). Recent advances in biomaterials for 3D scaffolds: A review. *Bioactive Materials*, 4:271–292.

Noh, S., Jung, W., Sim, S., Son, H., Choi, J.-H., and Koo, J. (2023). Effect of Drawing Conditions on Crystal Structure and Mechanical Properties of Melt-Spun Polylactic Acid Fibers. *Fibers and Polymers*, 24(2):483–488.

Ozdil, D., Wimpenny, I., Aydin, H. M., and Yang, Y. (2017). *Biocompatibility of biodegradable medical polymers*, pages 379–414. Elsevier.

Pai, C.-L., Boyce, M. C., and Rutledge, G. C. (2011). On the importance of fiber curvature to the elastic moduli of electrospun nonwoven fiber meshes. *Polymer*, 52(26):6126–6133.

Paulos, L. E., Rosenberg, T. D., Grewe, S. R., Tearse, D. S., and Beck, C. L. (1992). The GORE-TEX anterior cruciate ligament prosthesis:A long-term followup. *The American Journal of Sports Medicine*, 20(3):246–252.

Pena, J., Corrales, T., Izquierdo-Barba, I., Serrano, M. C., Portoles, M. T., Pagani, R., and Vallet-Regi, M. (2006). Alkaline-treated poly(ε-caprolactone) films: degradation in the presence or absence of fibroblasts. *J Biomed Mater Res A*, 76(4):788–97.

Perez, J. (2018). *Physics and mechanics of amorphous polymers.* Physics and mechanics of amorphous polymers. Routledge, Place of publication not identified.

Picu, C. R. (2020). Constitutive models for random fiber network materials: A review of current status and challenges. *Mechanics Research Communications*, 114:103605.

Picu, C. R. (2022). *Time Dependent Behavior*, book section 9, pages 338–369. Cambridge University Press, Cambridge.

Picu, R. C. (2011). Mechanics of random fiber networks—a review. *Soft Matter*, 7(15):6768.

Pinar, H. and Gillquist, J. (1989). Dacron augmentation of a free patellar tendon graft: A biomechanical study. *Arthroscopy: The Journal of Arthroscopic & Related Surgery*, 5(4):328–330.

Pitt, C. G., Chasalow, F. I., Hibionada, Y. M., Klimas, D. M., and Schindler, A. (1981a). Aliphatic polyesters. I. The degradation of poly(ε-caprolactone) *in vivo*. *Journal of Applied Polymer Science*, 26(11):3779–3787.

Pitt, C. G. and Gu, Z.-w. (1987). Modification of the rates of chain cleavage of poly(ε-caprolactone) and related polyesters in the solid state. *Journal of Controlled Release*, 4(4):283–292.

Pitt, G. G., Gratzl, M. M., Kimmel, G. L., Surles, J., and Sohindler, A. (1981b). Aliphatic polyesters II. The degradation of poly (DL-lactide), poly (ε-caprolactone), and their copolymers in vivo. *Biomaterials*, 2(4):215–220.

Polak-Kraśna, K., Abaei, A. R., Shirazi, R. N., Parle, E., Carroll, O., Ronan, W., and Vaughan, T. J. (2021). Physical and mechanical degradation behaviour of semi-crystalline PLLA for bioresorbable stent applications. *Journal of the Mechanical Behavior of Biomedical Materials*, 118.

Polińska, M., Rozanski, A., Galeski, A., and Bojda, J. (2021). The Modulus of the Amorphous Phase of Semicrystalline Polymers. *Macromolecules*, 54(19):9113–9123.

Rashid, T. U., Gorga, R. E., and Krause, W. E. (2021). Mechanical Properties of Electrospun Fibers—A Critical Review. *Advanced Engineering Materials*, page 2100153.

Ratner, B. D., Hoffman, A. S., Schoen, F. J., and Lemons, J. E. (2004). *Biomaterials science: an introduction to materials in medicine.* Elsevier.

Rawal, A. (2022). *2 - Micromechanics of nonwoven materials*, pages 13–47. Elsevier.

Rawal, A., Rao, P. V. K., Kumar, V., and Kukovecz, A. (2019). A critical review on the absorptive glass mat (AGM) separators synergistically designed via fiber and structural parameters. *Journal of Power Sources*, 430:175–192.

Reddy, J. N. (2013). *An introduction to continuum mechanics.* Cambridge University Press, Cambridge, second edition.

Reneker, D. H. and Fong, H. (2006). *Polymeric nanofibers.* ACS symposium series. American Chemical Society, Washington, DC.

Reneker, D. H. and Yarin, A. L. (2008). Electrospinning jets and polymer nanofibers. *Polymer*, 49(10):2387–2425.

Richard-Lacroix, M. and Pellerin, C. (2013). Molecular Orientation in Electrospun Fibers: From Mats to Single Fibers. *Macromolecules*, 46(24):9473–9493.

Ridruejo, A., González, C., and Llorca, J. (2011). Micromechanisms of deformation and fracture of polypropylene nonwoven fabrics. *International Journal of Solids and Structures*, 48(1):153–162.

Rizvi, M. S., Kumar, P., Katti, D. S., and Pal, A. (2012). Mathematical model of mechanical behavior of micro/nanofibrous materials designed for extracellular matrix substitutes. *Acta Biomaterialia*, 8(11):4111–4122.

Roach, P., Eglin, D., Rohde, K., and Perry, C. C. (2007). Modern biomaterials: a review—bulk properties and implications of surface modifications. *Journal of Materials Science: Materials in Medicine*, 18(7):1263–1277.

Roos, E. M. (2005). Joint injury causes knee osteoarthritis in young adults. *Current Opinion in Rheumatology*, 17(2):195–200.

Rothrauff, B. B., Lauro, B. B., Yang, G., Debski, R. E., Musahl, V., and Tuan, R. S. (2017). Braided and Stacked Electrospun Nanofibrous Scaffolds for Tendon and Ligament Tissue Engineering. *Tissue Eng Part A*, 23(9-10):378–389.

Rutledge, G. C. and Fridrikh, S. V. (2007). Formation of fibers by electrospinning. *Advanced Drug Delivery Reviews*, 59(14):1384–1391.

Rutledge, G. C., Lowery, J. L., and Pai, C.-L. (2009). Characterization by Mercury Porosimetry of Nonwoven Fiber Media with Deformation. *Journal of Engineered Fibers and Fabrics*, 4(3):155892500900400.

Sadd, M. H. (2019). *Chapter 9 - Constitutive relations and formulation of theories incorporating material microstructure*, pages 331–379. Academic Press.

Sailema-Palate, G. P., Vidaurre, A., Campillo-Fernández, A. J., and Castilla-Cortázar, I. (2016). A comparative study on Poly(ε-caprolactone) film degradation at extreme pH values. *Polymer Degradation and Stability*, 130:118–125.

Samanta, D., Koithan, J. A., Muliana, A. H., and Pharr, M. (2025). Effect of mechanical loading on PLGA biodegradation. *Polymer Degradation and Stability*, 240.

Sanders, T. L., Maradit Kremers, H., Bryan, A. J., Larson, D. R., Dahm, D. L., Levy, B. A., Stuart, M. J., and Krych, A. J. (2016). Incidence of Anterior Cruciate Ligament Tears and Reconstruction: A 21-Year Population-Based Study. *The American Journal of Sports Medicine*, 44(6):1502–1507.

Savić, L., Augustyniak, E. M., Kastensson, A., Snelling, S., Abhari, R. E., Baldwin, M., Price, A., Jackson, W., Carr, A., and Mouthuy, P.-A. (2021). Early development of a polycaprolactone electrospun augment for anterior cruciate ligament reconstruction. *Materials Science and Engineering: C*, 129:112414.

Schmied, F. J., Teichert, C., Kappel, L., Hirn, U., and Schennach, R. (2012). Joint strength measurements of individual fiber-fiber bonds: an atomic force microscopy based method. *Rev Sci Instrum*, 83(7):073902.

Seguela, R. (2005). Critical review of the molecular topology of semicrystalline polymers: The origin and assessment of intercrystalline tie molecules and chain entanglements. *Journal of Polymer Science Part B: Polymer Physics*, 43(14):1729–1748.

Sensini, A. and Cristofolini, L. (2018). Biofabrication of Electrospun Scaffolds for the Regeneration of Tendons and Ligaments. *Materials*, 11(10):1963.

Sethuraman, V., Makornkaewkeyoon, K., Khalf, A., and Madihally, S. V. (2013). Influence of scaffold forming techniques on stress relaxation behavior of polycaprolactone scaffolds. *Journal of Applied Polymer Science*.

Silberstein, M. N., Pai, C.-L., Rutledge, G. C., and Boyce, M. C. (2012). Elastic–plastic behavior of non-woven fibrous mats. *Journal of the Mechanics and Physics of Solids*, 60(2):295–318.

Siparsky, G. L., Voorhees, K. J., Dorgan, J. R., and Schilling, K. (1997). Water transport in polylactic acid (PLA), PLA/ polycaprolactone copolymers, and PLA/polyethylene glycol blends. *Journal of environmental polymer degradation*, 5(3):125–136.

Sisson, A. L., Ekinci, D., and Lendlein, A. (2013). The contemporary role of ε-caprolactone chemistry to create advanced polymer architectures. *Polymer*, 54(17):4333–4350.

Song, P., Trivedi, A. R., and Siviour, C. R. (2023). Mechanical response of four polycarbonates at a wide range of strain rates and temperatures. *Polymer Testing*, 121.

Sozumert, E., Farukh, F., Sabuncuoglu, B., Demirci, E., Acar, M., Pourdeyhimi, B., and Silberschmidt, V. V. (2020). Deformation and damage of random fibrous networks. *International Journal of Solids and Structures*, 184:233–247.

Sozumert, E. and Silberschmidt, V. V. (2022). *1 - Mechanics of fibrous networks: Basic behaviour*, pages 1–12. Elsevier.

Stace, E. T., Mouthuy, P.-A., Carr, A. J., and Ye, H. (2019). *5.33 - Biomaterials: Electrospinning*, pages 424–441. Pergamon, Oxford.

Stachewicz, U., Bailey, R. J., Wang, W., and Barber, A. H. (2012). Size dependent mechanical properties of electrospun polymer fibers from a composite structure. *Polymer*, 53(22):5132–5137.

Stachewicz, U., Hang, F., and Barber, A. H. (2014). Adhesion anisotropy between contacting electrospun fibers. *Langmuir*, 30(23):6819–25.

Struik, L. C. E. (1987). The mechanical and physical ageing of semicrystalline polymers: 1. *Polymer*, 28(9):1521–1533.

Stylianopoulos, T., Bashur, C. A., Goldstein, A. S., Guelcher, S. A., and Barocas, V. H. (2008). Computational predictions of the tensile properties of electrospun fibre meshes: Effect of fibre diameter and fibre orientation. *Journal of the Mechanical Behavior of Biomedical Materials*, 1(4):326–335.

Sun, H., Mei, L., Song, C., Cui, X., and Wang, P. (2006). The in vivo degradation, absorption and excretion of PCL-based implant. *Biomaterials*, 27(9):1735–1740.

Suwantong, O. (2016). Biomedical applications of electrospun polycaprolactone fiber mats. *Polymers for Advanced Technologies*, 27(10):1264–1273.

Tan, E. P. and Lim, C. T. (2006). Effects of annealing on the structural and mechanical properties of electrospun polymeric nanofibres. *Nanotechnology*, 17(10):2649–54.

Tan, E. P. S. and Lim, C. T. (2004). Physical properties of a single polymeric nanofiber. *Applied Physics Letters*, 84(9):1603–1605.

Tan, E. P. S., Ng, S. Y., and Lim, C. T. (2004). Tensile testing of a single ultrafine polymeric fiber. *Biomaterials*, 26(13):1453–1456.

Tao, J. and Shivkumar, S. (2007). Molecular weight dependent structural regimes during the electrospinning of PVA. *Materials Letters*, 61(11):2325–2328.

Teo, W. E. and Ramakrishna, S. (2006). A review on electrospinning design and nanofibre assemblies. *Nanotechnology*, 17(14):R89–R106.

Therin, M., Christel, P., Li, S., Garreau, H., and Vert, M. (1992). In vivo degradation of massive poly(α-hydroxy acids): Validation of In vitro findings. *Biomaterials*, 13(9):594–600.

Tsuji, H. and Ikada, Y. (1998). Blends of aliphatic polyesters. II. Hydrolysis of solution-cast blends from poly(L-lactide) and poly(ε-caprolactone) in phosphate-buffered solution. *Journal of Applied Polymer Science*, 67(3):405–415.

Tsuji, H., Ono, T., Saeki, T., Daimon, H., and Fujie, K. (2005). Hydrolytic degradation of poly(ε-caprolactone) in the melt. *Polymer Degradation and Stability*, 89(2):336–343.

Vaid, R., Yildirim, E., Pasquinelli, M. A., and King, M. W. (2021). Hydrolytic Degradation of Polylactic Acid Fibers as a Function of pH and Exposure Time. *Molecules*, 26(24).

van Dommelen, J. A. W., Parks, D. M., Boyce, M. C., Brekelmans, W. A. M., and Baaijens, F. P. T. (2003). Micromechanical modeling of the elasto-viscoplastic behavior of semi-crystalline polymers. *Journal of the Mechanics and Physics of Solids*, 51(3):519–541.

Vass, P., Szabó, E., Domokos, A., Hirsch, E., Galata, D., Farkas, B., Démuth, B., Andersen, S. K., Vigh, T., Verreck, G., Marosi, G., and Nagy, Z. K. (2020). Scale-up of electrospinning technology: Applications in the pharmaceutical industry. *WIREs Nanomedicine and Nanobiotechnology*, 12(4).

Venugopal, J. and Ramakrishna, S. (2005). Applications of polymer nanofibers in biomedicine and biotechnology. *Applied Biochemistry and Biotechnology*, 125(3):147–157.

Vieira, A. C., Vieira, J. C., Ferra, J. M., Magalhaes, F. D., Guedes, R. M., and Marques, A. T. (2011). Mechanical study of PLA-PCL fibers during in vitro degradation. *J Mech Behav Biomed Mater*, 4(3):451–60.

Waheed, S., Butcher, A. L., and Oyen, M. L. (2018). The viscoelastic response of electrospun poly(vinyl alcohol) mats. *Journal of the Mechanical Behavior of Biomedical Materials*, 77:383–388.

Wan, L. Y., Wang, H., Gao, W., and Ko, F. (2015). An analysis of the tensile properties of nanofiber mats. *Polymer*, 73:62–67.

Ward, I. M. and Sweeney, J. (2012). *Mechanical properties of solid polymers.* John Wiley & Sons, Chichester, West Sussex, third edition edition.

Wasanasuk, K. and Tashiro, K. (2012). Theoretical and Experimental Evaluation of Crystallite Moduli of Various Crystalline Forms of Poly(l-lactic acid). *Macromolecules*, 45(17):7019–7026.

Wei, X., Xia, Z., Wong, S.-C., and Baji, A. (2009). Modelling of mechanical properties of electrospun nanofibre network. *International Journal Of Experimental And Computational Biomechanics*, 1(1):pp45–57.

Wex, C., Arndt, S., Stoll, A., Bruns, C., and Kupriyanova, Y. (2015). Isotropic incompressible hyperelastic models for modelling the mechanical behaviour of biological tissues: a review. *Biomedical Engineering / Biomedizinische Technik*, 60(6):577–592.

Wong, D., Verron, E., Andriyana, A., and Ang, B. C. (2019). Constitutive modeling of randomly oriented electrospun nanofibrous membranes. *Continuum Mechanics and Thermodynamics*, 31(1):317–329.

Wong, S.-C., Baji, A., and Leng, S. (2008). Effect of fiber diameter on tensile properties of electrospun poly(ε-caprolactone). *Polymer*, 49(21):4713–4722.

Woodard, L. N. and Grunlan, M. A. (2018). Hydrolytic Degradation and Erosion of Polyester Biomaterials. *ACS Macro Lett*, 7(8):976–982.

Woodruff, M. A. and Hutmacher, D. W. (2010). The return of a forgotten polymer—Polycaprolactone in the 21st century. *Progress in Polymer Science*, 35(10):1217–1256.

Woodward, S. C., Brewer, P. S., Moatamed, F., Schindler, A., and Pitt, C. G. (1985). The intracellular degradation of poly(ε-caprolactone). *J Biomed Mater Res*, 19(4):437–44.

Xue, J., Wu, T., Dai, Y., and Xia, Y. (2019). Electrospinning and Electrospun Nanofibers: Methods, Materials, and Applications. *Chemical Reviews*, 119(8):5298–5415.

Yavuz, H., Babaç, C., Tuzlakoğlu, K., and Pişkin, E. (2002). Preparation and degradation of l-lactide and ε-caprolactone homo and copolymer films. *Polymer Degradation and Stability*, 75(3):431–437.

Yee, W. A., Nguyen, A. C., Lee, P. S., Kotaki, M., Liu, Y., Tan, B. T., Mhaisalkar, S., and Lu, X. (2008). Stress-induced structural changes in electrospun polyvinylidene difluoride nanofibers collected using a modified rotating disk. *Polymer*, 49(19):4196–4203.

Zadpoor, A. A. (2015). Mechanics of Biological Tissues and Biomaterials: Current Trends. *Materials (Basel, Switzerland)*, 8(7):4505–4511.

Zanetti Ferreira, T., Chen, H., Chen, K., Mouthuy, P. A., and Brassart, L. (2026). Hydrolytic degradation behaviour of electrospun poly(ε-caprolactone) filaments for biological tissue repair. *J Mech Behav Biomed Mater*, 175:107308.

Zhang, J., Liu, H., Ding, J.-X., Zhuang, X.-L., Chen, X.-S., and Li, Z.-M. (2015). Annealing regulates the performance of an electrospun poly(ε-caprolactone) membrane to accommodate tissue engineering. *RSC Advances*, 5(41):32604–32608.

Zhang, M., Chen, Y., Chiang, F.-P., Gouma, P. I., and Wang, L. (2019). Modeling the Large Deformation and Microstructure Evolution of Nonwoven Polymer Fiber Networks. *Journal of Applied Mechanics*, 86(1).

Zhang, M., Lu, W., Gouma, P. I., Xu, Z., and Wang, L. (2021). Theoretical prediction of effective stiffness of nonwoven fibrous networks with straight and curved nanofibers. *Composites Part A: Applied Science and Manufacturing*, 143:106311.

Zhang, Q., Jiang, Y., Zhang, Y., Ye, Z., Tan, W., and Lang, M. (2013). Effect of porosity on long-term degradation of poly (ε-caprolactone) scaffolds and their cellular response. *Polymer Degradation and Stability*, 98(1):209–218.

Zhang, X., Bogdanowicz, D., Erisken, C., Lee, N. M., and Lu, H. H. (2012). Biomimetic scaffold design for functional and integrative tendon repair. *J Shoulder Elbow Surg*, 21(2):266–77.

Zhao, L., Duan, G., Zhang, G., Yang, H., He, S., and Jiang, S. (2020). Electrospun Functional Materials toward Food Packaging Applications: A Review. *Nanomaterials*, 10(1):150.

Zhu, X., Cui, W., Li, X., and Jin, Y. (2008). Electrospun Fibrous Mats with High Porosity as Potential Scaffolds for Skin Tissue Engineering. *Biomacromolecules*, 9(7):1795–1801.

Zong, X.-H., Wang, Z.-G., Hsiao, B. S., Chu, B., Zhou, J. J., Jamiolkowski, D. D., Muse, E., and Dormier, E. (1999). Structure and Morphology Changes in Absorbable Poly(glycolide) and Poly(glycolide-co-lactide) during in Vitro Degradation. *Macromolecules*, 32(24):8107–8114.

Zuo, W., Zhu, M., Yang, W., Yu, H., Chen, Y., and Zhang, Y. (2005). Experimental study on relationship between jet instability and formation of beaded fibers during electrospinning. *Polymer Engineering & Science*, 45(5):704–709.

Zussman, E., Burman, M., Yarin, A. L., Khalfin, R., and Cohen, Y. (2006). Tensile deformation of electrospun nylon-6,6 nanofibers. *Journal of Polymer Science Part B: Polymer Physics*, 44(10):1482–1489.

Zündel, M., Ehret, A. E., and Mazza, E. (2019). The multiscale stiffness of electrospun substrates and aspects of their mechanical biocompatibility. *Acta Biomaterialia*, 84:146–158.

Zündel, M., Mazza, E., and Ehret, A. E. (2017). A 2.5D approach to the mechanics of electrospun fibre mats. *Soft Matter*, 13(37):6407–6421.